

DISS. ETH NO. 17663

**MICROSTRUCTURAL AND TEXTURAL DEVELOPMENT IN
SYNTHETIC ROCKSALT DEFORMED IN TORSION**

A dissertation submitted to

ETH ZURICH

for the degree of

Doctor of Science

presented by

MARINA ARMANN

Diplom-Geologin
Universität Erlangen-Nürnberg

born on February 14th, 1979

Citizen of Germany

accepted on the recommendation of

Prof. Dr. Jean-Pierre Burg
PD Dr. Luigi Burlini
Dr. Karsten Kunze
Prof. Dr. Chris J. Spiers

ETH Zürich
ETH Zürich
ETH Zürich
University of Utrecht

examiner
co-examiner
co-examiner
co-examiner

2008

"Das Schönste, was wir erleben können, ist das Geheimnisvolle. Es ist das Grundgefühl, das an der Wiege von wahrer Wissenschaft und Kunst steht. Wer es nicht kennt und sich nicht mehr wundern oder staunen kann, der ist sozusagen tot und sein Auge erloschen."

~

"The most beautiful thing we can experience is the mysterious. It is the source of all true art and all science. He to whom this emotion is a stranger, who can no longer pause to wonder and stand rapt in awe, is as good as dead: his eyes are closed."

~Albert Einstein~

Für meine Eltern

Jürgen & Gudrun

Table of contents

Acknowledgements	iv
Abstract	v
Kurzfassung	viii
Chapter 1 – Introduction	1
1.1 General background and motivation	1
1.2 Aim of the study	5
1.3 Organisation of the thesis	5
1.4 References	6
Chapter 2 – Deformation mechanisms	10
2.1 Elastic versus plastic deformation	10
2.2 Crystal defects	10
2.2.1 Point defects	10
2.2.2 Line defects	11
2.2.3 Planar defects	12
2.3 Ductile deformation mechanisms	12
2.3.1 Diffusional mass transfer	12
2.3.2 Intracrystalline plasticity	15
2.4 Microstructures	17
2.4.1 Recovery microstructure	17
2.4.2 Dynamic recrystallisation microstructure	19
2.5 Crystallographic preferred orientations and texture models	21
2.6 References	22
Chapter 3 – Methodology	25
3.1 Material	25
3.1.1 Struktur and properties of NaCl	25
3.2 Methods	26
3.2.1 Preparation of the starting material	26
3.2.2 Deformation apparatus – Paterson rig	28
3.2.3 Fourier transformation infrared spectroscopy (FTIR)	31
3.2.4 Optical microscopy	32
3.2.5 Electron backscatter diffraction (EBSD) technique	33
3.3 References	39
Chapter 4 – Mechanical behaviour of synthetic rocksalt deformed in torsion	40
4.1 Introduction	40
4.2 Method for determining jacket strength	40
4.3 Results	41
4.3.1 Behaviour of rocksalt samples in copper jacket	41
4.3.2 Behaviour of PTFE samples in copper jacket	46
4.3.3 Behaviour of salt sample in PE and PTFE jackets	48

4.4	Discussion	50
4.5	Conclusions	52
4.6	References	52
Chapter 5 – Polygonization and recrystallisation in synthetic rocksalt - observations from torsion experiments		57
5.1	Introduction	54
5.2	Methods	55
5.3	Results	58
	5.3.1 Starting material	58
	5.3.2 Deformed samples	59
5.4	Discussion	91
	5.4.1 Activity of slip systems	91
	5.4.2 Deformation mechanisms and recrystallisation	92
	5.4.3 Effect of strain and temperature	95
5.5	Conclusions	96
5.6	References	97
Chapter 6 – CPO development in synthetic rocksalt during torsion up to large shear strain		101
	Abstract	101
6.1	Introduction	101
6.2	Methods	102
	6.2.1 Starting material	104
	6.2.2 Deformation experiments	103
	6.2.3 Microscopy and EBSD	103
6.3	Results	104
	6.3.1 Starting material	104
	6.3.2 Mechanical behaviour	105
	6.3.3 Microstructure	106
	6.3.4. CPO	110
6.4	Discussion	117
	6.4.1 Deformation and recrystallisation mechanisms	117
	6.4.2 CPO	118
	6.4.3 Effect of strain	120
6.5	Conclusions	120
6.6	References	120
Chapter 7 – Summary and further research		124
7.1	Summary	124
7.2	Further research	125
7.3	References	127
Curriculum vitae		128

CD ROM

Appendices

Appendix A – List of conducted experiments

Appendix B – HKL files of NaCl

Appendix C – List of EBSD bulk scans
EBSD bulk orientation maps

Appendix D – List of EBSD detail scans
EBSD detail orientation maps

Appendix E – Uniaxial compression of single sodium chlorate crystals –
application to pressure solution

Acknowledgements

First of all I would like to say thank you to my Doktorvater, Jean-Pierre Burg, for his continual support – particularly during those difficult early years when the project changed focus. I would like to thank him too, for taking me to see rocksalt in its natural habitat. Merci beaucoup for everything! The next thank you goes to Luigi Burlini, who adopted me in his lab and introduced me to the experience of working with "Paty". That experience was sometimes a challenging one – especially with the endless leaking troubles, faulty furnaces and flying motors. However, it was fun! I would also like to thank Luigi for his invaluable support and for all the discussions we had. The wonderful looking EBSD orientation maps and the texture analysis would not have been in the thesis if Karsten Kunze had not been involved in this project. I thank Karsten for all the discussions and all the new things he taught me about texture analysis. The final stages of this work would just not have been possible without the support of Chris Spiers. A big thank you to him for all his help and support, and for all the time he made for our discussions.

At this point I would like to say thanks to Robert Hofmann, who always made sure that "Paty" was working efficiently and to Peter van Krieken, without whom I probably would be still in the lab trying to polish and etch rocksalt "monsters".

During the years here in Zürich I met a truly wonderful friend, Diane Seward, who looked after me as my mum would have done. Thanks, Diane and Terry for everything! The life of a PhD student would be much more difficult without the help of Regula Schaelchli, our secretary, Regula merci vielmals für alles! There are many more thank you's to spread, but space is limited and as we say in German: *In der Kürze liegt die Würze*, many thanks to:

Martin Burkhard, Rudy Wenk, Djordje Grujic, Yuri Podladchikov, Stefan Schmalholz, Neil Mancktelow, Jan Bisshop, Michel Bestmann, Martine Vernooji, Boris Kaus, Thomas Kocher, Martin Wipf, Urs Gerber, Hans de Bresser, Gill Pennock, Taras Gerya, Fernando Ornelas Marques, Ingrid Okanta, Frowin Pirowino, Peter Wägli, Asghar Dolati, Eliane Wuethrich, Chris Krugh, Michi Strasser, Claudio Delle Piane, Weronika Gorczyk, Luca Carrichi, Marion Campani, Pierre Bouilhol, Marcel Frehner, Marc Lambert, Beatriz Quintal, Brian Steiner, Sonja Scarselli, Jeroen Smit, Santanu Misra, Pauline Rais, Tonny Thomsen, Bettina Baitsch-Ghirardello, Emilia Liteaneu, Susanne Hangx, Rainer van Noort, Marielle Fraefel, Kerstin Zucali, Flo Büch, Jamie Ward and Andreas von Rétyi.

The last lines belong to my family, who supported me throughout all the years, who always believed in me, who sent me out to explore the world and who let me live the dream I had when I was five years old: to become a geologist.

Danke!

Mutti & Vati ~ Oma Anna ~ Oma & Opa und mein Bruderherz Toni

Abstract

This study deals with the development of microstructures and crystallographic preferred orientations (CPOs) in synthetic rocksalt (NaCl) deformed at 100, 200 and 300°C up to shear strains of $\gamma \sim 8$ in torsion. The aim of the study was to investigate the deformation mechanisms, the resulting microstructural processes and the development of CPOs with increasing shear strain and increasing temperature.

To achieve high shear strains, torsion experiments on cylindrical samples of synthetic rocksalt were carried out using a high temperature/high pressure Paterson gas medium apparatus. Experiments were conducted at constant twist rates corresponding to nominal strain rates of 3×10^{-5} , 3×10^{-4} and $3 \times 10^{-3} \text{ s}^{-1}$ and under a constant confining pressure of 250MPa. Microstructures were analysed using reflected light microscopy on polished and etched surfaces and were investigated in detail by means of the electron backscatter diffraction (EBSD) technique, which was also used for determining the crystallographic preferred orientations.

We observed that recrystallisation (dynamic and static), the amount of shear strain and temperature have a striking effect on the microstructure and the CPO. The experimentally produced microstructures and the corresponding CPOs are the result of three different regimes:

Deformation regime:

Shear deformation leads to elongated and flattened grains in approximate agreement with the finite strain ellipse. The deformed grains contain slip bands with a wavy character, which are interpreted as due to cross-slip of screw dislocations with $\langle 110 \rangle$ Burgers vector. The deformed grains contain a dense network of subgrains. The subgrains either have a blocky shape or a polygonal shape. Blocky subgrains are formed preferentially at low temperature (100°C) and are due to the intersection of horizontally and vertically running slip bands. Polygonal subgrains occur at higher temperature (200-300°C) by the process of climb controlled recovery. The CPO developed during shear deformation is characterised by a monoclinic symmetry and by two texture components, a pronounced $\{111\}\langle 110 \rangle$ and a weaker $\{001\}\langle 110 \rangle$ component.

Recrystallisation regime:

With increasing shear strain dynamic recrystallisation becomes dominant. Dynamic recrystallisation occurred by two processes; subgrain rotation recrystallisation and grain boundary migration recrystallisation. Subgrain rotation recrystallisation, which caused a major grain size reduction, occurred in samples with a shear strain $\gamma \geq 3$ and becomes dominant at shear strains of $\gamma \sim 6$ at 100°C and of $\gamma \sim 8$ at 200°C. Grain boundary migration recrystallisation, on the other hand, is indicated by irregular shaped grains with a cusped/lobate or bulged grain boundary geometry and the presence of an internal deformation structure in form of subgrains. It becomes important at higher temperatures (200 and 300°C) and dominates the microstructure at 300°C. The dynamic recrystallisation CPO that correspondingly developed is characterised by a single and strong $\{001\}\langle 110 \rangle$ texture component, resulting in orthorhombic sample symmetry.

Grain growth regime:

Static recrystallisation in form of grain growth occurred to a different amount in nearly all samples. The characteristic microstructure consists of large grains, showing no internal deformation features and with straight or sometimes bulged grain boundaries. The corresponding CPO is characterized by a slightly rotated $\{110\}\{110\}$ texture component.

We can conclude that the occurrence of subgrains, slip bands and a CPO suggests that rocksalt at all investigated temperatures deformed by dislocation processes. At 100°C the process of dislocation glide is dominant, whereas at 200 and 300°C climb-controlled recovery also occurred. The increase in shear strain leads to a decrease in grain size that is caused by dynamic recrystallisation in form of subgrain rotation recrystallisation at 100 and 200°C. An increase in temperature leads to an increase in grain size in connection with grain boundary migration recrystallisation. A decrease in strain rate leads to a microstructure that corresponds to a microstructure developed at higher temperature, i.e. at lower shear stress. The CPO that develops agrees and reflects the produced microstructure. The deformation microstructure is characterised by a deformation CPO that changes with increasing shear strain into a recrystallisation CPO in accordance with the observed recrystallisation microstructure.

Kurzfassung

Diese Arbeit befasst sich mit der Entwicklung von Mikrostrukturen und kristallographischen Vorzugsrichtungen (CPOs) in experimentell deformierten synthetischem Steinsalz (NaCl). Das Steinsalz wurde in Torsion unter Temperaturen von 100, 200 und 300°C zu hohen Scherbeträgen ($\gamma \sim 8$) verformt. Das Ziel der Arbeit war es die Deformationsmechanismen, die aus der Deformation resultierende Mikrostruktur, sowie die Entwicklung der Textur (auch kristallographische Vorzugsrichtungen, CPOs) als Folge von zunehmendem Scherbetrag und zunehmender Temperatur zu bestimmen und zu charakterisieren. Die Torsionsexperimente wurden an zylindrischen Steinsalzproben in einem Hochtemperatur/Hochdruck Paterson Apparat durchgeführt. Die Experimente erfolgten unter konstanten Rotationsraten, die nominalen Scherverformungsraten von 3×10^{-5} , 3×10^{-4} und $3 \times 10^{-3} \text{ s}^{-1}$ entsprechen, konstanten Temperaturen von 100, 200 und 300°C und unter einem konstanten Umgebungsdruck von 250MPa. Die Analyse der Mikrostrukturen erfolgte durch Lichtmikroskopie an polierten und geätzten Oberflächen unter einem Reflexionsmikroskop, detaillierte Untersuchungen der Mikrostrukturen wurde an Hand von Elektronenrückstreubeugung (EBSD) vorgenommen. Diese Methode wurde ebenfalls verwendet, um die CPOs zu ermitteln.

In dieser Studie konnte gezeigt werden, dass die experimentell produzierten Mikrostrukturen und die dazugehörigen CPOs in Abhängigkeit vom Scherverformungsbetrag und der Temperatur in drei verschiedene Regimes eingeteilt werden können:

Deformationsregime:

Scherdeformation führt in den verformten Proben zu ausgelängten und geplätteten Körnern nahezu in Übereinstimmung mit der finiten Verformungsellipse. Die deformierten Körner sind gekennzeichnet durch Gleitbänder, die zum Teil eine wellenförmige Geometrie zeigen, was auf die Quergleitung von Stufenversetzungen mit einem $\langle 110 \rangle$ Burgersvektor zurückzuführen ist. Desweiteren zeigen die deformierten Körner ein dichtes Netzwerk von Subkörnern. Diese Subkörner sind entweder blockförmig oder vieleckig ausgebildet. Blockförmige Subkörner werden vor allem bei 100°C gebildet und entstanden durch die Überschneidung von horizontalen und vertikalen Gleitbändern. Vieleckige Subkörner treten bevorzugt bei höheren Temperaturen von 200 und 300°C auf. Die Entstehung dieser Subkörner ist auf das Klettern von Versetzungen infolge von Erholungsprozessen zurückzuführen. Die kristallographische Vorzugsorientierung, die sich während der Scherdeformation entwickelte, ist charakterisiert durch eine monokline Symmetrie und zeichnet sich durch zwei Texturkomponenten aus, eine stärkere $\{111\}\langle 110 \rangle$ und eine abgeschwächte $\{001\}\langle 110 \rangle$ Komponente. Dieses CPO wird als Scherdeformations-CPO bezeichnet.

Rekristallisationsregime:

Dynamische Rekristallisation gewinnt mit zunehmendem Scherbetrag immer mehr an Bedeutung. In den deformierten Proben erfolgte die dynamische Rekristallisation durch zwei Prozesse; Subkornrotation und Korngrenzwanderung. Rekristallisation durch Subkornrotation erfolgte in Proben mit einem Scherbetrag $\gamma \geq 3$ und wird zum dominierenden Prozess bei höheren Scherbeträgen von $\gamma \sim 6$ bei 100°C und $\gamma \sim 8$ bei 200°C. Dieser Prozess verursachte eine wesentliche Verkleinerung in der Korngrösse. Rekristallisation durch Korngrenzwanderung äussert sich durch unregelmässig geformte Körner mit spitzigen

und/oder gebogenen Korngrenzen und der Anwesenheit einer internen Deformationsstruktur in Form von Subkörnern. Korngrenzwanderung ist ein wichtiger Rekristallisationsprozess bei höheren Temperaturen (200 und 300°C) und dominiert die Mikrostruktur in diesem Temperaturbereich. Die kristallographische Vorzugsrichtung, welche sich aufgrund der dynamischen Rekristallisation ausgebildet hat, ist gekennzeichnet durch eine orthorhombische Symmetrie und eine einzelne und starke $\{001\}\langle 110 \rangle$ Texturkomponente. Dieses CPO wird als Rekristallisations-CPO bezeichnet.

Kornwachstumsregime:

Statische Rekristallisation konnte in nahezu allen Proben beobachtet werden. Die hierfür typische Mikrostruktur ist gekennzeichnet durch grosse Körner, die keine Anzeichen von interner Deformation (Subkörner) zeigen und die gerade oder teilweise auch gebuchtete Korngrenzen aufweisen. Das CPO das sich infolge von Kornwachstum entwickelte zeigt eine leicht rotierte $\{110\}\langle 110 \rangle$ Texturkomponente mit einer monoklinen Symmetrie und wird Kornwachstums-CPO genannt.

Zusammenfassend kann gesagt werden, dass das Auftreten von Subkörnern, Gleitbändern und einer kristallographischen Vorzugsrichtung darauf schliessen lässt, dass die Deformation von Steinsalz bei 100, 200 und 300°C durch Versetzungsbewegung erfolgte. Die Deformation bei 100°C erfolgt durch Versetzungsgleiten, wohingegen Versetzungsklettern bei 200 und 300°C der dominierende Prozess ist. Eine Erhöhung des Scherverformungsbetrages führt zu einer Verringerung in der Korngrösse, das zurückzuführen ist auf dynamische Rekristallisation durch Subkornrotation bei hohen Scherverformungsbeträgen (100 und 200°C). Eine Erhöhung der Temperatur führt zu Kornvergrößerung in Verbindung mit Korngrenzwanderung. Eine Verringerung in der Scherverformungsrate führt zu einer Mikrostruktur, die einer Mikrostruktur bei höheren Temperaturen, beziehungsweise geringeren Scherspannungen entspricht. Die entstandenen kristallographischen Vorzugsorientierungen, entsprechen den Mikrostrukturen. Die Deformationsmikrostruktur wird durch eine Deformationstextur angezeigt die mit grösser werdenden Scherbetrag in eine Rekristallisationstextur übergeht.

Chapter 1

Introduction

This chapter provides a general background on the importance of rocksalt in nature, on shear zones, dynamic recrystallisation, the formation of crystallographic preferred orientation (CPO) and the evolution of texture. Additionally, the aim, scope and organisation of the thesis are presented.

1.1 General background and motivation

Crystalline halite (NaCl) is commonly known as rocksalt and belongs to the group of the evaporites. Evaporites form by evaporation of seawater from closed beds, playas and seas. The oldest salt deposits are Precambrian in age, e.g. Hormuz Formation in Iran (e.g. Bahroudi & Talbot 2003). Rocksalt occurs as layers in sedimentary basins all over the world (e.g. Death Valley, Fig. 1.1).

Salt dessication patterns on the surface



Fig. 1.1. Salt deposited at Badwater, Death Valley, USA, with typical dessication polygons formed at the surface. Photograph courtesy of R. Holliday, <http://www.mountaininterval.org>

The physical properties of rocksalt are unique compared to other rocks. It is a very soluble and weak material and it easily flows under solid state conditions because of its low yield strength. During compaction it develops a polycrystalline microstructure with a low permeability ($<10^{-20}\text{m}^2$) and stays nearly incompressible throughout burial and metamorphism. Rocksalt has an anomalously low density of 2.17g/cm^3 , compared to all other rocks which have densities of $2.6 - 3.0\text{g/cm}^3$.

Deformation on the large scale takes place by halokinesis and salt tectonics. Jackson & Talbot (1986) described several halokinesis mechanisms under which salt deformation can take place:

- i) Halokinesis by buoyancy is effective if the buried salt structure has a pre-existing relief and if the thickness of the denser overburden is $\sim 700\text{m}$. Then, density inversion may trigger the rise of salt into the lateral overburden.
- ii) For salt buried close to the surface, where the cover has a thin thickness halokinesis takes place by differential loading consequent to lateral variations in thickness, density, strength or strain rate in the salt layer and in the cover. The surface relief is efficient in initiating the flow of the salt.
- iii) Salt extruding on the Earth's surface becomes unstable due to its own weight and flows by gravity down the slope. For instance, in Iran, the salt is driven above its level for neutral buoyancy, forming extrusive salt domes that spread under their own weight. Here the fastest geologic strain rates (10^{-11} to 10^{-9}s^{-1} , Jackson 1985) are achieved.
- iv) A fourth mechanism put forward is halokinesis due to thermal convection. Salt buried in the crust is subjected to the Earth's heat flow. This creates a thermal gradient, which results in a density gradient in the salt, such that deeper salt may be unstable. This is because light, hot salt is overlain by dense, cold salt, which may result in thermal convection that increases the rate of heat flow upward through the salt. The thermal gradient combined with gravity makes the system unstable. Note, however, that this mechanism as put forward by Jackson & Talbot (1986), has been shown to be physically infeasible by van Keken et al. (1993) via a more vigorous consideration of the Rayleigh number.

Associated with halokinesis is the formation of typical salt structures. They can be classified following Jackson & Talbot (1986), in concordant, discordant intrusive and extrusive salt structures with increasing amplitude. Concordant salt structures with low amplitude are salt pillows, salt anticlines (Fig. 1.2) and salt rollers. Intrusive, discordant salt structures are salt diapirs, salt walls and salt stocks. Extrusive salt structures form when salt flows on the surface to form salt glaciers, one of the most spectacular salt structures (Fig 1.3).



Fig. 1.2. Salt dome structure in Great Kavir, Zagros (Iran). Photo courtesy of A. Bahroudi, www.diogenes.ethz.ch.

Salt dome and salt glacier



Fig. 1.3. Salt dome and salt glacier (left side of photo) in Kuh-e-Namak (Dashti Province, Iran). Neoproterozoic-Cambrian Hormuz salt basin, Zagros Mountains, southwestern Iran, pierced Tertiary country rocks and salt glaciers spread over a paleotopography from the dome summit. Photograph courtesy of A. Bahroudi, www.diogenes.ethz.ch.

Salt domes have been recognised and intensively studied because they frequently create traps for hydrocarbons. Additionally, salt domes have been recognised as a potentially long-term storage medium for dangerous materials such as high-low level radioactive waste or for strategic storage of oil, natural gas or hydrogen fuel. For these reasons, deformation experiments investigating the long-term stability and the mechanical behaviour of rocksalt have been carried out intensively (Heard 1972, Burke et al. 1981, Arieli et al. 1982, Carter & Hansen 1983, Wawersik & Zeuch 1986, Franssen & Spiers 1990, Horseman & Handin 1990, Horseman et al. 1992, Carter et al. 1993, Franssen 1994, Hunsche & Hampel 1999, Ter Heege et al. 2005). Comparison of microstructures from laboratory experiments with these seen in natural salt deformed at natural strain rates (five to eight orders of magnitude difference) has demonstrated that the deformation mechanisms activated in experiments are identical to those identified in natural samples (Spiers & Carter 1998). Most of the experimental work has been performed in axi-symmetric compression, where it is not possible to reach high strains (Fig. 1.4); only a few studies dealt with simple shear geometry (Knapp et al. 1987, Chester 1989, Shimamoto 1986, 1989a,b, Chester & Logan 1990). These simple shear experiments were performed at room temperature to understand the brittle and ductile behaviour of rocksalt. A detailed study on rheology, microstructure and texture in simple shear was done by Franssen & Spiers (1990), but these experiments were only able to reach shear strains of $\gamma \sim 2$, whilst shear strains of at least $\gamma = 10$ -20 have been reported in nature (e.g. Ramsay & Graham 1970).

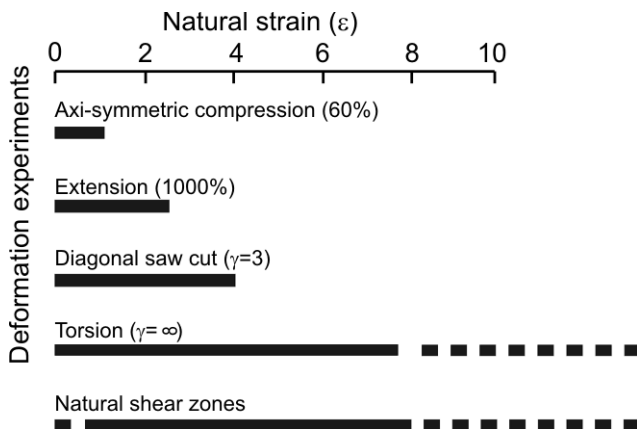


Fig. 1.4. Comparison of experimentally obtained strains in different deformation modes with the strain in natural shear zones. Figure modified after Barnhoorn (2003).

For this reason, it is important to extend the list of experiments to shear deformation mode, with the purpose to gain knowledge on the high shear strain behaviour of rocksalt.

Shear zones, an example is shown in Fig. 1.5. accommodate much deformation and can range from only a few millimetres, as shown in the work of Hobbs (1968), to kilometre scale (Schmid 1975). Commonly, rocks in shear zones are characterised by a pervasive grain size reduction, a strong foliation and a crystallographic preferred orientation (CPO).

Natural shear zone



Fig. 1.5. Natural shear zone in Patan (Pakistan) showing near symmetrical strain gradient from coarse grained protolith to strongly foliated, fine grained mylonite (dark band). Photograph courtesy of J.P. Burg, www.diogenes.ethz.ch

Grain size reduction in mylonitic rocks of shear zones is caused by dynamic recrystallisation and by metamorphic reactions. Dynamic recrystallisation can be attributed to two processes: Subgrain rotation recrystallisation (White 1976, Urai et al. 1986, Drury & Urai 1990) and migration recrystallisation, involving nucleation and the growth of the nucleus by grain boundary migration (Gordon & Vandermeer 1966, Drury & Urai 1990). Subgrain rotation recrystallisation involves the formation of new grains by the progressive rotation of subgrains. The misorientation between single subgrains and the host increases progressively with ongoing deformation until a misorientation of 10-15° is reached, when subgrain boundaries become high angle boundaries. On the other hand, migration recrystallisation involves the formation of new grains by local migration of grain boundaries from grains possessing a low dislocation density into grains with a higher dislocation density, which eventually get consumed. The driving force for migration recrystallisation lies in the difference of strain energy. However, water also plays a key role in recrystallisation processes because of its influence on grain boundary mobility. Several studies on deformed rocksalt (e.g. Peach et al. 2001, Ter Heege et al. 2005) showed that the rate of recrystallisation is enhanced with increasing water content.

Dynamic recrystallisation has a major influence on rheology, microstructure and on the development of CPOs. CPOs are attributed mainly to dislocation creep (e.g. Passchier &

Trouw 1998). CPOs can be used to determine the sense of shear, the strain path (simple or pure shear), the amount of strain or the deformation mechanism active during shearing (e.g. Passchier & Trouw 1998). Shear zones allow studying the progressive change in microstructure and CPO from the undeformed wall rock to the most deformed interior of the shear zone. Torsion experiments provide an excellent tool understanding the development of shear zones. In particular, these experiments allow studying the mechanics (rheology), microstructure and CPO over a large shear strain range and under controlled experimental conditions, such as temperature, shear strain rate and confining pressure. If the experimental microstructure and CPOs are similar to natural ones, the experimentally obtained properties may be extrapolated to natural deformation conditions. Nevertheless, one should still be cautious that strain rates accessible to experiments are several orders of magnitude higher than strain rates in nature. Torsion experiments were applied to several single phase materials; anhydrite (Heidelbach et al. 2001), anorthite (Ji et al. 2004), carrara marble (Barnhoorn et al. 2004, Pieri et al. 2001), calcite (Barber et al. 2007), gypsum (Barberini et al. 2005), dolomite (Delle Piane et al. 2007), quartz (Schmocker et al. 2003), olivine (Bystricky et al. 2000), magnesiowuestite (Heidelbach et al. 2003) and ice (Durand & Comes 1974, Durand 1975, Bouchez & Duval 1982). Rocksalt was chosen for this study because not many data on the evolution of microstructure and CPO of this mineral are available at high shear strains. Furthermore, rocksalt can be considered as good analogue model for magnesiowuestite which has the same structure and slip systems as halite.

1.2 Aim of the study

Despite the amount of work that has been carried on rocksalt, a number of interesting questions remained on the deformation behaviour, microstructural processes and the development of CPOs, particularly in simple shear geometry for which only limited shear strains have been achieved to date.

It is therefore the aim of this study to investigate the influence of shear strain, shear strain rate and temperature on the

- i) mechanical behaviour,
- ii) microstructure and
- iii) CPO (texture)

of polycrystalline synthetic rocksalt using torsion experiments at conditions favouring intracrystalline plasticity in the temperature range of 100-300°C and at shear strain rates of $\dot{\gamma} = 3 \times 10^{-5} \text{ s}^{-1}$, $3 \times 10^{-4} \text{ s}^{-1}$ and $3 \times 10^{-3} \text{ s}^{-1}$.

1.3 Organisation of the thesis

The thesis is organised in seven chapters.

Chapter 2 gives a general introduction into the research topic. It deals with the deformation mechanisms acting in rocks or materials that have undergone plastic deformation. Plastic deformation can occur by grain size sensitive or grain size insensitive mechanisms. The result of plastic deformation in a material can be seen in a characteristic microstructure and in the development of preferred crystallographic orientations.

Chapter 3 describes the methods used in this study. The high pressure/high temperature Paterson apparatus was used to carry out the experimental part of this study. Preparation techniques for the starting material and the preparation for microstructure analysis of the deformed samples are described in detail. Microstructural analysis was carried out by reflected light microscopy and by orientation mapping using the electron backscatter diffraction (EBSD) technique. Texture analysis was done on pole figures and inverse pole figures derived from EBSD.

Chapter 4 evaluates the mechanical data of rocksalt deformed in torsion experiments. It reports and discusses the influence of the jacket material on the strength of rocksalt and shows the difficulties in finding the appropriate jacket material.

Chapter 5 reports the influence of shear strain on the microstructure of rocksalt deformed at 100-300°C in torsion. It addresses the change from a shear deformation microstructure at low shear strains into a recrystallisation microstructure at high shear strains. It discusses the influence of strain, strain rate and temperature on the developing microstructure and the recrystallisation as well as the deformation mechanisms that are active under the investigated conditions. For a detailed microstructural analysis high resolution orientation maps were obtained by using EBSD.

Chapter 6 describes the influence of shear strain on the crystallographic preferred orientations (CPOs) and the texture formation. It extends the previous chapter and compares the microstructure with the development of CPOs.

Chapter 7 summarises the results in a common framework. The thesis concludes with a discussion of remaining questions, problems that have arisen during this study and further possible research topics conclude this thesis.

The Appendices comprise details on the experiments and microstructural analyses (EBSD orientation maps) as well as a brief summary of a further investigated study performed on uniaxial compression of single sodium chlorate crystals – applications to pressure solution.

1.4 References

Arieli, A., Heard, H.C. and Mukherjee, A.K. 1982. Deformation modelling in sodium chloride at intermediate and elevated temperatures. In: *Mechanical Testing for Deformation Model Development, ASTM STP 765* (edited by Rhode, R.W. & Swearingen, J. C.), 342-365.

Bahroudi, A. & Talbot, C.J. 2003. The configuration of the basement beneath the Zagros Basin. *Journal of Petroleum Geology* 26, 257-282.

Barber, D.J., Wenk, H.R., Gomez-Barreiro, J., Rybacki, E. & Dresen, G. 2007. Basal slip and texture development in calcite: new results from torsion experiments. *Physics and Chemistry of Minerals* 34(2), 73-84.

Barberini, V., Burlini, L., Rutter, E.H. & Dapiaggi, M. 2005. High-strain deformation tests on natural gypsum aggregates in torsion. In: *High-Strain Zones: Structure and Physical Properties* (edited by Bruhn, D. & Burlini, L.) 245. Geological Society London, Special Publications, 277-290.

- Barnhoorn, A., Bystricky, M., Burlini, L. & Kunze, K. 2004. The role of recrystallisation on the deformation behaviour of calcite rocks: large strain torsion experiments on Carrara marble. *Journal of Structural Geology* 26(5), 885-903.
- Bouchez, P.D. & Duval, P. 1982. The fabric of polycrystalline ice deformed in simple shear: experiments in torsion, natural deformation and geometrical interpretation. *Textures and Microstructures* 5, 171-190.
- Burke, P.M., Cannon, R.W. & Sherby, O.D. 1981. Intermediate and high temperature creep of sodium chloride. *Workshop on Structural Behaviour of Repository Materials, Sandia National Laboratories, Albuquerque, N.M., April 29.*
- Bystricky, M., Kunze, K., Burlini, L. & Burg, J.-P. 2000. High shear strain of olivine aggregates: Rheological and seismic consequences. *Science* 290(5496), 1564-1567.
- Carter, N.L. & Hansen, F.D. 1983. Creep of Rocksalt. *Tectonophysics* 92(4), 275-333.
- Carter, N.L., Horseman, S.T., Russell, J.E. & Handin, J. 1993. Rheology of Rock-Salt. *Journal of Structural Geology* 15(9-10), 1257-1271.
- Chester, F.M. 1989. Dynamic Recrystallization in Semi-Brittle Faults. *Journal of Structural Geology* 11(7), 847-858.
- Chester, F.M. & Logan, J.M. 1990. Frictional faulting in polycrystalline halite: correlation of microstructure, mechanism of slip, and constitutive behaviour. In: *The Brittle-Ductile Transition in Rocks* (edited by Duba, A.G. et al.) 56. Geophysical Monograph, 49-65.
- Delle Piane, C., Burlini, L. & Grobety, B. 2007. Reaction-induced strain localization: Torsion experiments on dolomite. *Earth and Planetary Science Letters* 256(1-2), 36-46.
- Drury, M.R. & Urai, J.L. 1990. Deformation-Related Recrystallization Processes. *Tectonophysics* 172(3-4), 235-253.
- Durand, E. 1975. L'essai de torsion et al resistace au cisaillement des roched. *Rock Mechanics* 7, 199-230.
- Durand, E. & Comes, G. 1974. L'essai de torsion et la resistance au cisaillement des roches. In: *Advances in Rock Mechanics: Proceedings of the Third Congress of the International Society for Rock Mechanics*, Denver, Colorado, September 1-7, 226-232.
- Franssen, R.C.M.W. 1994. The Rheology of Synthetic Rock-Salt in Uniaxial Compression. *Tectonophysics* 233(1-2), 1-40.
- Franssen, R.C.M.W. & Spiers, C.J. 1990. Deformation of polycrystalline salt in compression and in shear at 250-350°C. In: *Deformation Mechanisms, Rheology and Tectonics* (edited by Knipe, R.J. & Rutter, E.H.) 45. Geological Society Special Publication, 201-213.
- Gordon, P. & Vandermeer, R.A. 1966. *Recrystallisation, grain growth and textures*. A.M.S., Ohio.
- Heard, H.C. 1972. Steady-state flow in polycrystalline halite at pressure of 2 Kilobars. In: *Flow and Fracture of Rocks* (edited by Heard, H.C. et al.) 16. Geophysical Monograph, 99-115.

- Heidelbach, F., Stretton, I. & Kunze, K. 2001. Texture development of polycrystalline anhydrite experimentally deformed in torsion. *International Journal of Earth Sciences* 90, 118-126.
- Heidelbach, F., Stretton, I., Langenhorst, F. & Mackwell, S. 2003. Fabric evolution during high shear strain deformation of magnesiowuestite (Mg_{0.8}Fe_{0.2}O). *Journal of Geophysical Research-Solid Earth* 108(B3), 14.
- Hobbs, B. E. 1968. Recrystallization of Single Crystals of Quartz. *Tectonophysics* 6(5), 353-401.
- Horseman, S.T. & Handin, J. 1990. Triaxial compression tests on rock salt at temperatures from 50° to 200° and strain rates from 10⁻⁴ to 10⁻⁹/s. In: *The Brittle-Ductile Transition in Rocks* (edited by Duba, A.G. et al.) 56. Geophysical Monographs, 103-110.
- Horseman, S.T., Russell, J.E., Handin, J. & Carter, N.L. 1992. Slow experimental deformation of Avery Island salt. In: *7th International Symposium on Salt*, Kyoto, Japan.
- Hunsche, U. & Hampel, A. 1999. Rock salt - the mechanical properties of the host rock material for a radioactive waste repository. *Engineering Geology* 52(3-4), 271-291.
- Jackson, M.P.A. 1985. Natural strain in diapiric and glacial rock salt, with emphasis on Oakwood Dome, East Texas (edited by Bureau of Economic Geology, TX).
- Jackson, M.P.A. & Talbot, C.J. 1986. External shapes, strain rates and dynamics of salt structures. *Geological Society of America Bulletin* 97, 305-323.
- Ji, S.C., Jiang, Z.T., Rybacki, E., Wirth, R., Prior, D. & Xia, B. 2004. Strain softening and microstructural evolution of anorthite aggregates and quartz-anorthite layered composites deformed in torsion. *Earth and Planetary Science Letters* 222(2), 377-390.
- Knapp, S.T., Friedman, M. & Logan, J.M. 1987. Slip and Recrystallization of Halite Gouge in Experimental Shear Zones. *Tectonophysics* 135(1-3), 171-183.
- Passchier, C.W. & Trouw, R.A.J. 1998. *Microtectonics*. Springer-Verlag, Berlin Heidelberg.
- Peach, C.J., Spiers, C.J. & Trimby, P.W. 2001. Effect of confining pressure on dilatation, recrystallization, and flow of rock salt at 150 degrees C. *Journal of Geophysical Research-Solid Earth* 106(B7), 13315-13328.
- Pieri, M., Burlini, L., Kunze, K., Stretton, I. & Olgaard, D.L. 2001. Rheological and microstructural evolution of Carrara marble with high shear strain: results from high temperature torsion experiments. *Journal of Structural Geology* 23(9), 1393-1413.
- Ramsay, J.G. & Graham, R.H. 1970. Strain Variation in Shear Belts. *Canadian Journal of Earth Sciences* 7(3), 786-&.
- Schmid, S.M. 1975. The Glarus overthrust: field evidence and mechanical model. *Eclogae geologicae Helveticae* 68, 247-280.
- Schmocker, M., Bystricky, M., Kunze, K., Burlini, L., Stunitz, H. & Burg, J.-P. 2003. Granular flow and Riedel band formation in water-rich quartz aggregates experimentally deformed in torsion. *Journal of Geophysical Research-Solid Earth* 108(B5).

- Shimamoto, T. 1986. Transition between Frictional Slip and Ductile Flow for Halite Shear Zones at Room-Temperature. *Science* 231(4739), 711-714.
- Shimamoto, T. 1989a. Mechanical behaviours of simulated halite shear zones: implications for the seismicity along subducting plate-boundaries. In: *Rheology of solids and of the Earth* (edited by Karato, S. & Toriumi, M.), 351-373.
- Shimamoto, T. 1989b. The Origin of S-C Mylonites and a New Fault-Zone Model. *Journal of Structural Geology* 11(1-2), 51-64.
- Spiers, C.J. & Carter, N.L. 1998. Microphysics of rocksalt flow in nature. In: *The mechanical behavior of salt, Proceedings of the 4th conference* (edited by Aubertin, M. and Hardy, H.R.), 115-128.
- Ter Heege, J.H., De Bresser, J.H.P. & Spiers, C.J. 2005. Rheological behaviour of synthetic rocksalt: the interplay between water, dynamic recrystallization and deformation mechanisms. *Journal of Structural Geology* 27(6), 948-963.
- Urai, J.L., Spiers, C.J., Zwart, H.J. & Lister, G.S. 1986. Weakening of Rock Salt by Water During Long-Term Creep. *Nature* 324(6097), 554-557.
- van Keken, P.E., Spiers, C.J., van den Berg, A.P. & Muzyert, E.J. 1993. The effective viscosity of rocksalt: implementation of steady-state creep laws in numerical models of salt diapirism. *Tectonophysics* 225(4), 457-476.
- Wawersik, W.R. & Zeuch, D.H. 1986. Modeling and Mechanistic Interpretation of Creep of Rock Salt below 200-Degrees-C. *Tectonophysics* 121(2-4), 125-152.
- White, S. 1976. Effects of Strain on Microstructures, Fabrics, and Deformation Mechanisms in Quartzites. *Philosophical Transactions of the Royal Society of London Series a-Mathematical Physical and Engineering Sciences* 283(1312), 69-86.

Chapter 2

Deformation mechanisms

Halite may deform already at room temperature by intracrystalline plasticity or by pressure solution or by a combination of the two processes. These deformation mechanisms are explained in the following section. For the sake of completeness, the other deformation processes, like grain boundary and volume diffusion and grain boundary sliding are briefly described. Because of its relevance to this thesis, the characteristic deformation microstructure will be described only for intracrystalline plasticity. The chapter concludes with an overview on crystallographic preferred orientations (CPO).

2.1 Elastic versus plastic deformation

A rock or any solid crystal deforms as soon as stress is applied. At the beginning, the material undergoes a linear stress – strain behaviour until the yield strength is reached. If deformation stops before this point, the material reacts in an elastic way and turns back to its original shape. If a material undergoes deformation that exceeds the yield point, the atomic bonds will break and will re-establish in different places, therefore a non-reversible and permanent plastic deformation will occur. Plastic deformation includes brittle and ductile deformation. Depending on temperature and confining pressure, rocks can deform in both ways. Ductile deformation occurs at higher temperatures and lithostatic pressure, i.e. at deeper crustal levels than brittle deformation, which is dominant at low temperature and pressure, i.e. shallower crustal levels. Experiments in this study were carried out under elevated temperatures and under a medium confining pressure and fall into the field of ductile deformation. Therefore, the focus in this chapter lies on ductile deformation mechanisms.

2.2 Crystal defects

Before describing the plastic deformation mechanisms a brief introduction into the subject of crystal defects is necessary. Crystal defects are imperfections in the crystal lattice and can be divided into three groups: point defects, line defects and planar defects.

2.1.1 Point defects

Point defects (Fig. 2.1) are defects in a crystal lattice where an atom is missing or the atom is located on an irregular place. Vacancies, self-interstitial atoms, interstitial impurity atoms and substitutional atoms belong to the group of point defects. Vacancies are empty sites in the crystal lattice, where atoms are missing. They are common at high temperatures when atoms frequently and randomly change their positions leaving empty lattice sites behind. Self-interstitials atoms are extra atoms which occupy a site in the lattice at which there is usually no atom. Substitutional impurity atoms are atoms of a different type than the bulk atoms, which replace bulk atoms in the lattice.

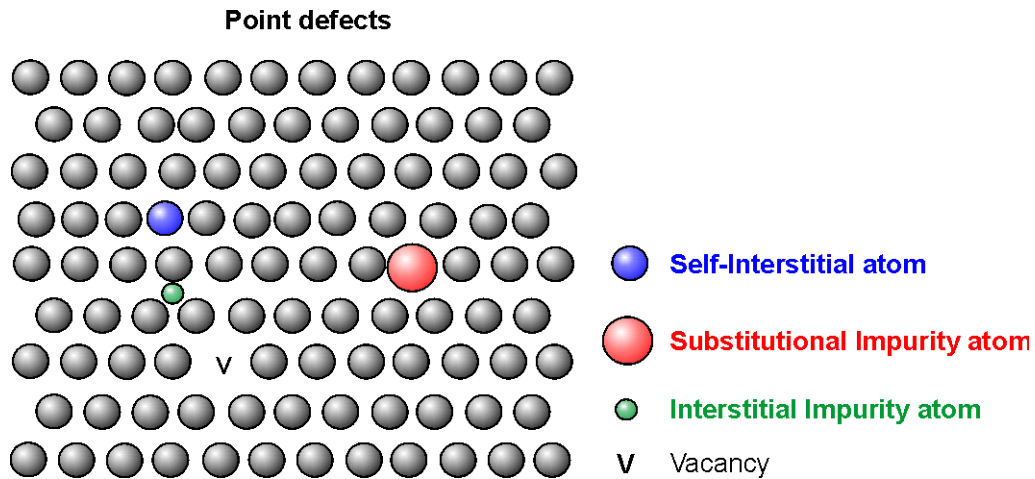


Fig. 2.1. Point defects in a crystal lattice; self-interstitial atoms (blue), substitutional impurity atoms (red), interstitial atoms (green) and vacancies (v). Figure modified after van der Pluijm and Marshak (1997).

2.1.2 Line defects

Line defects are usually known as dislocations. Dislocations are lines around which the atoms are out of their periodic position in the crystal lattice. They are characterised by the direction of the lattice displacement (Burgers vector) and the dislocation line. Two end-member types of dislocations (Fig. 2.2) are edge and screw dislocations. Edge dislocations are defects where an extra half plane is introduced into the crystal lattice. In edge dislocations the Burgers vector and the dislocation line are perpendicular. In screw dislocations, the atoms are arranged in a cork-screw like fashion and the axis of the screw marks the dislocation line. In this case the Burgers vector and the dislocation line are parallel.

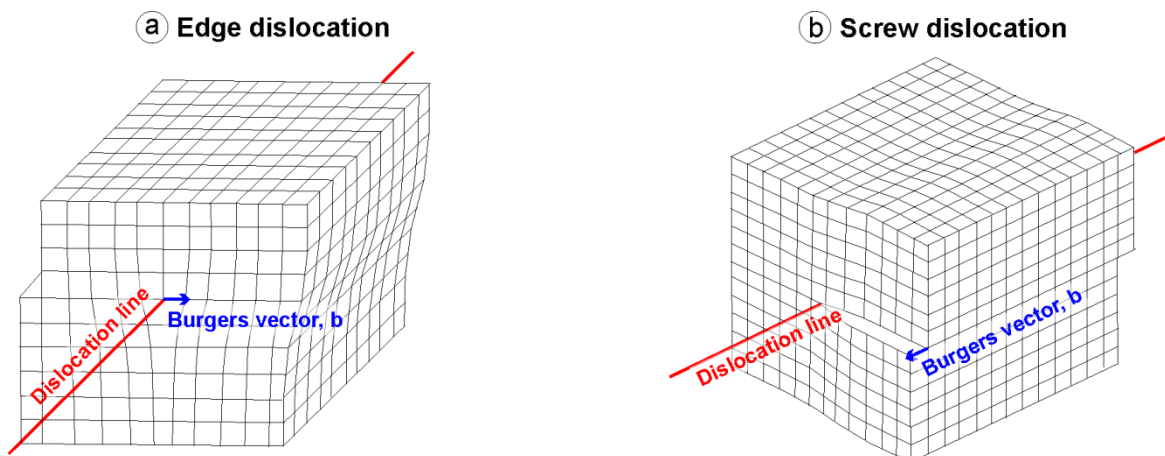


Fig. 2.2. a) Edge dislocation in crystal lattice; dislocation line and Burgers vector b are perpendicular to each other. b) Screw dislocation; dislocation line and Burgers vector b are parallel to each other.

2.1.3 Planar defects

Planar or two-dimensional defects include grain boundaries, twin boundaries, stacking faults and anti phase boundaries. Grain boundaries are defects separating grains of different lattice orientation (Poirier 1985). Two types of boundaries can be distinguished, if the misorientation between the grains is small, then the boundary is called a low angle boundary, if the misorientation between the grains is large then the boundary is called a high angle boundary. A twin boundary develops during deformation twinning. A stacking fault is a local region in the crystal where the regular sequence of identical atom layers has been interrupted (Poirier 1985).

2.3 Ductile deformation mechanisms

Ductile deformation in rocks occurs by two main mechanisms: diffusional mass transfer and intracrystalline plasticity. Diffusional mass transfer includes the processes of volume and grain boundary diffusion and pressure solution. These processes are grain size sensitive and deformation is achieved by the movement of point defects. The second mechanism, intracrystalline plasticity includes the processes of dislocation glide and dislocation climb. This mechanism is (in a certain range) insensitive to grain size and deformation occurs by the movement of dislocations. Fig. 2.3 shows a general deformation mechanisms map under which conditions these processes are expected to occur.

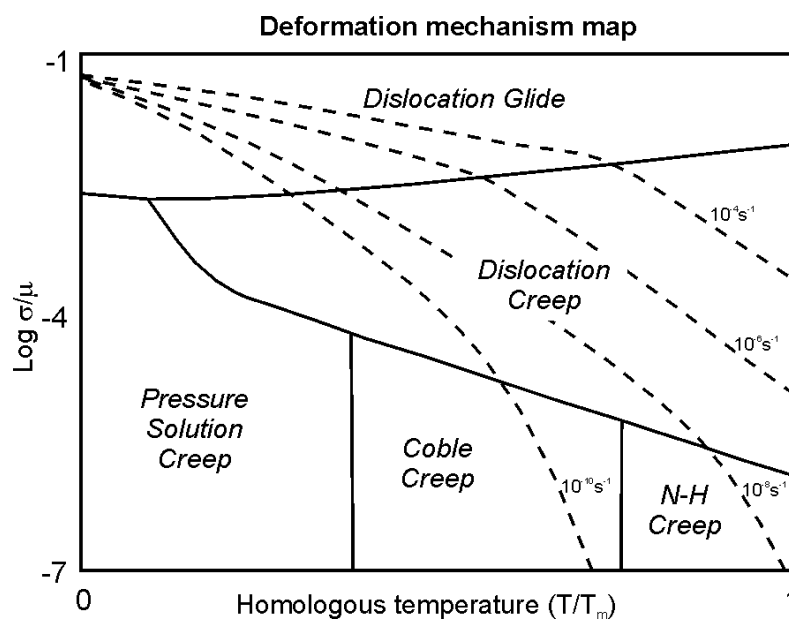


Fig. 2.3. Schematic illustration of a general and simplified deformation mechanism map showing normalised stress vs homologous temperature, where μ is the shear modulus and T_m the melting temperature. Dashed lines represent constant strain rates. N-H stands for Nabarro-Herring Creep. Figure from Spiers (2006).

2.3.1 Diffusional mass transfer

Deformation in the diffusion creep field takes place by transfer of material from areas of high compressive stress to areas of low compressive stress. Deformation can occur by the following processes: grain boundary diffusion, volume diffusion and pressure solution. Diffusion processes are thermally activated because the thermal energy causes the atoms to vibrate and thus makes it easier to break atomic bonds and to reattach easier.

Grain boundary diffusion and volume diffusion

Grain boundary diffusion (also known as Coble creep) and volume diffusion (known as Nabarro-Herring creep) are processes, where diffusion occurs without the presence of a fluid. Therefore, they are called solid state diffusion processes. In both processes vacancies migrate to sites where the stress is highest and atoms move to sites where the stress is lowest, as illustrated in Fig. 2.4. The difference between the two processes lies in the path of the migrating vacancies and atoms. In the case of the grain boundary diffusion, the diffusion process occurs along grain boundaries, whereas during volume diffusion, diffusion occurs within the crystal or grain. However, the result of this migration is a change in the distribution of mass and thus leads to a change in the shape of the crystal, without altering the crystal lattice.

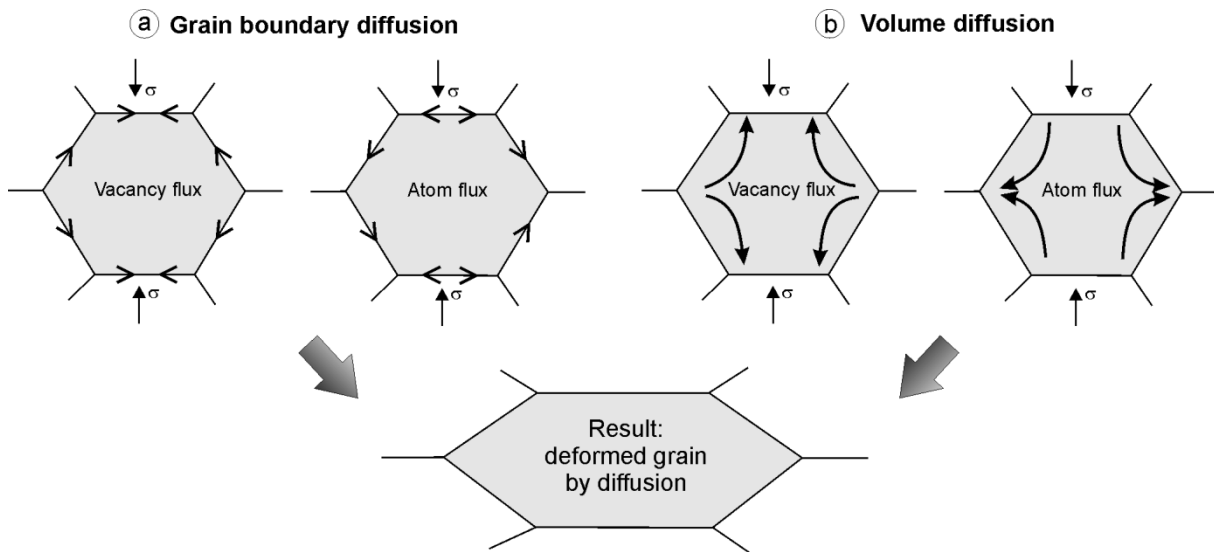


Fig. 2.4. a) Grain boundary diffusion (Coble creep), diffusion of vacancies and atoms takes place along the grain boundaries, indicated by arrows. b) Volume diffusion (Nabarro-Herring creep), diffusion process of vacancies and atoms takes place within the grain volume. Diffusion of vacancies and atoms in both processes leads to a change of the grain shape.

The transport of atoms and vacancies in the diffusion creep field is a thermally activated process and the diffusion depends strongly on the grain size. It is characterised by a linear relationship between the strain rate ($\dot{\epsilon}$) and the differential stress (σ).

The rate equation for diffusion creep can be expressed as:

$$\dot{\epsilon} = A \exp\left(\frac{-Q}{RT}\right) \frac{\sigma}{d^m} \quad \text{Eq. 2.1}$$

In this equation, A is a pre-exponential factor, Q is the activation energy, R is the gas constant, T is the temperature, d is the grain size, m the grain size exponent ($m=2$ for volume diffusion, and $m=3$ for grain boundary diffusion). For Coble creep the activation energy is lower than for Nabarro-Herring creep. Coble creep, where grain boundary diffusion controls the creep rate is more significant in crustal rocks and at lower temperatures, whereas Nabarro-Herring creep is active at higher temperatures, like in the mantle. The strain rate is more sensitive to a change in grain size for Coble creep than it is for Nabarro-Herring creep. Coble creep is more dominant at smaller grain sizes.

Pressure solution

In contrast to grain boundary and volume diffusion processes, pressure solution or solution transfer requires the presence of a fluid along the grain boundaries. During pressure solution, dissolution of the material takes place at sites of high compressional stress. The dissolved material diffuses along the grain boundaries in a fluid film and along a chemical gradient. Precipitation of the transported material occurs at sites with low compressional stress. Fig. 2.5 illustrates how pressure solution works. The strain rate associated with this process in salt is controlled by grain boundary diffusion and can be expressed by the following equation from de Meer & Spiers (1999):

$$\dot{\epsilon} = \frac{ADC\delta\Omega}{RTd^3} \quad \text{Eq. 2.2}$$

Where, $\dot{\epsilon}$ is the strain rate, A is a geometrical factor (dependent on grain shape and porosity), D is the diffusivity of the solute in the grain boundary fluid, C_0 is the solubility of the solute, δ is the effective grain boundary width, Ω is the molare volume of the solid, R is the gas constant, T the absolute temperature and d is the grain size.

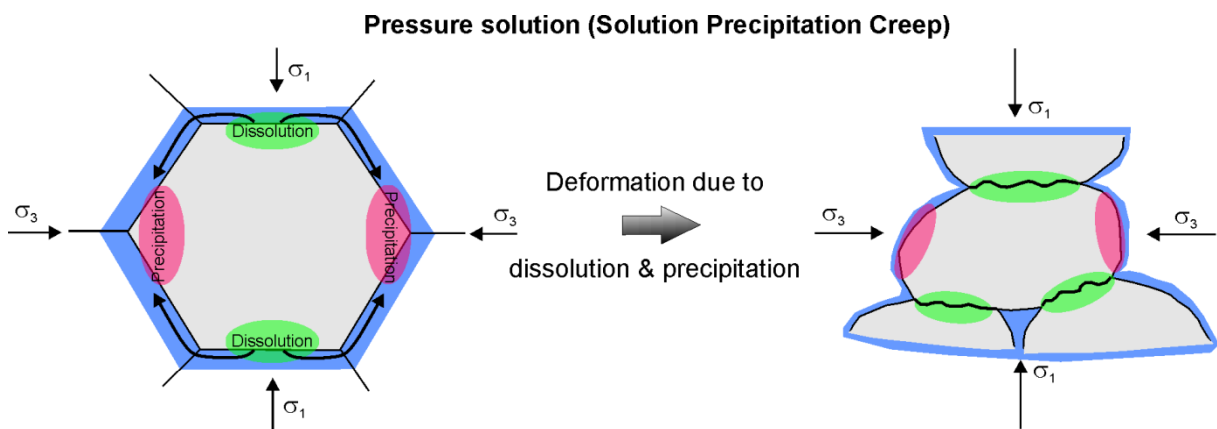


Fig. 2.5. Change of grain shape during pressure solution occurs due to the migration of dissolved material from sites with high stress, through a fluid along the grain boundaries to sites with low stress where precipitation of the material occurs.

Pressure solution is an important deformation mechanism in rocks deforming in the Earth's crust, because it can be activated at lower temperatures than diffusional mass transfer. Pressure solution in deformed halite was observed by e.g. Spiers et al. (1990), Spiers & Carter (1998), Schutjens & Spiers (1999) and Ter Heege et al. (2005).

Superplasticity or grain boundary sliding

Grain boundary sliding occurs when grains slide past each other and accommodate deformation by switching their neighbours (Fig. 2.6). Due to this process large amount of strain can be accommodated in rocks. Grain boundary sliding is characterised by a power-law rheology with a stress exponent n between 1 and 2 and is operative only in materials with very small grain sizes and at high temperature to facilitate diffusion.

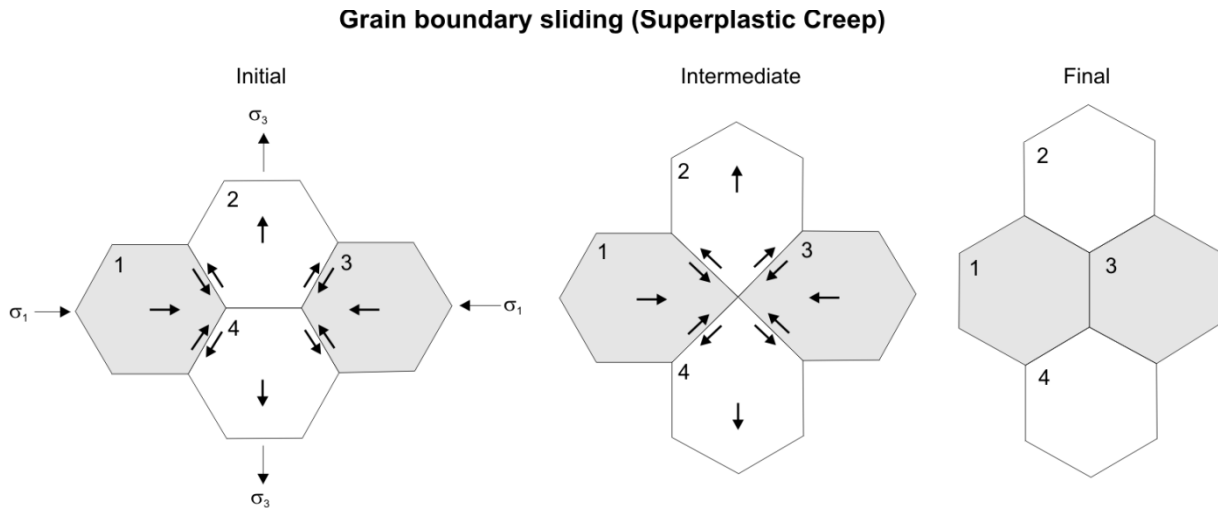


Fig. 2.6. Deformation is accommodated by the switching of neighbour grains as illustrated in this figure, where in the final state grain1 and grain3 become neighbours. Figure modified after van der Pluijm and Marshak (1997).

2.3.2 Intracrystalline plasticity

Intracrystalline plasticity is the mechanism where deformation is achieved by the movement of dislocations. This movement occurs by glide or a combination of glide and climb, depending upon temperature. Dislocation glide (glide-controlled creep) and dislocation creep (recovery-controlled creep) lead to the deformation of rocks. These two processes will be described in the following section. Dislocation glide and dislocation creep can be described by a power-law relationship where between the strain rate ($\dot{\epsilon}$) and the differential (σ):

$$\dot{\epsilon} = A \exp\left(\frac{-Q}{RT}\right) \sigma^n \quad \text{Eq. 2.3}$$

Where, A is a pre-exponential factor, Q is the activation energy, R is the gas constant, T is the temperature and n the stress exponent.

Dislocation glide

At low temperature the movement of dislocations is restricted to glide on slip planes under an applied shear stress. Deformation by this process is achieved by the glide movement of dislocation under an applied stress in a glide plane and in a glide direction (Fig. 2.7). Migration of dislocations through the crystal lattice occurs if stress is applied to the crystal. However, the movement of the dislocation can be impeded by the lattice friction (i.e. Peierls force) and by obstacles. This resistance is overcome by stress-assisted thermal vibrations. A moving dislocation separates a slipped from an unslipped region. When a dislocation reaches the edge of a crystal it leaves an offset (on the atomic level) at its edge, which produces a stair-step structure along the grain boundary of the crystal or grain if many dislocations accumulate closely.

Glide controlled creep is a mechanism that takes place at low temperature and high stress. It typically is associated with work hardening. Near steady state establishes if accompanied by

dynamic recrystallisation. Dislocation glide is dominant in halite at low temperature and high stress.

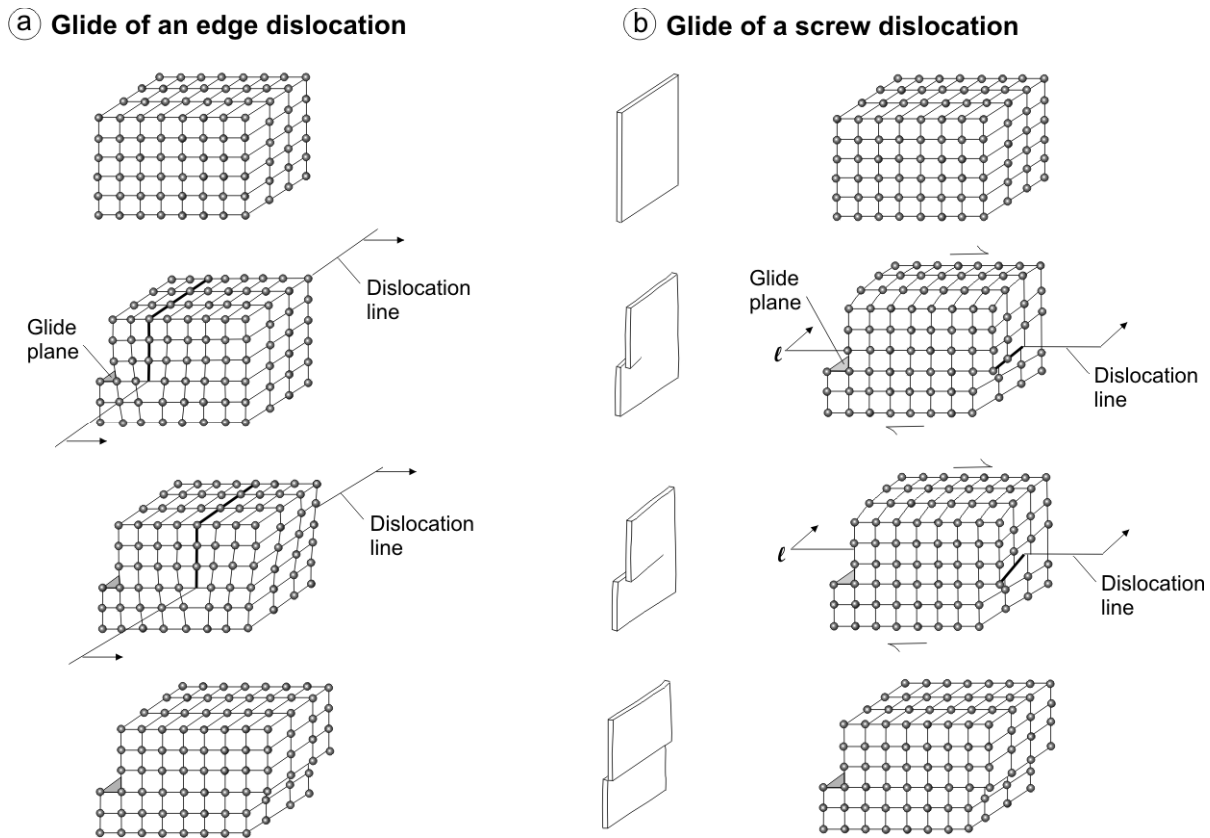


Fig. 2.7. a) Movement of an edge dislocation through a cubic lattice. b) Movement of a screw dislocation through the crystal lattice. The movement is analogous to tearing a paper. Once the dislocation passes through the lattice it leaves a perfect crystal with a changed shape behind in both cases. Figure modified after van der Pluijm and Marshak (1997).

Dislocation creep

The rate of glide deformation is limited by obstacles which are too large to be overcome by stress-assisted thermal vibration. Instead, long range recovery processes (dislocation climb and/or cross slip) are needed to by-pass or annihilate obstacles. When temperature is enhanced and vacancies diffuse through the dislocations cores, edge dislocations are able to climb out of their plane.

Dislocation climb

The climb process (Fig. 2.8) enables edge dislocations to climb out of their slip plane, to annihilate under the action of attractive forces, to untangle, and to order themselves into low energy (stable) configurations such as tilt walls. The walls form a 3-D polygonal network, called subgrains. The climb of edge dislocations is facilitated at higher temperature.

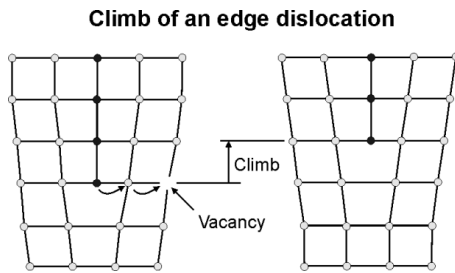


Fig. 2.8. Climb of an edge dislocation at elevated temperature, enabled due to the migration of vacancies. Figure modified after van der Pluijm and Marshak (1997).

Cross-slip

Cross-slip (Fig. 2.9) is the glide of screw dislocations from one plane to another with the same slip direction (same Burgers vector). Cross-slip allows screw dislocations an extra mobility. In the microstructure, cross-slip can be recognised in the form of wavy slip bands. Cross-slip on $\{111\}$ planes, operating in halite was recognised by Matucha (1968) and by Strunk (1975). The mechanism takes place at high stresses.

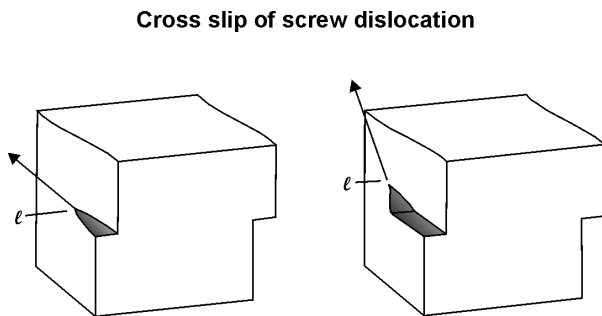


Fig. 2.9. Cross slip. Screw dislocations are able to move out of their plane to the next lattice plane to overcome obstacles. Figure modified after van der Pluijm and Marshak (1997).

2.4 Microstructures

Microstructures developing during intracrystalline plasticity are also the result of two additional processes; recovery and recrystallisation.

Recovery is a process by which the material lowers its internal strain energy, which it derived from the insertion of dislocations into the crystal lattice during plastic deformation. Recrystallisation is the process of the formation of new grains. The process can occur during deformation, called dynamic recrystallisation or after deformation, called static recrystallisation.

2.4.1 Recovery microstructure

If two dislocations of the opposite sign meet each other (Fig. 2.10), then they will annihilate each other, whereas their contribution to the internal strain energy will be released and dislocation tangles and forests will be removed. This process happens until no annihilation can take place anymore. After annihilation, these dislocations will arrange themselves into arrays, or dislocation walls (tilt walls). With further deformation more and more dislocations

will arrive in that wall which leads to a progressive misorientation across the wall, which will become a subgrain boundary. The process leads to some subdivision of the grain into smaller grains – which is referred to subgrain formation or polygonization (Poirier 1985). The subgrains are characterised by low angle boundaries, with misorientation angle $\theta < 15^\circ$. In literature there is no clear assignment for the limit of a low angle boundary, some authors use 10° , whereas others use 15° . An increase in the misorientation of the boundary will increase the energy of the boundary but decrease the number of dislocations around and therefore the material lowers its internal strain energy.

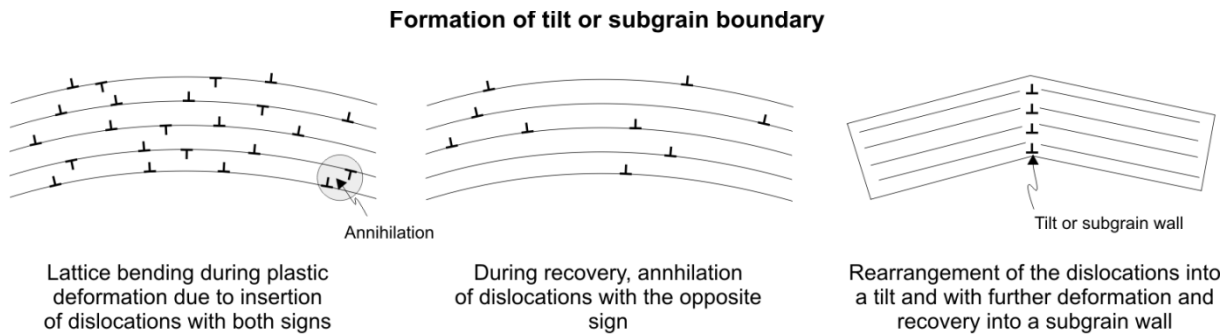


Fig. 2.10. Recovery of a bent crystal containing edge dislocations. Figure modified after Humphreys and Hatherly (2004).

Subgrain formation in halite has been observed in wet and in dry deformed samples (e.g. Guillopé & Poirier 1979, Franssen 1993, Ter Heege et al. 2005). An example is shown in Fig. 2.11 below.

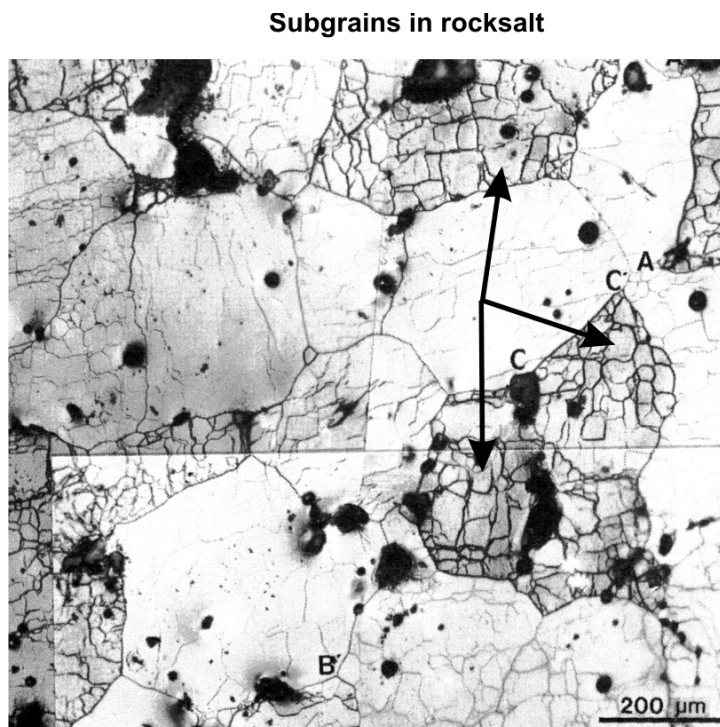


Fig. 2.11. Subgrains (black arrows) in dry experimentally sheared rocksalt at $T=365^\circ\text{C}$ to a shear strain $\gamma \sim 0.3$, Photo taken from Franssen (1993).

2.4.2 Dynamic recrystallisation microstructure

Recrystallisation during deformation (dynamic recrystallisation) involves two basic processes: the migration of grain boundaries and the formation of new grain boundaries (e.g. Drury and Urai 1990). The migration of grain boundaries involves the transfer of material across the grain boundary and occurs at elevated temperatures ($T > 0.3 T_m$). The formation of new grains on the other hand takes place by progressive misorientation of subgrain boundaries (e.g. Poirier & Nicolas 1975, White 1976, Guillopé & Poirier 1979) or by nucleation.

Subgrain rotation recrystallisation

Subgrain rotation recrystallisation is the process of the progressive misorientation of neighbour subgrains until they exceed a misorientation angle $\theta > 15^\circ$ and become newly formed strain free grains (Fig. 2.12). In deformed halite it was observed e.g. by Guillopé & Poirier 1979, Franssen 1994, Pennock et al. 2005.

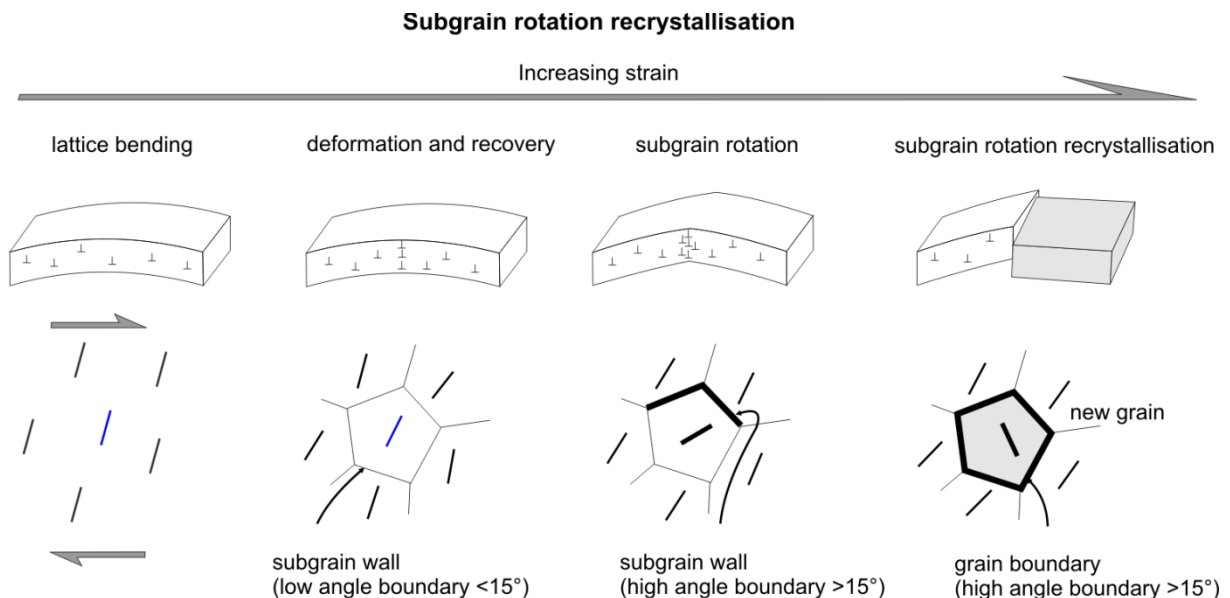


Fig.2.12. Subgrain rotation recrystallisation. Formation of new grains with increasing strain due to the progressive misorientation of subgrains. Onset of deformation as shown by lattice bending. With increasing shear strain deformation and recovery processes become active and dislocations move into a subgrain wall. With further strain, rotation of subgrain and finally formation a new high angle boundary. Figure from Bestmann and Prior (2003).

Grain boundary migration recrystallisation

Migration recrystallisation (Fig. 2.13) is the process where new grains are formed by nucleation, and growth occurs by migration of grain boundaries. Grain boundaries of grains, which possess no or little internal strain energy (dislocation defects) move into grains which have a high internal strain energy, and thus consume these grains. A characteristic feature of grain boundary migration are bulged or lobate grain boundaries.

The movement of the grain boundaries takes place by transport of single atoms from one grain across the boundary to the other grain. This motion results in the migration of the boundary in the opposite direction. There are several driving forces for grain boundary migration (GBM), in decreasing order of magnitude they are chemical, strain energy (stored as dislocations), elastic energy, grain boundary energy. Driving force for migration is the difference between, for example, the dislocation energy state on either side of the boundary (GBM driven by dislocation density contrasts). The rate at which a boundary migrates is both a function of this driving force and the mobility of the boundary, thus migration is mostly operative at higher temperature. However, the presence of a fluid along grain boundaries enhances their migration. Grain boundary migration recrystallisation in halite (Fig. 2.14) is an ubiquitous mechanism as shown in several studies (e.g. Guillopé & Poirier 1979, Urai et al. 1986, Franssen 1993, Trimby et al. 2000, Peach et al. 2001, Ter Heege et al. 2005).

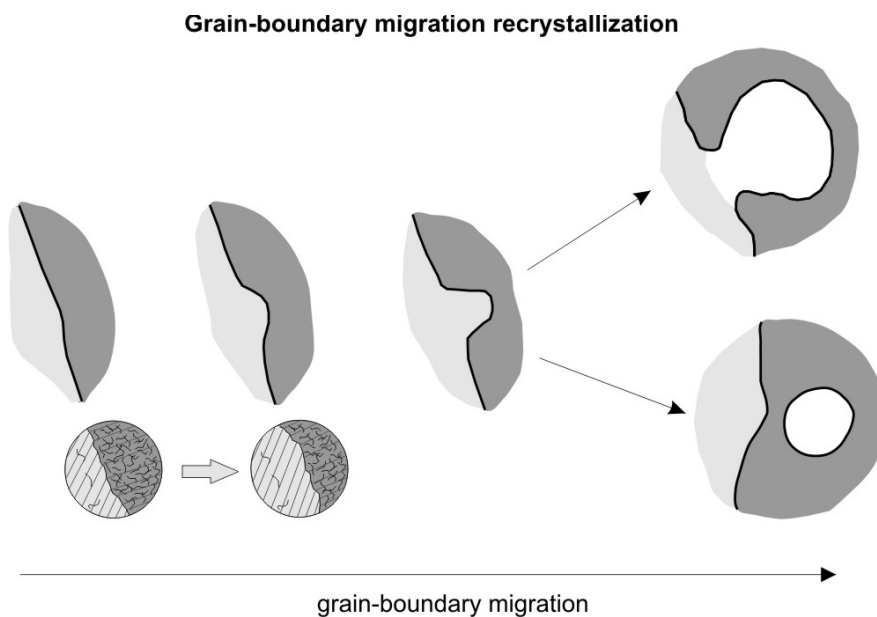


Fig. 2.13. Formation of new grains as a result of the migration of grain boundaries. GBM starts with bulging of the grain boundary into a grain with higher internal strain energy, leaving behind a relatively strain free region that eventually develops into a recrystallised grain. Figure modified after van der Pluijm and Marshak (1997).

GBM recrystallisation in halite

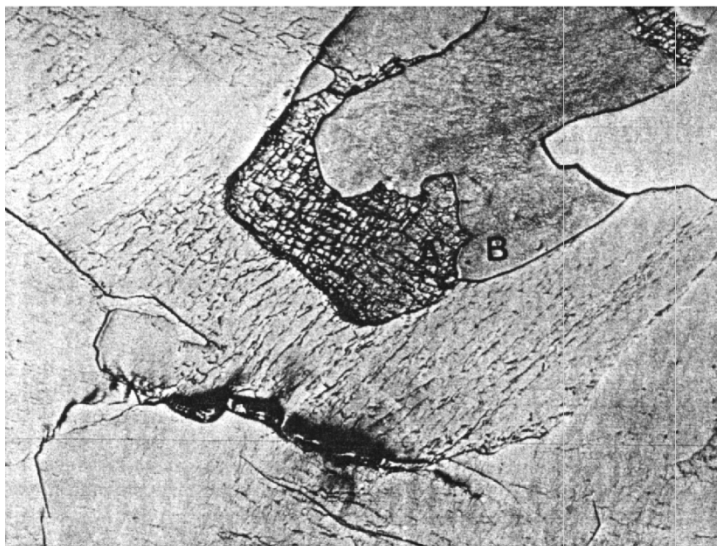


Fig. 2.14. Grain boundary migration recrystallisation in experimentally deformed halite. Grain B moves into dark, substructure containing grain. Note the bulged grain boundaries of B. Photo taken from Guillopé & Poirier (1979).

2.5 Crystallographic preferred orientations and texture models

In an isotropic rock, the orientation of grains is random with little or no crystallographic preferred orientation (CPO or “texture”). During deformation, grains realign their crystal lattices in preferred orientation, which is a result of the activity of slip systems. The slip systems active in a grain are dependent on the crystal orientation and the critical resolved shear stress (crss) necessary to initiate slip on that slip system. The magnitude of the crss for slip systems is temperature and strain rate dependent (Hobbs 1985). The CPOs developing are thus a function of temperature and strain rate. The amount of strain and recrystallisation play an important role in the development of CPOs.

Therefore, CPOs can be a useful tool to estimate the strain path (pure shear or simple shear), the sense of shear, the temperature during their formation, and they can also provide information on the deformation kinetics (Bons & den Brok 2000). The symmetry of a CPO can be used to determine the strain paths (e.g. Wenk & Christie 1991): CPOs showing an orthorhombic symmetry are an indicator for pure shear, while a monoclinic symmetry is an indicator for simple shear (Fig. 2.14).

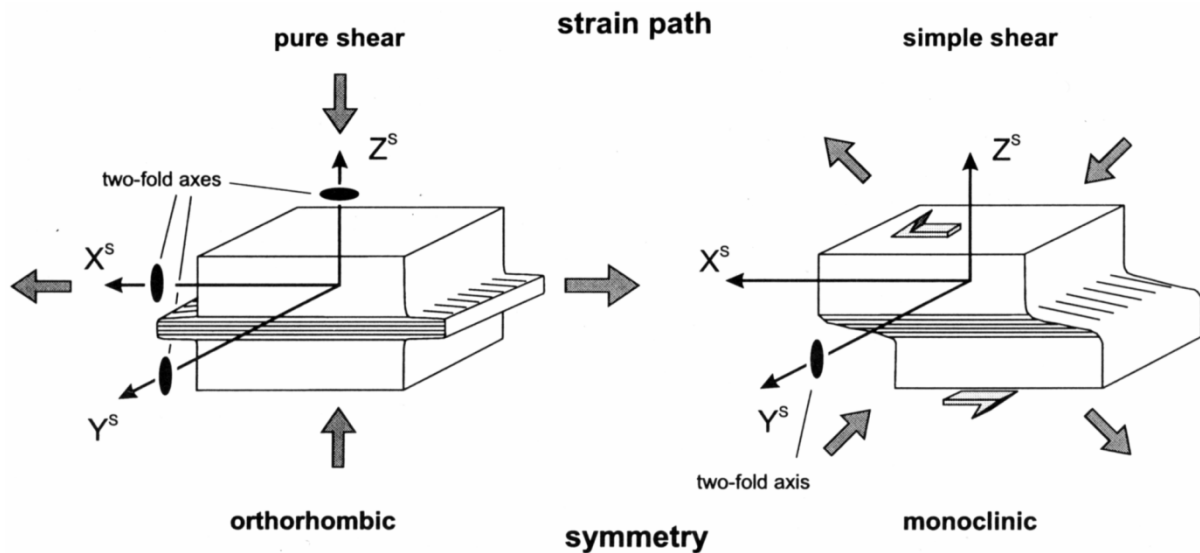


Fig. 2.14. CPO as an indicator for the strain path as inferred from the symmetry. Orthorhombic symmetry of a CPO indicates deformation by pure shear, whereas monoclinic CPO symmetry indicates deformation by simple shear (Figure from Bestmann 2000).

Numerical texture simulations can be used to determine the slip system processes and the deformation history of naturally deformed rocks. Two end-member situations of these texture models are the lower bound Sachs model and the upper bound Taylor model. The model of Sachs (1928) assumes stress equilibrium and predicts stable end orientation by rotation of intracrystalline slip systems in a grain aggregate. Each grain deforms independently of its neighbour grains and on the slip system that has the largest resolved shear stress. However, this model has the greatest deficiency in its strain discontinuity across the grain boundaries leading to overlaps and cavities (Skrotzki 1994).

The model of Taylor (1938) is based on the assumption that each grain deforms by the same increment, thus assuming strain compatibility. Strain in an aggregate can be represented by six components. However, when strain is composed of shear strains only, i.e. without volume

change, than it is reduced to five independent strain components. To match these five independent components, slip on five independent slip systems is required (von Mises, 1928). The slip systems which will be active in a grain depends on the crss for the slip systems. Taylor assumed that the combination of slip systems selected for a grain during an increment of deformation is that one, that achieves the required strain with the minimum amount of internal work, the macroscopic strain requirement is fulfilled by rigid body rotations of the crystal lattice, which is specific for the crystal orientation of the grain. As the crss changes, with increasing temperature, different slip systems become active and crystals undergo different rotation.

However, since these models represent end member situations, a review of other texture models is given, by e.g. Wenk & Christie 1991, Schmid 1994, Herwegh & Handy 1998.

2.6 References

- Bestmann, M. 2000. Evolution of a shear zone in calcite marble on Thassos Island, Northern Greece: results from microfabrics and stable isotopes. *Erlanger geologische Abhandlungen* 131, 127.
- Bestmann, M. & Prior, D.J. 2003. Intragranular dynamic recrystallization in naturally deformed calcite marble: diffusion accommodated grain boundary sliding as a result of subgrain rotation recrystallization. *Journal of Structural Geology* 25(10), 1597-1613.
- Bons, P.D. & den Brok, B. 2000. Crystallographic preferred orientation development by dissolution-precipitation creep. *Journal of Structural Geology* 22(11-12), 1713-1722.
- de Meer, S. & Spiers, C.J. 1999. Influences of pore-fluid salinity on pressure solution creep in gypsum. *Tectonophysics* 308, 311-330.
- Drury, M.R. & Urai, J.L. 1990. Deformation-Related Recrystallization Processes. *Tectonophysics* 172(3-4), 235-253.
- Franssen, R.C.M.W. 1993. Rheology of synthetic rocksalt. PhD thesis, Universiteit Utrecht.
- Guillopé, M. & Poirier, J.P. 1979. Dynamic Recrystallization During Creep of Single-Crystalline Halite - Experimental-Study. *Journal of Geophysical Research* 84(NB10), 5557-5567.
- Herwegh, M. & Handy, M.R. 1998. The origin of shape preferred orientations in mylonite: inference from in-situ experiments on norcamphor. *Journal of Structural Geology* 20, 681-694.
- Humphreys, F.J. & Hatherly, M. 2004. Recrystallization and related annealing phenomena. Elsevier, 628.
- Matucha, K.H. 1968. Electron Microscopy of Slip Lines on Deformed NaCl. *Physica Status Solidi* 26(1), 291-.
- Peach, C.J., Spiers, C.J. & Trimby, P.W. 2001. Effect of confining pressure on dilatation, recrystallization, and flow of rock salt at 150 degrees C. *Journal of Geophysical Research-Solid Earth* 106(B7), 13315-13328.

- Pennock, G.M., Drury, M.R. & Spiers, C.J. 2005. The development of subgrain misorientations with strain in dry synthetic NaCl measured using EBSD. *Journal of Structural Geology* 27(12), 2159-2170.
- Poirier, J.P. 1985. *Creep of crystals*. Cambridge University Press.
- Sachs, G. 1928. Plasticity problems in metals. *Transactions of the Faraday Society* 24, 0084-0091.
- Schmid, S.M. 1994. Textures of geological materials: computer model predictions versus empirical interpretations based on rock deformation experiments and field studies. In: *Textures of Geological Materials* (edited by Bunge, H. J., Siegesmund, S., Skrotzki, W. & Weber, K.). DGM Informationsgesellschaft, Oberusel, 279-291.
- Schutjens, P. & Spiers, C.J. 1999. Intergranular pressure solution in NaCl: Grain-to-grain contact experiments under the optical microscope. *Oil & Gas Science and Technology-Revue De L Institut Francais Du Petrole* 54(6), 729-750.
- Skrotzki, W. 1994. Mechanisms of texture development in rocks. In: *Textures of Geological Materials* (edited by Bunge, H. J. et al.). DGM Informationsgesellschaft, Oberusel, 167-186.
- Spiers, C.J., Schutjens, P.M.T.M., Brzesowsky, R.H., Peach, C.J., Liezenberg, J.L. & Zwart, H.J. 1990. Experimental determination of constitutive parameters governing creep of rocksalt by pressure solution. In: *Deformation Mechanisms, Rheology and Tectonics* (edited by Knipe, R. J. & Rutter, E.H.) 54. Geological Society Special Publication, 215-227.
- Spiers, C.J. & Carter, N.L. 1998. Microphysics of rocksalt flow in nature. In: *4th Conference on the Mechanical Behaviour of Salt*, 115-128.
- Spiers, C.J. 2006. Lecture script: "Continuum mechanics and rheology of the crust and mantle" (Utrecht University).
- Strunk, H. 1975. Investigation of Cross-Slip Events in NaCl-Crystals by Transmission Electron-Microscopy. *Physica Status Solidi a-Applied Research* 28(1), 119-126.
- Taylor, G.I. 1938. Plastic strain in metals. *Journal of the Institute of Metals* 62, 307-324.
- Ter Heege, J.H., De Bresser, J.H.P. & Spiers, C.J. 2005. Rheological behaviour of synthetic rocksalt: the interplay between water, dynamic recrystallization and deformation mechanisms. *Journal of Structural Geology* 27(6), 948-963.
- Trimby, P.W., Drury, M.R. & Spiers, C.J. 2000. Recognising the crystallographic signature of recrystallisation processes in deformed rocks: a study of experimentally deformed rocksalt. *Journal of Structural Geology* 22(11-12), 1609-1620.
- Urai, J.L., Spiers, C.J., Zwart, H.J. & Lister, G.S. 1986. Weakening of Rock Salt by Water During Long-Term Creep. *Nature* 324(6097), 554-557.
- van der Pluijm, B.A. & Marshak, S. 1997. *Earth Structure - An Introduction to Structural Geology and Tectonics*. McGraw Hill.
- von Mises, R. 1928. Mechanics of the ductile form changes of crystals. *Zeitschrift Fur Angewandte Mathematik Und Mechanik* 8, 161-185.

Wenk, H.R. & Christie, J.M. 1991. Comments on the Interpretation of Deformation Textures in Rocks. *Journal of Structural Geology* 13(10), 1091-1110.

White, S. 1976. Effects of Strain on Microstructures, Fabrics, and Deformation Mechanisms in Quartzites. *Philosophical Transactions of the Royal Society of London Series a-Mathematical Physical and Engineering Sciences* 283(1312), 69-86.

Chapter 3

Methodology

This chapter first describes the material used in this study. The second part contains the methods applied for producing the starting material and describes the deformation apparatus. The last part deals with the methods used for analysing the microstructure and texture.

3.1 Material

3.1.1 Structure and properties of NaCl

Sodium chloride (NaCl) is a cubic hexaisoctahedric salt and crystallises in one of the most common structure type; the NaCl structure. Many ionic crystals like the salt minerals, e.g. KCl, AgBr, KBr and the oxides e.g. MgO and FeO crystallise in this structure. Each Cl^- ion is surrounded by six Na^+ ions and vice versa each Na^+ ion is surrounded by six Cl^- ions. The Na^+ ions and the Cl^- ions form each a face centred cubic (fcc) lattice. Both lattices are geometrically displaced against each other by $\frac{1}{2}$ edge length and are placed into each other. The point group of NaCl is $m\bar{3}m$ ($4/m\bar{3}2/m$), the space group $Fm\bar{3}m$ ($F4/m\bar{3}2/m$) and the lattice constant $a=5.64 \text{ \AA}$.

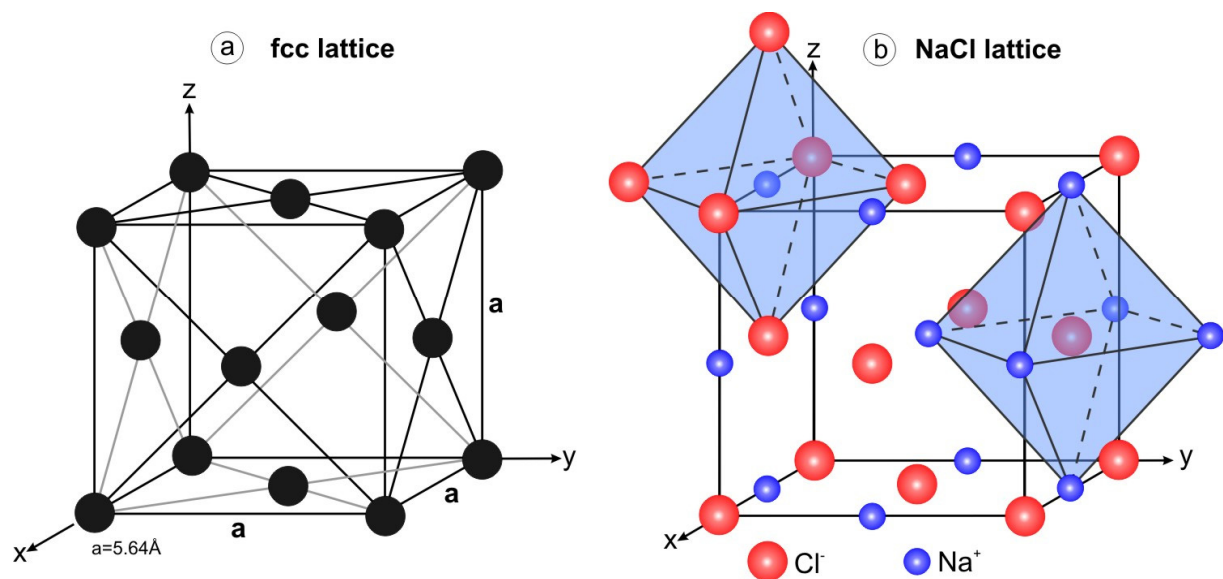


Fig. 3.1. a) fcc lattice, with the lattice constant $a=5.64 \text{ \AA}$ for NaCl. b) NaCl lattice where, every Na^+ and every Cl^- ion is octahedrally surrounded by six Cl^- or six Na^+ ions (Figure modified after Riedel (1990)).

The typical properties of NaCl are listed in Table 3.1 and can be linked to the structure of NaCl. The low hardness is caused by the heteropolar bonding force between the two large monovalent ions. The perfect cleavage along $\{100\}$ is due to the relatively dense ion occupation in the $\{100\}$ planes. The amount of bonds normal to $\{100\}$ is smaller than perpendicular to any other plane. The transparency of the colourless rocksalt can be explained

in a crystal physical way by the fact that no free electrons are available for absorption of the incoming light.

Melting point	801 °C (1074 K)
Density at 20°C	2.17 g/cm ³
Point group	$m\bar{3}m; \left(\frac{4}{m}\right)\bar{3}\left(\frac{2}{m}\right)$
Space group	$Fm\bar{3}m; \left(F\frac{4}{m}\right)\bar{3}\left(\frac{2}{m}\right)$
Lattice constant	a=5.64 Å
Hardness after Mohs	2
Cleavage	{100} perfectly

Table 3.1. Properties of sodium chloride (NaCl). Data from <http://www.saltinstitute.org> and Matthes (1996).

3.2 Methods

3.2.1 Preparation of the starting material

The NaCl used in this study was obtained from the company AppliChem. The salt was delivered as an analytical fine grained powder (Fig. 3.2) with a grain size of ~500µm. According to AppliChem the purity is 99.9% with traces of Bromide, Iodide, Sulfate and with cations of Ba, Ca, Fe, K, Mg and Pb.

Analytical grade powder

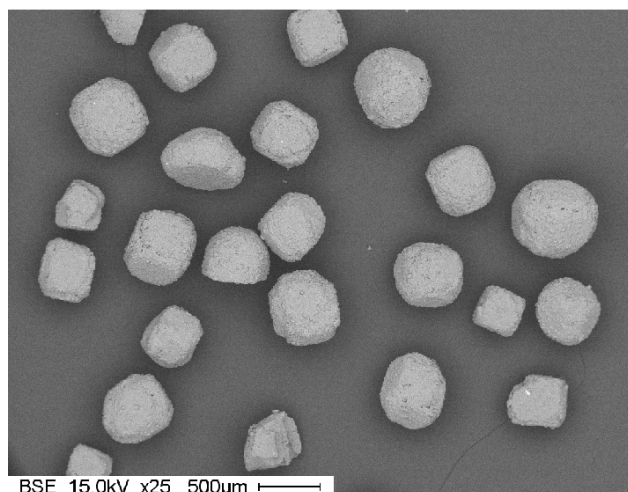


Fig. 3.2. BSE image of the analytical grade powder used for the cold pressing and annealing.

The starting material was produced by cold pressing (at room temperature) the analytical grade powder using a uniaxial press (Fig. 3.3a, ENERPAC Press). The powder was filled in single portions of 30 ml in a stainless steel cylinder with a diameter of 5cm and a length of 25cm. Each powder filling was uniaxially pressed by applying a load of 40t for 20s on a surface of 20.43cm², corresponding to 200MPa. This step was repeated until the cylinder was

completely filled. Finally, the material inside the cylinder was uniaxially pressed by applying a load of 30t ($\approx 150\text{MPa}$) for 1h. After the final cold-pressing the cylinder was enclosed by two stainless steel plates (Fig. 3.3b,c) from the sides as well as from top and bottom. The parts were screwed tight together to keep the material under confining pressure. The assembly was then placed in a furnace for one week at a temperature of 150°C .

Cold pressing

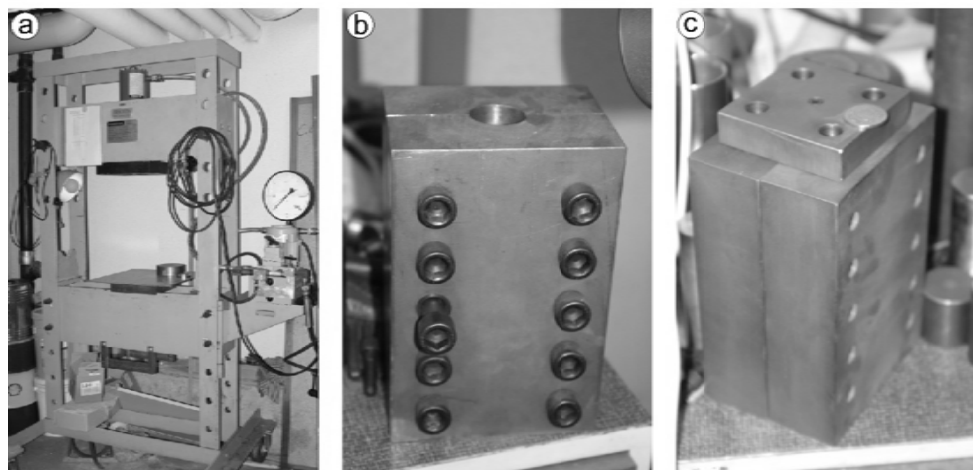


Fig. 3.3. a) ENERPAC cold pressing rig. b) and c) Steel parts used for enclosure of the cylinder containing the cold pressed starting material.

The result of the cold pressing and the annealing afterwards was a dense, milky and solid rocksalt sample – the starting material. The typical microstructure of the starting material is shown in Fig. 3.4. The grain size of the starting material was between 150 and $300\mu\text{m}$. Density measurement of the starting material was carried out using a pycnometer. The density of the material was 2.15g/cm^3 . From the measured density, the porosity of the material was calculated, which was 0.6%.

Cold pressed and annealed starting material

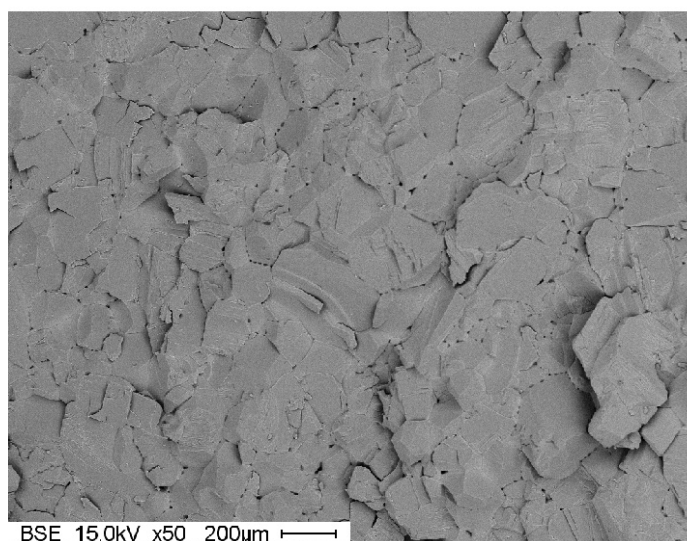


Fig. 3.4. BSE image of the cold pressed starting material. Broken surface. Porosity indicated along the grain boundaries.

For torsion experiments small cylinders 15mm in diameter were used. The cylinders were drilled from the large starting material cylinder under dry conditions. The small cylinders were then cut and polished dry, using silicon carbide polishing (SiC) paper of various grades, to a length of 5 or 10mm, depending on the chosen strain- and twist rate. Because salt is a hygroscopic material all small starting material samples were stored always in the furnace at 100°C (because a dry room with low humidity was not available) prior to the actual experiment.

3.2.2 Deformation apparatus – Paterson rig

All experiments were carried out using the high temperature/high pressure Paterson apparatus with an additional set up feature for torsion. The apparatus is installed at the Rock Deformation Laboratory at ETH Zürich and was developed by Prof. Mervin Paterson (Paterson Instruments/ANUtech Canberra). The Paterson rig is internally heated and argon is used as a confining medium. In the following, only a brief description of the Paterson apparatus will be given. More details can be found in the work of Pieri (1999), Paterson & Olgaard (2000), Schmocker (2002) and Barnhoorn (2003).

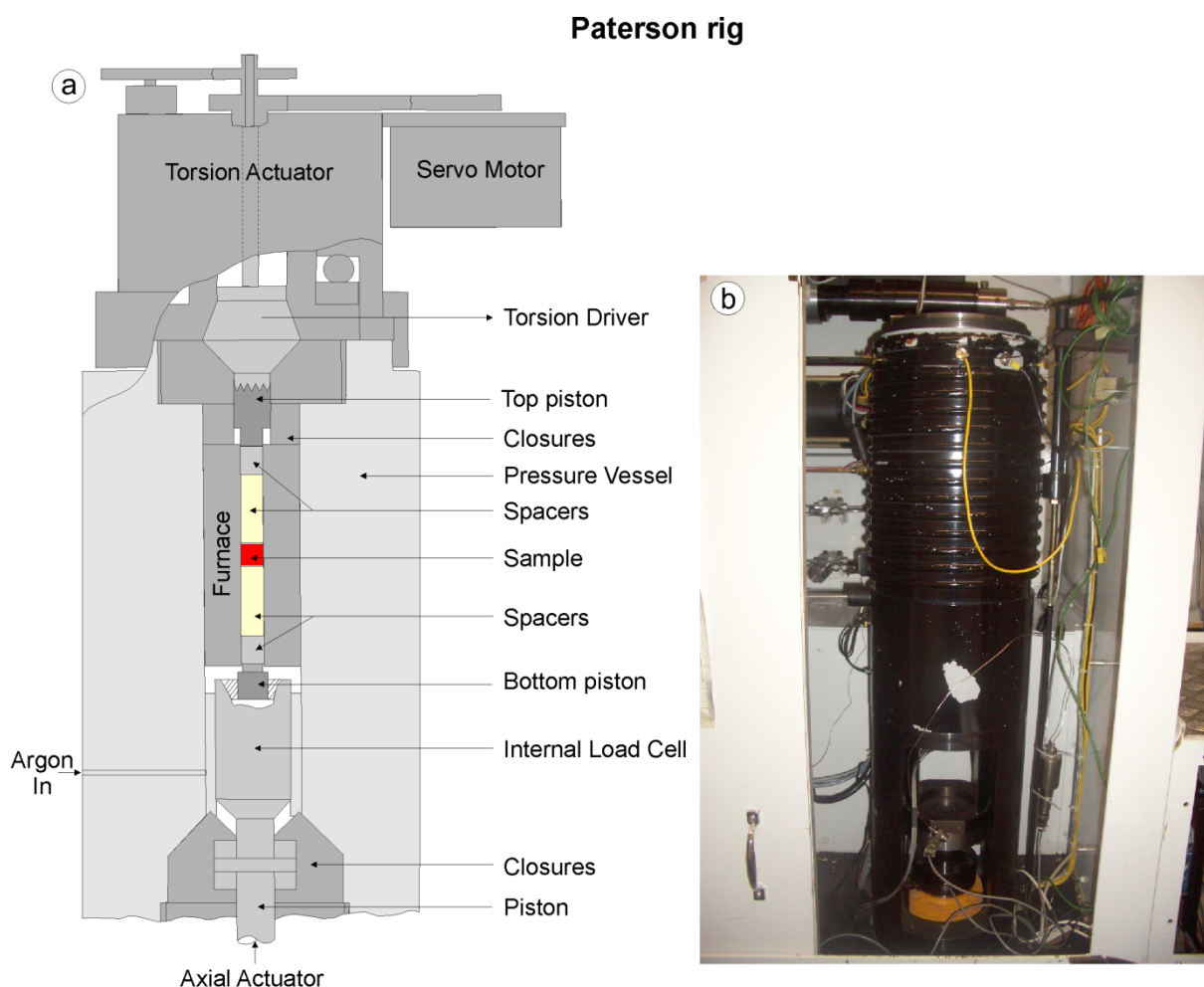


Fig. 3.5. a) Schematic drawing of the Paterson rig (not in scale). Figure modified after Paterson & Olgaard (2000). b) Photograph of the pressure vessel inside the Paterson apparatus.

The apparatus, as shown in Fig. 3.5, consists of a pressure vessel made out of hardened steel to resist the high applied confining pressure. Inside the vessel the internal load cell, the furnace and the sample assembly is located. Deformation in torsion is driven by an actuator that is located on top of the vessel. The velocity of the actuator is transmitted on to the sample in the way that the teeth of the bottom part of the external load cell grip into the teeth of the top piston of the sample assembly. The bottom part of the sample assembly consists of a piston with teeth as well. This bottom piston grips into a teeth part at the top of the internal load cell and keeps the sample assembly in a fixed position. During twist the bottom part of the assembly stays in a fixed position while the top part connected to the motor is moving. Deformation is accommodated in the sample, because the other parts of the assembly consist of a material stronger than the sample. The internal load cell records the torque that is applied on the sample. The twist of the specimen is recorded by a rotary displacement transducer. The twist rate (displacement rate) is determined by the length of the sample and the strain rate by using the following Equation:

$$\dot{\theta} = \dot{\gamma} \cdot \frac{l}{r}; \quad \text{Eq. 3.1}$$

where, $\dot{\theta}$ = twist rate, $\dot{\gamma}$ = strain rate, l = sample length and r = radius of the sample.

The amount of twist that can be applied in torsion tests is theoretically unlimited, but it is actually limited by slip that may occur at the interfaces between the spacers and the sample ends.

Deformation assembly and experimental procedure

The deformation assembly is shown in Fig. 3.6. It consists of the cylindrical salt sample in the middle, surrounded by two 3mm thick alumina discs. These discs are bounded to both sides by alumina spacers (~50mm long) and zirconia spacers (~30mm long). The last parts in the assembly are a top and a bottom steel piston. The length of the assembly was between 175-180mm, depending on the sizes of each element.

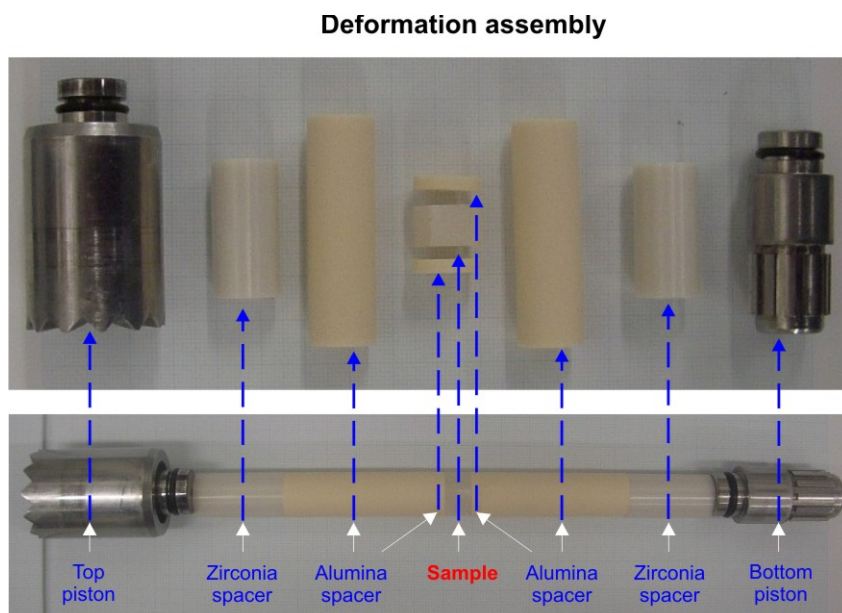


Fig. 3.6. Single parts of the deformation assembly for experiments in torsion as used in this study. The columnar alignment in the lower photograph is ready to be inserted in the copper jacket and then placed in the deformation apparatus.

All these parts were placed into a copper jacket tube. We used copper since we were working at temperatures between 100 and 300°C. In that temperature range, copper is soft and ductile. The copper tubes had an inner diameter of 15mm and a wall thickness of 0.25mm. The tubes were cut with a mechanical saw to the exact length of the assembly. The polishing was done to remove sawing burrs, scratches and oxidation pits from the surfaces revealing a nearly perfect surface. Afterwards, the copper tube was cleaned with alcohol and the assembly parts were carefully placed into the jacket. The top and bottom piston were equipped with two o-rings to seal the assembly. Five longitudinal scratches (one double scratch and three other scratches every 90°) were made on the copper jacket as displacement markers. The last step was to wrap alumina paper around the top piston to reduce the gas convection above the sample, which improves the thermal profile along the sample length. The available angular displacement rates range between 10^{-3} to 10^{-8} rad/s. For carrying out experiments with a strain rate of 10^{-3}s^{-1} samples with a length of 5mm were used. The sample assembly was placed in the pressure vessel including a thermocouple for measuring the temperature and the system was pressurised up to a confining pressure of 200MPa. At this confining pressure, the furnace was switched on and temperature was raised up to the target temperature. As the target temperature was reached, the confining pressure was raised up to 250Ma. In Fig. 3.7 a time – temperature plot is provided to show how long the sample was exposed to temperature before torsion started and how fast the quenching occurred. For samples deformed at 100 °C the stable target temperature was reached after 13min, whereas for samples deformed at 200 °C a stable temperature was reached after 23min and for 300°C the temperature was stable after 35 min. As soon as the temperature was stable torque was applied. After the experiment was finished, i.e. after stopping the torsion motor, the furnace was switched off immediately; the confining pressure was released whereas the sample was cooled down. The cooling occurred at the same speed for all temperatures. However, the final cooling temperature was different, samples cooled down from 100°C had an end temperature of 28°C, from 200°C the end temperature was 71°C and for 300°C the temperature of the sample after cooling was 115°C. This end cooling temperatures as well as the pre-heating had some effect on the microstructure developed during the experiments.

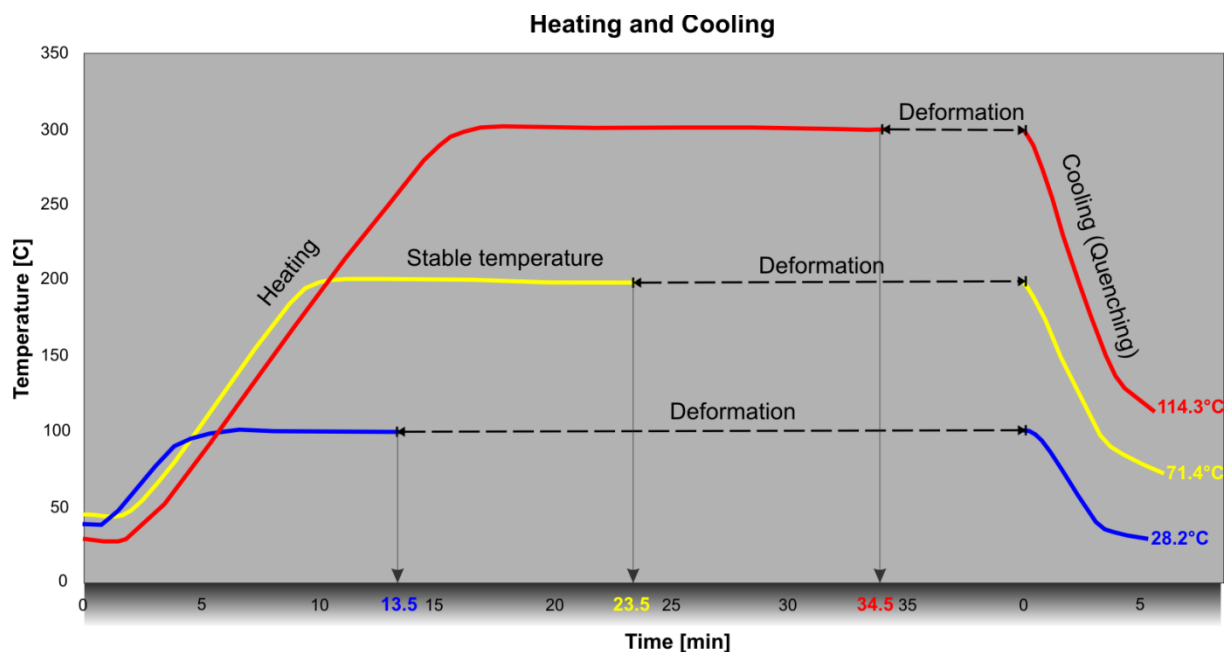


Fig. 3.7. Curves for the up-heating and the cooling time of the experiments (explanation given in text).

3.2.3 Fourier transform infrared spectroscopy (FTIR)

The measurements of the water content were conducted by means of FTIR (Fourier Transformation InfraRed) spectroscopy. These analyses were carried out at the University of Utrecht (NL) in the HPT Laboratory. Fig. 3.8 shows the FTIR apparatus (company Jasco). A good review about the theory and practise of FTIR can be found in Griffiths & de Haseth (1986).

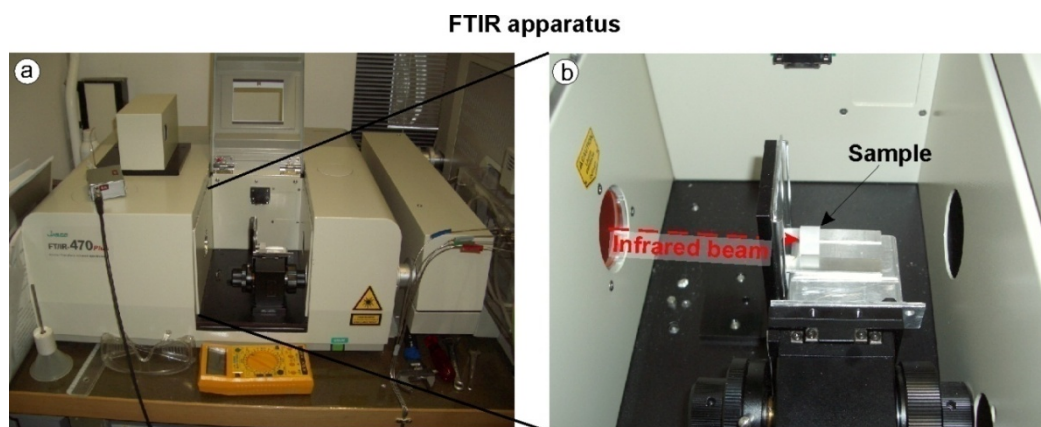


Fig. 3.8. a) FTIR apparatus with open chamber (at HPT Laboratory Utrecht University). b) closer look with sample placed on a sample holder inside the chamber. The sample holder contains a 4mm hole where the incoming laser beam passes through to hit the sample surface. The sample can be moved vertical to measure the spectrum at different positions along the sample surface.

Experimental procedure

The top and the bottom parts of the deformed rocksalt sample were polished dry using SiC polishing paper of various grades. After each polishing step, the surface was cleaned with compressed air to avoid that particles stay on the surface.

After cleaning, the sample was placed in the chamber of the FTIR apparatus. The measurements with the infrared beam occurred at four different positions on the polished sample surface at the centre and then 4mm, 6mm and 7mm away from the centre.

The spectra were recorded and analyzed with the Jasco Software SpectraManager 1.53™. For calculating the amount of water the area of the 1650 cm⁻¹ wavelength water peak is used. Fig. 3.9 shows a typical spectrum obtained from the measurement.

The amount of water is calculated using Beer-Lambert law written in the form:

$$H_2O [ppm] = \frac{50 \cdot A_p \cdot 42}{l \cdot 22.6}, \quad \text{Eq 3.2}$$

where, the numbers are constants, A_p is the peak area and l is the length of the sample in mm.

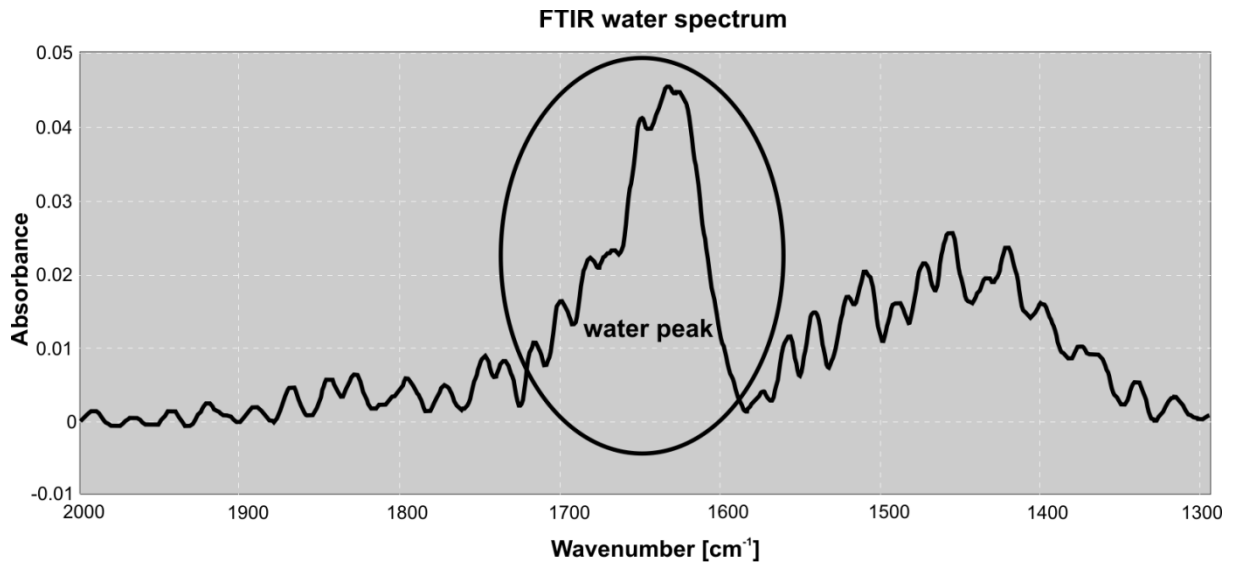


Fig. 3.9. FTIR water spectrum of sample P0671 measured in the centre of the sample. The water peak is usually found at 1650cm^{-1} .

3.2.4 Optical microscopy

The microstructures of the deformed samples were studied on polished sections using a reflected light microscope of the company Nikon.

Because we were interested in the high strain area, only the outer part of the cylindrical samples were polished. This is because, the amount of strain changes with the radial position within the sample (Fig. 3.10). The amount of strain is zero at the central axis of the sample and reaches the maximum at the cylindrical periphery. Any element along a radius of the cylinder undergoes simple shear in a plane normal to the radius, the displacements being in the direction normal to the cylinder axis.

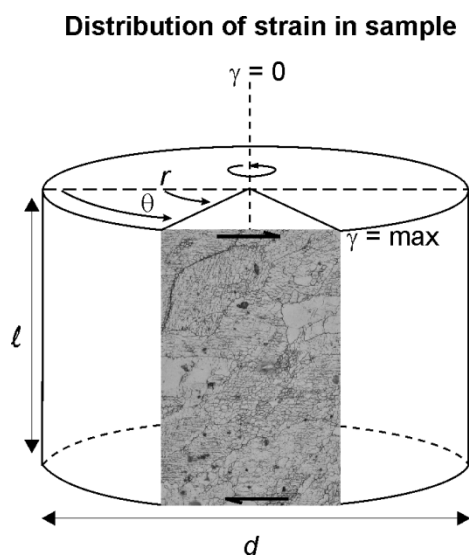


Fig. 3.10. Sketch of the strain distribution in the deformed sample. Strain is highest at outside of the margin and decreases to zero strain at the centre of the cylinder. L , is sample length, r is radius of sample, θ is twist rate and γ the amount of shear. The grey image shows the location of the polished section for microstructural analysis.

Sample preparation

The preparation of the deformed samples was carried out at the HPT Laboratory at the University of Utrecht. The polishing was carried out dry, using first 1200 grid SIC polishing paper. After that, the samples with the polished surface were embedded in resin that contained hardener (mixing ratio 4:1). The embedded samples were stored for 24h in a vacuum oven for the resin to dry. 24h later, the samples were polished again, but now polishing was carried out wet, using evaporating oil (company Shell) as a lubricant. The first polishing took place with 1200 grid SIC paper to remove the resin layer. After the resin layer was removed, 2500 grid SIC paper was used to remove the scratches from the first polishing. Final polishing was done with 4000 grid SIC paper to reveal a nearly scratch free surface. Between the different polishing steps the surface was cleaned by using evaporating oil to remove the polishing particles from the surface. Otherwise these particles can contaminate the surface during the finer polishing steps and produce deep scratches on the surface. The sample was then cleaned with compressed air and then flushed with n-Hexane containing some MgO crystals to bind the water in the n-Hexane. Cleaning was done to remove leftover evaporating oil. Then the sample was held horizontal and the etching solution (95% saturated NaCl solution containing 8 wt% $\text{FeCl}_3 \times 6 \text{H}_2\text{O}$) was placed on the surface. The solution must cover the whole surface and the surface was etched for 4 s. After the 4 s, the surface was flushed immediately with n-Hexane and dried by using a hair dryer. Etching is necessary to highlight the grain- and subgrain boundaries and to obtain a surface layer free of defects introduced during mechanical polishing.

3.2.5 Electron backscatter diffraction (EBSD) technique

The Electron BackScatter Diffraction (EBSD) technique (Venables 1973, Adams 1993) is a very useful tool for the quantitative characterisation of microstructures and for obtaining the complete crystallographic orientation of grains. EBSD measurements were carried out using a CamScan CS44 SEM (scanning electron microscope equipped with a EDAX-TSL Digi-View forward scattered detector) at the Electron Microscopy Center ETH Zürich/Hönggerberg.

Before placing the sample in the SEM chamber, the sample was coated with a thin (~2nm) carbon layer to avoid charging effects. The sample for EBSD measurements was tilted 70° in the SEM chamber. A focused stationary electron beam initiated by the electron gun hits the sample surface. Hereby, the electrons are subject to a diffuse inelastic scattering. Those electrons that lost very little energy can also undergo elastic scattering and satisfy therewith Bragg's law and will be diffracted by crystallographic planes (hkl). The electron diffraction pattern is imaged on a phosphor screen of the EBSD detector and the light is detected by a CCD camera where the image is digitised. The resulting electron backscattered diffraction patterns or backscatter Kikuchi patterns are analysed and indexed by an automated program (TSL OIM Data Collection 4.0) running on a PC. The pattern analysis makes use of a Hough transformation, which allows the position of Kikuchi bands to be located automatically (Wright 1992, Wilkinson 2001). The angles between the planes corresponding to located Kikuchi bands are calculated and compared to expected angles for the known crystal structure. The best match between measured interplanar angles and those expected for the known crystal type allows the pattern to be indexed and hence the crystal orientation calculated. From the raw scan data orientation maps were produced using the TSL OIM Data Analysis 4.0 or 5.0 software. A detailed description of the technique is given for example by Mauler Steinmann (2000).

Scan parameters and reference frame

For all samples two different kinds of scans have been carried out. Bulks scans were carried out by scanning the complete polished surface to obtain the texture and hence the CPO. Detail scans were carried out for microstructural analysis, e.g. to investigate the relationship between grains and subgrains. The parameters used for bulk and detail scans are listed in Table 3.2.

	Bulk scan	Detail scan
Working distance (mm)	35	35
Acceleration voltage (kV)	15	15
Binning	8x8	8x8
Scan mode	Beam and stage scan	Beam scan
Scan grid	Frame	Frame
Magnification	100x	300 or 150x
Step size (μm)	10	0.5 or 1.0

Table 3.2. Scan parameters used for bulk scans and detail scans.

The working distance for all scans was 35mm, using an acceleration voltage of 15kV, a binning of 8x8 and a frame rate of 29frames/s. The bulk scans were carried out using a combined beam and stage mode with a beam scan step size of 10 μm . In this mode a frame of 1mm² is scanned and then the stage moves laterally to the next scan field. This allows scanning the complete sample surface in a relatively short time and collecting a sufficient number of orientation data. The detail scans were carried out in beam scan mode, where the stage stays in a fixed position. The step size used for the detailed scans was 0.5 or 1.0 μm , which allows a higher resolution of the orientation maps.

All samples were placed in the SEM in the same way, with a same reference frame as it is shown in Fig. 3.11. In metallurgy, the reference frame consists of the following directions: normal direction (ND), transverse direction (TD) and rolling direction (RD). For this application, the directions correspond to the following: ND = intermediate strain axis, TD = shear direction (SD), RD = shear plane normal (SPN).

For texture and microstructure analysis the obtained raw orientation data were filtered using a confidence index $CI > 0.1$. The confidence index is a parameter describing how confident the software is, that it has found the correct indexing for a given pattern when using the automatic indexing algorithm. It ranges from 0 to 1. The average confidence index also depends on the polishing of the sample surface, grain size, step size and the amount of defects in the grains. Areas with a rough surface show a low confidence index or were not indexed at all (black points in the orientation map, Fig. 3.12). This happened especially at grain boundaries or at dust particles, pore space etc. Orientation maps with inverse pole figure (IPF) colour keys for the shear direction (SD) and for the shear plane normal (SPN) were commonly used. Additionally, grain boundary maps were used to differentiate between low angle and high angle boundaries.

Texture or CPO analysis was carried out by using pole and inverse pole figures. The obtained crystallographic orientations were plotted in contoured pole figures for the {100}, {110} and {111} plane and contoured inverse pole figures for ND, SD and SPN (Fig. 3.11). In the pole

figures the shear plane is horizontal and the sense of shear is dextral (Fig. 3.11). The contoured pole and inverse figures were processed using a Gaussian convolution with a half width of 15° and a harmonic series expansion up to $L=26$.

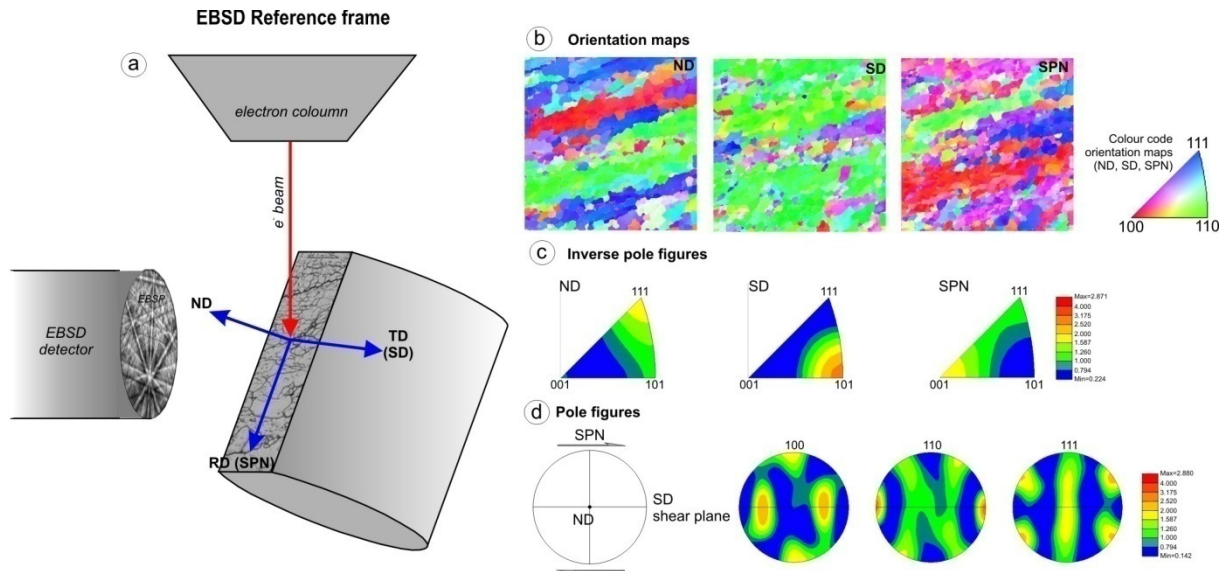


Fig. 3.11. a) Sketch of sample inside the SEM chamber showing the electron beam hitting the tilted (70°) sample surface. b) Example of orientation map for ND, SD and SPN direction of a scanned sample. The corresponding colour code is shown in the triangle next to the orientation images. c) Example for contoured inverse pole figures for ND, SD and SPN. d) Reference frame for reading the pole figure. Shear sense is dextral, the shear plane is horizontal, the shear direction to the east and the shear plane normal to the north. To the right, contoured pole figures for 100, 110 and 111 plane.

Fig. 3.12 to 3.14 on the following pages show the post processing of the raw data to study the microstructure. Fig. 3.12 shows the difference between CI filtered orientation map, revealing the non-indexed points (black dots) and the same orientation map cleaned. Cleaning was obtained by using a grain confidence index standardization and a confidence index correlation and finally a grain dilation. Fig. 3.13 shows the post processing of a detailed orientation map and Fig. 3.14 shows the processing of an orientation map in terms of misorientation analysis between grains.

From a raw map to a cleaned map

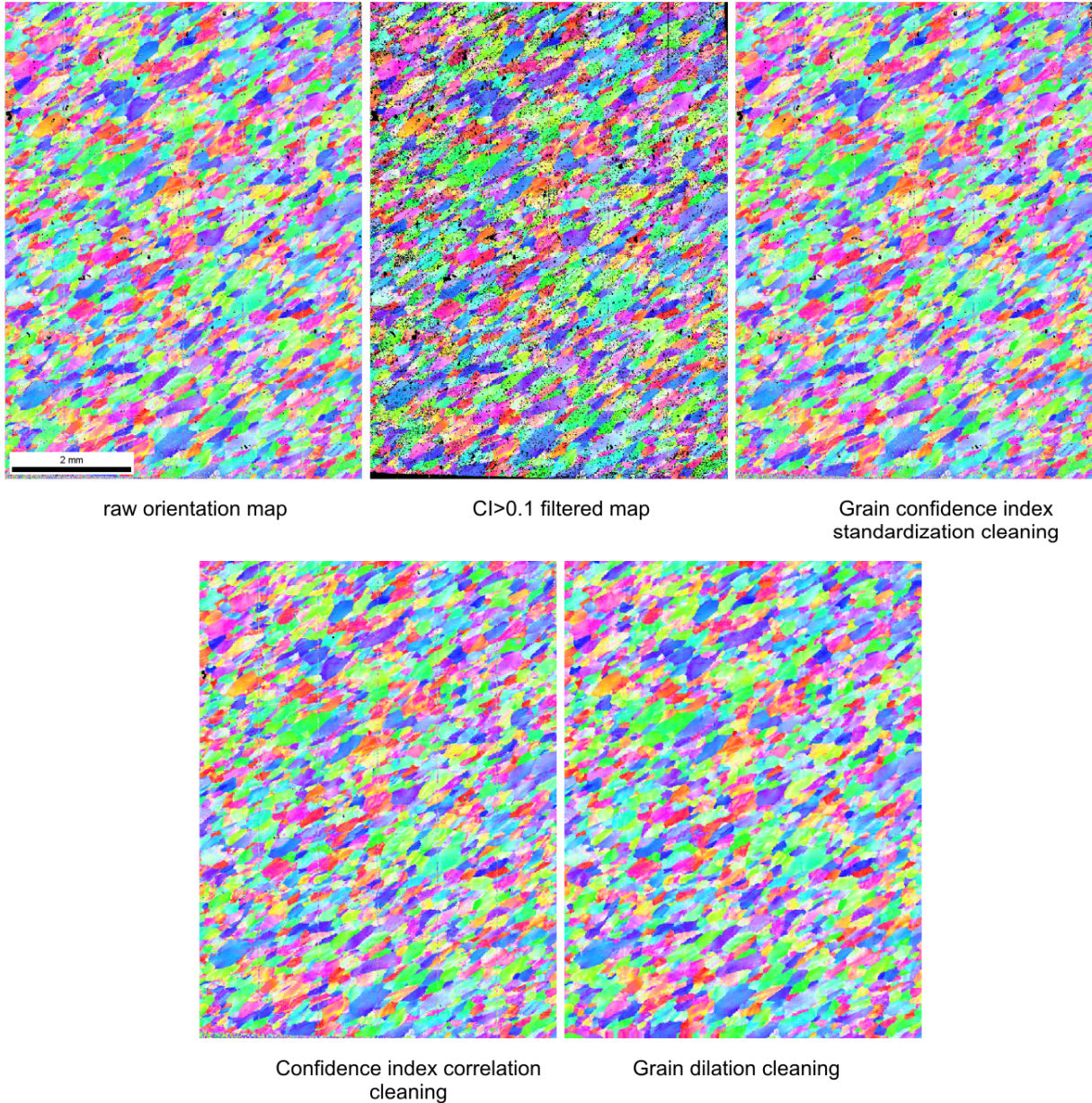


Fig. 3.12. Orientation maps of normal direction (sample P0671). Left map is filtered using a confidence index of >0.1 indicated by the black dots in the map. Black dots (not indexed) occur mostly along grain boundaries or around dust particles. Confidence filtered maps were used to obtain pole figures. The following maps are cleaned, using a grain confidence index standardization and a confidence index correlation and a final grain dilation. These maps were mainly used for grain size analysis and for misorientation profiles.

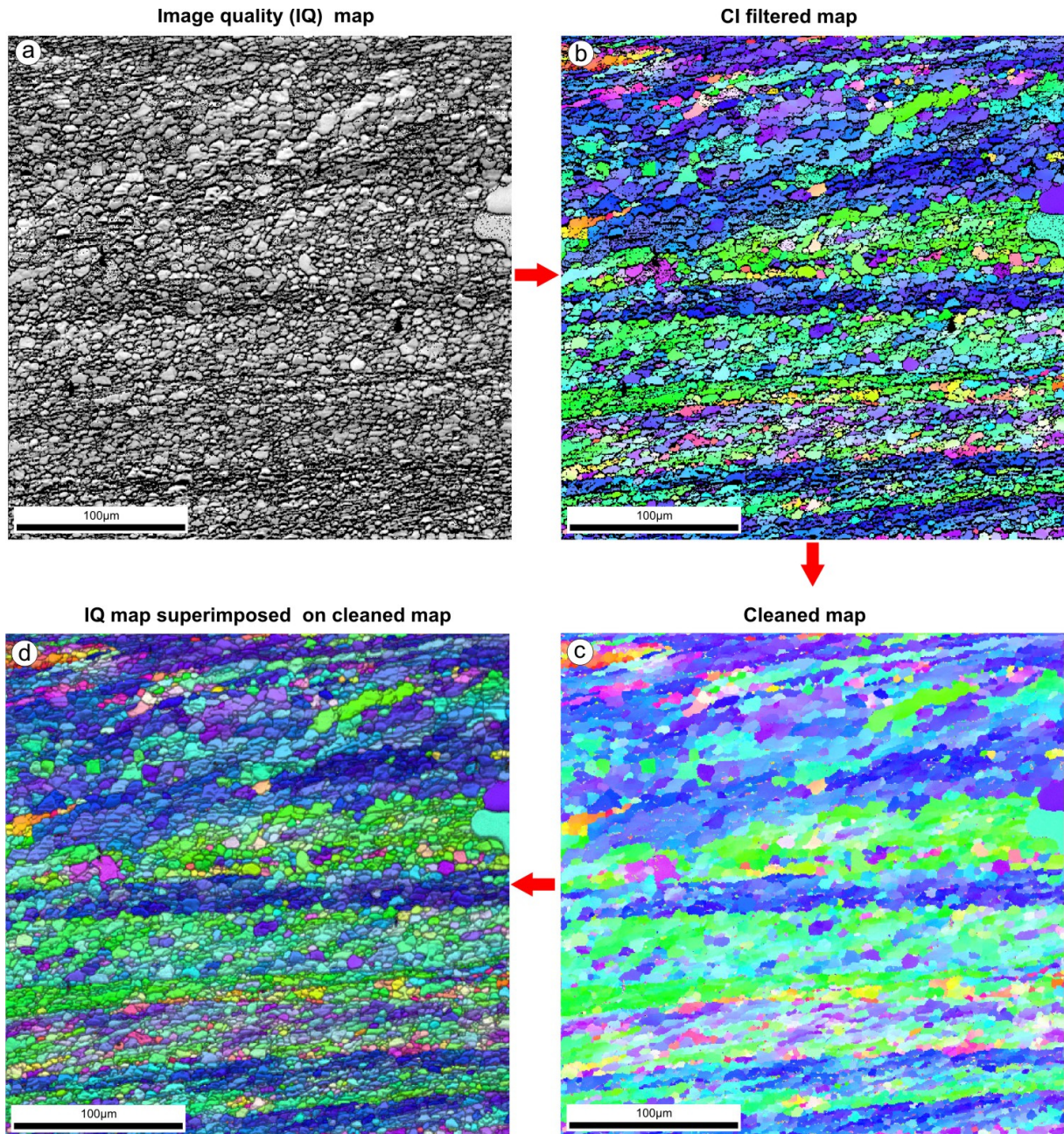


Fig.3.13. Post processing of an EBSD orientation map. (a) Image quality map ($CI > 0.1$) of the scanned area. (b) Confidence index filtered ($CI > 0.1$) orientation map of the scanned area. (c) Cleaned orientation map using a grain confidence index standardization and a confidence index correlation and a final grain dilation. (d) Image quality map superimposed on orientation map.

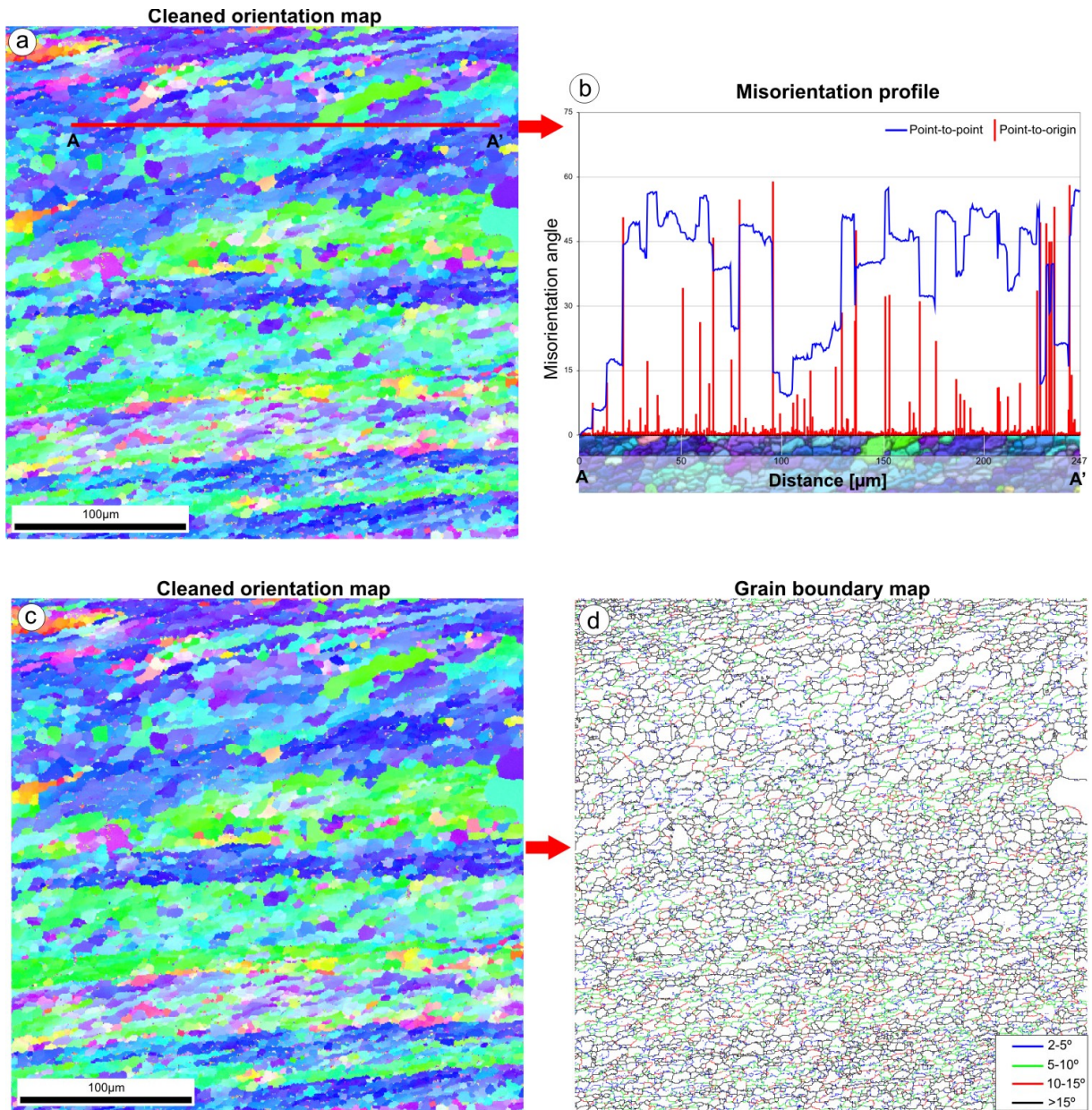


Fig. 3.14. Analysis of an EBSD orientation map in terms of misorientation between grains and grain boundary map. (a) Cleaned orientation map using a grain confidence index standardization and a confidence index correlation and a final grain dilation. Misorientation profile across the analysed area. (b) Resulting misorientation profile of (a) showing point-to-point and point-to-origin misorientations angles across the profile. (d) Boundary map showing low angle and high angle misorientation angles between nearest neighbours as derived from the cleaned orientation map in (c).

3.3 References

- Adams, B.L., Wright, S.I. & Kunze, K. 1993. Orientation Imaging - the Emergence of a New Microscopy. *Metallurgical Transactions a-Physical Metallurgy and Materials Science* 24(4), 819-831.
- Barnhoorn, A. 2003. Rheological and microstructural evolution of carbonate rocks during large strain torsion experiments. PhD thesis, ETH Zurich.
- Griffiths, P.R. & de Haseth, J.A. 1986. Fourier Transform Spectroscopy. John Wiley & sons, New York.
- Matthes, S. 1996. *Mineralogie*. Springer-Verlag, Berlin, Heidelberg.
- Mauler Steinmann, A. 2000. Texture and microstructures in eclogites. Electron backscatter diffraction applied to samples from nature and experiment. PhD thesis, ETH Zurich.
- Paterson, M.S. & Olgaard, D.L. 2000. Rock deformation tests to large shear strains in torsion. *Journal of Structural Geology* 22(9), 1341-1358.
- Pieri, M. 1999. Shear deformation of calcite rocks : rheology and microfabric evolution of Carrara marble under dynamic recrystallization during torsion experiments. PhD thesis, ETH Zurich.
- Riedel, E. 1990. *Anorganische Chemie*. de Gruyter.
- Schmocker, M. 2002. Rheology and microfabrics of quartz: experimental deformation in torsion. PhD thesis, ETH Zurich.
- Venables, J.A. & Harland, C.J. 1973. Electron back-scattering patterns - A new technique for obtaining crystallographic information in the scanning electron microscope. *Philosophical Magazine* 27(5), 1193-1200.
- Wilkinson, A.J. 2001. A new method for determining small misorientations from electron backscatter diffraction patterns. *Scripta Materialia* 44(10), 2379-2385.
- Wright, S.I. & Adams, B.L. 1992. Automatic analysis of electron backscatter diffraction patterns. *Metallurgical and Material Transactions A* 23(3), 759-767.

Chapter 4

Mechanical behaviour of rocksalt deformed in torsion

This chapter discusses the mechanical results from torsion experiments carried out at 100, 200 and 300°C, at constant strain rates of 3×10^{-5} up to $3 \times 10^{-3} \text{ s}^{-1}$ and at a constant confining pressure of 250MPa. Strain rate stepping tests were carried out to determine the stress exponent n . Additionally, the chapter deals with the influence of the jacket material on the estimated strength of rocksalt.

4.1 Introduction

Rocksalt has physical properties which are unique compared to other rocks. Rocksalt is characterised by low density (2.17 g/cm^3), low permeability ($< 10^{-20} \text{ m}^2$), very low water content ($< 100 \text{ ppm}$), high ductility, low creep strength and high solubility. From the mechanical point of view, rocksalt is strong and brittle over a short period of time, but weak and ductile over geological times. Rocksalt domes are tectonic traps for hydrocarbons and they are increasingly viewed as a possible storage medium for radioactive and chemical waste and for CO_2 . As a consequence, rocksalt tectonics has been recognised as an important subject to study. For these reasons, various experimental studies on the deformation behaviour of natural and synthetic rocksalt have been carried out (e.g. Heard 1972, Burke et al. 1981, Arieli 1982, Carter & Hansen 1983, Wawersik & Zeuch 1986, Horseman & Handin 1990, Horseman et al. 1992, Senseny et al. 1992, Franssen 1994, Peach & Spiers 1996, Ter Heege et al. 2005). These experiments showed that rocksalt deforms in the dislocation creep field and to some extent in the pressure solution creep field.

High shear strain experiments have been carried out by Shimamoto (1986, 1989a) and by Hiraga & Shimamoto (1987). The interest in these studies was to study the brittle – ductile transition in shear zones with the application to plate boundaries. The experiments were carried out on 0.5mm halite layers placed between sandstone at room temperature using a triaxial deformation apparatus. Franssen & Spiers (1990) and Franssen (1996) carried out simple shear experiments in the temperature range 250-600°C up to shear strains of $\gamma \sim 2$. In both cases dry rocksalt was used.

The focus of this chapter lies on the mechanical behaviour of ‘wet’ rocksalt deformed in torsion (simple shear geometry) up to shear strains of $\gamma \sim 8$ at 100-300°C applying shear strain rates from $3 \times 10^{-5} \text{ s}^{-1}$ up to $3 \times 10^{-3} \text{ s}^{-1}$ by applying a constant confining pressure of 250MPa.

4.2 Method for determining jacket strength

In this study we used a copper jacket because the experiments were carried out between 100 and 300 °C. In that temperature range copper is soft and ductile (Barton et al. 1997) which allows reaching large shear strains (up to $\gamma \sim 8$). However, it is a strong material compared to rocksalt at 100 to 300 °C. Therefore, to obtain the strength of the deformed rocksalt, corrections for the strength of the copper jacket had to be attempted. Jacket corrections are usually carried out on samples with insignificant strength. For a first attempt PTFE

(polytetrafluoroethylene, Teflon) was used. The strength of PTFE between 100 and 300°C is of a few MPa. A second attempt was carried out using PE (polyethylene) and PTFE as jacket instead of copper. Experiments were carried out by applying the same confining pressure, temperature, strain rate and shear strain conditions as for experiments carried out with the copper jacket.

4.3 Results

4.3.1 Behaviour of rocksalt samples in copper jacket

Constant strain rate tests

Fig. 4.1, 4.2 and 4.3 display torque vs shear strain curves for rocksalt samples deformed using copper jackets. Experiments were conducted at 100, 200 and 300°C, at shear strain rates of $3 \times 10^{-5} \text{s}^{-1}$, $3 \times 10^{-4} \text{s}^{-1}$ and $3 \times 10^{-3} \text{s}^{-1}$ applying a confining pressure of 250MPa. Details of these experiments are listed in Table 4.1.

Sample = Run #	Length [mm]	Diameter [mm]	Water content [ppm]	T [°C]	Strain rate [s ⁻¹]	Yield torque [Nm]	Flow torque [Nm]	Torque at finite strain [Nm]	Finite strain [γ]	Comments
P0740	9.6	14.8	47.9	100	3×10^{-5}	25.0	25.25	28.3	0.3	–
P0671	10.0	14.7	37.5	100	3×10^{-4}	25.0	–	33.7	1.1	–
P0686	9.9	14.7	30.2	100	3×10^{-4}	25.9	31.68	31.6	2.1	stick slip
P0682	10.0	14.7	37.0	100	3×10^{-4}	21.9	–	40.0	3.1	–
P0675	10.1	14.8	95.5	100	3×10^{-4}	27.8	–	46.2	6.2	stick slip
P0797	5.0	14.7	–	100	3×10^{-3}	31.7	–	36.5	0.4	–
P0799	5.1	14.8	15.3	100	3×10^{-3}	37.5	–	49.8	3.1	–
P0746	5.0	14.8	55.2	100	3×10^{-3}	23.3	–	50.6	5.0	stick slips
P0735	9.8	14.8	36.7	200	3×10^{-5}	17.7	17.9	16.9	1.1	–
P0725	9.9	14.7	70.8	200	3×10^{-4}	23.5	25.0	24.9	1.0	–
P0731	10.0	14.8	29.6	200	3×10^{-4}	20.3	23.0	20.0	2.3	–
P0728	10.1	14.8	48.6	200	3×10^{-4}	22.6	24.2	22.0	3.4	stick slip
P0768	9.1	14.8	20.1	200	3×10^{-4}	22.0	23.0	20.5	5.2	–
P0742	5.0	14.8	64.0	200	3×10^{-3}	21.3	32.5	32.1	7.9	–
P0791	8.7	14.8	20.3	300	3×10^{-4}	17.0	16.6	15.3	1.1	–
P0773	9.5	14.8	12.9	300	3×10^{-4}	16.9	16.5	13.8	2.4	–
P0766	8.8	14.8	9.7	300	3×10^{-4}	14.7	16.4	8.9	3.5	–
P0747	5.1	14.8	32.1	300	3×10^{-3}	17.4	19.1	14.7	7.9	–

Table 4.1. Details of torsion experiments using copper jackets. Strain rates are valid for the sample margin.

At 100°C (Fig. 4.1) and at all applied shear strain rates there is strain hardening after the yield point (22-38Nm) up to $\gamma \sim 5$. Samples deformed at a shear strain rate of $3 \times 10^{-3} \text{s}^{-1}$ show a higher

strength than samples deformed at shear strain rates of $3 \times 10^{-4} \text{ s}^{-1}$ and $3 \times 10^{-5} \text{ s}^{-1}$, respectively. Applying different strain rates results in different yield points. Samples deformed with strain rates at $3 \times 10^{-4} \text{ s}^{-1}$ and $3 \times 10^{-5} \text{ s}^{-1}$ have a lower yield point ($\sim 25 \text{ Nm}$) than samples deformed at $3 \times 10^{-3} \text{ s}^{-1}$, with a yield point of 32-38 Nm.

Fig. 4.2 displays the torque vs shear strain curves for samples deformed at a temperature of 200°C . The samples at these conditions are more than 1/3 weaker than at 100°C . Under these conditions, samples deformed at a shear strain rate of $3 \times 10^{-3} \text{ s}^{-1}$ are stronger than samples deformed at a shear strain rate of $3 \times 10^{-4} \text{ s}^{-1}$, which in turn are stronger than sample P0735 deformed at $3 \times 10^{-5} \text{ s}^{-1}$. The faster deformed sample ($3 \times 10^{-3} \text{ s}^{-1}$) shows strain hardening after an apparent yield point up to shear strain of $\gamma \sim 6$. After this shear strain, steady state flow is approached with some oscillations in the torque of a wavelength of approximately $\gamma \sim 0.5$. Experiments at a slower strain rate ($3 \times 10^{-4} \text{ s}^{-1}$) shows a short strain hardening after the apparent yield point until shear strains of $\gamma \leq 0.5$. Slight weakening takes place followed by a second steady state that begins at a shear strain of $\gamma \sim 3.5$ with slight oscillations in the torque. The sample deformed at a strain rate of $3 \times 10^{-5} \text{ s}^{-1}$ shows no strain hardening but steady state flow up to the final shear strain.

Torque vs shear strain curves for material deformed at 300°C are shown in Fig. 4.3. In all deformed samples weakening occurred up to the finite strain after initial strain hardening. The samples are 50% weaker than at lower temperatures. No difference in the yield point applying different strain rates is obvious at this temperature. The yield point for the two applied strain rates is 17 Nm. However, samples deformed at $3 \times 10^{-3} \text{ s}^{-1}$ are stronger than those deformed at a strain rate of $3 \times 10^{-4} \text{ s}^{-1}$.

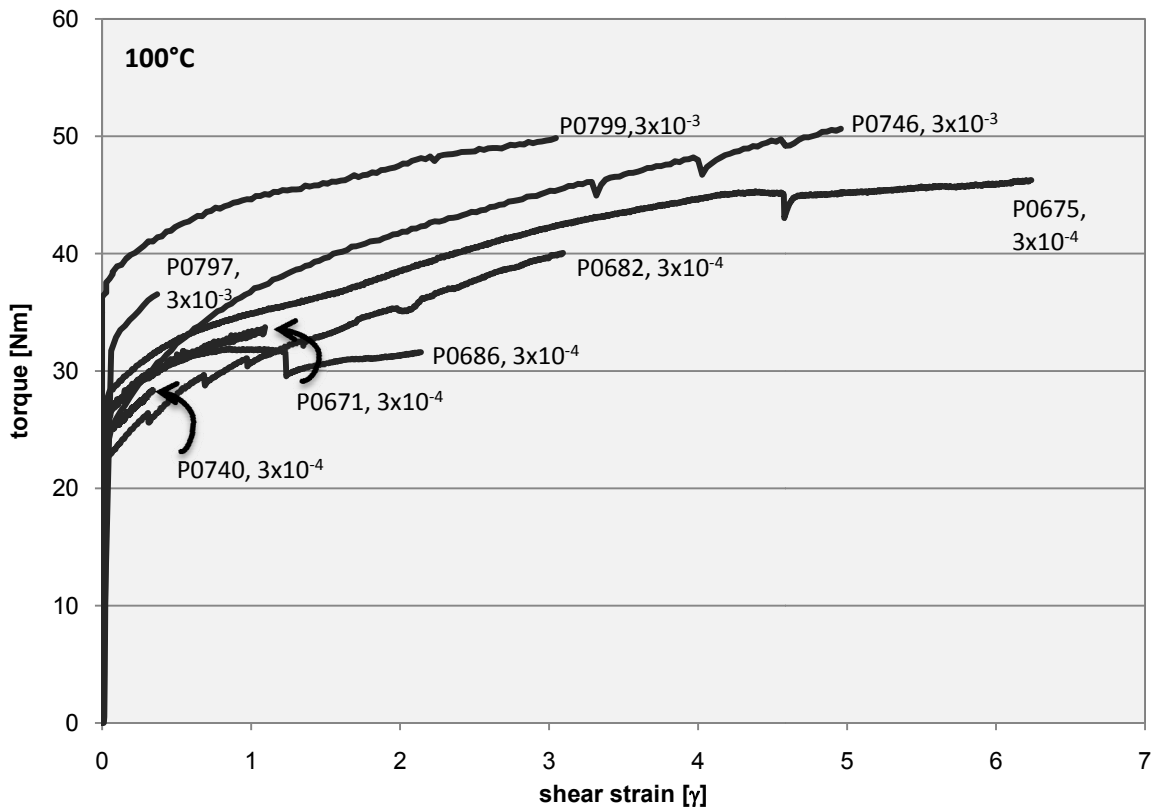


Fig. 4.1. Torque vs shear strain curves for samples deformed at 100°C (raw data, not jacket corrected). Steps in curve at sample P0682 are due to pressure pumps. Jumps in curves P0746 and P0675 are small stick slips. Strain rate is given next to the experiment number in $[\text{s}^{-1}]$.

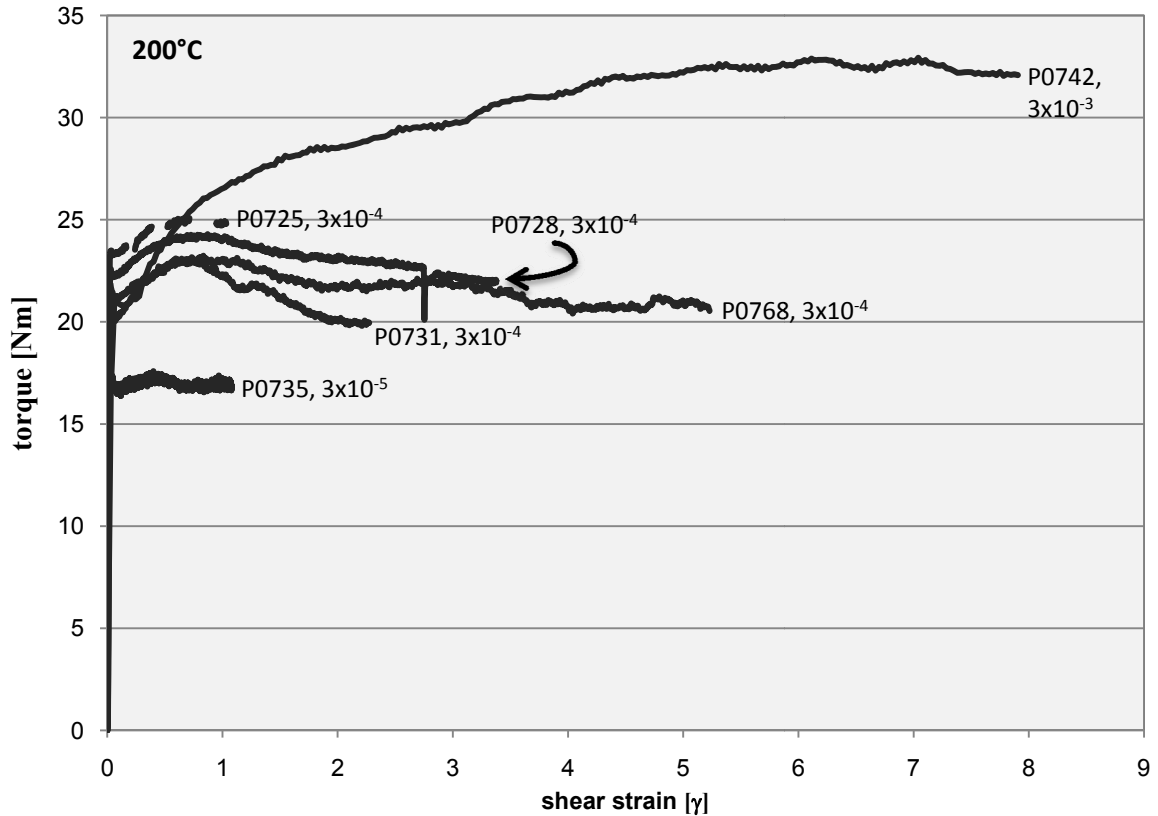


Fig. 4.2. Torque vs shear strain curves for samples deformed at 200°C (raw data, not jacket corrected). Jump in curve P0728 is due to a small stick slip. Strain rate is given next to experiment number in s^{-1} .

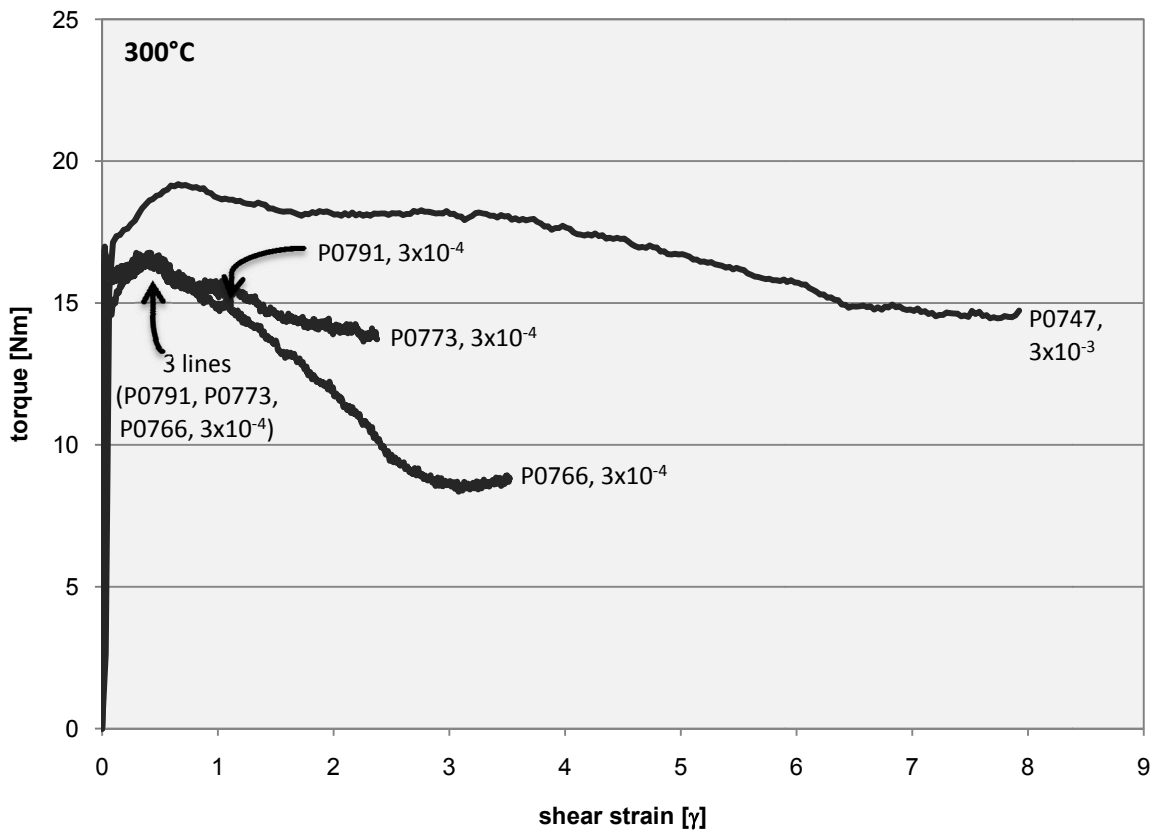


Fig. 4.3. Torque vs shear strain curves for samples deformed at 300°C (raw data, not jacket corrected). Strain rate is given next to experiment number in s^{-1} .

Strain rate stepping tests

Fig. 4.4 shows the torque vs shear strain curves for strain rate stepping tests conducted at 100, 200 and 300°C. The tests were performed in order to determine the value of the stress exponent n (Fig. 4.4). The trends observed are similar to those seen in constant strain rate tests, where work hardening increases with strain rate and the flow torque decreases with increasing temperature.

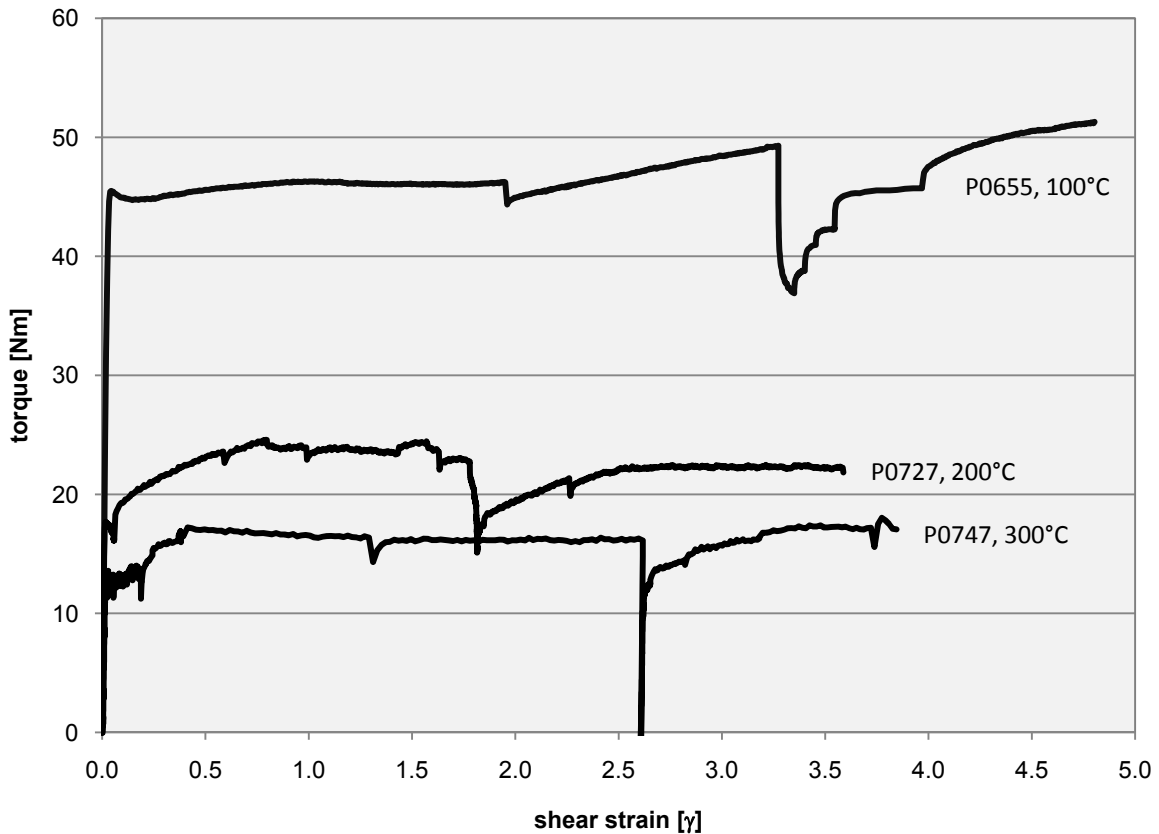


Fig. 4.4. Strain rate stepping tests conducted at 100, 200 and 300°C (data not jacket corrected).

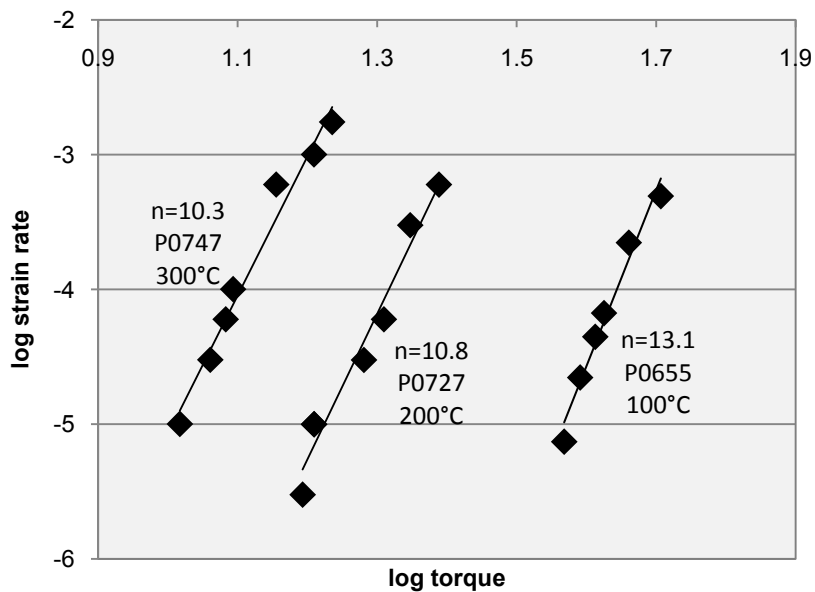


Fig. 4.5. Log strain rate vs log torque diagram, the slope gives value for stress exponent n (data not jacket corrected).

The tests were carried out in the following way; the experiments were run with a constant twist rate until steady state flow was reached. Then the twist rate was decreased until the torque had reached a new constant equilibrium. After this the twist rate was increased in small steps until steady state flow was reached for each twist rate and then the twist rate was increased again. The data for the flow torque at the corresponding shear strain rate were plotted in a log-log diagram (Fig 4.5). The slope of log torque and log strain rate give the stress exponent n . The plotted data for 100°C give an n value of 13, for 200 n=11 and 300°C n=10. Table 4.2 gives the values for the used strain rates and the corresponding flow torque values.

run	T [°C]	CP [MPa]	strain rate increments [s ⁻¹]	flow torque [Nm]	n value
P0655	100	250	7.42E-06	37.0	13
			2.22E-05	39.0	
			4.45E-05	41.0	
			6.67E-05	42.2	
			2.22E-04	45.8	
			4.92E-04	50.9	
P0727	200	250	3.00E-06	15.6	11
			9.99E-06	16.2	
			9.99E-06	16.2	
			3.00E-05	19.1	
			6.00E-05	20.4	
			3.00E-04	22.3	
			6.00E-04	24.5	
P0748	300	250	1.00E-05	10.4	10
			3.00E-05	11.5	
			6.00E-05	12.1	
			1.00E-04	12.4	
			6.00E-04	14.3	
			1.00E-03	16.2	
			1.75E-03	17.2	

Table 4.2. Details of strain rate stepping tests using copper jackets.

4.3.2 Behaviour of PTFE samples in copper jacket

Fig. 4.6 displays shear strain versus torque curves for PTFE samples deformed at 100°C and at two different shear strain rates ($3 \times 10^{-4} \text{ s}^{-1}$ and $3 \times 10^{-3} \text{ s}^{-1}$). Both curves show the same torque-strain behaviour. After the yield point there is strain hardening up to a shear strain of $\gamma \sim 1.5$ followed by a short weakening up to a shear strain of $\gamma \sim 3$ and then nearly steady-state torque.

Fig. 4.7 shows the curves for PTFE samples deformed at 200°C applying shear strain rates of $3 \times 10^{-4} \text{ s}^{-1}$ and $3 \times 10^{-3} \text{ s}^{-1}$. The assembly is slightly weaker than at 100 °C. Both experiments show strain hardening after the yield point. However, sample deformed at a shear strain rate of $3 \times 10^{-4} \text{ s}^{-1}$ continues hardening up to $\gamma \sim 2.5$, approaches a peak torque at $\gamma \sim 3$ and descends into a strong and fast strain weakening up to a shear strain of $\gamma \sim 3.5$. From there, shear strain weakening occurs slower but steady up to the finite strain of $\gamma \sim 7$. In contrast, the sample deformed with a faster strain rate ($3 \times 10^{-3} \text{ s}^{-1}$) displays a continuous steady state behaviour from a shear strain of $\gamma \sim 1.4$ up to the finite shear strain of $\gamma \sim 9$.

Fig. 4.8 illustrates torque vs shear strain curves for PTFE samples deformed at 300°C at two different shear strain rates ($3 \times 10^{-4} \text{ s}^{-1}$ and $3 \times 10^{-3} \text{ s}^{-1}$). The assembly is weaker at 300°C than at 200°C. At this temperature there is an obvious difference in the mechanical behaviour of the two samples according to the shear strain rates applied. The sample deformed at $3 \times 10^{-3} \text{ s}^{-1}$ shows, after the yield point, a constant and continuous strain hardening up to the finite shear strain of $\gamma \sim 3.2$. In contrast, the sample deformed at $3 \times 10^{-4} \text{ s}^{-1}$ displays, after strain hardening up to a peak torque, a continuous strain weakening up to the finite shear strain of $\gamma \sim 4$.

Fig. 4.9 shows a torque vs shear strain diagram for direct comparison of the strength as a function of temperature and shear strain rate.

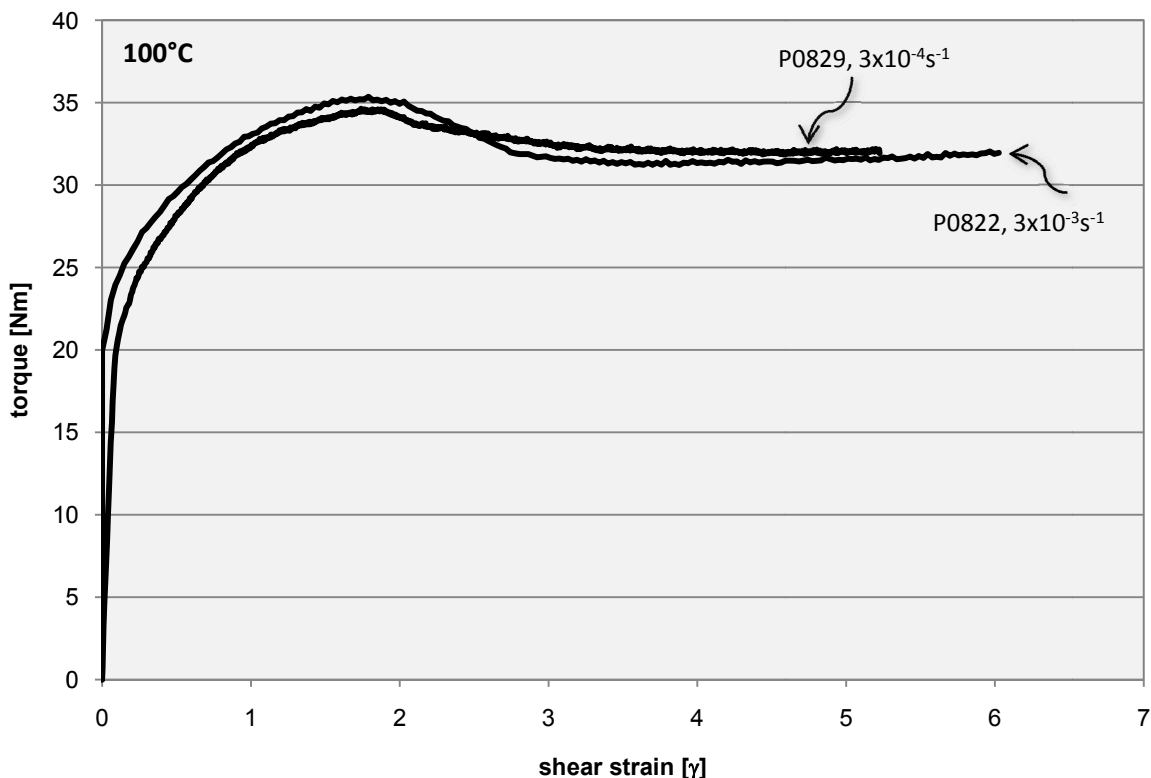


Fig. 4.6. Torque vs shear strain diagram for PTFE samples deformed at 100°C.

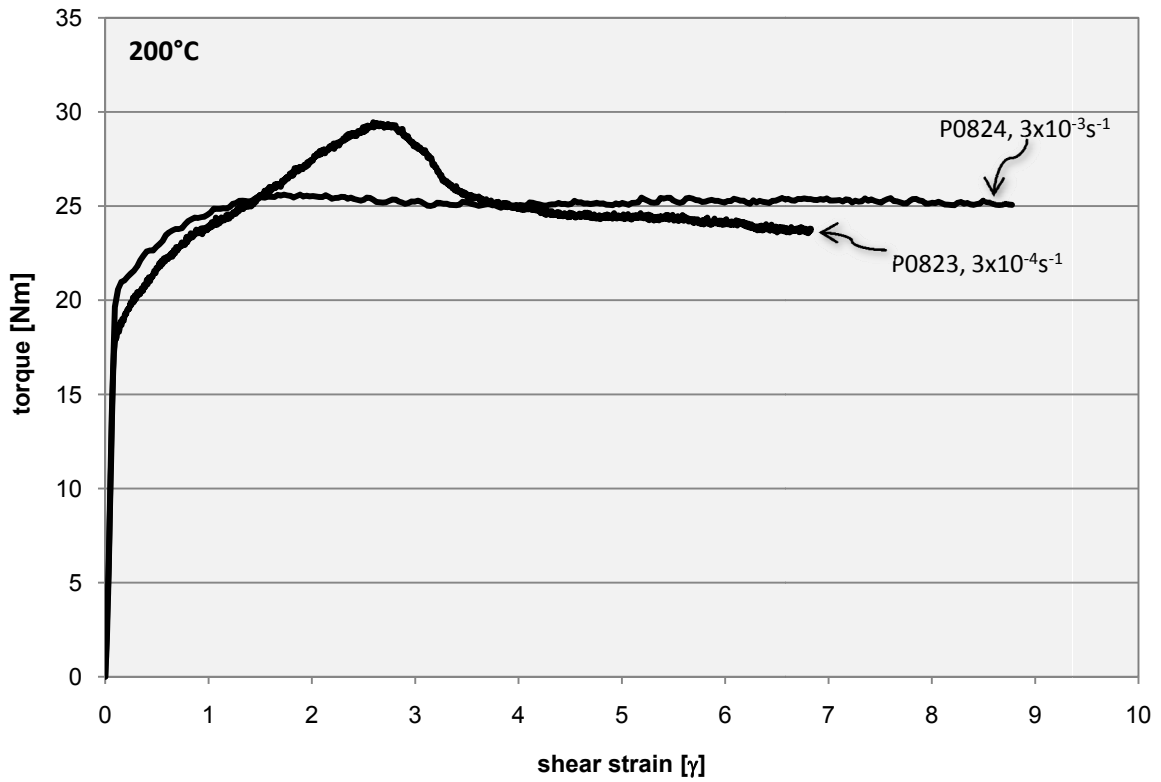


Fig. 4.7. Torque vs shear strain plot for PTFE samples deformed at 200°C.

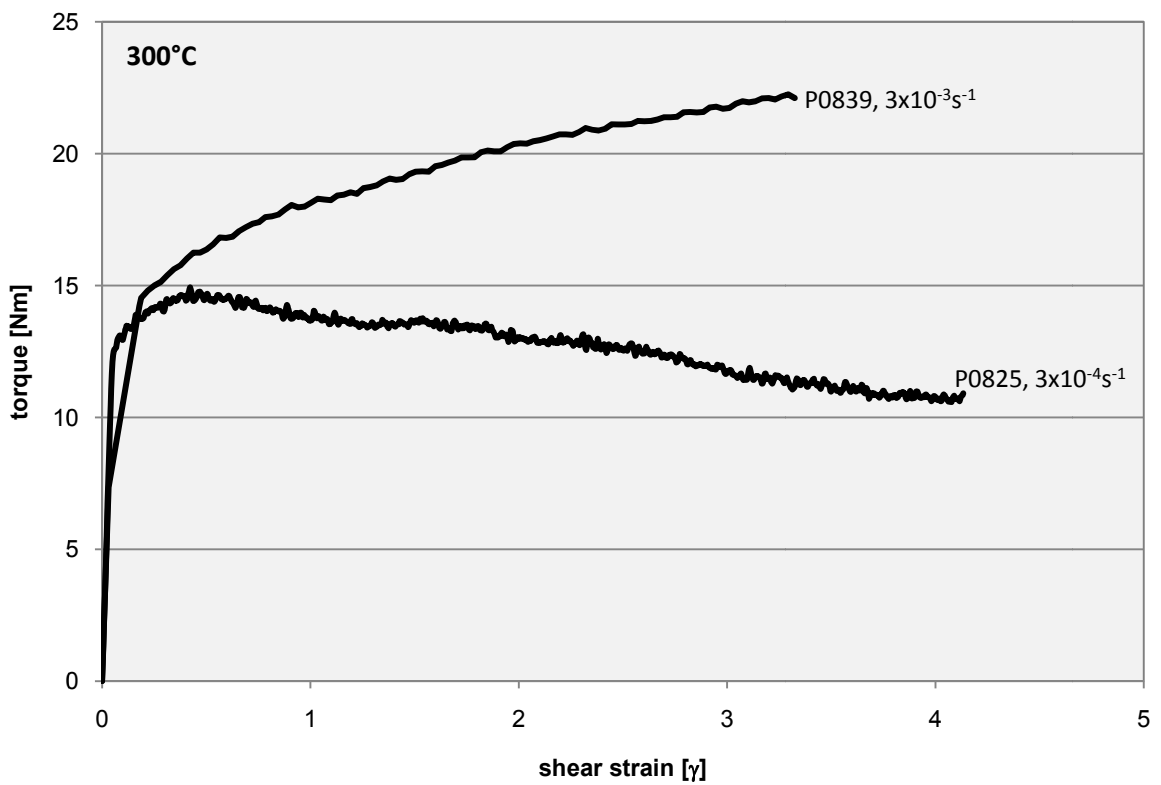


Fig. 4.8. Torque vs shear strain diagram for PTFE samples deformed at 300°C.

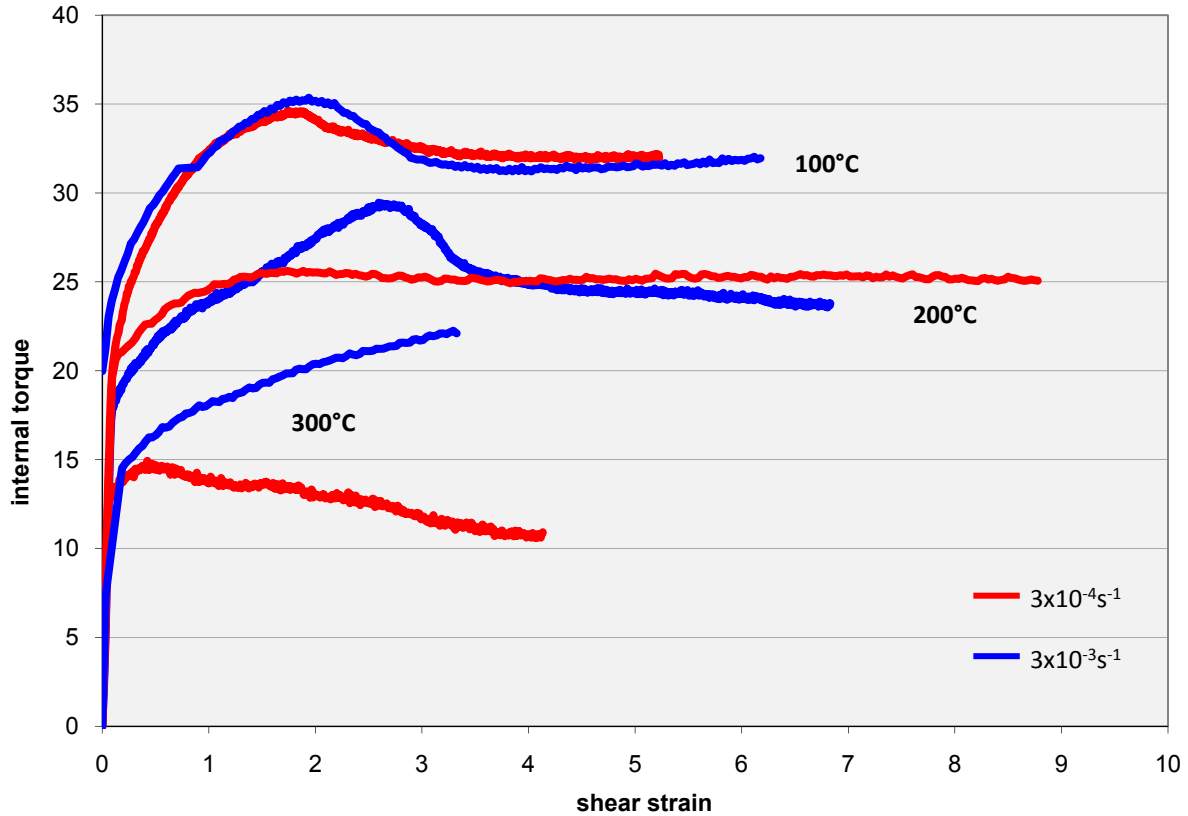


Fig. 4.9. Combined plot of torque vs shear strain for all PTFE samples deformed in torsion, for visualising the difference in strength with an increase in temperature.

4.3.3 Behaviour of rocksalt samples in PE and PTFE jackets

Fig. 4.10 shows the torque vs shear strain curve for rocksalt samples deformed in a PE (polyethylene) and PTFE jacket. These two experiments were another attempt to constrain the actual mechanical behaviour of rocksalt. In these experiments strain rate stepping tests were included after the torque reached steady state flow. The samples are constantly strain hardening up to a shear strain of $\gamma \sim 1.6$ (100°C) and $\gamma \sim 1.5$ (200°C) and approach steady state flow. After steady torque, the strain rate was varied to obtain the stress exponent n at the two temperatures. The obtained n -exponents for 100 ($n=4.5$) and 200°C ($n=5.4$) are shown in a log torque vs log strain rate plot in Fig. 4.11. Table 4.3 gives details on used strain rates and the corresponding flow torque.

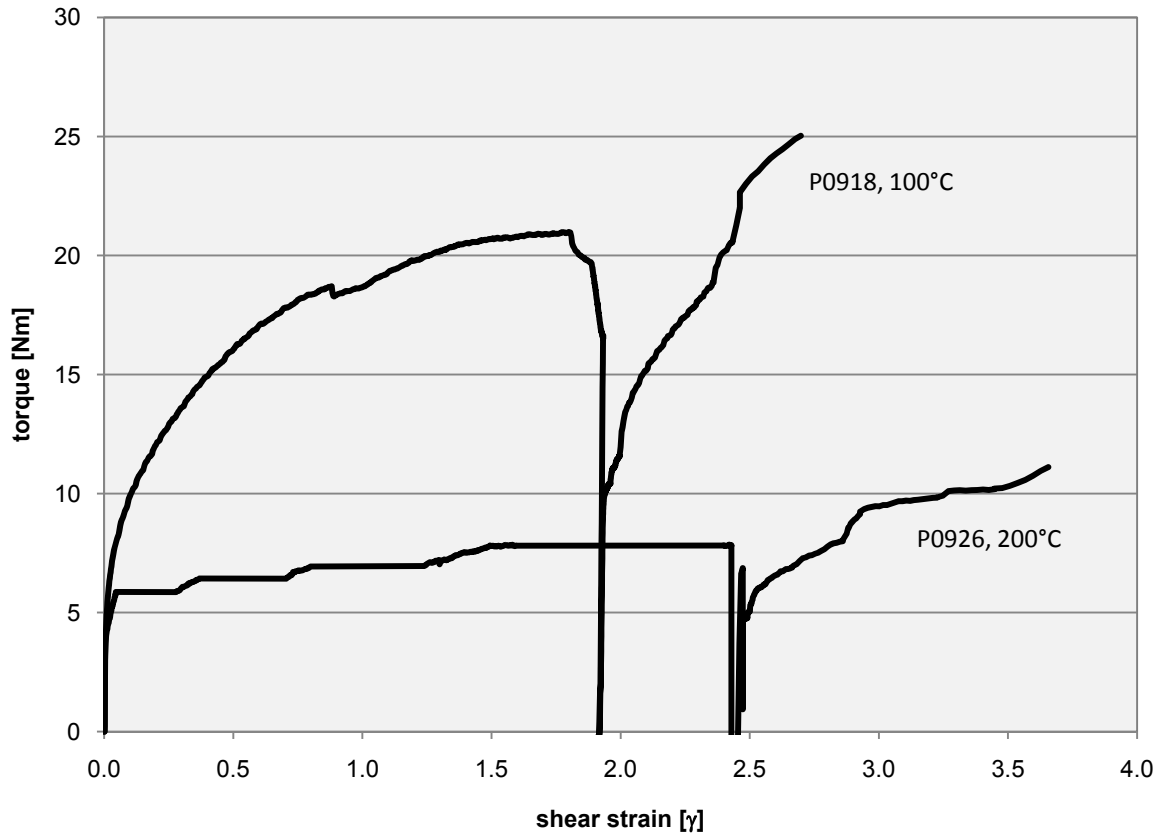


Fig. 4.10. Torque vs shear strain diagram for rocksalt samples inside PE and PTFE jackets deformed at 100°C (blue curve) and 200°C (red curve).

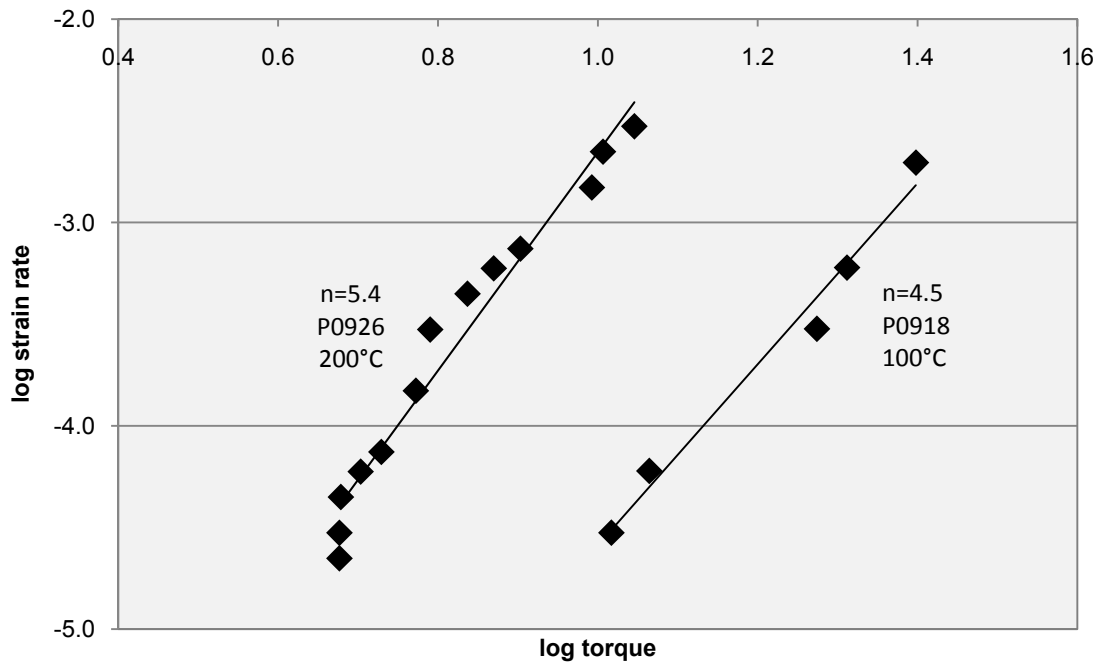


Fig. 4.11. Log strain rate vs log torque diagram of strain stepping tests from curves in Fig. 4.10., the slope gives value for stress exponent n .

run	T [°C]	CP [MPa]	strain rate increments [s ⁻¹]	flow torque [Nm]	n value
P0918	100	250	3.00E-04	20.9	4.5
			2.98E-05	10.4	
			6.00E-05	11.6	
			3.00E-04	18.8	
			6.00E-04	20.5	
			1.97E-03	25.0	
P0926	200	250	2.23E-05	4.8	5.4
			2.98E-05	4.8	
			4.46E-05	4.8	
			5.95E-05	5.1	
			7.44E-05	5.2	
			1.49E-04	5.9	
			2.98E-04	6.2	
			4.46E-04	6.9	
			5.95E-04	7.4	
			7.44E-04	8.0	
			1.49E-03	9.8	
			2.23E-03	10.2	
2.98E-03	11.1				

Table 4.3. Details of strain rate stepping tests using PE (P0918) and PTFE (P0926) as jacket material.

4.4 Discussion

Results show that rocksalt surrounded by the copper jacket is stronger than PTFE surrounded by the copper jacket. PTFE inside the copper jacket, in turn, is stronger than rocksalt surrounded by PE and PTFE jackets. Therefore, the strength of the copper jacket must be considered to obtain the strength of rocksalt. Furthermore, the stress exponents obtained for rocksalt samples in the copper jacket are far too high and thus cannot be used to determine the deformation mechanism active in the deformed samples.

The attempts to correct the strength of the jacket by carrying out experiments using PTFE as a sample material were not satisfactory. PTFE, as obvious in the torque-shear strain curves, show a non-negligible shear strength and shows a distinctive bump in the torque – strain behaviour, especially at 100 and 200 °C. A possibility to determine the strength of rocksalt exists in experiments where PE and PTFE were used as jacket material. The stress exponents calculated from these experiments, $n=4.5$ (100 °C) and $n=5.4$ (200 °C), agree well with n values obtained from previous experiments carried out in compression and simple shear (Table 4.4).

author	deformation mode	T (°C)	n-value
this study	torsion (simple shear)	100	4.5
		200	5.4
<i>Ter Heege et al. (2005)</i>	compression	75-250	5.6
<i>Heard (1972)</i>	compression	23-400	5.5
<i>Heard and Ryerson (1986)</i>	compression	23-400	5.8
<i>Wawersik and Zeuch (1986)</i>	compression	23-160	4.1-6.3
<i>Franssen (1994)</i>	compression	250-450	5.7
<i>(Franssen 1993)</i>	simple shear	250	5.2
<i>Arieli et al. (1982)</i>	compression		
low stress		200-400	5.3
high stress		200-400	11.3
<i>Heard/Arieli et al. recalculated by Franssen(1994)</i>	compression		
low stress		200-400	5.8
high stress		200-400	6.5
<i>Carter et al. (1993)</i>	compression		
natural rocksalt: high strain rate		50-200	5.3
natural rocksalt: low strain rate		100-200	3.4

Table 4.4. Comparison of n values from this study with previously conducted experiments on rocksalt.

This suggests that PE and PTFE can be used as a jacket material at least at 100 and 200 °C. At T>250 °C, these materials cannot be used because both are instable.

In the light of these results, predictions on the deformation mechanism active in rocksalt, can only be done for rocksalt deformed at 100 and 200°C. The stress exponent of n=4.5 (at 100°C) and n=5.4 (at 200°C) suggest that deformation occurred in the dislocation creep field, which agrees with the microstructure and the presence of a CPO, as reported in chapter 5 and chapter 6.

Even though we did not obtained absolute values of the strength on the copper jacketed samples, the relative behaviour was consistent with the microstructure produced.

In all tests strain hardening is possibly caused by an increase in the dislocation density and the interaction of dislocations in the material. Dislocations pile up in front of obstacles (tangling) and movement is prohibited. This leads to an increase in the strength of the material and is expressed in strain hardening. This type of behaviour is common in cold-worked metals (e.g. copper). A microstructure resulting from strain hardening should thus show grains containing a high dislocation density. No TEM work was conducted in this study, therefore it is difficult to link the microstructure with strain hardening. But, from Fig. 4.10 it is obvious that rocksalt is strain hardening at 100°C up to shear strains of $\gamma \sim 2$. In the investigated samples at this temperature and at this strain, the microstructure consists of sheared grains containing dense networks of subgrains (cf. chapter 5).

Steady state is caused by the balancing processes of strain hardening and recovery. Dislocations are still produced but recovery mechanisms as the formation and growth of subgrains counteract strain hardening. The steady state microstructure is thus a microstructure consisting of subgrains, as it is the case in the microstructure of the deformed samples at 100 and 200 °C (cf. chapter 5).

Strain softening or strain weakening are caused by the reduction of the dislocation density in the deformed material. This reduction can occur by dynamic recrystallisation. Comparing this with the microstructure observed strain weakening must have taken place in samples deformed at 200 and 300°C.

We conclude that the geometry of the torque-strain curves of the uncorrected data reflects the mechanical behaviour of rocksalt. The uncertainty clearly lies in the actual strength of the samples, clearly at 100°C the material is stronger than at 200°C and at 300°C.

4.5 Conclusions

- The stress exponents $n=4.5$ at 100°C and $n=5.4$ at 200°C from rocksalt samples using PE and PTFE jackets suggest that deformation at these temperatures occurred in the dislocation creep field. This is consistent with the microstructure and the presence of a CPO.
- No conclusion can be drawn on the rheology of rocksalt from the data without correction for the copper jacket strength.
- Copper at 100-300°C is not a suitable jacket material because it is stronger than the rocksalt to be deformed.
- PE jackets however, seem to be a good solution, at least for 100°C and PTFE jackets for 200°C. For 300°C another material has to be found to investigate the mechanical behaviour of rocksalt.

4.6 References

- Arieli, A., Heard, H.C. and Mukherjee, A.K. 1982. Deformation modelling in sodium chloride at intermediate and elevated temperatures. In: *Mechanical Testing for Deformation Model Development, ASTM STP 765* (edited by Swearingen, R. W. R. a. J. C.), 342-365.
- Barton, D.C., Mirza, M.S., Waheed, M., Sturges, J.L. & Church, P. 1997. The high strain-rate fracture characteristics of ductile metals at elevated and sub-ambient temperatures. *Fatigue and Fracture of Engineering Materials and Structures* 20(4), 573-581.
- Burke, P.M., Cannon, R.W. & Sherby, O.D. 1981. Intermediate and high temperature creep of sodium chloride. *Workshop on Structural Behaviour of Repository Materials, Sandia National Laboratories, Albuquerque, N.M., April 29*.
- Carter, N.L. & Hansen, F.D. 1983. Creep of Rocksalt. *Tectonophysics* 92(4), 275-333.
- Carter, N.L., Horseman, S.T., Russell, J.E. & Handin, J. 1993. Rheology of Rock-Salt. *Journal of Structural Geology* 15(9-10), 1257-1271.
- Franssen, R.C.M.W. 1993. Rheology of synthetic rocksalt. PhD thesis, Universiteit Utrecht.
- Franssen, R.C.M.W. 1994. The Rheology of Synthetic Rock-Salt in Uniaxial Compression. *Tectonophysics* 233(1-2), 1-40.

- Franssen, R.C.M.W. 1996. Mechanical anisotropy of synthetic polycrystalline rocksalt. In: *Fourth Conference on the Mechanical Behaviour of Salt*. TTP Trans Tech Publications, Clausthal-Zellerfeld, Germany, The Pennsylvania State University, June 17 and 18, 1996, 63-75.
- Franssen, R.C.M.W. & Spiers, C.J. 1990. Deformation of polycrystalline salt in compression and in shear at 250-350°C. In: *Deformation Mechanisms, Rheology and Tectonics* (edited by Knipe, R.J. & Rutter, E.H.) 45. Geological Society Special Publication, 201-213.
- Heard, H.C. 1972. Steady-state flow in polycrystalline halite at pressure of 2 Kilobars. In: *Flow and Fracture of Rocks* (edited by H.C. Heard et. al.) 16. Geophysical Monograph, 99-115.
- Heard, H.C. & Ryerson, F.J. 1986. Effect of cation impurities on steady-state flow of salt. In: *Mineral and Rock Deformation: Laboratory Studies, AGU Geophysical Monograph Series* (edited by Hobbs, B.E. & Heard, H.C.), 99-115.
- Hiraga, H. & Shimamoto, T. 1987. Textures of sheared halite and their implications for the seismogenic slip of deep faults. *Tectonophysics* 144(1-3), 69-86.
- Horseman, S.T. & Handin, J. 1990. Triaxial compression tests on rocksalt at temperatures from 50° to 200° and strain rates from 10⁻⁴ to 10⁻⁹/s. In: *The Brittle-Ductile Transition in Rocks* (edited by Duba, A. G. et al.) 56. Geophysical Monographs, 103-110.
- Horseman, S.T., Russell, J.E., Handin, J. & Carter, N.L. 1992. Slow experimental deformation of Avery Island salt. In: *7th International Symposium on Salt*, Kyoto, Japan.
- Peach, C.J. & Spiers, C.J. 1996. Influence of crystal plastic deformation on dilatancy and permeability development in synthetic salt rock. *Tectonophysics* 256(1-4), 101-128.
- Senseny, P.E., Hansen, F.D., Russell, J.E., Carter, N.L. & Handin, J.W. 1992. Mechanical-Behavior of Rock Salt - Phenomenology and Micromechanisms. *International Journal of Rock Mechanics and Mining Sciences & Geomechanics Abstracts* 29(4), 363-378.
- Shimamoto, T. 1986. Transition between Frictional Slip and Ductile Flow for Halite Shear Zones at Room-Temperature. *Science* 231(4739), 711-714.
- Shimamoto, T. 1989a. Mechanical behaviours of simulated halite shear zones: implications for the seismicity along subducting plate-boundaries. In: *Rheology of solids and of the Earth* (edited by Karato, S. & Toriumi, M.), 351-373.
- Ter Heege, J.H., De Bresser, J.H.P. & Spiers, C.J. 2005. Rheological behaviour of synthetic rocksalt: the interplay between water, dynamic recrystallization and deformation mechanisms. *Journal of Structural Geology* 27(6), 948-963.
- Wawersik, W.R. & Zeuch, D.H. 1986. Modeling and Mechanistic Interpretation of Creep of Rock Salt Below 200-Degrees-C. *Tectonophysics* 121(2-4), 125-152.

Chapter 5

Polygonization and recrystallisation in synthetic rocksalt – observations from torsion experiments

This chapter deals with the microstructures developed in synthetic rocksalt during torsion experiments at temperatures from 100-300°C. Subgrain formation, subgrain rotation and dynamic recrystallisation play a major role in the deformed rocksalt and will be systematically investigated using optical micrographs and detailed orientation maps obtained by EBSD.

5.1 Introduction

Polygonization – the process of subgrain formation – fragments a crystal or grain into subgrains (Poirier 1985). Subgrains are blocks of nearly constant crystal orientation and are separated by low angle boundaries, which are dislocations walls (Jenkins & Mellor 1935, Wyon & Crussard 1951, McLean 1952). Subgrain formation is a recovery process, accompanied by vacancy diffusion and the ability for edge dislocation to climb onto a different glide plane (Poirier 1985).

With increasing density of dislocations in the subgrain boundary the misorientation increases and may reach values higher than 15°, when grains have formed from subgrains. There is no clear distinction between low angle and high angle boundaries in literature; usually a limit is set at a misorientation of about 10 or 15° (Poirier 1985). In this study, we have chosen a misorientation larger than 15° as high angle boundary.

The formation of new grains is called recrystallisation. This process involves the formation/nucleation and growth of new grains. Recrystallisation during deformation is defined as dynamic or synkinematic recrystallisation (Hobbs 1968, Hobbs et al. 1982, Urai et al. 1986a). Several mechanisms of dynamic recrystallisation could be distinguished (e.g. Urai et al. 1986a and Drury & Urai 1990). Important in this chapter are the processes of subgrain rotation recrystallisation (SGR) and grain boundary migration recrystallisation (GBMR). Subgrain rotation recrystallisation belongs to the recovery processes. The driving force for SGR is the reduction in the internal strain energy of the deforming aggregate. The reduction in the internal strain energy is achieved by the movement of dislocation into dislocations walls (e.g. Urai et al. 1986a). With ongoing deformation more dislocations arrive in the wall where the misorientation between the subgrains increases until high angle boundaries are formed from subgrain boundaries. Evidences that SGR occurred are a core and mantle structure (Gifkins 1976), where the core consists of the parent grain and the mantle is characterised by subgrains that have a higher misorientation in relation to the parent grain. Around the core new recrystallized grains, that have a similar size and orientation to the nearby subgrains, are present (White 1976). This observation can also be used as an indicator that subgrain rotation recrystallisation occurred if a core and mantle structure is not developed.

The second process of dynamic recrystallisation described in this chapter is grain boundary migration recrystallisation (GBMR). The process results in the migration of grain boundaries

from strain free (dislocation free) nuclei/grains into deformed grains containing a high dislocation density (Poirier 1986). The driving force for this process is also the reduction in internal stored strain energies. The process is also called strain-induced grain boundary migration (SIGBM). Grains with low defect densities (low internal strain energy) consume grains with a high defect density (high internal strain energy). The microstructural features for this process are bulged grain boundaries (White 1976).

Polygonization and dynamic recrystallisation have been observed in dry deformed single and polycrystalline halite and in deformed wet halite aggregates (e.g. Guillopé & Poirier 1979, Friedman et al. 1981, Carter & Hansen 1983, Urai et al. 1986b, Nadgornyi & Strunk 1987, Franssen 1993, Pennock et al. 2004, Ter Heege et al. 2005). Observations on the dry (water content <5 ppm) and wet deformed samples showed major differences in the microstructure. It has been shown by e.g. Spiers et al. (1986), Urai et al. (1986b) and by Spiers & Carter (1998) that the mobility of grain boundaries increases when small amounts of water are present. If no water is present recrystallisation by grain boundary migration in deformed salt would otherwise not occur until a temperature of above 500°C as shown by Guillopé & Poirier (1979).

Despite the huge work on rocksalt some questions remain. Most of the experimental work was carried out at low strains and under coaxial experiments, except the work of Franssen & Spiers (1990) and Franssen (1996) who carried out simple shear experiments up to shear strains of $\gamma \sim 2$. However, in nature most deformation occurs under non-coaxial condition reaching high shear strains. It is therefore of great interest to study the effect of shear strain on the microstructure and the corresponding deformation and recrystallisation mechanisms in the low temperature field (100-300°C).

In the following sections, detailed analysis on the microstructure formed in wet polycrystalline halite (water content >9ppm, as inferred from FTIR, cf. chapter 4) and the dominant microstructural mechanisms will be presented and described.

5.2 Methods

Deformation experiments were carried out in torsion, applying temperatures of 100, 200 and 300°C and strain rates of 3×10^{-5} , $3 \times 10^{-4} \text{s}^{-1}$ and $3 \times 10^{-3} \text{s}^{-1}$. Details on the experimental set up can be found in chapter 3. The mechanical behaviour of rocksalt deformed under the investigated conditions is described in chapter 4.

Optical microscopy in reflected light, on polished and etched sections, was carried out to investigate the microstructure of the starting material and the deformed samples. Etching was done to remove surface damages from mechanical polishing and to reveal the grain and subgrain boundaries. Details of the polishing and etching procedure can be found in chapter 3. Optical microscopy is limited in determining whether subgrain rotation and subgrain rotation recrystallisation occurred, since it is not possible to determine misorientation angle by optical microscopy. Therefore, the electron backscatter diffraction (EBSD) technique (Venables & Harland 1973, Dingley 1984, Prior et al. 1999) was used. Automated EBSD data collection enables the construction of quantitative microstructural orientation maps (Adams et al. 1993; Wright 1993). Orientation maps are coloured grain maps which contain the full crystallographic information of every pixel, obtained from the electron backscatter diffraction patterns. For analysing the misorientation relationship between subgrains and new formed grains high resolution detail scans were performed. Orientation maps were used and

misorientation profiles were drawn across the grains. In addition, grain boundary maps show the distribution of low angle and high angle boundaries. Misorientation distribution charts are useful to describe the distribution of lattice misorientations across grain boundaries (Fliervoet et al. 1999). In the charts, the correlated curve represents the frequency of misorientation angles related to the nearest neighbours. The uncorrelated curve shows the misfit relationship between every grain over the entire measured area. The random curve corresponds to the distribution for a reference sample with no CPO. The maximum misorientation angle of 63° is due to the cubic symmetry of halite.

Scans of the bulk samples were performed to obtain data for calculating the mean grain size, achieved by using the commercial EDAX OIM Analysis software. The orientation maps as well as the image pattern quality maps reproduce the microstructure observed in the reflected light micrographs accurately, apart from a small amount of occasional misindexing. In the processed orientation maps the grains are colour coded with respect to the scanning reference frame (cf. chapter 3) and highlight orientation changes within and between individual grains.

EBSA was carried out in an SEM (CamScanCS44LB and FEI Quanta 200 FEG) using scanning parameters listed in Table 5.1. Scanning details of the orientations maps obtained by EBSA can be found in the appendix.

SEM type	WD [mm]	beam current [nA]	step size [μm]	voltage [kV]	binning	frames /sec	spot size
CamScan CS 44LB	35	2 - 3	10 ^(*1) , 0.5 ^(*2)	15	8x8	29	3
FEI Quanta 200 FEG	15	2 - 3	0.2	20	6x6	40	5

(*1) used for bulk sample scans (*2) used for detailed scans

Table 5.1 Scanning parameters used for EBSA analysis.

Because this chapter deals with orientation of crystallographic planes in NaCl; an overview of these crystallographic planes in the NaCl crystal lattice is provided in Fig. 5.1.

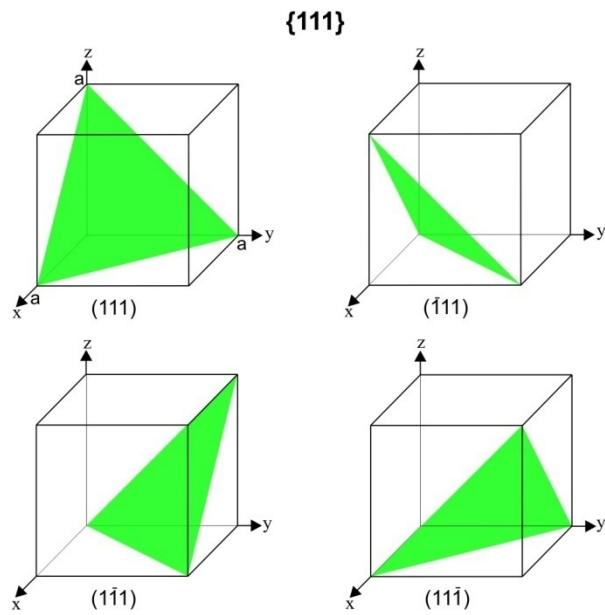
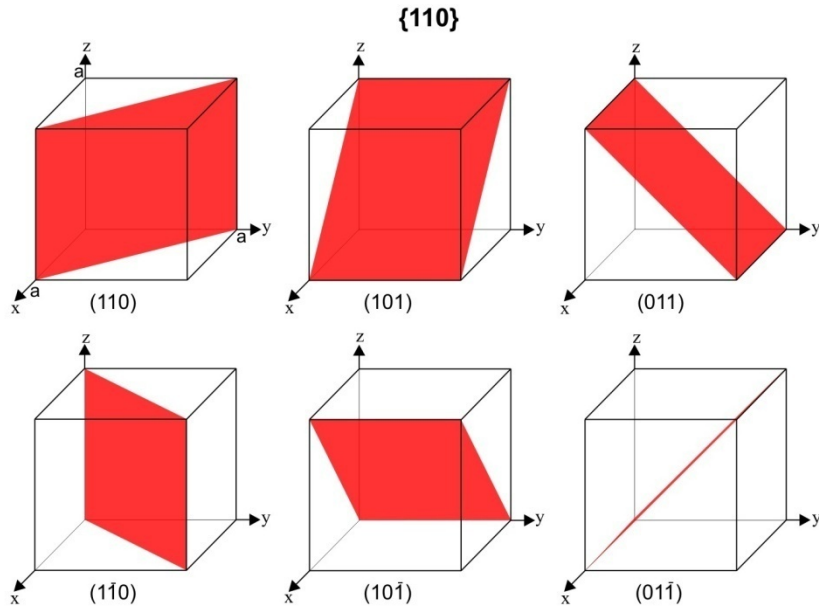
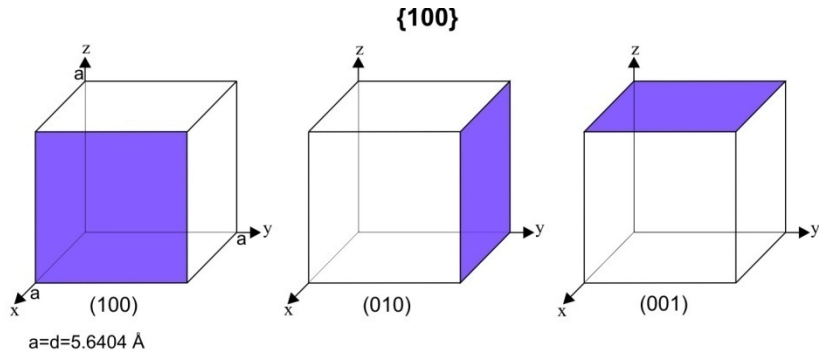


Fig. 5.1. Crystallographic families of {100}, {110} and {111} planes in the NaCl lattice.

5.3 Results

5.3.1 Starting material

The starting material, after cold-pressing and annealing of the original NaCl powder, is characterised by polygonal grains with an unimodal grain size distribution (Fig. 5.2). Grains with a grain size of $140\mu\text{m}$ have the highest number fraction, whereas the highest area fraction is assigned to grains with $200\mu\text{m}$ in size.

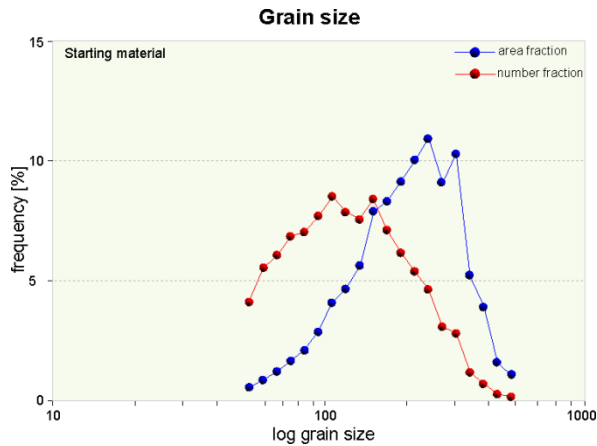


Fig. 5.2. Frequency distribution of the grain size using equivalent grain diameter in log scale.

The grain boundaries of the starting material are smooth and gently curved and grain triple junctions intersect at an angle of roughly 120° (Fig. 5.3). All grains show nearly no internal deformation substructures, as indicated in the grain boundary map of the bulk sample scan and in the low frequency of low angle boundaries in the misorientation chart in Fig. 5.4. The microstructure represents a typically static recrystallised equilibrium foam structure.

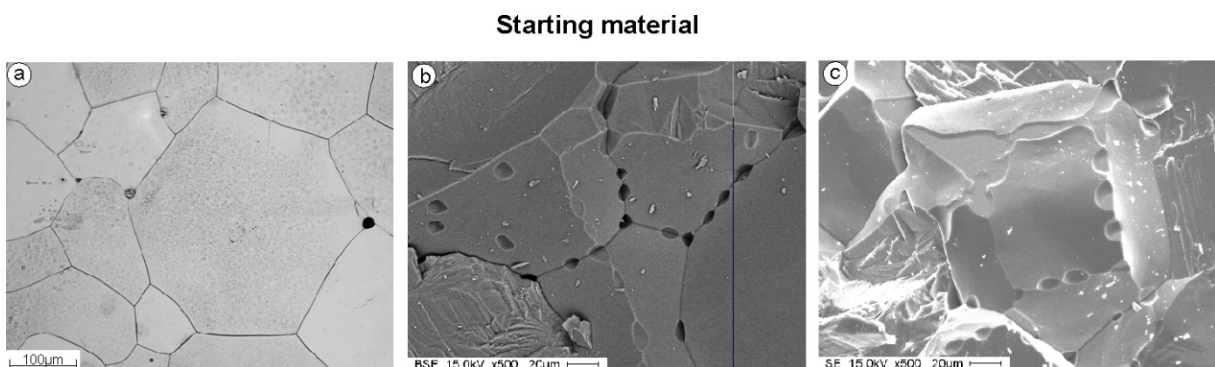


Fig. 5.3. a) Reflected light micrograph of polished and etched section shows polygonal grains with gently curved grain boundaries. No internal deformation structure is visible. b) BSE image of a broken surface with pores along grain boundaries and at triple junctions, indicating that water in pockets is present. Porosity of the starting material is less than 1%. c) SE image of a broken surface with so called “island and channel” structure on the grain boundary face, indicating fluid pathway.

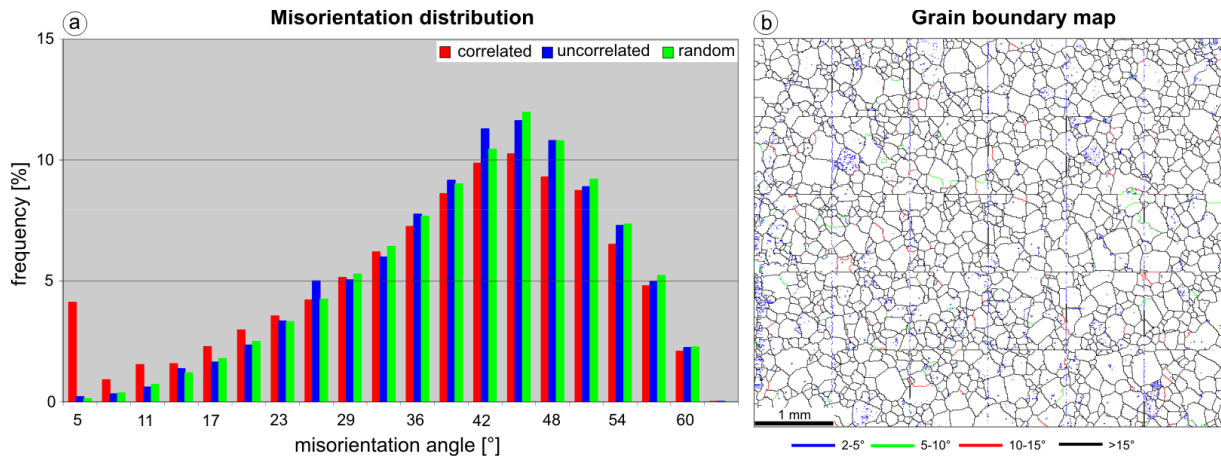


Fig. 5.4. a) Misorientation angle distribution, showing that low misorientation angles ($<15^\circ$) are the minority in the sample. b) Grain boundary map, showing boundaries with misorientation between $2-5^\circ$ (blue), $5-10^\circ$ (green), $10-15^\circ$ (red) and boundaries with misorientations $> 15^\circ$ (black). The vertical and horizontal black lines are artefacts from the OIM software caused by stitching the scan frames together, thus creating artificial high angle grain boundaries.

5.3.2 Deformed samples

In the following, the characteristic features observed in the deformed samples will be described.

Grain boundaries

In the deformed samples four characteristic grain boundary types could be observed:

- (1) Straight grain boundaries (Fig. 5.5) are present in grains with no internal deformation substructure.
- (2) Serrated grain boundaries (Fig. 5.6) are the characteristic feature of deformed grains at 100°C up to shear strains of $\gamma \sim 3$. They also occur in samples deformed at 200 and 300°C .
- (3) Cusped/lobate grain boundaries (Fig. 5.7) formed in samples deformed at 200 and 300°C . The wavelength of the cusps and lobes is similar to the size of the subgrains.
- (4) Bulged grain boundaries (Fig. 5.8) occur in grains deformed at 200 and 300°C . This type of boundary can be observed in new formed grains containing a deformation substructure and in new formed grains lacking deformation substructure.

Straight grain boundaries

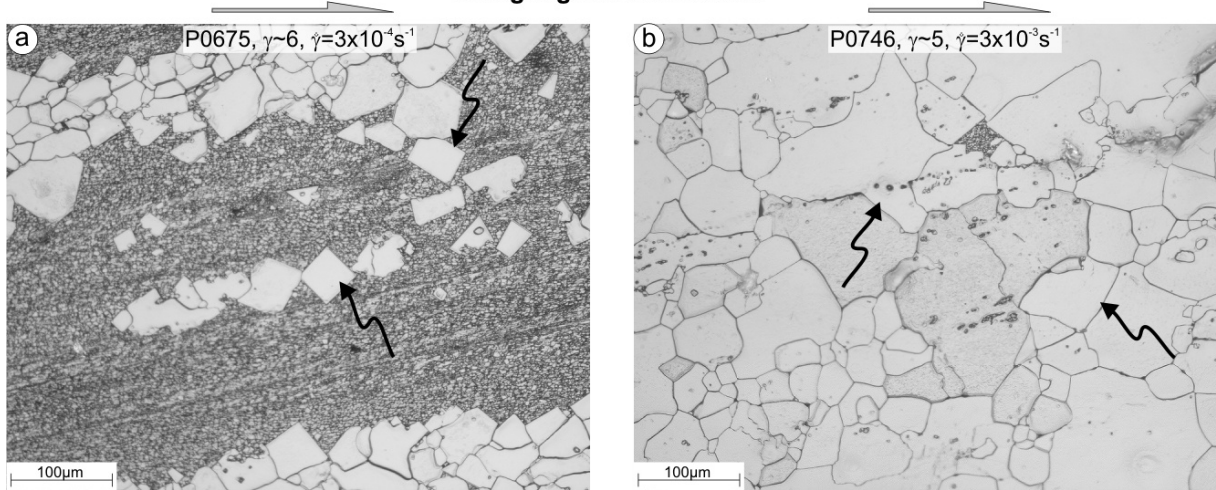


Fig.5.5. Reflected light micrographs of samples deformed at 100°C. (a) Idiomorphic grains (black arrows) with straight grain boundaries. (b) polygonal shaped grains with straight and gently curved grain boundaries, indicated by black arrows.

Serrated grain boundaries

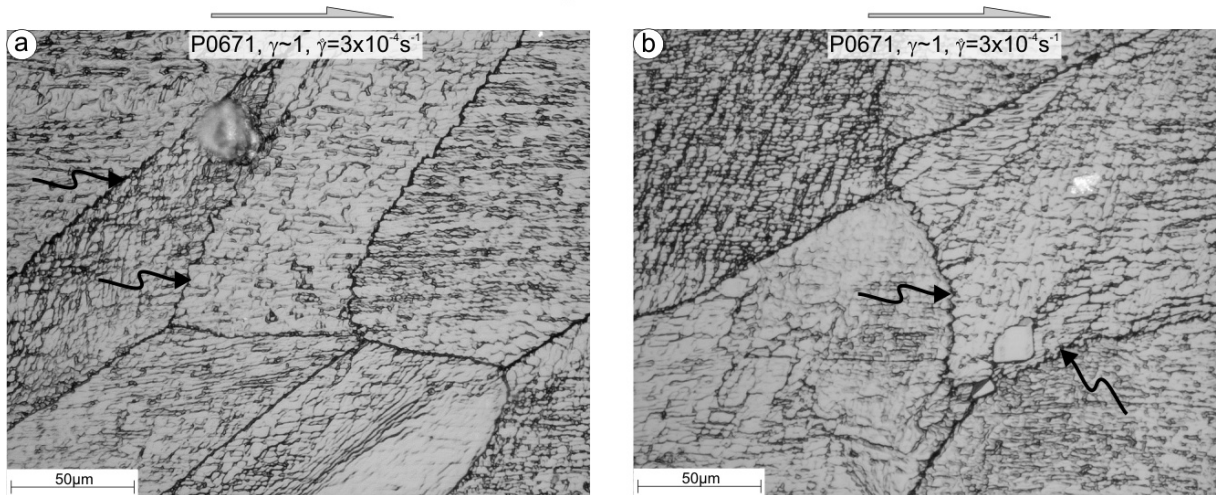


Fig.5.6. a) and b) Reflected light micrographs of serrated grain boundaries with stair case geometry in sample deformed at 100°C.

Cusplate/lobate grain boundaries

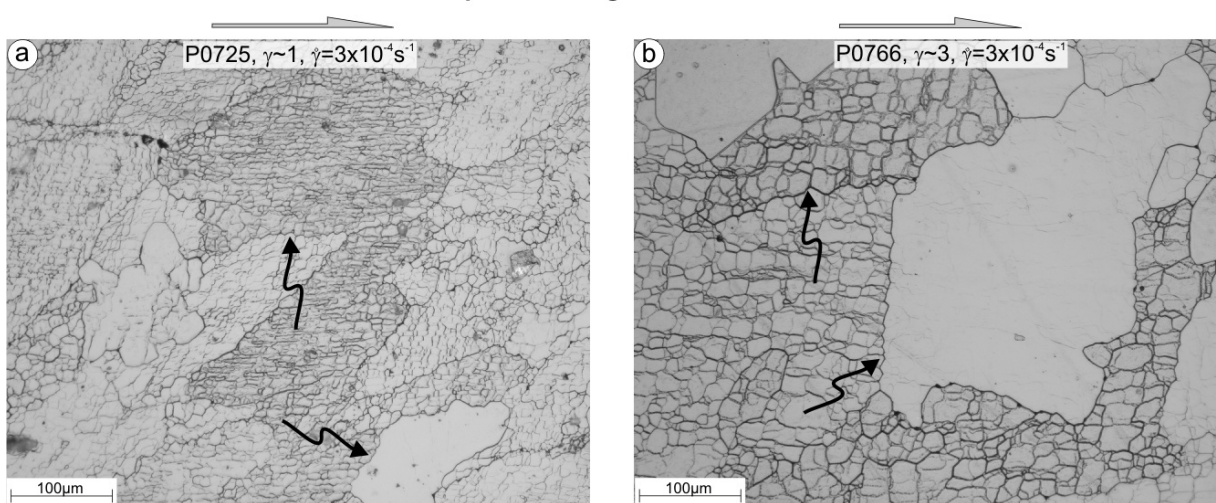


Fig.5.7. Reflected light micrographs showing cusplate and lobate grain boundaries with wavelengths similar to the subgrain size in samples deformed at 200°C in (a) and in samples deformed at 300°C (b).

Bulged grain boundaries

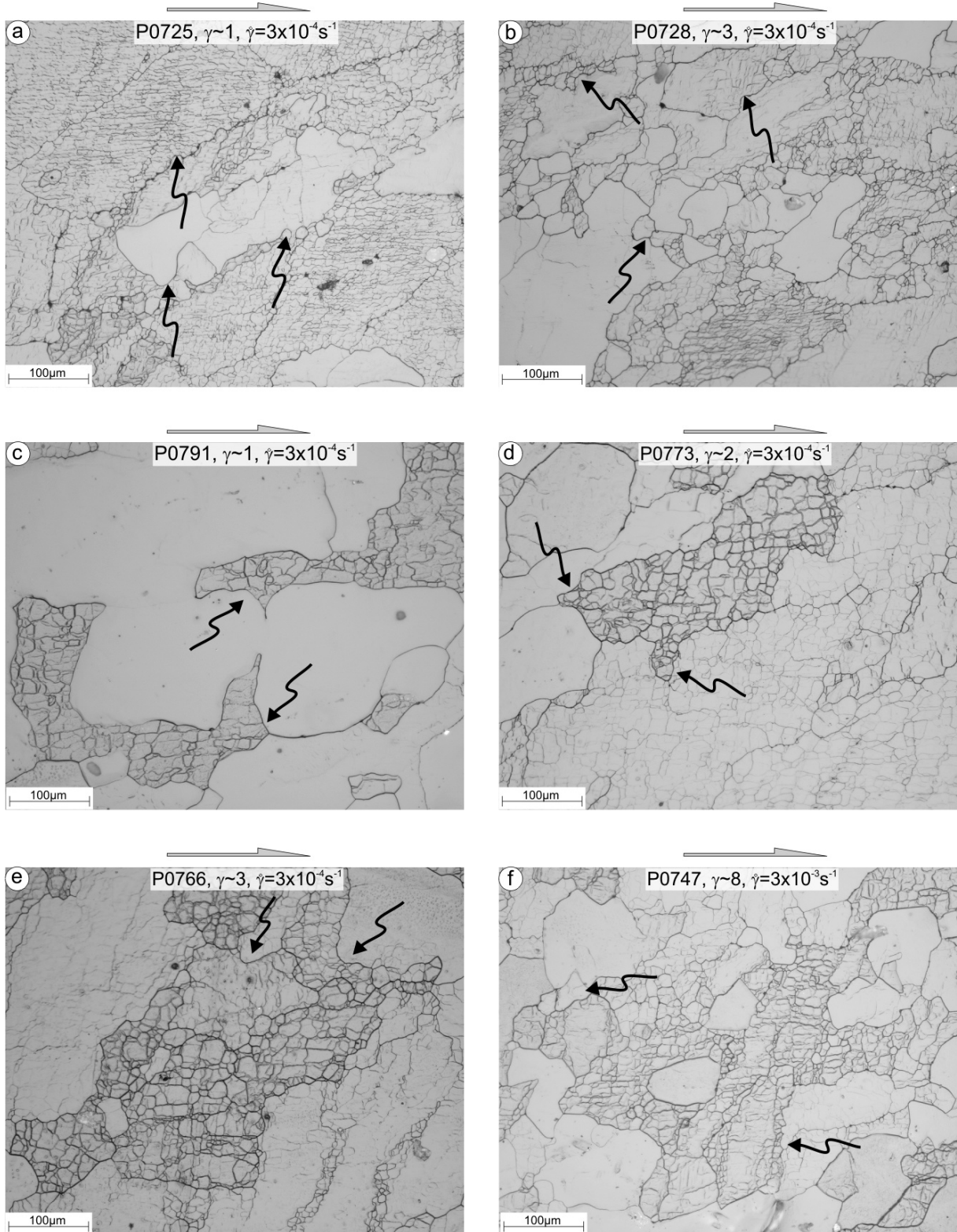


Fig. 5.8. Reflected light micrographs showing bulged grain boundaries as indicated by black arrows in grains containing no deformation substructure and in grains with deformation substructure. a) and b) samples deformed at 200°C. c) to f) samples deformed at 300°C.

Slip bands

Slip bands are bands, where the shear strain is highly concentrated along thin layers. They represent planes along which dislocation movement in form of glide takes place. In the optical micrographs and in the orientation maps they are visible due to the etching procedure. Samples deformed to a low shear strain ($\gamma \leq 3$) at 100°C and $\gamma \sim 1$ at 200°C are characterised by grains showing sets of nearly parallel thin etched lines (Fig. 5.9). The lines are often close to parallel with the shear direction. By tracing the thin lines to the edge of the grain, small offsets or steps in the grain boundary are visible (Fig. 5.9). The spacing between the slip bands is not regular and in some grains the bands occur in pairs (Fig. 5.9). Also, grains were observed in which the slip bands are not straight, but have a rather wavy appearance.

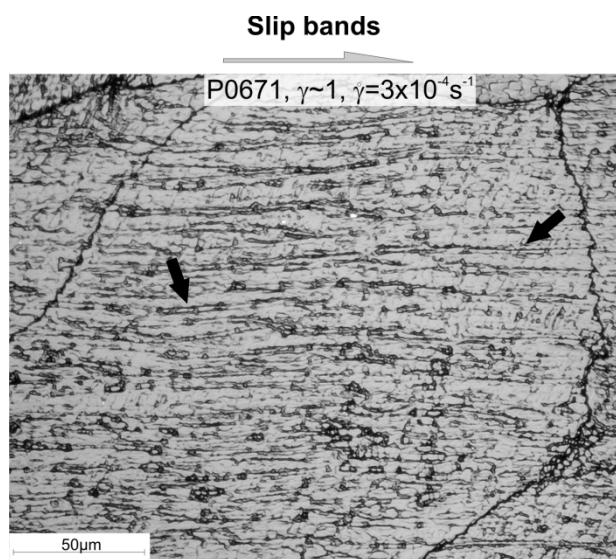


Fig. 5.9. Reflected light micrographs of slip bands. Wavy horizontal running slip bands (black arrows) in sample P0671, deformed at 100°C to shear strain of $\gamma \sim 1$. The bands produce steps in the grain boundary as seen on the right grain boundary.

The wavy character of such bands has been observed in other fcc materials (e.g. Malin & Hatherly 1979, Bay et al. 1992, Huang 1998) and is attributed to the presence of cross-slip, in which screw dislocations are able to change to a different slip plane, if obstacles impede the movement of the dislocation.

From optical micrographs it is not possible to relate these lines to crystallographic planes, therefore orientation maps were created by means of EBSD. As an example a detailed orientation map of the sample deformed at 100°C to a shear strain of $\gamma \sim 1$ is used (Fig. 5.10).

The orientation map (Fig. 5.10a) clearly reveals that the grain does not only consist of bands parallel to the shear direction, but also of slip bands perpendicular to the shear direction, which were not so obvious from the reflected light micrographs (cf. Fig. 5.9). The horizontal slip bands can be attributed to one of the (111) planes and the oblique running slip bands are the trace of one of the (100) planes. The slight colour change in the orientation map (Fig. 5.10a) indicates that the misorientation within the grain is minor. The misorientation profile (A-A', Fig. 5.10c) across the grain shows that the change in the misorientation between individual neighbours is usually 1-2°, and never exceeds 7°. The grain boundary map in Fig. 5.10b displays misorientation boundaries of low angle (<15°) and high angle misorientations (>15°). The map shows that low angle boundaries (2-10°) are formed within the grain. It is interesting to note, that the slip bands perpendicular to the shear direction show

misorientations of 2-5°, whereas higher misorientations of 5-10° occur along slip bands parallel to the shear direction. Also, a few misorientation angles of 10-15° and >15° occur along the horizontal bands. The pole figure of the grain in Fig. 5.10d shows sharp and dense point cluster maxima.

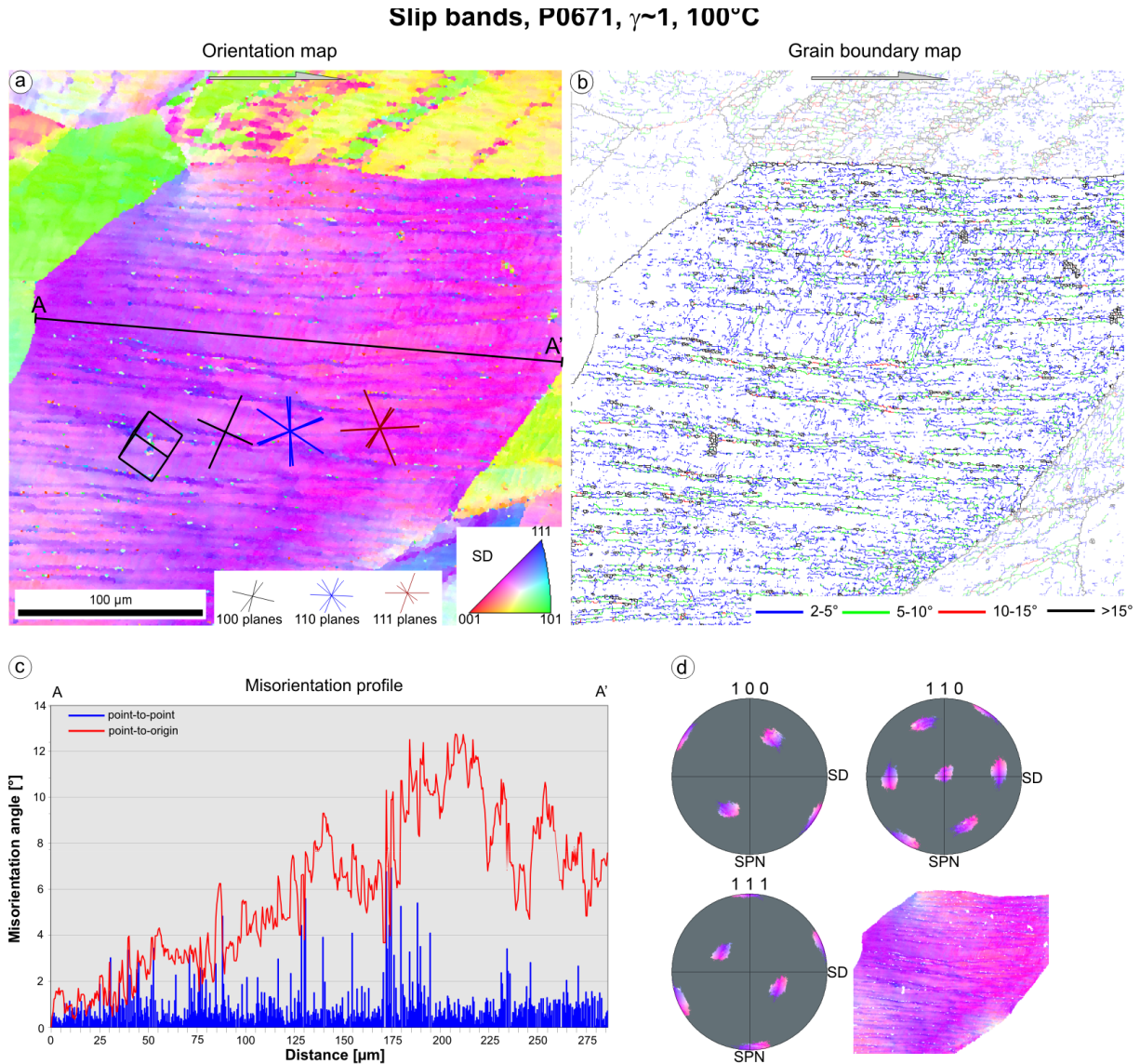


Fig. 5.10. a) Orientation map for shear direction (SD) showing a grain in sample P0671 containing slip bands. Crystal orientation is shown schematic as cube with the corresponding plane traces, 100 (black), 110 (blue) and 111 (red) superimposed on map. A-A' shows location of misorientation profile of c). Shear sense is top to the right. b) Grain boundary map showing boundaries with misorientation of 2-5° (blue), 5-10° (green), 10-15° (red) and >15° (black). c) Misorientation profile of location A-A' in the orientation map a). Blue bars show misorientation from point to point and red line represents misorientation from point to origin. d) Pole figures of investigated grain, equal area projection, upper hemisphere. Colour of maxima corresponds to ipf

To exactly determine the crystallographic orientation of the slip bands, a second cut perpendicular to the shear direction was made. The orientation map of this cut is shown in Fig. 5.11a. This map shows that the slip bands in the lower part of the grain are bent and show a wavy character. The grain contains slip bands perpendicular to the shear direction as in the parallel cut. These bands are related to the trace of a (100) plane and the horizontal bands belong to a (111) plane (Fig. 5.11a). The grain boundary map in Fig. 5.11b shows that within the grain low angle boundaries have formed, mainly with misorientations between 2-10°. By drawing a misorientation profile (Fig. 5.10a,c) along the horizontal slip bands it is obvious that the misorientation relationship between neighbours does not exceed 5°. The pole figure of the investigated grain in Fig. 5.11d shows, like in the parallel cut, sharp and dense point maxima.

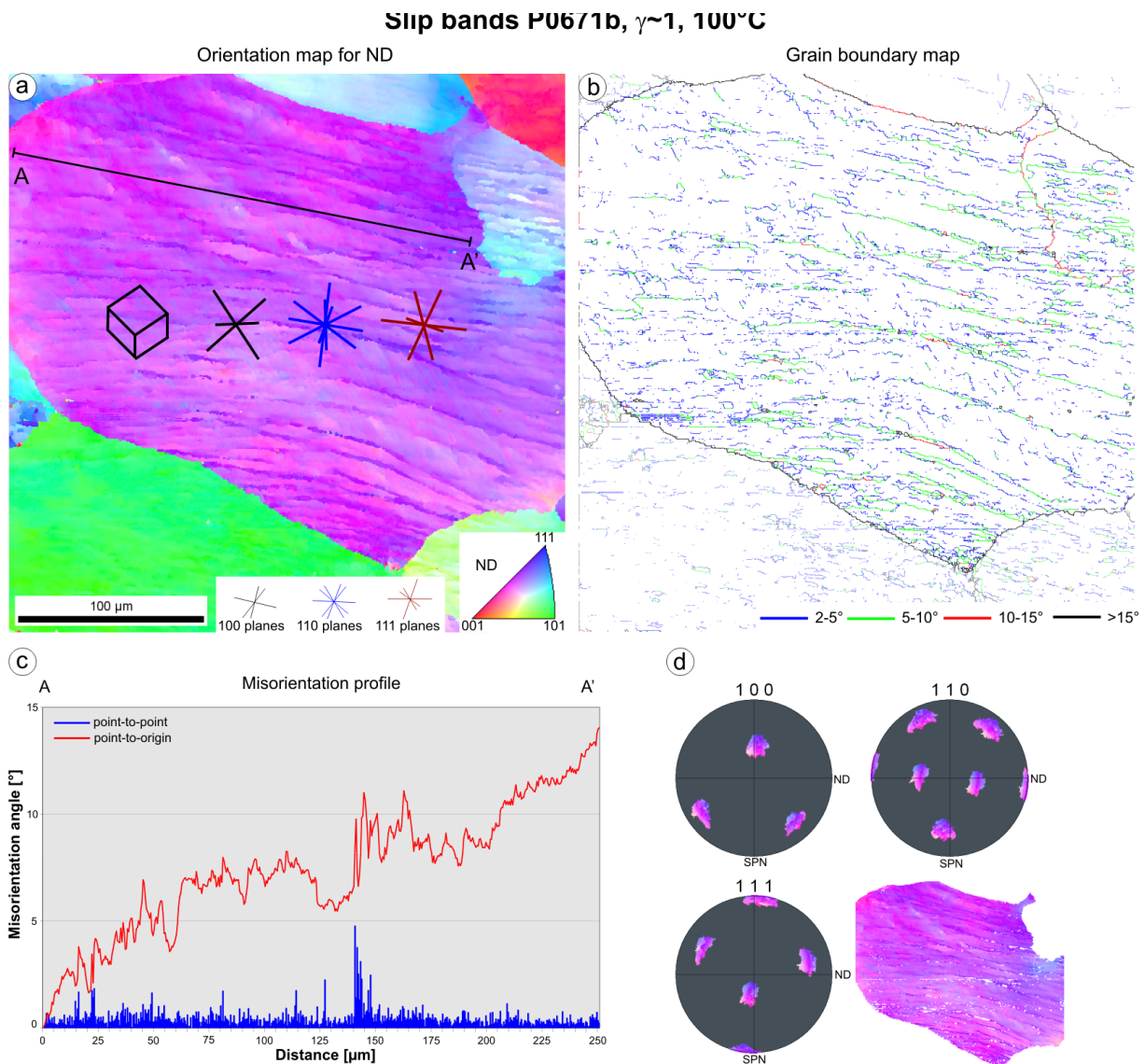


Fig. 5.11. a) Orientation map of sample P0671b (100°C, $\gamma \sim 1$), cut perpendicular to the shear direction. Grain with horizontal and oblique wavy slip bands. Crystal orientation is shown schematic as cube with the corresponding plane traces, 100 (black), 110 (blue) and 111 (red) superimposed on map. A-A' shows location of misorientation profile of c). b) Grain boundary map showing boundaries with misorientation of 2-5° (blue), 5-10° (green), 10-15° (red) and >15° (black). c) Misorientation profile of location A-A' in the orientation map a). Blue bars show misorientation from point to point and red line represents misorientation from point to origin. d) Pole figures of investigated grain, equal area projection, upper hemisphere. Colour of maxima corresponds to ipf colour code for ND.

In summary, the orientation maps of the two cuts clearly show that the horizontal bands in each cut belong to one of the (111) planes, which can possibly interact with (100) planes for cross-slip, in a manner resembling “pencil glide” (Taylor & Elam 1926).

Subgrains

From the optical micrographs (Fig. 5.12) two main types of subgrains could be distinguished: i) subgrains exhibiting a blocky shape and ii) subgrains characterised by a polygonal shape. Blocky subgrains are the characteristic feature of the low temperature experiments (100°C), whereas the polygonal subgrains dominate at higher temperatures (200 and 300°C). However, also blocky subgrains formed at this temperature, especially at low shear strain ($\gamma \sim 1$). The blocky subgrains are smaller in size (Fig. 5.12a,b) than the polygonal subgrains (Fig. 5.12c,d). Furthermore, it appears that the blocky subgrains show a relationship with the before described slip bands. The horizontal subgrain borders coincide with the horizontal slip bands and the oblique subgrain boundaries seem to coincide with the oblique slip bands. The blocky subgrains are arranged in a geometric and regular way, whereas the polygonal subgrains are arranged more irregular.

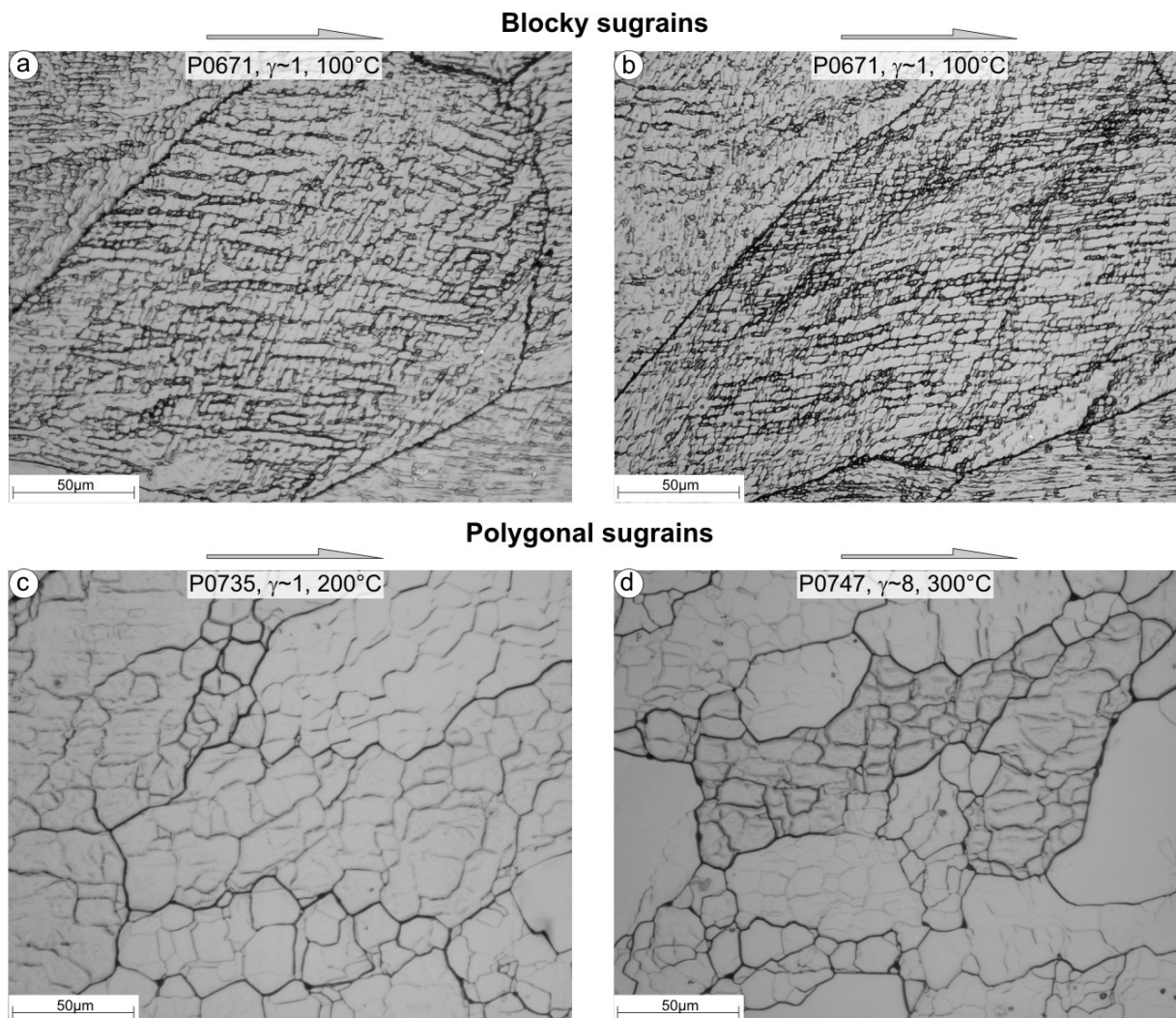


Fig. 5.12. Reflected light micrographs of two subgrain types. a) and b) Blocky subgrains arranged in a geometric fashion (strain rate $3 \times 10^{-4} s^{-1}$). c) and d) Polygonal shaped subgrains irregular arranged in the grains. Sample in c) deformed at strain rate $3 \times 10^{-5} s^{-1}$ and sample in d) deformed at strain rate $3 \times 10^{-3} s^{-1}$. Note, blocky subgrains at 100°C are smaller in size than polygonal subgrains at 200 and 300°C.

Domain structures

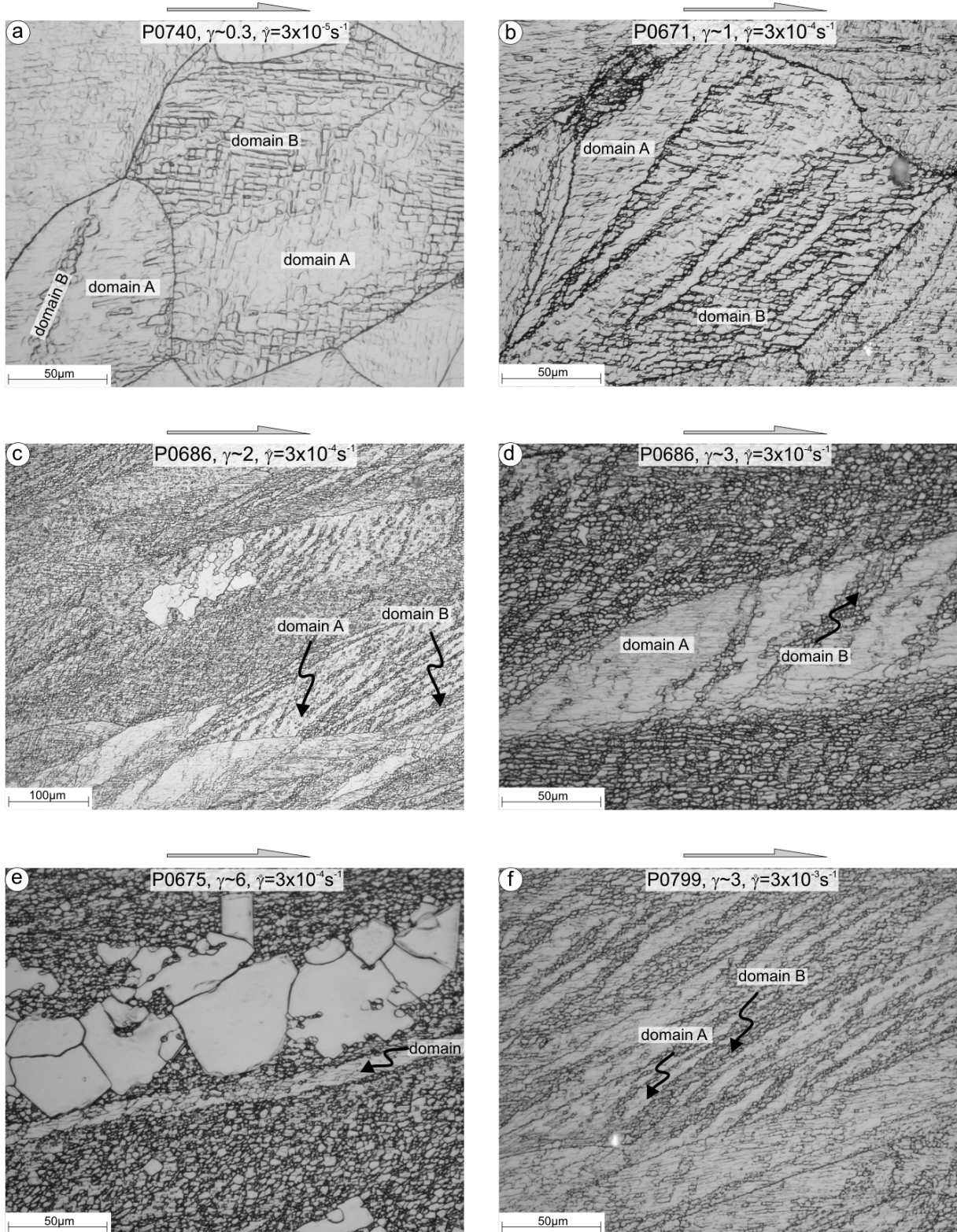


Fig. 5.13. Formation of domain structures in samples deformed at 100°C. a) At low shear strain ($\gamma \sim 0.3$) domains already start to form in deformed grains containing subgrains. With increasing shear strain b) to f) domains continuously develop up to high shear strains ($\gamma \sim 6$) as seen in e).

Domain structures

In all samples deformed at 100°C up to shear strains of $\gamma \sim 6$, there are grains that contain strong visible domains as shown on the previous page in Fig. 5.13. One domain (domain A) has a band shaped appearance without much substructure. In the optical micrograph the bands have a milky appearance and are oriented at roughly 60° to the shear plane. Within the bands very thin etched horizontal and oblique lines are visible. The other domain (domain B) in these grains, consist of subgrains. The boundary between these two domains is sharp and clearly visible in optical micrographs. To investigate the orientation relationship between the two domains orientation maps, grain boundary maps, misorientation profiles and pole figures were used. As an example, sample P0671 deformed at 100°C to a shear strain of $\gamma \sim 1$ is presented.

Fig. 5.14a (next page) shows an orientation map for the shear direction (SD) of the investigated sample. Parts displaying a green colour belong to domain A and parts that show a purple to bluish colour belong to domain B. The frequent colour switch between individual subgrains from blue to purple in domain B is striking. This already is an indicator for strong misorientation between the individual subgrains. However, in domain A, the colour switch is not so peculiar, indicating that the misorientation misfit between individual neighbours within that band is not as large as between the individual subgrains in domain B. However, the colour change between the two domains is sharp from green to violet, this is already a good indicator that the misorientation between the two domains is high. By drawing a misorientation profile (Fig. 5.14c) across the domains the amount of misorientation is visible. In domain A the misorientation between each neighbour pixel lies in the range of 2° and less. A strong jump in the misorientation angle of 20-30° at the borders from domain A to domain B is measured. The misorientation between the single subgrains in domain B does not exceed 7°. The high misorientation between domain A and B clearly shows that a high angle boundary formed between these two domains. By looking at the grain boundary map (Fig. 5.14b), it can be clearly seen that a high angle boundary formed along the border between domain A and B, but this boundary is not continuously closed. This in turn is evidence that domain A cannot yet be treated as an individual grain and that both domains originate from the same initial grain by orientation splitting, due to the activation of different sets of slip systems in the two domains.

The difference in misorientation between the two domains is also visible by placing the crystallographic cube into the domains (Fig. 5.14a). The orientation of the cubes clearly shows that both domains have a different orientation and that a rotation must have occurred, around a 111 axis near ID. The pole figure in Fig 5.14d shows that the domain structure shows a dispersion path of the green and the purple/blue domain and indicates the most common rotation axis. This dispersion path is a common characteristic feature of the domain structures, also shown in Fig. 5.15. The plane traces in addition show which crystallographic planes are responsible for the thin etched lines in the banded structure. It can be seen that in domain A, the horizontal thin lines are the trace of one of the (100) planes. And the oblique bands are the trace of one of the (110) planes. In the domain B the horizontal lines can be attributed to one of the (111) planes and the oblique lines are the trace of one of the (110) planes.

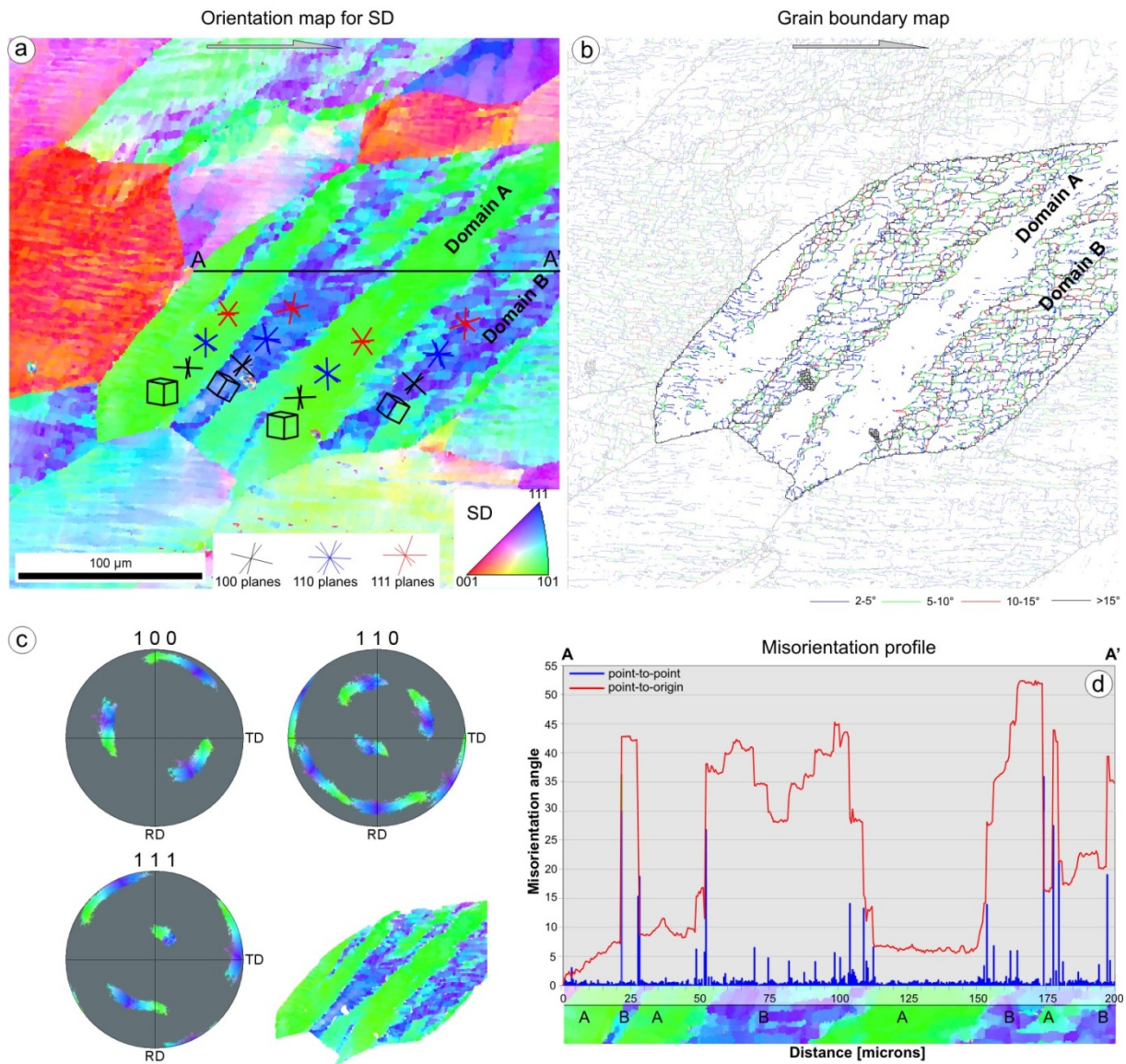
P0671, $\gamma \sim 1$, 100°C

Fig. 5.14. Detailed investigation of a domain structure formed in sample deformed to $\gamma \sim 1$ at 100°C. Shear sense top to the right. a) Orientation map with cubes and traces of 100, 110 and 111 planes, indicating the relationship between the crystallographic planes and the structures (bands and subgrains) developed, explanation in main text. b) Grain boundary map. c) Misorientation profile shows the high jump in misorientation from the green band to the part with the blue-purple subgrains. The point-to-point misorientation within the green band is low with values of 2°. The point-to-origin misorientation increases constantly up to the green domain-blue/purple subgrain domain. In the blue-purple subgrain domain the misorientation is higher than in the green domain. d) Pole figures for 100, 110 and 111 of investigated grain. Colour of point maxima corresponds to ipf colour code for SD. Equal area projection, upper hemisphere.

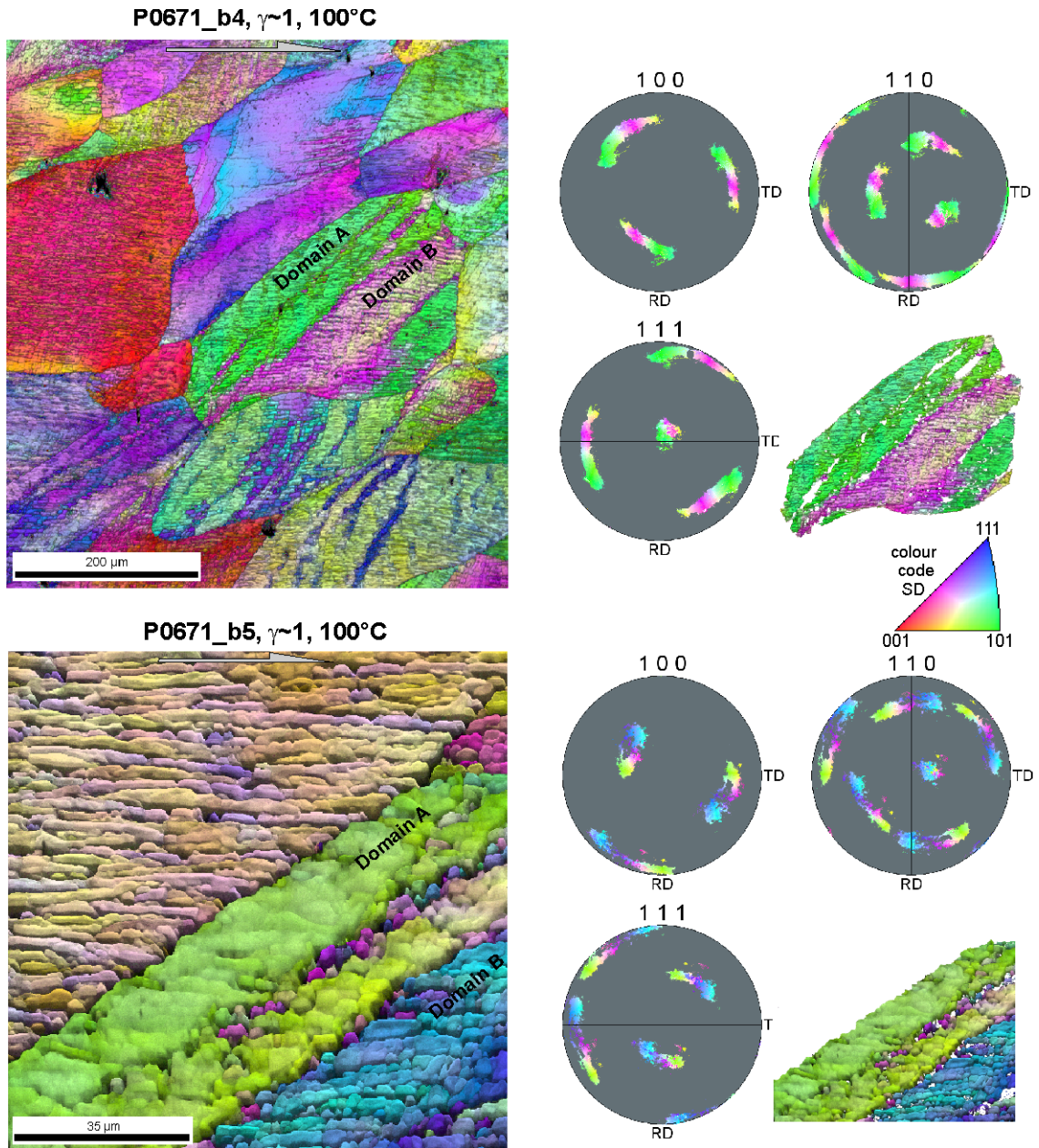


Fig. 5.15. Orientation maps for SD of domain structures in sample P0671 at 100°C (shear sense top to the right), and pole figures of the domains showing the characteristic dispersion path. Point maxima are coloured corresponding ipf colour code for SD. Pole figures for 100, 110 and 111 are equal area

New grains with internal deformation structure

New grains with an internal deformation structure (e.g. subgrains) start to appear in the deformed samples at a shear strain of $\gamma \sim 2$ at 100°C and dominate the microstructure at high shear strains ($\gamma \sim 6$). In contrary, at higher temperatures ($200\text{--}300^\circ\text{C}$) these grains are present already at low shear strains ($\gamma \sim 1$) and at a low shear strain rate (10^{-5}s^{-1}) and are the major characteristic feature up to high shear strains ($\gamma \sim 8$). Furthermore, these newly grown grains are characterised by an irregular shaped appearance and if the grains are larger than the subgrain size by bulged or cusped/lobate grain boundaries. Fig. 5.16 and Fig. 5.17 show examples for the occurrence of grains with an internal deformation structure.

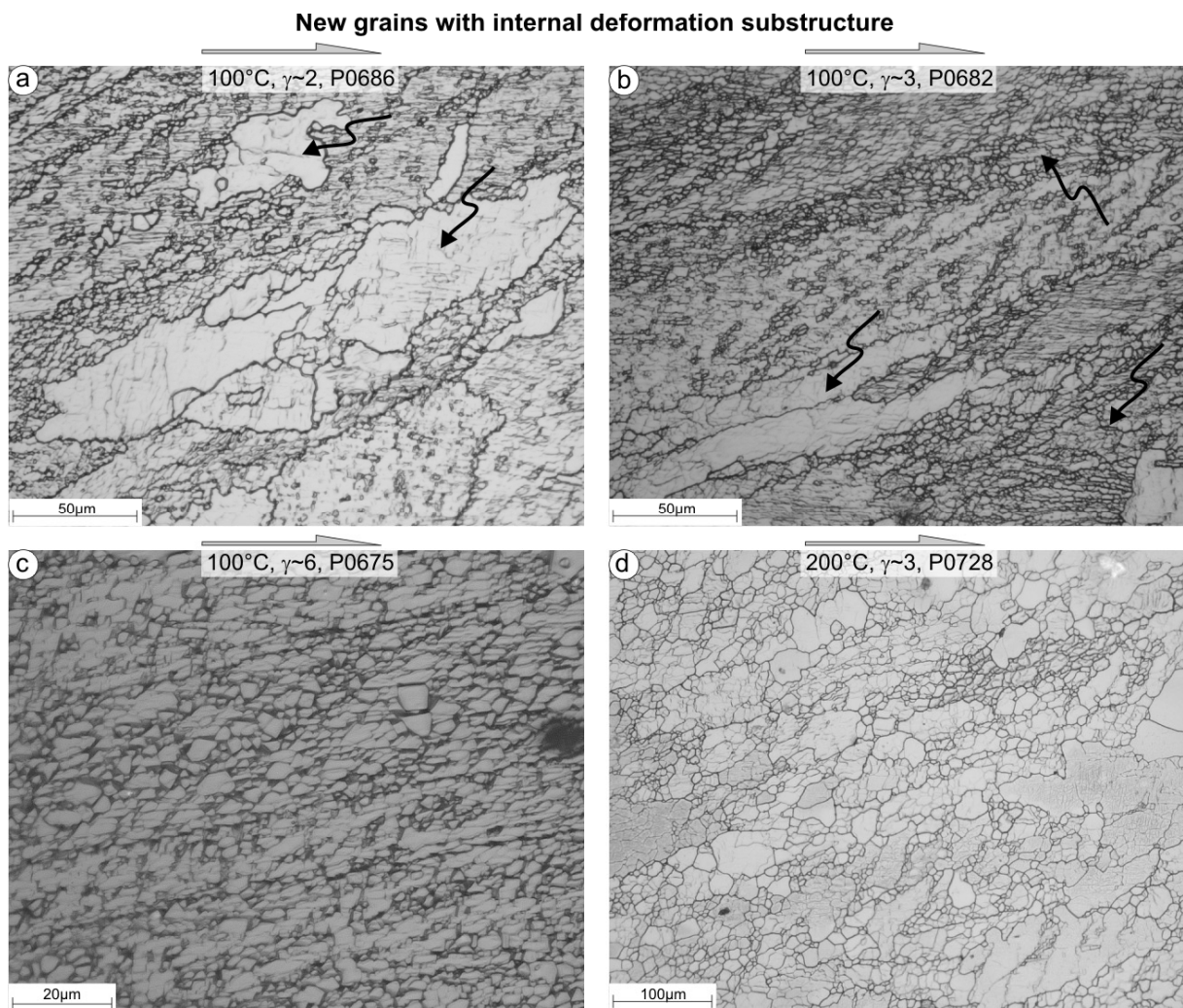


Fig. 5.16. New formed grains with an internal deformation structure at all applied temperatures (100 , 200 , 300°C). Grains are characterised by bulged and irregular serrated grain boundaries and by an internal deformation structure (subgrains). a, b) Grains with internal structure and bulged grain boundaries (red arrows). c) Small, new formed grains at highest shear strain at 100°C . d) Small, new formed grains, irregular in shape at 200°C . Shear sense in all images top to the right.

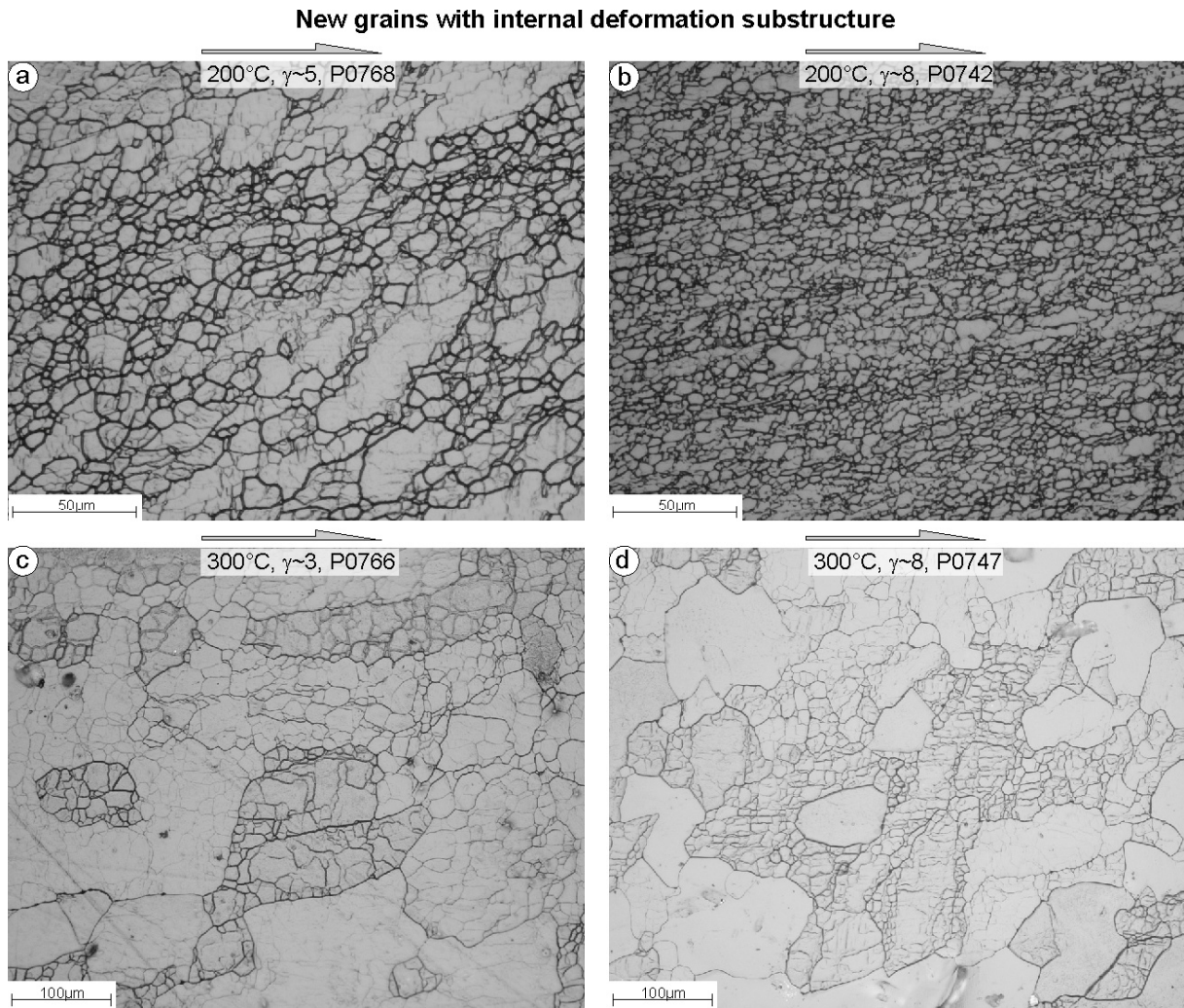


Fig. 5.17. *a, b) Small new grains formed at high shear strains at 200°C. c, d) New formed grains at 300°C characterised by the typical bulged and cusped/lobate grain boundary structure and the presence of subgrains. Shear sense in all images top to the right.*

However, from the optical micrographs it is hard to distinguish if the small grains are still subgrains or if they are already new formed grains and therefore surrounded by high angle boundaries. The two cases are distinguished by analysing the misorientation relationship with respect to individual subgrains. If the misorientation between the two neighbours exceeds 15° then a high angle grain boundary formed. In Fig. 5.18-5.23 orientation maps (with image quality map superimposed) with the corresponding grain boundary maps are displayed, showing examples for the formation of new grains at different temperatures and at different shear strains.

Sample P0686 and P0682 (100°C)

The two new formed grains in Fig. 5.18a in sample P0686 show serrated grain boundaries (frame 1) and bulged grain boundaries (frame 2). The slight colour change in these grains indicates that low angle boundaries developed within the grains, which is also confirmed by the grain boundary map.

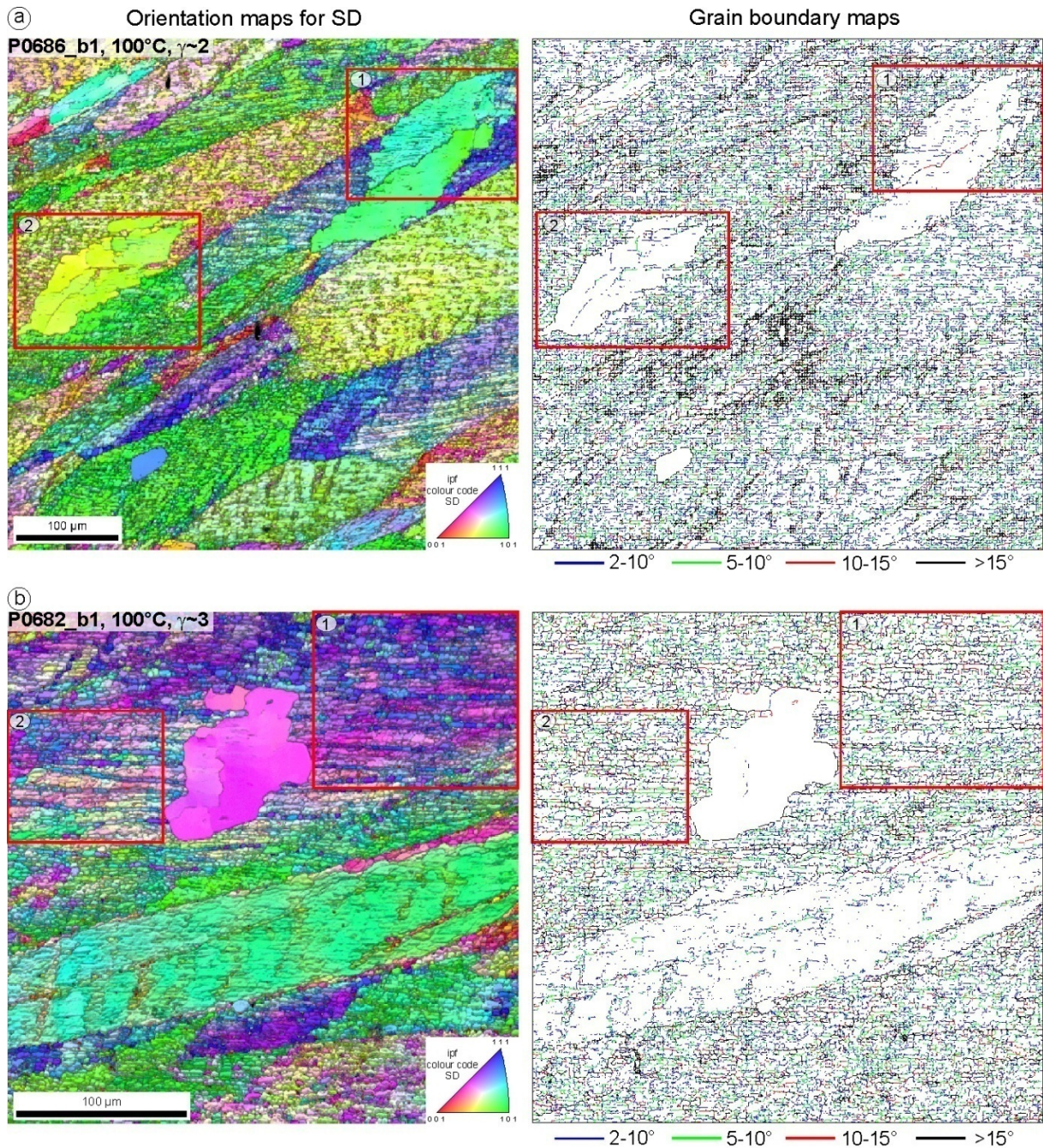


Fig. 5.18. Orientation maps (shear sense top to the right), left (for SD) and corresponding grain boundary maps, right. a) Development of new grains (red frames 1,2) in sample P0686. Grains show irregular shape and serrated (frame1) or bulged (frame2) grain boundaries, as well as the development of low angle boundaries in these grains. b) Sample P0686, strong colour (orientation) change between individual subgrains and formation of mostly horizontal high angle boundaries in frames 1,2.

Sample P0682 (Fig. 5.18b) shows a strong colour change between the single subgrains in the areas of the red frames. It is to note, that the colour change in these frames is much stronger perpendicular across the horizontal subgrain rows, whereas the colour change within the horizontal subgrain rows is not as peculiar. The grain boundary map shows that high angle boundaries ($>15^\circ$) developed along the horizontal subgrain rows, which explains the strong colour change perpendicular the horizontal rows. Within the horizontal subgrain rows a majority of low ($2-5^\circ$) and medium ($5-10^\circ$) angle boundaries formed. A second detail scan of this sample (Fig. 5.19) shows that a strong colour change occurs between neighbouring subgrains (red frame). The grain boundary map shows that a high number of high angle boundaries ($>15^\circ$) developed. The high angle boundaries are completely closed showing that new grains have formed. These grains have a similar size as the subgrains.

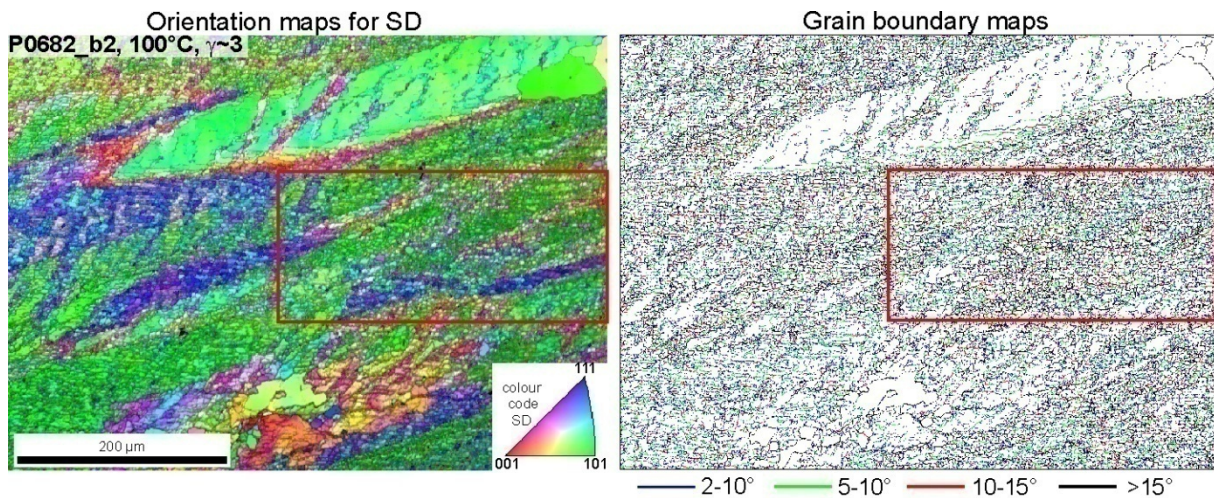


Fig. 5.19. Orientation map (right) shear sense top to the right. Colour change in subgrains in red frame, indicates high misorientation between individual subgrains. Grain boundary map (left) shows that high angle boundaries developed, indicating formation of new grains.

Samples P0725 and P0728 (200°C)

Figure 5.20a) shows orientation map of a detailed scan of sample P0725 deformed at 200°C. The purple grain in frame 1 is characterised by an irregular shape showing bulged grain boundaries. Within that grain subgrains have formed, indicated by low angle boundaries in the grain boundary map. The small blue grains seem to be independent from each other and separated by high angle boundaries as shown in the grain boundary map. Similar small grains, with different colours and thus different orientations are found in frame 2. The grain boundary map shows that these grains are surrounded by high angle boundaries and thus can be treated as individual grains. The detail scan in Fig. 2.20b of sample P0728 shows a very nice example for a strong colour and therefore orientation contrast within a sheared grain. The grain boundary map shows that high angle boundaries around the small grains have formed.

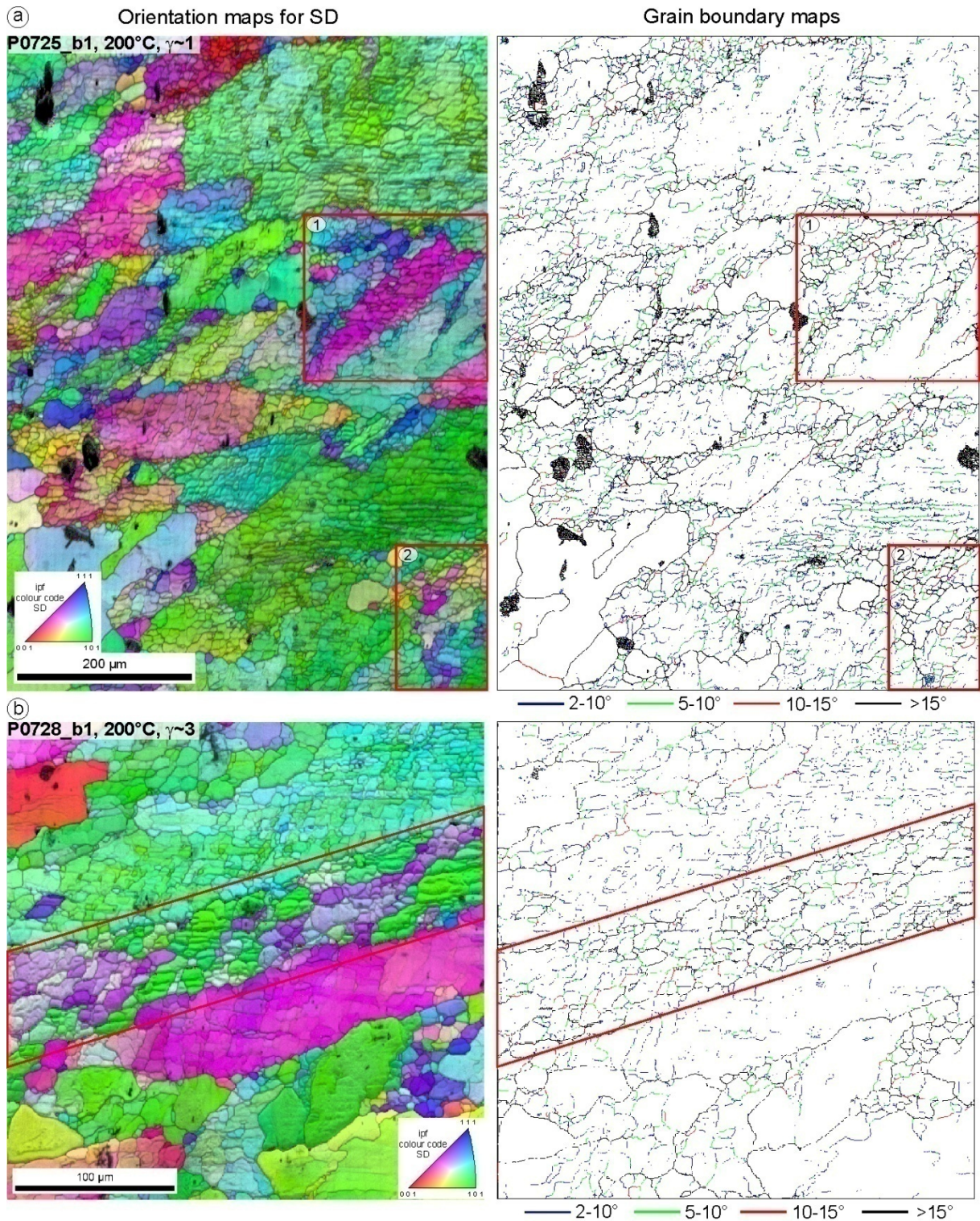


Fig. 5.20. Orientation maps (left), shear sense top to the right, and grain boundary maps right. a) Formation of new grains in frames 1 and 2, indicated by colour change in orientation map and occurrence of high angle boundaries in grain boundary map. b) Strong colour change in orientation map between individual subgrains in sheared grain. Development of high angle boundaries in this area as inferred from grain boundary map, showing that new grains formed.

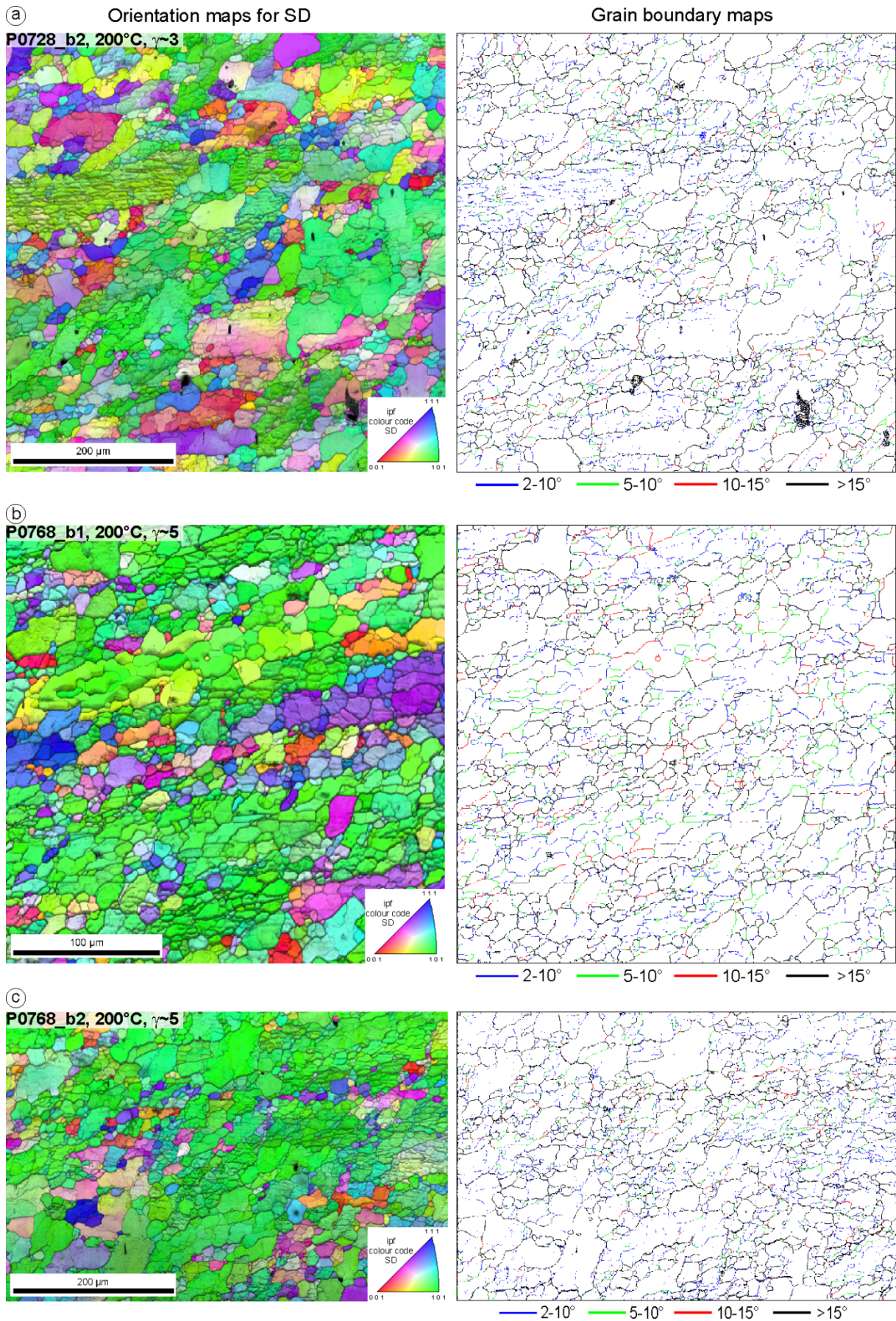


Fig. 5.21. Orientation maps (left), shear sense top to the right showing frequent colour and hence orientation change between single grains and subgrains a) to c), explanation given in main text. Grain boundary maps to the right show formation of high angle boundaries corresponding to orientation and colour change.

Samples P0728 and P0768 (200°C)

All three orientation maps (Fig. 5.21a-c) show that new grain have developed in the deformed samples as indicated by the varying colours and the development of high angle boundaries as shown in the grain boundary map. Old sheared grains are still present containing subgrains with low angle boundaries.

Samples P0766 and P0747 (300°C)

Sample P0766 shown in Fig. 5.22 shows a nice example for the formation of a new grain containing subgrains (red grain) within a deformed grain. The new formed grain contains subgrains and has a completely different orientation than the host grain. The red grain is characterised by high angle boundaries as seen in the grain boundary map. Low angle boundaries developed but must be smaller than 2° , otherwise they would occur in the grain boundary map. All grains show bulged grain boundaries. In the case of the orange grain (lower part of the map) the grain boundaries have a cusped/lobate structure.

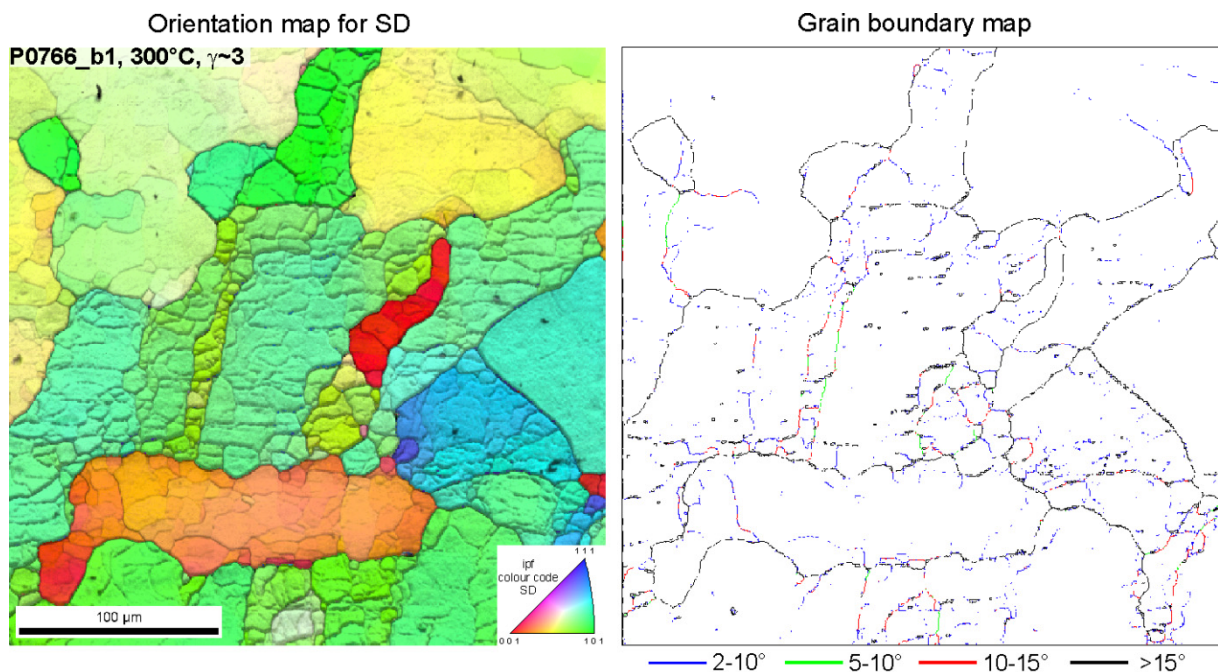


Fig. 5.22. Orientation map (left) with shear sense top to the right, and grain boundary map, right. New formed red grain with different orientation in respect to the host grain. Grain showing bulged grain boundaries and are characterized by and internal deformation structure in form of subgrains.

Sample P0747 in Fig. 5.23 shows another example for the formation of new grains containing deformation substructure (purple grains). These grains have also a different orientation in respect to host. The grains are surrounded by high angle boundaries, as indicated in the grain boundary map.

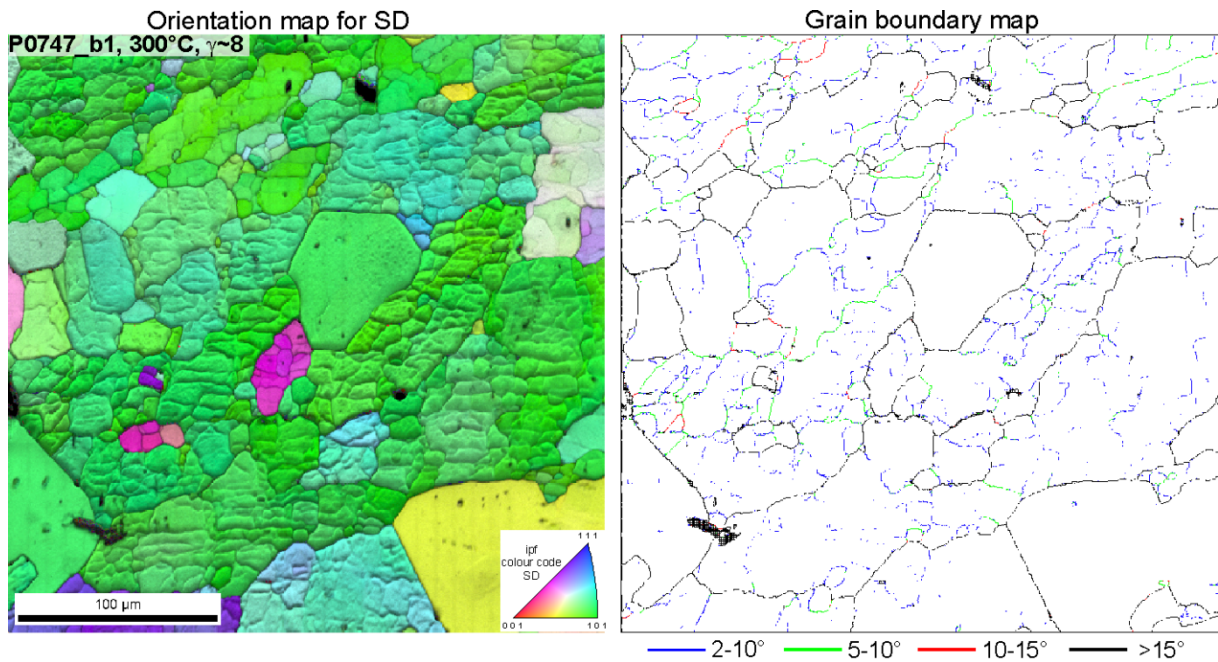


Fig. 5.23. Orientation map (left) with shear sense top to the right, and grain boundary map, right. New formed grains in purple show different orientation in respect to host green grain.

New grains without internal deformation structure

New grains without internal deformation structure (Fig. 5.24) occur in nearly all samples, but to a different amount. In the optical micrographs they appear as bright white idiomorphic grains (Fig. 5.24a) and are characterised by straight and gently curved, sometimes bulged grain boundaries (Fig. 5.24b).

The main characteristic of these grains is that no internal deformation substructures in form of subgrains or slip bands are visible. Two deformed samples, investigated by EBSD (Fig. 5.25) are shown as an example on the next page. In the orientation maps (Fig. 5.25a,b) no colour change within these grains is visible. The misorientation profile (Fig. 5.25c,d) across the grains shows no fluctuation in the misorientation angle between neighbouring pixels within the grain. A high misorientation is only reached where the profile crosses the grain boundary from one grain to the next grain.

New grains without internal deformation substructure

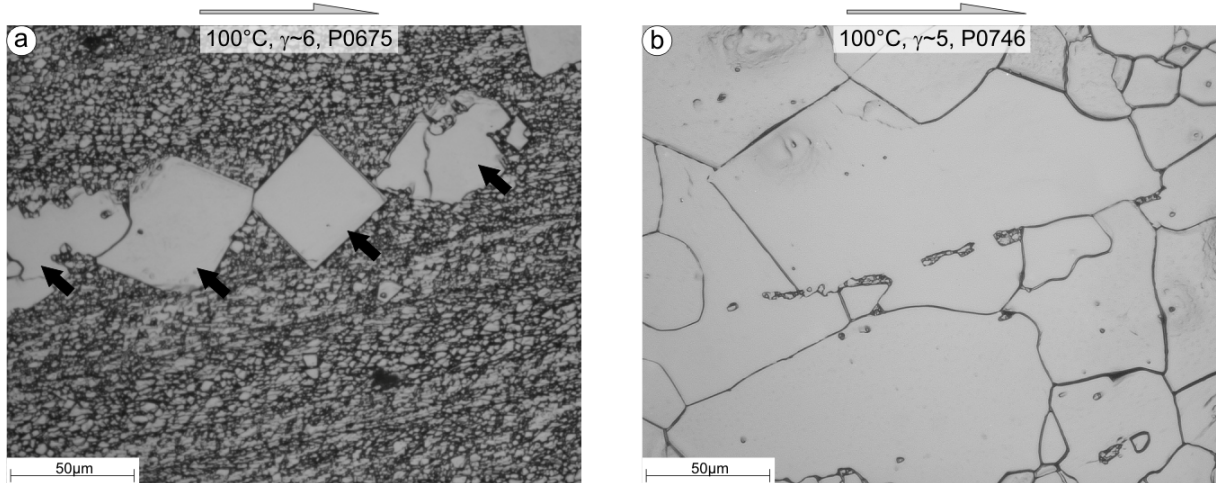


Fig. 5.24. a) idiomorphic grains formed after deformation, black arrows. b) new grains formed in deformed sample showing bulged and straight grain boundaries.

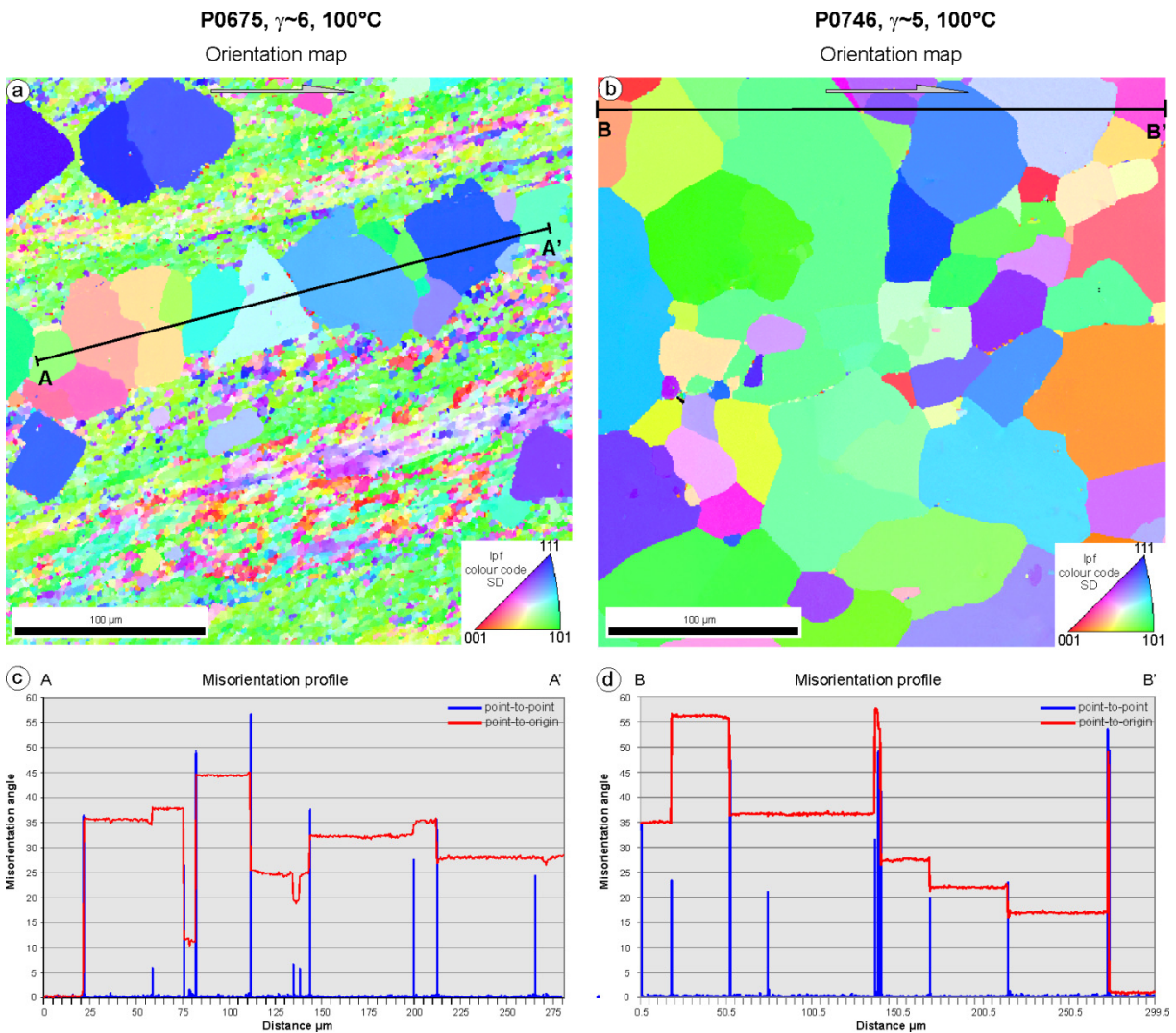


Fig. 5.25. a,b) Orientation map with shear sense top to the right. Grains show no internal deformation structure, as indicated in the misorientation profile below the images c and d). The misorientation inside the grains is less than 2° . The misorientation only changes to high values above 15° at grain boundaries to the next grains.

Evolution of microstructure with increasing shear strain

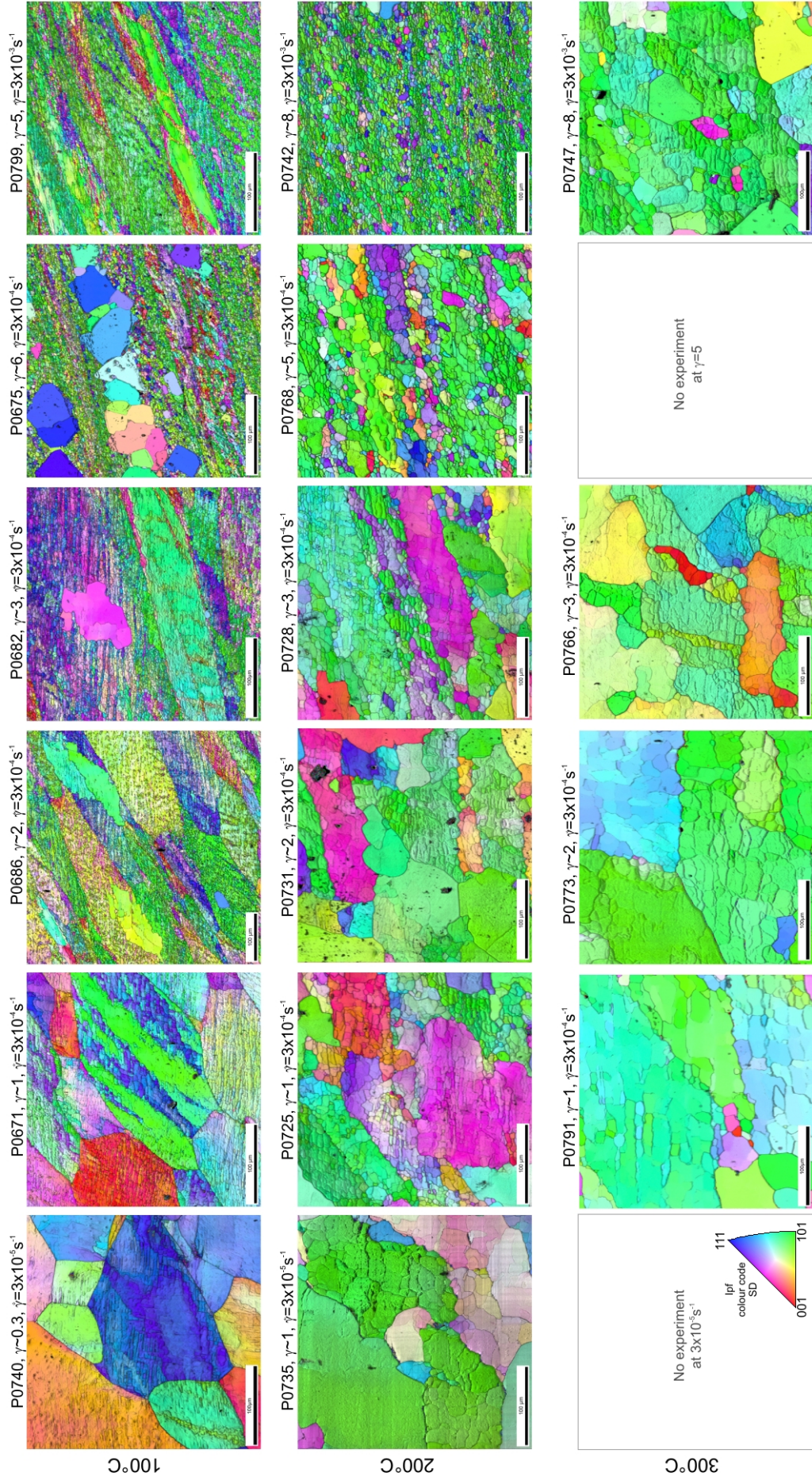


Fig. 5.26. Evolution of microstructure with increasing shear strain. In samples deformed at 100 and 200°C grain refinement with increasing shear strain takes place. At high shear strains (g-6, 100°C and g-8, 200°C) a nylonitic microstructure develops with grain sizes similar to the subgrain size in samples deformed at lower shear strains. In contrary, samples deformed at 300°C show nearly no evolution with increasing shear strain. Shear sense in all images top to the right.

Effect of strain

Figure 5.26 provides an overview, in form of orientation maps for the shear direction, of the microstructure developed in the deformed samples with increasing shear strain for each temperature. From these images a clear evolution from low strain to high strain is visible, especially in samples deformed at 100 and 200°C, whereas in samples deformed at 300°C no such evolution with increasing shear strain was observed.

At 100 and 200°C with increasing shear strain the deformed grains become more and more elongated and flattened. The original straight grain boundaries become serrated and bulged. The striking features occurring in the evolution with increasing shear strain are:

- i) a major reduction in grain size culminating in a mylonitic fabric at the highest shear strains,
- ii) a big change in the misorientation relationship between individual subgrains and new formed grains and
- iii) a change in the low angle vs high angle grain boundary distribution.

Grain size reduction

The grain size distribution of all deformed samples is shown in Fig. 5.27. Details on grain size are listed in Table 5.2. At 100 and 200°C up to a shear strain of $\gamma \sim 2$ the grain size diagrams show that the curves for the number fraction and area fraction indicates bimodal distributions. The curve for the number fraction is shifted to smaller grain sizes (between 80 and 120 μm), whereas the curve for the area fraction is shifted to larger grain sizes. From a shear strain of $\gamma \sim 3$ up to $\gamma \sim 8$, both curves for the area fraction and number fraction overlap. The total grain size is shifted to much smaller grain sizes, which have the highest frequency in number and area fraction. In summary, with increasing shear strain at these temperature a substantial grain size reduction occurred. The grain size of the 300°C series differs from the lower temperature series. At 300°C in the low shear strain range the grain size is characterised by a high area fraction of large grains (from 500-900 μm). Grains with a diameter between 50-150 μm show the highest number frequency. At the highest shear strain of $\gamma \sim 8$, the grain size decreases to slightly smaller values with the highest number frequency between 50-100 μm and grains between 150-200 μm take up the highest area fraction. Overall, the effect of an increase in shear strain on the grain size at 300°C has not as a drastic effect in a grain size reduction as at the lower temperatures.

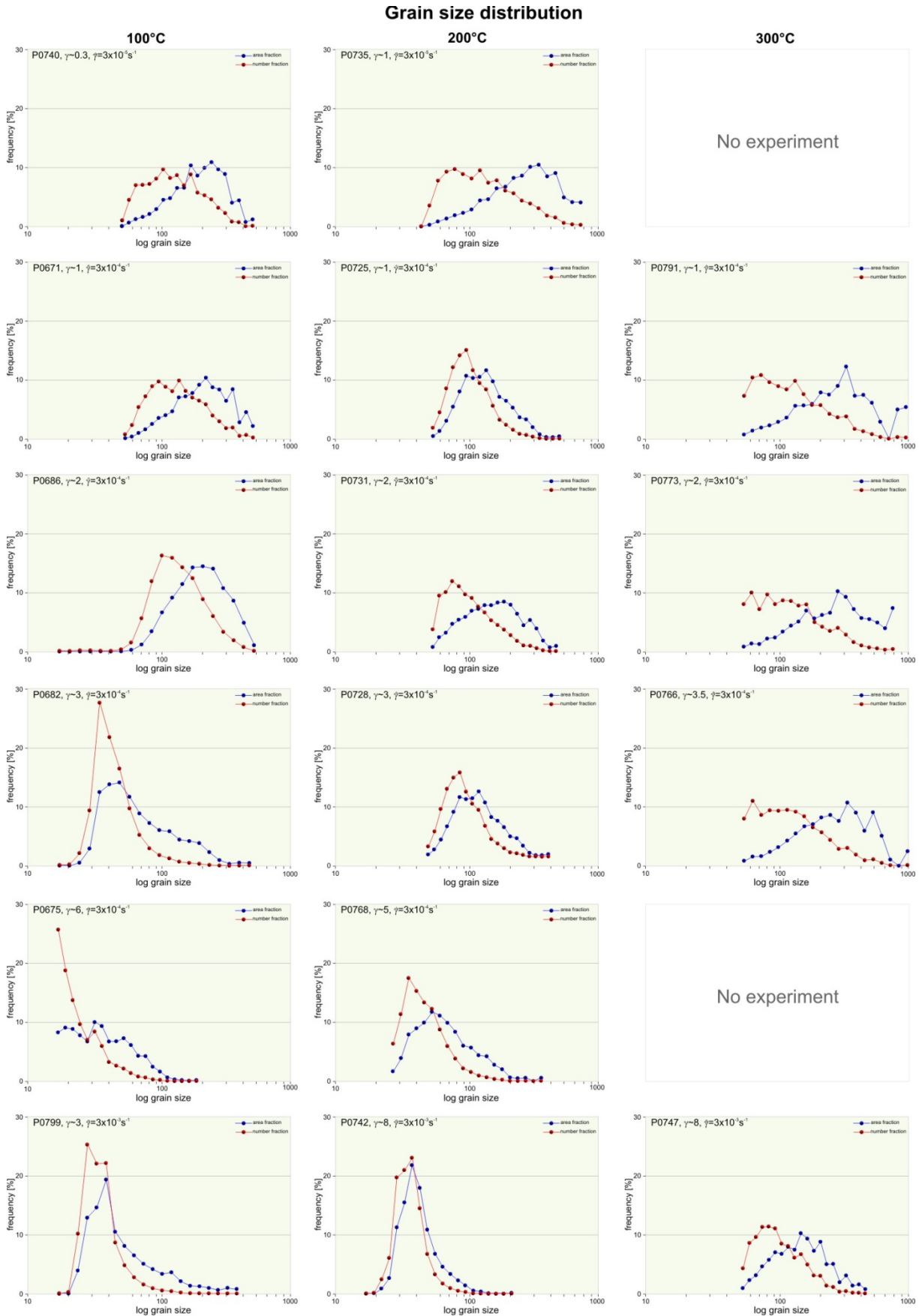


Fig. 5.27. Grain size diagrams in frequency-log plot for deformed samples. Grain size was estimated by EDAX software OIM4.

sample	T [°C]	strain rate [s ⁻¹]	shear strain [γ]	size OIM map [mm]	data points CI>0.1	number of grains	grain size [μm]		
							average number	average area	Standard Deviation
starting	—	—	—	6x7	377 249	3 369	140	216	72
P0740	100	3×10 ⁻⁵	0.3	4x9	328 440	4 195	135	206	67
P0671	100	3×10 ⁻⁴	1.1	6x8	424 744	22 619	143	220	71
P0686	100	3×10 ⁻⁴	2.2	7x7	244 469	31 555	144	210	66
P0682	100	3×10 ⁻⁴	3.1	7x7	129 075	18 160	47	81	22
P0675	100	3×10 ⁻⁴	6.2	6x8	132 477	30 354	26	40	12
P0799	100	3×10 ⁻³	3.4	4x5	48 393	5 809	37	62	16
P0746	100	3×10 ⁻³	5.3	7x5	290 646	14 355	70	110	33
P0735	200	3×10 ⁻⁵	1.1	6x10	544 391	6 731	146	290	97
P0725	200	3×10 ⁻⁴	1.0	6x9	432 825	20 041	118	182	58
P0731	200	3×10 ⁻⁴	2.3	7x8	445 720	20 492	107	165	51
P0728	200	3×10 ⁻⁴	3.4	6x9	439 482	39 015	105	141	40
P0768	200	3×10 ⁻⁴	5.2	3x7	161 858	23 685	49	73	21
P0742	200	3×10 ⁻³	7.9	6x5	112 250	14 110	37	44	10
P0791	300	3×10 ⁻⁴	1.1	5x8	383 027	4 856	141	318	99
P0773	300	3×10 ⁻⁴	2.4	3x9	258 168	2 889	140	303	96
P0766	300	3×10 ⁻⁴	3.5	5x7	329 713	3 909	141	295	95
P0747	300	3×10 ⁻³	7.9	6x4	208 814	6 921	106	158	48

Table 5.2. Details of deformed samples at different temperature. Shear strain and shear strain rate are valid for the outer sample margin. Grain size values were estimated by EDAX OIM software.

Misorientation relationship between individual subgrains

At low shear strain (Fig. 5.28a) the rotation of the single subgrains (in red frame) did not exceed values above 15° misorientation, otherwise new high angle boundaries would be visible in the grain boundary map (Fig. 5.28). In the pole figure sharp and dense point maxima are observed. With increasing shear strain (Fig. 5.28b) dispersion paths occur in the pole figures and high angle boundaries formed (red frame) as indicated in the grain boundary map. The highest shear strain sample is characterised by the development of new small grains surrounded by high angle boundaries (Fig. 5.28c, red frame) as indicated in the grain boundary map. Also, the two misorientation profiles across the grain indicate the high misorientation angles between the single new formed grains. The pole figures show single but dense point maxima which are related to the new formed grains.

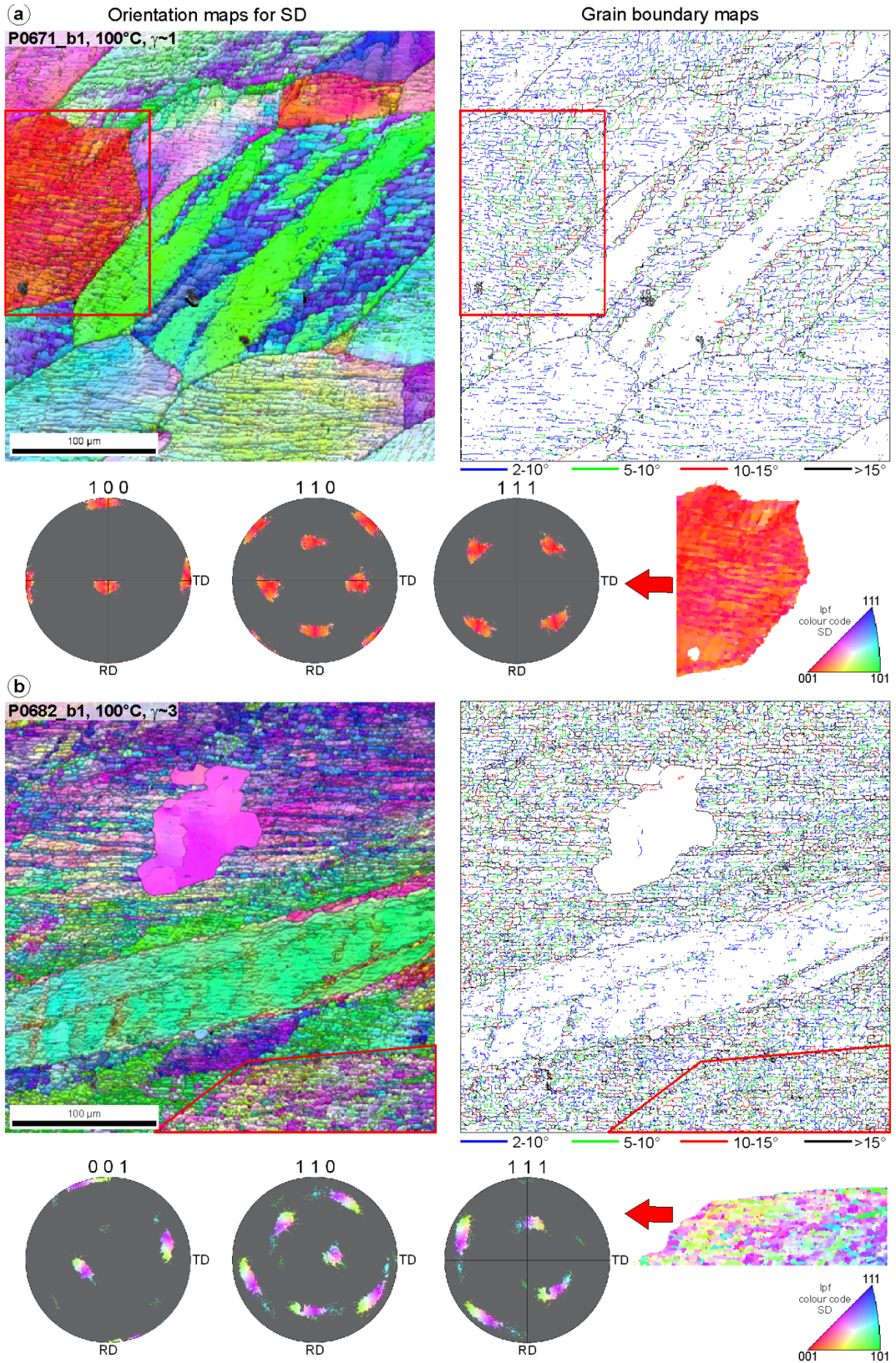


Fig. 5.28. caption on page next page.

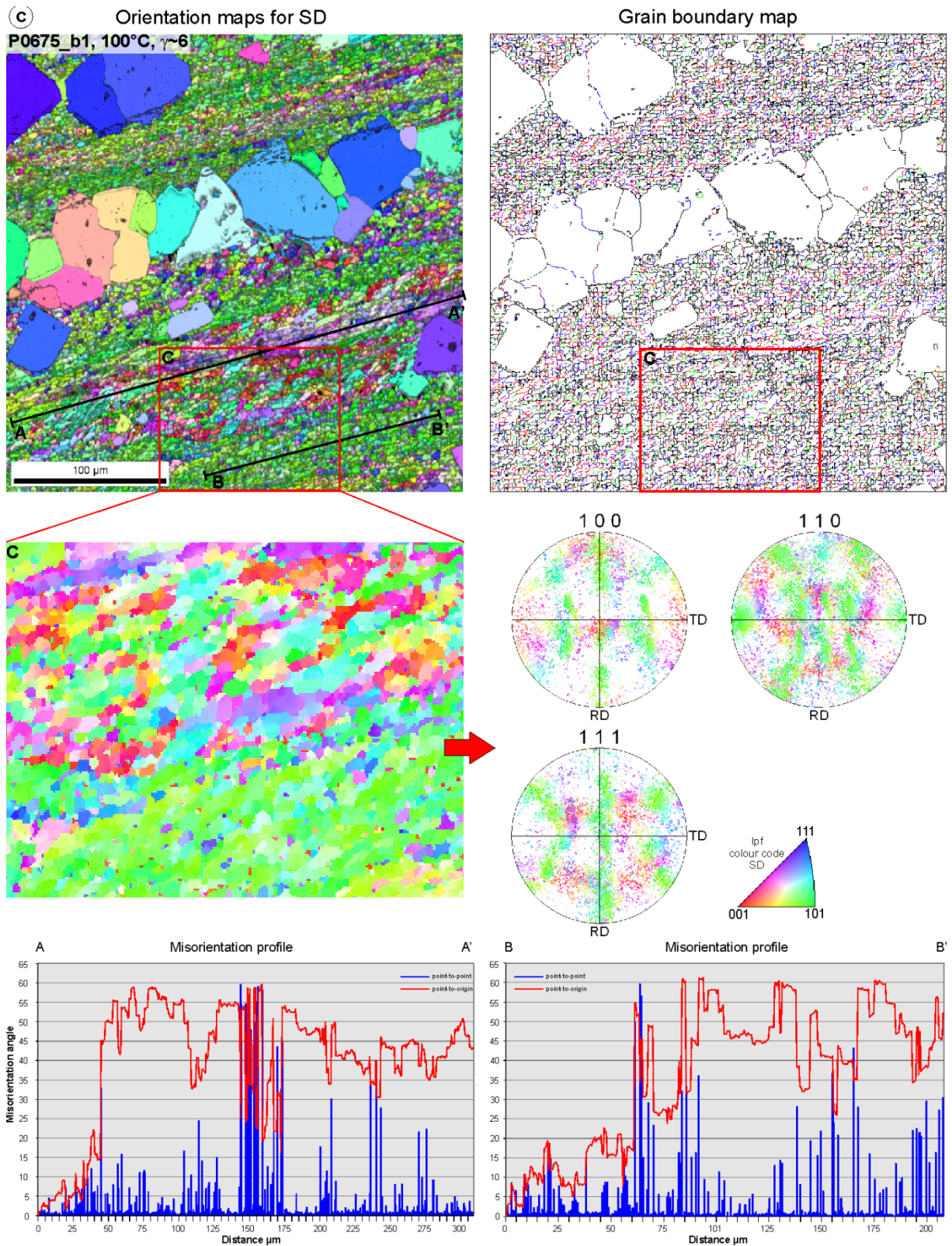


Fig. 5.28 previous page and this page. Orientation maps shear sense top to the right, corresponding grain boundary maps (gb maps) and polefigures of the investigated grains. a) Low shear strain, no high angle boundaries formed in investigated grain as seen in gb map. Pole figures show sharp and dense single point maxima. b) Medium shear strain, some high angle boundaries developed as indicated in gb map, pole figures show dispersion path of subgrains. c) High shear strain, pole figures of detail area. (c) show many sharp single point maxima. Gb map shows high frequency of high angle boundaries. Misorientation profile A-A' and B-B' show many high misorientation between nearest neighbours. Pole figures are equal area projection, upper hemisphere.

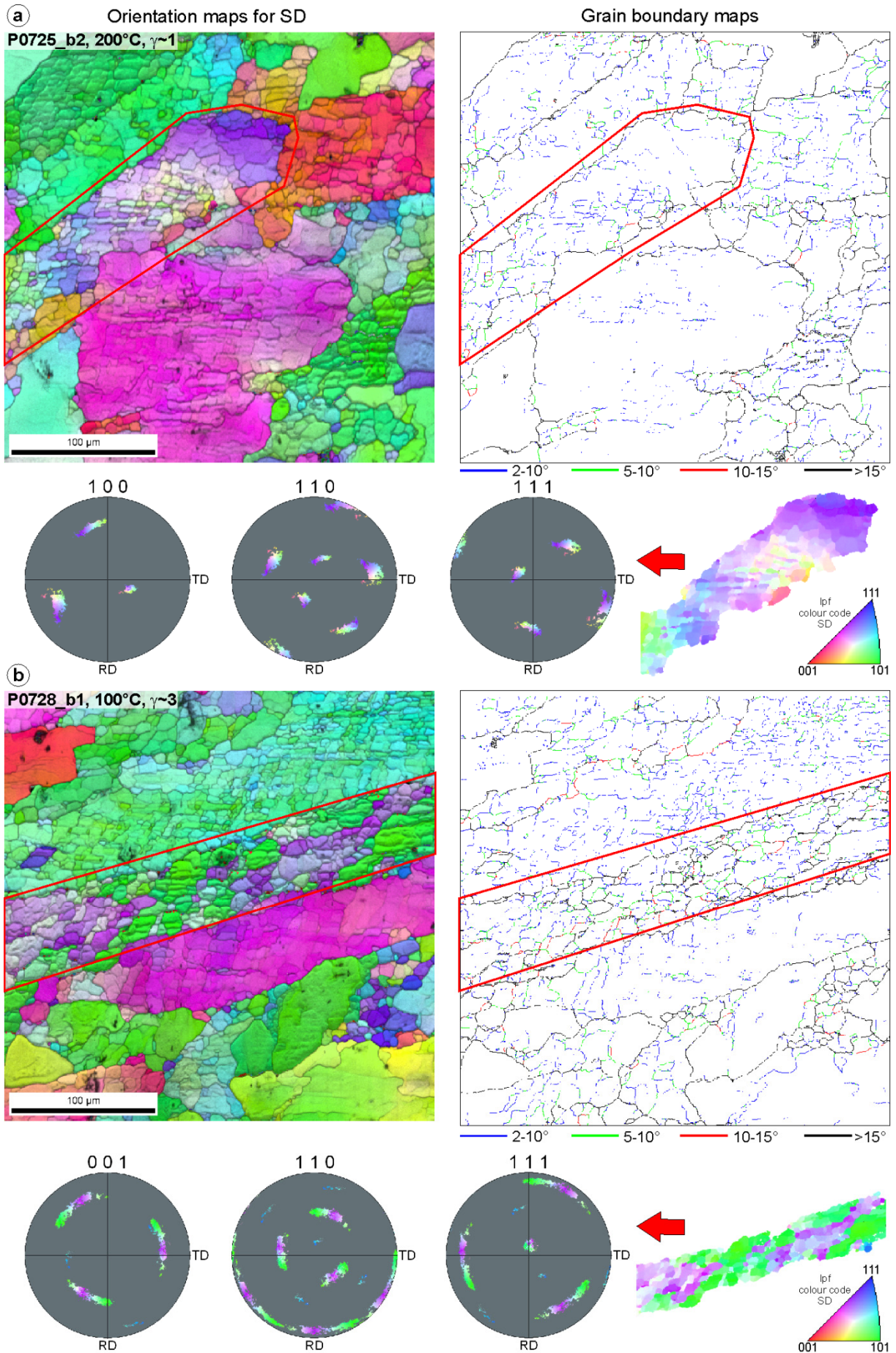


Fig. 5.29. caption next page.

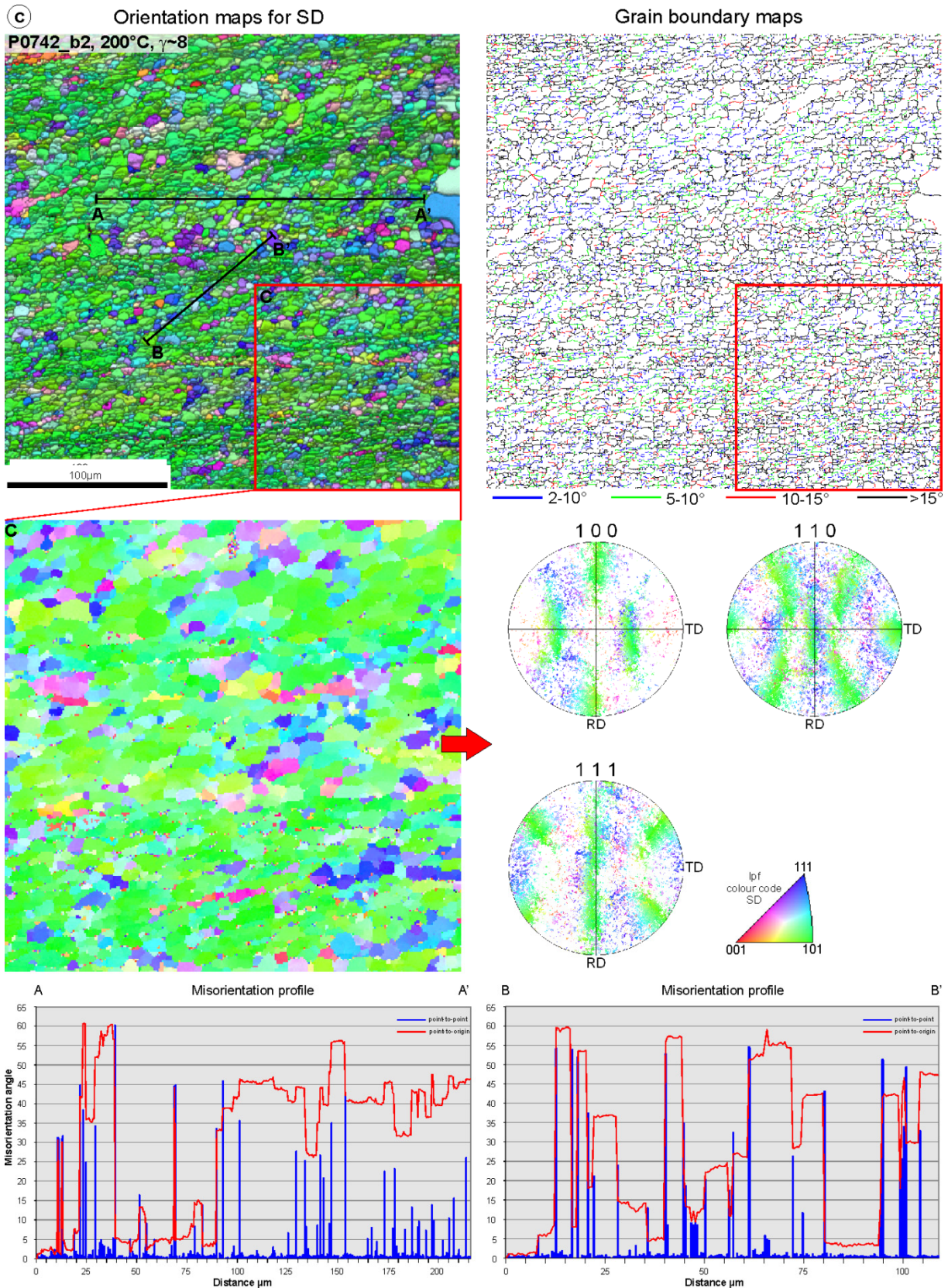


Fig. 5.29 *previous page and this page.* Orientation maps, shear sense top to the right, corresponding grain boundary maps (gb maps) and pole figures of the investigated grains. a) Low shear strain, minor high angle boundaries formed in investigated grain as seen in gb map. Pole figures show sharp and dense point maxima with weak dispersion path. b) Medium shear strain, some high angle boundaries developed as indicated in gb map, pole figures show dispersion path of subgrains. c) High shear strain, pole figures of detail area (c) show many sharp single point maxima with a strong preference. Gb map shows high frequency of high angle boundaries. Misorientation profile A-A' and B-B' show many high misorientations between nearest neighbours. Pole figures are equal area projection, upper hemisphere.

The same development is observed at 200°C, however the rotation of subgrains in this series already starts at low shear strains of $\gamma \sim 1$ (Fig. 5.29a, red frame) as indicated by the weak dispersion path in the pole figures and in the appearance of high angle boundaries in the investigated grain in the grain boundary map. With increasing shear strain ($\gamma \sim 3$, Fig. 5.29b, red frame) the misorientation between individual subgrains increases, as shown in the pole figure in form of the development of a dispersion path. As a consequence high angle boundaries increasingly formed. The highest shear strain sample ($\gamma \sim 8$, Fig. 5.29c, red frame) is, like the 100°C high shear strain sample, characterised by small new grains that are surrounded by high angle boundaries and by a high misorientation angle between the individual new grains as indicated in the misorientation profile. The pole figures show dense single point maxima resulting from the new formed grains.

Low angle vs high angle boundary distribution

The distribution of misorientation angles in a sample is a useful parameter to estimate the relationships between low angle (subgrain) boundaries (boundaries less than 15°) and high angle (grain) boundaries (boundaries larger than 15°) and hence if recrystallisation occurred. For this purpose misorientation angle charts were plotted for all deformed samples (Fig. 5.30). At 100 and 200°C the frequency of the low angle boundaries decreases with increasing shear strain, whereas the frequency for the high angle boundaries increases with increasing shear strain. At 300°C this observation could not be made, but the frequency for both low angle and high angle boundaries does not change with increasing shear strain, but remains constant over the strain range, except for sample P0747, where a slight reduction in low angle frequency could be observed.

At low shear strain the microstructure is dominated by low angle boundaries (<15°), indicating that these subgrain boundaries are formed due to polygonization. An increase in shear strain cause the subgrains to rotate until misorientation between neighbours exceeded 15° and further, thus new high angle boundaries are formed. In summary, an increase in shear strain causes a switch from low angle boundaries that are dominant at low shear strains to high angle boundaries that dominate at high shear strains and are formed from previous low angle boundaries. This prominent change occurs especially at 100 and 200°C. At 300°C, no difference in terms of the boundary misorientation between low and high shear strain samples could be identified. The amount of low and high angle boundaries stays constant over the whole strain range.

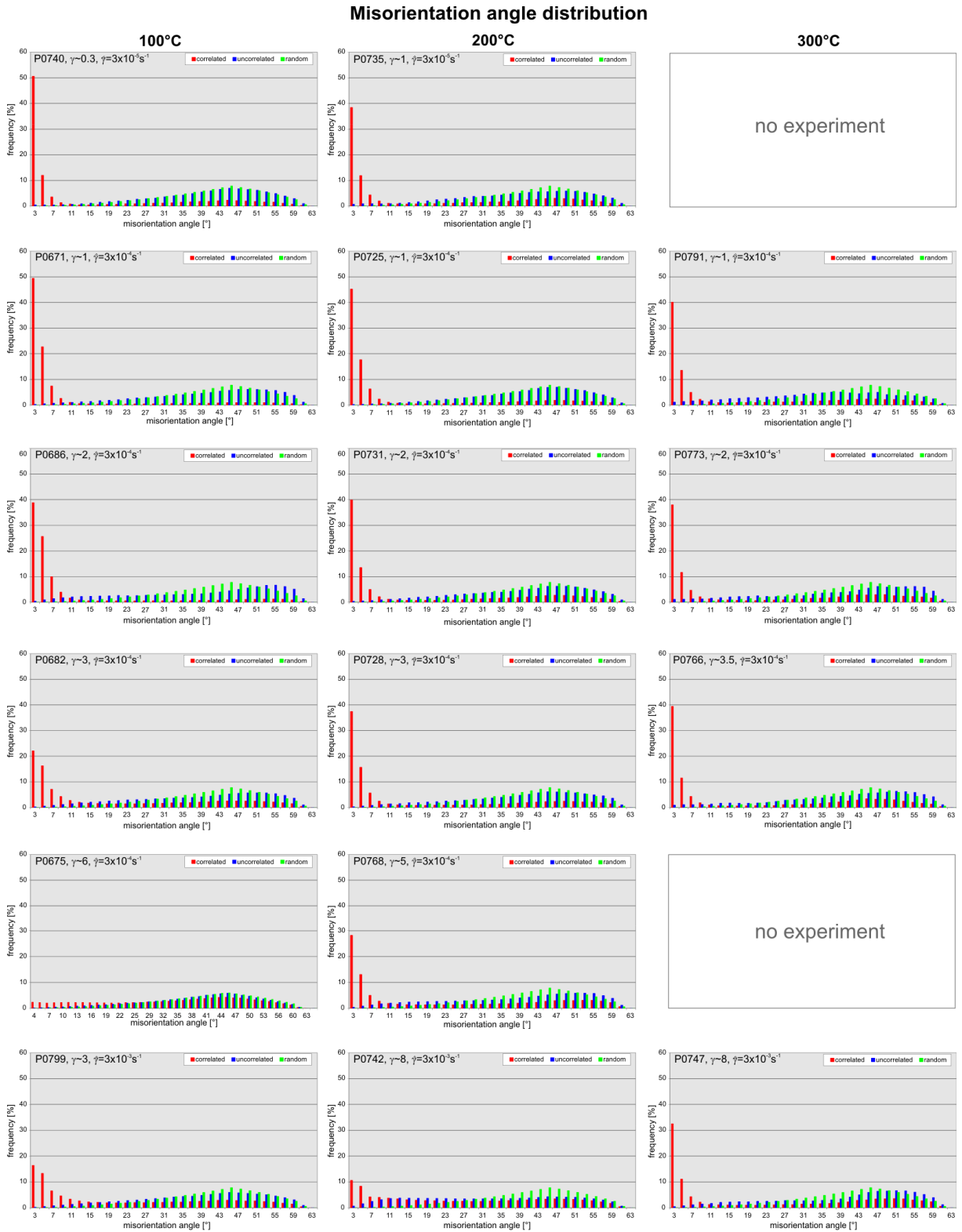


Fig. 5.30. Distribution of misorientation angles in all deformed samples. At 100 and 200°C with increasing shear strain, a change from a high frequency of low angle boundaries to a high frequency of high angle boundaries can be observed. This change can't be seen in samples deformed at 300°C.

Effect of temperature

Orientations maps in Fig. 5.31 show the effect of temperature on three samples deformed to equivalent shear strain of $\gamma \sim 3$ at different temperatures (100, 200 and 300°C).

Fig. 5.31a displays the sample (P0682) deformed at 100°C. The sheared elongated grains contain blocky subgrains (grain A and grain B) and the grains are characterised by serrated grain boundaries. Grain C displays the characteristic domain structure, formed in the low temperature samples. Grain D, however, is characterised by a bulged grain boundary and a lack of internal subgrain grain development.

Fig 5.31b shows the sample (P0728) deformed at 200°C. The increase in temperature had an effect on the microstructure in terms of subgrain size and shape. Subgrains are now larger in size and more irregularly shaped. New small grains form (grains D) and the grain boundaries show a cusped/lobate structure as visible in grain A, grain B and grain C. The wavelengths of the cusps and lobes is approximately the size of the subgrains. Bulged grain boundaries can be observed in grain E.

Fig. 5.31c shows a sample (P0766) deformed at 300°C. At this temperature the microstructure is dominated by grains larger in size as at 100 and 200°C. Additionally, the subgrain size increased compared to the low temperature samples. The bulged boundaries of the grains with less substructure (grains A, D and E) move into grains containing subgrains (grain B). Cusped/lobate grain boundary structure is nicely shown in grain D, where the cusps and the lobes is similar to the subgrain size. Because the new formed grains developed a deformation substructure inside the grains (grains B and C) these grains must have formed during deformation.

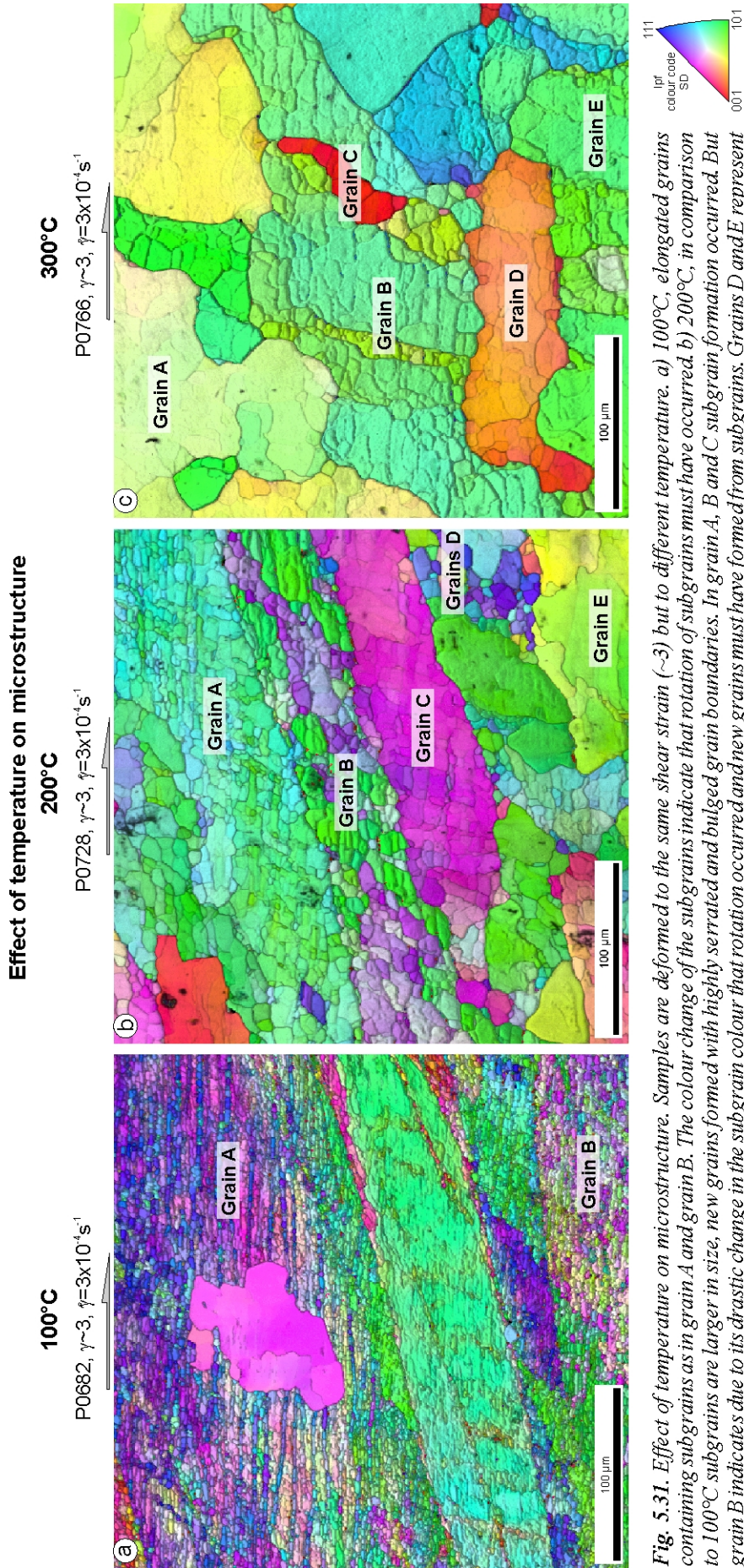


Fig. 5.31. Effect of temperature on microstructure. Samples are deformed to the same shear strain (~ 3) but to different temperature. a) 100°C, elongated grains containing subgrains as in grain A and grain B. The colour change of the subgrains indicate that rotation of subgrains must have occurred. b) 200°C, in comparison to 100°C subgrains are larger in size, new grains formed with highly serrated and bulged grain boundaries. In grain A, B and C subgrain formation occurred. But grain B indicates due to its drastic change in the subgrain colour that rotation occurred and new grains must have formed from subgrains. Grains D and E represent new formed grains during deformation. c) 300°C, in comparison with 200°C grain size increased and the microstructure exhibits a reworking due to formation of new grains. Migration of grain boundaries occurs frequently as indicated in grain A and D that show bulged grain boundaries migrating in grain B which has a higher substructure density. Grain D with less deformation structure moves into grain B with higher deformation structure. Grain C is a new formed grain, nicely shown by the complete different orientation with respect to the host grain B.

5.4 Discussion

5.4.1 Activity of slip systems

Halite deforms at room temperature mainly by slip on $\{110\}\langle 1\bar{1}0\rangle$, at higher temperatures $\{100\}\langle 011\rangle$ and $\{111\}\langle 1\bar{1}0\rangle$ become equally active as shown in (Fig. 5.32) and determined by e.g. Carter & Heard (1970 and references there in).

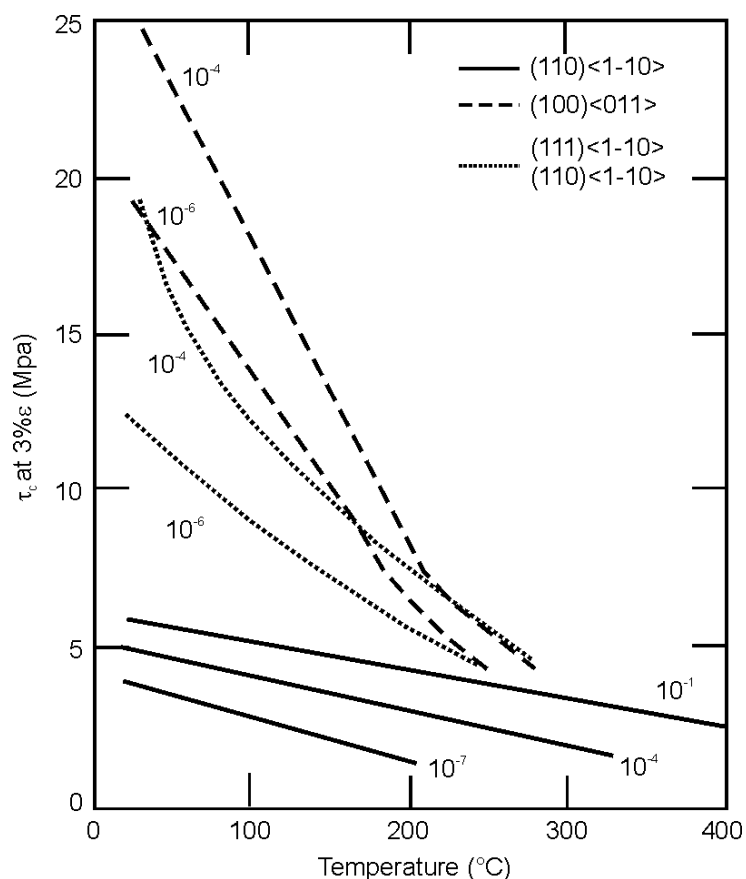


Fig. 5.32. CRSS values for the three slip systems active in halite obtained from single crystal experiments. Figure from Carter & Heard (1970).

Despite the fact that halite is a cubic mineral and has many slip systems, it is plastically highly anisotropic especially at low temperatures. This is because out of the six crystallographically equivalent $\{110\}\langle 1\bar{1}0\rangle$ slip systems, only two representatives are independent (e.g. Skrotzki et al. 1996, Wenk et al. 1997). Slip alone on this slip system does not fulfil the von Mises criterion (von Mises 1928) to accommodate homogenous deformation. In order to obtain an arbitrary shape change three of the harder subsidiary slip systems, with three variants for the six crystallographic equivalent $\{100\}\langle 011\rangle$ systems and five variants for the 12 crystallographic equivalent $\{111\}\langle 1\bar{1}0\rangle$ systems must be activated simultaneously with the weakest slip system (Skrotzki et al. 1995, 1996). Consequently, halite displays at a low temperature (100°C) a highly anisotropic single crystal yield surface, which results in large stress difference and thus in a heterogeneous stress distribution in grains. As a result, grains need an alternative way to deform. A solution seems to be the formation of domain structures, which are thus a strain accommodation feature. The dispersion path in the pole figures as well as the orientation of the crystallographic cubes superimposed on the orientation maps, indicates that rotation of the crystal lattice between the two domains has

occurred. Further investigations on the rotation axis and the influence of the grain orientation on the occurrence of the domain structures are needed to explain this feature more in detail.

Drury & Pennock (2007) described the domain boundaries as orientation splitting boundaries, which develop between subgrains that are deforming on different slip systems. Drury and Pennock further report that these boundaries only develop in grains that have an unstable initial orientation. Pennock et al. (2004) observed in dry deformed NaCl that orientation splitting mainly occurs in grains with $\langle 111 \rangle$ close to the compression axis. This orientation splitting is also reported in cube oriented f.c.c. metals (Akef & Driver 1991). Kink bands cannot be considered as an explanation for these boundaries, because the boundaries occur in material deforming on one easy slip system.

The blocky subgrain structure observed at low temperature, that coincide with the horizontal slip bands, which could be assigned to a (111) plane, and the oblique slip bands, that could be assigned to a (100) plane, thus suggests that two slip systems $\{100\}\langle 011 \rangle$ and $\{11\bar{1}\}\langle 011 \rangle$ with the same Burgers vector were active simultaneously. This simultaneous activation of two slip systems suggests that cross-slip and/or pencil glide with slip direction in $\langle 011 \rangle$ is active at 100°C, forming intersecting slip bands and misoriented subgrain boundaries, giving rise to the blocky subgrain structure. Pencil glide was mainly reported in fcc and bcc metals (e.g. Taylor & Elam 1926, Masui 1999, Ngan & Wen 2001).

Especially at 100°C and low shear strain, grains that are not in a favourable position for deformation will be harder to deform than grains that are in a more favourable position. That is, grains in the harder orientation should deform less than grains in a soft orientation (Lebensohn et al. 2003). This behaviour is expressed in the shape of the grains and in the size of the subgrains. Hard grains show a more rounded shape, which in turn is an indicator that deformation was not able to change the grain shape as much. However, grains that are easier to deform exhibit a deformed, elongated grain shape. The size of the subgrains is also different. Hard grains contain subgrains much smaller than in softer grains. Since harder grains need more strain to deform, the stress is higher for these grains than for the soft grains. Higher stress in the hard grains leads to a smaller subgrain size.

At higher temperatures (200°C and 300°C) the difference in the crss for the three slip systems is not as high as at 100°C, and the three slip systems $\{110\}\langle 1\bar{1}0 \rangle$, $\{100\}\langle 011 \rangle$ and $\{111\}\langle 1\bar{1}0 \rangle$ are equally active (cf. Fig. 5.32). Stress is more homogeneously distributed and, therefore, the grains deform more homogeneously. This explains the absence of domain structures and pencil glide features at higher temperature.

5.4.2 Deformation mechanisms and recrystallisation processes

Deformation mechanisms

Straight and wavy slip bands and the occurrence of subgrains are evidences of dislocation processes in deformed wet polycrystalline halite in this study.

At 100°C, dislocation glide is indicated by straight slip bands and blocky subgrains due to the intersection of two slip systems. Wavy slip bands in salt were recognised also by Skrotzki & Liu (1982), Senseny et al. (1992) and Carter et al. (1993). These authors interpreted the wavy slip lines as the result of cross-slip of screw dislocations on $\{100\}$ and $\{111\}$ planes bridging parallel $\{110\}$ slip planes. At 200 and 300°C, subgrains are more polygonal and irregularly

shaped indicating that subgrain formation is due to climb-controlled recovery processes modifying the blocky structure formed by intersecting slip bands.

Recrystallisation processes

Recrystallisation is dynamic or static. Evidences for dynamic recrystallisation are: i) highly irregular shaped grains with serrated and bulged grain boundaries and ii) subgrain development inside the grains. The observation of grains with an internal deformation structure (e.g. subgrains) and the occurrence of serrated and bulged grain boundaries in our deformed samples show clearly that these grains are dynamically recrystallised. Two main dynamic recrystallisation mechanisms are distinguished (e.g. Guillopé & Poirier 1979 and Drury & Urai 1990): rotation recrystallisation and migration recrystallisation.

The progressive misorientation of subgrain boundaries results in the formation of new high angle boundaries, where new grains are formed and is called subgrain rotation recrystallisation. Evidence that rotation recrystallisation took place is a typically developed core and mantle structure, where the core is the parent grain and the mantle structure consists of new daughter grains. A further indicator is a recrystallized grain size similar to the subgrain size (White 1976). However, a typical core and mantle structure was not observed in the deformed samples in this study. Nevertheless, the decrease in grain size (down to subgrain size) and the development and the increase of new high angle boundaries with increasing shear strain in samples deformed at 100°C and 200°C thus suggests that recrystallisation by subgrain rotation occurred. The dispersion paths in the pole figures are an additional indicator that subgrain rotation occurred (Bestmann & Prior 2003). Therefore, the dispersion path occurring in samples containing subgrains suggests that subgrain rotation took place. With increasing shear strain the subgrains rotate by up to misorientations of 15° and further, and low angle boundaries become high angle boundaries and hence new grains are formed, indicated by the single point maxima in the pole figures. The new recrystallised grains furthermore show a similar size as the parent subgrains as seen in the samples deformed to high shear strains at 100 and 200°C. Therefore, we can conclude that new grains formed with increasing shear strain by subgrain rotation recrystallisation (Fig. 5.33 on the next page).

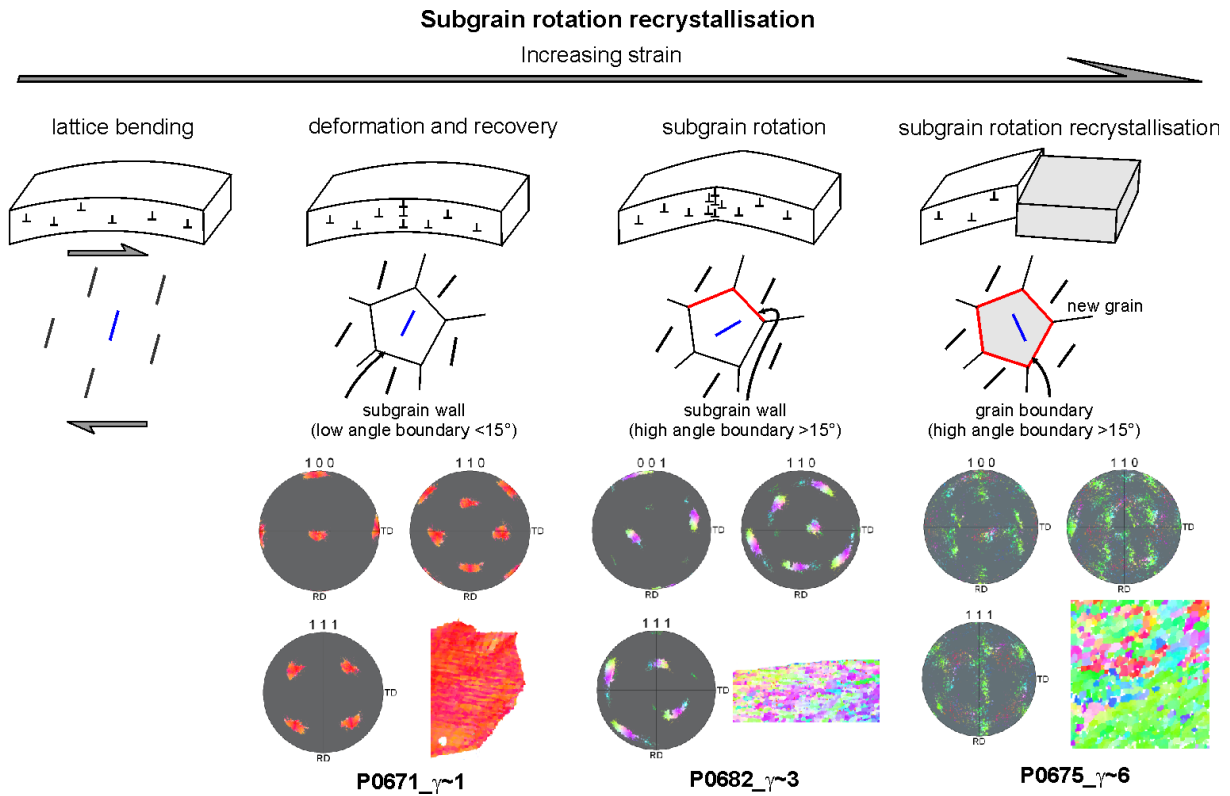


Fig. 5.33. Sketch of the process of subgrain rotation recrystallisation due to the progressive misorientation of subgrains (Figure from Bestmann & Prior (2003) linked with the observations on pole figures from deformed samples in this study). The formation of subgrains results in dense point maxima. With increasing shear strain, subgrains rotate and produce a dispersion path in the pole figure. With further increasing shear strain the misorientation between single subgrains exceeds 15° , and new grains with high angle boundaries formed from subgrains displaying single point maxima in the pole figure.

The second recrystallisation mechanism is inferred from highly serrated, bulged, cusped and lobate grain boundaries indicating that recrystallisation occurred by migration of grain boundaries. Recrystallisation by grain boundary migration is mainly active at higher temperature (Drury & Urai 1990) and occurs in this study in samples deformed at 100°C only to a minor amount. However, it becomes dominant at 200°C and is the main characteristic of samples deformed at 300°C . The special boundary structure can be explained by the driving force for the boundary migration, which is the stored internal strain energy in form of dislocations (Vernon 1976). Grain boundaries will hence migrate and become bulged in the direction of grains containing higher strain energy. Because grain boundary mobility increases with temperature (e.g. Piazzolo et al. 2006) this process occurs at mainly at 200°C and becomes dominant at 300°C . The presence of subgrains shows that recrystallisation occurred during deformation.

Ter Heege et al. (2005) observed in grain boundary migration in wet samples deformed in the same temperature range as in this study and concluded that GBM must be fluid-assisted, since in grain boundary migration in dry salt occurs at temperatures higher than in this study (Guillopé & Poirier 1979, Franssen 1993). Therefore, as water was present in samples deformed in this study, it can be also concluded that grain boundary migration in this study was assisted by fluids.

New formed grains without any deformation substructure like subgrains, as observed in this study are a feature of static recrystallisation. Static recrystallisation is a process that occurs if

temperature was relatively high when deformation stopped or if much water was present along the grain boundaries (Passchier & Trouw 1998). The driving force is the same as for grain boundary migration: decreasing the stored internal strain energy. Surface energy leads to straight grain boundaries.

5.4.3 Effect of strain and temperature

Increasing shear strain leads to a change in the grain shape from polygonal at low shear strain to elongate in agreement with the finite strain ellipse at high shear strain as observed in the deformed samples. Also with increasing shear strain a major grain size reduction could be observed in samples deformed at 100 and 200°C (Fig. 5.17). This reduction in grain size can clearly be attributed to dynamic recrystallisation by subgrain rotation. The fact that the new grains retain an equi-dimensional shape even to very high shear strains, while the elongated old grain boundaries are still visible, suggests maintenance of a foam texture by grain boundary migration.

An increase in temperature causes an increase in grain size as shown in the grain size distribution diagrams. Associated with an increase in temperature is the increase in the mobility of grain boundaries, which enables the grain boundaries to migrate, which does not dominate at the low temperature (100°C). As a secondary effect, static recrystallisation occurs after the deformation. This is caused by the relatively high sample temperature after quenching, and grain boundary migration continues until temperature is too low for this process to continue. The effect of this post deformation annealing is, that most of the deformation microstructure was erased in some samples. Another feature of higher temperature compared to low temperature (100°C) deformation is the shape and size of the subgrains. At higher temperature subgrains are more polygonal, irregular in shape and larger in size than at lower temperature. That is caused by recovery mechanisms that are more active at higher than at lower temperature. Dislocations at higher temperature can start to climb out of their glide plane and therefore deformation is easier than at the low temperature.

Migration recrystallisation at higher temperature leads to grain growth and hence larger grain sizes in respect to starting material, due to removal of grains with strain hardening substructure by grains with little substructure. Grain boundary migration resulted in grain growth due to replacement of grains with well developed substructure by grains with little substructure.

Finally, the effect of temperature on grain boundary migration and recrystallisation explains why there is no evolution with increasing shear strain observed in the 300°C series. At this temperature recrystallisation by grain boundary migration dominates and is faster than subgrain rotation recrystallisation.

5.5 Conclusions

- Dynamic recrystallisation in form of subgrain rotation recrystallisation and grain boundary migration recrystallisation could be observed: subgrain rotation recrystallisation yielding misorientations $>15^\circ$ is dominant at 100 and 200°C, whereas the mechanism is suppressed at 300°C due to the dominance of grain boundary migration recrystallisation.
- A clear evolution in microstructure at 100 and 200°C with increasing shear strain is observed. An increase in shear strain leads to elongation of the original grains, in agreement with the finite strain ellipse, and rotation of subgrains to high misorientation angles. This in turn results, at high shear strains, in the formation of high angle boundaries and therefore new grains with the grain size of the low shear strain subgrains. Subgrain rotation recrystallisation is therefore mainly responsible for the grain size reduction at these temperatures. No evolution with shear strain at 300°C could be observed and can be explained by the higher mobility of grain boundaries favouring grain boundary migration.
- Wavy slip bands occurring at 100 and 200°C indicate that cross-slip is active as a recovery mechanism. Horizontal slip bands are produced by the glide of dislocations on $\{111\}\langle 1\bar{1}0\rangle$ slip system and oblique slip bands result from the glide of dislocations on $\{100\}\langle 011\rangle$ slip system with a shared Burgers vector.
- Blocky subgrains at 100°C are formed by the intersection of these two slip systems, in general by a mechanism that is called pencil glide. Thus, these low angle boundaries did not form due to recovery mechanisms but are rather interpreted to represent geometrically necessary misorientations associated with high densities of glide dislocations. However, polygonal subgrains formed at 200 and 300°C can be clearly assigned to climb-controlled recovery processes.
- The formation of the characteristic domain structure in grains at 100°C is a result of the high crystal plastic anisotropy of halite at this temperature. It is caused by the lack of a sufficient number of independent variants for the easiest $\{110\}\langle 1\bar{1}0\rangle$ slip system. Therefore, the harder to activate subsidiary $\{100\}\langle 011\rangle$ and $\{111\}\langle 1\bar{1}0\rangle$ slip systems have to be activated simultaneously to maintain strain compatibility. Domains are not present at higher temperature, because the three families of slip systems are then equally active (similar in strength).
- Temperature has an effect on the developing microstructure during deformation and after deformation. An increase in temperature leads to an increase in grain size, caused by grain boundary migration. This mechanism is the dominant mechanism at 300°C, caused by the higher mobility of the grain boundaries. However, samples deformed at this temperature are also exposed to post-deformational annealing, as quenching is not efficient to cool samples down to room temperature, therefore grain growth occurs under static conditions.

5.6 References

- Adams, B.L., Wright, S.I. & Kunze, K. 1993. Orientation Imaging - the Emergence of a New Microscopy. *Metallurgical Transactions a-Physical Metallurgy and Materials Science* 24(4), 819-831.
- Akef, A. & Driver, J.H. 1991. Orientation Splitting of Cube-Oriented Face-Centered Cubic-Crystals in Plane-Strain Compression. *Materials Science and Engineering a-Structural Materials Properties Microstructure and Processing* 132, 245-255.
- Bay, B., Hansen, N., Hughes, D.A. & Kuhlmann-Wilsdorf, D. 1992. Evolution of FCC deformation structures in polyslip. *Acta Metallurgica et Materialia* 40, 205-219.
- Bestmann, M. & Prior, D.J. 2003. Intragranular dynamic recrystallization in naturally deformed calcite marble: diffusion accommodated grain boundary sliding as a result of subgrain rotation recrystallization. *Journal of Structural Geology* 25(10), 1597-1613.
- Carter, N.L. & Hansen, F.D. 1983. Creep of Rocksalt. *Tectonophysics* 92(4), 275-333.
- Carter, N.L. & Heard, H.C. 1970. Temperature and Rate Dependent Deformation of Halite. *American Journal of Science* 269(3), 193-&.
- Carter, N.L., Horseman, S.T., Russell, J.E. & Handin, J. 1993. Rheology of Rock-Salt. *Journal of Structural Geology* 15(9-10), 1257-1271.
- Dingley, D.J. 1984. On-line determination of crystal orientation and texture determination in an SEM. *Proceedings of the Royal Society of London* 19, 74-75.
- Drury, M.R. & Pennock, G.M. 2007. Subgrain Rotation Recrystallization in Minerals. *Material Science Forum* 550, 95-104.
- Drury, M.R. & Urai, J.L. 1990. Deformation-Related Recrystallization Processes. *Tectonophysics* 172(3-4), 235-253.
- Fliervoet, T.F., Drury, M.R. & Chopra, P.N. 1999. Crystallographic preferred orientations and misorientations in some olivine rocks deformed by diffusion or dislocation creep. *Tectonophysics* 303(1-4), 1-27.
- Franssen, R.C.M.W. 1993. Rheology of synthetic rocksalt. PhD thesis, Universiteit Utrecht.
- Franssen, R.C.M.W. 1996. Mechanical anisotropy of synthetic polycrystalline rocksalt. In: *Fourth Conference on the Mechanical Behaviour of Salt*. TTP Trans Tech Publications, Clausthal-Zellerfeld, Germany, The Pennsylvania State University, June 17 and 18, 1996, 63-75.
- Franssen, R.C.M.W. & Spiers, C.J. 1990. Deformation of polycrystalline salt in compression and in shear at 250-350°C. In: *Deformation Mechanisms, Rheology and Tectonics* (edited by Knipe, R. J. R., E.H.) 45. Geological Society Special Publication, 201-213.
- Friedman, M., Dula, W.F., Gangi, A.F. & Gazonas, G.A. 1981. Structural petrology of experimentally deformed synthetic rocksalt. In: *First Conference on the Mechanical Behaviour of Rocksalt* (edited by Langer, M. & Hardy, R.). Transtech, Clausthal-Zellerfeld, 19-36.

- Gifkins, R.C. 1976. Grain-Boundary Sliding and Its Accommodation During Creep and Superplasticity. *Metallurgical Transactions a-Physical Metallurgy and Materials Science* 7(8), 1225-1232.
- Guillopé, M. & Poirier, J.P. 1979. Dynamic Recrystallization During Creep of Single-Crystalline Halite - Experimental-Study. *Journal of Geophysical Research* 84(NB10), 5557-5567.
- Hobbs, B.E. 1968. Recrystallization of Single Crystals of Quartz. *Tectonophysics* 6(5), 353-401.
- Hobbs, B.E., Means, W.D. & Williams, P.F. 1982. Relationships between foliation and strain: an experimental investigation. *Journal of Structural Geology* 4(4), 411-428.
- Huang, X. 1998. Grain orientation effect on the microstructure in tensile strained copper. *Scripta Materialia* 38, 1697-1703.
- Jenkins, C.H.M. & Mellor, G.A. 1935. Investigations of the behaviours of metals under deformation at high temperature. I-Structural changes in mild steel and commercial iron during creep. *Journal of the Iron and Steel Institute* 132, 179-227.
- Lebensohn, R.A., Dawson, P.R., Kern, H.M. & Wenk, H.R. 2003. Heterogeneous deformation and texture development in halite polycrystals: comparison of different modeling approaches and experimental data. *Tectonophysics* 370(1-4), 287-311.
- Malin, A.S. & Hatherly, M. 1979. Microstructures of cold-rolled copper. *Metal Sciences* 13, 463-472.
- Masui, H. 1999. Simulation for f.c.c. deformation texture by modified pencil glide theory. *Acta Materialia* 47(17), 4283-4298.
- McLean, D. 1952. Crystal fragmentation in aluminium during creep. *Journal of the Institute of Metals* 81, 287-292.
- Nadgorny, E.M. & Strunk, H.P. 1987. Dislocation-Structure of Plastically Deformed NaCl Polycrystals. *Physica Status Solidi a-Applied Research* 104(1), 193-202.
- Ngan, A.H.W. & Wen, M. 2001. Dislocation kink-pair energetic and pencil glide in body-centered-cubic crystals. *Physical Review Letters* 87(7), 075505-1-075505-4.
- Passchier, C.W. & Trouw, R.A.J. 1998. *Microtectonics*. Springer-Verlag, Berlin Heidelberg.
- Pennock, G.M., Drury, M.R. & Spiers, C.J. 2004. Investigation of subgrain rotation recrystallization in dry polycrystalline NaCl. In: *Recrystallization and Grain Growth, Pts 1 and 2. Materials Science Forum* 467-470. Trans Tech Publications Ltd, Zurich-Uetikon, 597-602.
- Piazolo, S., Bestmann, M., Prior, D.J. & Spiers, C.J. 2006. Temperature dependent grain boundary migration in deformed-then-annealed material: Observations from experimentally deformed synthetic rocksalt. *Tectonophysics* 427(1-4), 55-71.
- Poirier, J.P. 1985. *Creep of crystals*. Cambridge University Press.
- Prior, D.J., Boyle, A.P., Brenker, F., Chedale, M.C., Day, A., Lopez, G., Peruzzo, L., Potts, G.J., Reddy, S., Spiess, R., Timms, N.E., Trimby, P., Wheeler, J. & Zetterstrom, L. 1999. The

application of electron backscatter diffraction and orientation contrast imaging in the SEM to textural problems in rocks. *American Mineralogist* 84(11-12), 1741-1759.

Senseny, P.E., Hansen, F.D., Russell, J.E., Carter, N.L. & Handin, J.W. 1992. Mechanical-Behavior of Rock Salt - Phenomenology and Micromechanisms. *International Journal of Rock Mechanics and Mining Sciences & Geomechanics Abstracts* 29(4), 363-378.

Skrotzki, W., Helming, K., Brokmeier, H.-G., Dornbusch, H.-J. & Welch, P. 1995. Textures in pure shear deformed rock salt. *Textures and Microstructures* 24, 133-141.

Skrotzki, W., Dornbusch, H.-J., Helming, K., Dornbusch, H.-J. & Welch, P. 1996. Development of microstructure and texture in pure shear deformed salt. In: *4th Conference on the Mechanical Behaviour of Salt* (edited by Aubertin, M. & Hardy, H. R.), Montreal, Canada, 203-211.

Skrotzki, W. & Liu, Z. G. 1982. Analysis of the Cross Slip Process in Alkali-Halides. *Physica Status Solidi a-Applied Research* 73(2), K225-K229.

Spiers, C.J. & Carter, N.L. 1998. Microphysics of rocksalt flow in nature. In: *The mechanical behaviour of salt, proceedings of the 4th conference* (edited by Aubertin, M. & Hardy, H. R.) 22. Trans Tech Publication, 115-128.

Spiers, C.J., Peach, C.J., Urai, J.L., Lister, G.S., Boland, J.N. & Zwart, H.J. 1986. The influence of fluid-rock interaction on the rheology of salt rock. In: *European Communities-Commission, Nuclear Science and Technology Series*.

Taylor, G.I. & Elam, C.F. 1926. The distortion of Iron Crystals. *Proceedings of the Royal Society of London. Series A.* 112(761), 337-361.

Ter Heege, J.H., De Bresser, J.H.P. & Spiers, C.J. 2005. Dynamic recrystallization of wet synthetic polycrystalline halite: dependence of grain size distribution on flow stress, temperature and strain. *Tectonophysics* 396(1-2), 35-57.

Urai, J.L., Means, W.D. & Lister, G.S. 1986a. Dynamic recrystallization of minerals. *Geophysical Monograph, American Geophysical Union* 36, 161-199.

Urai, J.L., Spiers, C.J., Zwart, H.J. & Lister, G.S. 1986b. Weakening of Rock Salt by Water During Long-Term Creep. *Nature* 324(6097), 554-557.

Venables, J.A. & Harland, C.J. 1973. Electron back-scattering patterns - A new technique for obtaining crystallographic information in the scanning electron microscope. *Philosophical Magazine* 27(5), 1193-1200.

Vernon, R.H. 1976. *Metamorphic processes*. Murby, London.

von Mises, R. 1928. Mechanics of the ductile form changes of crystals. *Zeitschrift Fur Angewandte Mathematik Und Mechanik* 8, 161-185.

Wenk, H.R., Canova, G., Brechet, Y. & Flandin, L. 1997. A deformation-based model for recrystallization of anisotropic materials. *Acta Materialia* 45(8), 3283-3296.

White, S. 1976. Effects of Strain on Microstructures, Fabrics, and Deformation Mechanisms in Quartzites. *Philosophical Transactions of the Royal Society of London Series a-Mathematical Physical and Engineering Sciences* 283(1312), 69-&.

Wright, S. I. 1993. A review of automated orientation imaging microscopy. *Journal of Computer-Assisted Microscopy* 5(3), 207-221.

Wyon, G. & Crussard, C. 1951. Modifications de structure de l'aluminium au cours du fluage. *Rev. Metall.* 48, 1221-130.

Chapter 6*

CPO development in synthetic rocksalt during torsion up to large shear strains

This chapter describes the influence of shear strain on the development of crystallographic preferred orientations (CPOs) in synthetic rocksalt deformed at temperatures of 100-300°C. It furthermore correlates the observed CPOs with the microstructure formed during deformation.

Abstract

Torsion deformation experiments were performed on polycrystalline synthetic halite (NaCl) samples with water content above 9ppm up to shear strains of $\gamma \sim 8$ in order to investigate how microstructure and crystallographic preferred orientation (CPO) evolve with increasing temperature, shear strain rate and shear strain. The experiments were carried out at temperatures of 100°C, 200°C and 300°C, applying constant shear strain rates of $3 \times 10^{-5} \text{s}^{-1}$, $3 \times 10^{-4} \text{s}^{-1}$ and $3 \times 10^{-3} \text{s}^{-1}$ and a constant confining pressure of 250MPa. Microstructures were analysed using reflected light microscopy. Texture analyses were carried out by means of electron backscattered diffraction (EBSD).

At 100°C the microstructure comprises sheared elongated grains containing networks of blocky subgrains and slip bands. Dynamic recrystallisation in form of subgrain rotation recrystallisation occurs at shear strains $\gamma \geq 3$. The microstructure at 200 and 300°C is characterised over the whole shear strain range ($\gamma \sim 1$ to $\gamma \sim 8$) by polygonal subgrains and dynamically recrystallised grains resulting from grain boundary migration and subgrain rotation recrystallisation. Three main CPO types could be distinguished and are linked to the microstructure. At low shear strains ($\gamma \leq 3$) a shear deformation CPO develops that is characterised by two texture components: a strong $\{111\}\langle 110 \rangle$ and a weaker $\{001\}\langle 110 \rangle$ component. With increasing shear strain ($\gamma \geq 3$) a recrystallisation CPO with a single strong $\{001\}\langle 110 \rangle$ component develops. Grain growth leads to a slightly rotated $\{110\}\langle 1\bar{1}0 \rangle$ preferred orientation.

Keywords: Rocksalt, torsion, dynamic recrystallisation, texture, CPO, EBSD

6.1 Introduction

Crystallographic preferred orientations (CPOs) are a common feature in deformed rocks and are a useful tool as pointed out by Bons & den Brok (2000) for estimating the amount of strain, the temperature and/strain rate conditions during their formation, determination of the shear sense. CPOs can also provide information on the deformation kinematics. A CPO showing a monoclinic symmetry is interpreted as an indicator for simple shear, while pure shear results in an orthorhombic symmetry of the fabric (e.g. Wenk & Christie 1991).

* Paper to be submitted to Journal of Structural Geology (M.Armann, K. Kunze, L. Burlini and J.-P. Burg)

Generally, the presence of a CPO in a deformed rock is interpreted as an evidence for deformation by dislocation processes (e.g. Wenk 1985). The occurrence of a weak CPO in highly strained rocks is taken as evidence for diffusion creep and/or grain boundary sliding (e.g. Casey et al. 1998, Rutter et al. 1994), whereas a strong CPO on the other hand, indicates deformation by dislocation creep (e.g. Wenk & Christie 1991). However, Bons and den Brok (2000) postulated that solution-precipitation processes may also contribute to the formation of a CPO, and an increasing number of evidence is reported for CPOs formed in the grain-size sensitive creep field (Schmid et al. 1987, Goldsby & Kohlstedt 2001, Delle Piane et al. 2008).

Deformation in halite occurs on three families of slip systems: $\{110\}\{1\bar{1}0\}$, $\{100\}\{011\}$ and $\{111\}\{1\bar{1}0\}$ (e.g. Carter & Heard 1970). At low temperature these three systems have different critical resolved shear stresses (crss) with $\{110\}\{1\bar{1}0\}$ as the easiest slip system. This system comprises six crystallographic equivalent representatives, but only two of them are independent (e.g. Skrotzki et al. 1995, Wenk et al. 1997). This leads to difficulties in the deformation at low temperatures ($\leq 100^\circ\text{C}$), where the von Mises criterion (von Mises 1928) of five independent slip systems necessary for homogenous deformation of a polycrystalline aggregate is not fulfilled. In order to satisfy this criterion, the harder and subsidiary $\{100\}\{011\}$ and $\{111\}\{1\bar{1}0\}$ slip systems have to be activated simultaneously with the $\{110\}\{1\bar{1}0\}$ slip systems, which causes a high plastic anisotropy at low temperature (Skrotzki et al. 1995). At higher temperatures, however, the plastic anisotropy decreases and $\{110\}\{1\bar{1}0\}$ and $\{100\}\{011\}$ are equally active (Wenk et al. 1997).

Investigations on the deformation mechanisms and microstructure on rocksalt have been carried out extensively over the last years (e.g. Heard 1972, Carter & Hansen 1983, Carter et al. 1993, Franssen 1994, Ter Heege et al. 2005). Experiments on rocksalt are also of interest because salt domes are considered to offer a good storage medium for radioactive waste, other dangerous materials and for stratific storage of crude and/or natural gas. Data on the long term stability of rocksalt are therefore needed. However, only a few studies have dealt with the development of texture or CPOs in rocksalt (Kern & Braun 1973, Skrotzki and Welch 1983, Franssen & Spiers 1990, Franssen 1996, Skrotzki et al. 1996, Trimby et al. 2000, Lebensohn et al. 2003, Pennock et al. 2006). In these experiments no high strains were achieved.

In this study, we were interested in how the CPO evolves with large shear strain at different temperature and how dynamic recrystallisation will influence the development of preferred orientations. We conducted torsion experiments on synthetic rocksalt containing $>9\text{ppm}$ water up to shear strains (γ) of 8 and at temperatures of 100, 200 and 300°C . CPOs were measured on all deformed samples by means of electron backscatter diffraction (EBSD) and were evaluated using contoured pole and inverse pole figures.

6.2 Methods

6.2.1 Starting material

Analytical grade synthetic NaCl powder with grain size of about $500\mu\text{m}$ was uniaxially cold-pressed in a stainless steel canister at room temperature and ambient humidity. A uniaxial load of 40t was applied on a surface of 20cm^2 corresponding to about 200MPa. Afterwards, the material was annealed under a confining pressure of about 100MPa for one week at a temperature of 150°C . This procedure led to a large translucent cylinder of starting material

(synthetic aggregate of halite) whose typical grain size ranged between 150 and 300 μm . The density of the starting material measured with a pycnometer was 2.15g/cm³. From the measured density, the weight and the volume, a porosity of 0.6% was calculated. Fourier transform infrared spectroscopy (FTIR) was carried out to determine the water content of all samples.

6.2.2 Deformation experiments

Torsion experiments were performed in an internally heated (argon gas) high-pressure/high-temperature Paterson apparatus with a torsion set up installed at the rock deformation laboratory ETH Zürich. A detailed review of the apparatus and the deformation assembly is given in the work of Paterson & Olgaard (2000) and Pieri et al. (2001). The experiments to different shear strains were conducted at a confining pressure of 250MPa, at temperatures of 100, 200 and 300°C (0.35-0.53T_m) and at constant twist rates corresponding to shear strain rates of 3×10^{-3} , 3×10^{-4} and $3 \times 10^{-5} \text{s}^{-1}$ at the outer sample radius. Any volume element of the sample underwent simple shear deformation with direction and strain rate depending on the given position in the sample.

6.2.3 Microscopy and EBSD

For microstructural analysis, polished and etched sections were prepared from the deformed samples. Because we were interested in the high shear strain area of the sample and the amount of strain increases from zero at the centre of the cylindrical specimen to high shear strain at the sample margin, a flat surface was polished a few millimetres from the margin into the sample as shown in Fig. 6.1.

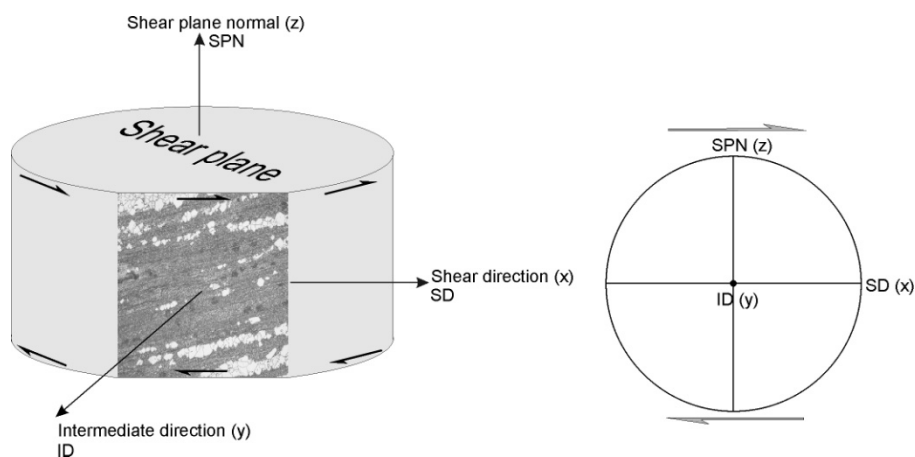


Fig. 6.1. Location of the polished section in the deformed sample and also shown the reference frame for EBSD analysis and for interpretation of pole figures.

Preparations of the deformed samples for light microscopy and EBSD analysis were done following the method described by Spiers et al. (1986) and by Urai et al. (1987). The samples were first polished and then etched for 4sec with a slightly undersaturated NaCl solution containing 8wt% FeCl₃·6H₂O. Etching was carried out to remove scratches obtained by mechanical polishing and to reveal the grain boundaries. The microstructures of the deformed

samples were analysed using an optical reflected light microscope. The reflected light images showed very detailed microstructures of the grains and of the subgrains.

The electron backscattered diffraction (EBSD) technique (Venables & Harland 1973, Dingley 1984, Prior et al. 1999) was used to obtain the texture and the hence the CPOs. EBSD is a very useful tool which allows the rapid measurement of the complete crystallographic orientation of any material (Trimby et al. 2000). The measurements were carried out at the Center for Electron Microscopy ETH Zürich (EMEZ), using a CamScan CS44 LB SEM. The polished section of the sample was coated with a 2nm thin carbon layer and the complete sample except the coated surface was covered with silver paint to minimise charging. The SEM operating parameters were: acceleration voltage of 15kV, working distance of 35mm, beam current of $\sim 2\text{-}3\text{nA}$, magnification of 100x, sample tilted 70° . Electron backscattered diffraction patterns (EBSP) were collected, indexed and analysed with the commercial TSL software OIM4 and OIM5. The texture measurements were obtained by scanning the sample surface with a step size of $10\ \mu\text{m}$ using a frame grid and a combined stage and beam scan. The number of measurements per run varied between $\sim 48'000\text{-}540'000$ data points depending on the size of the analysed sample area. The raw orientation data were rotated into a common reference frame with respect to the changing angle of the shear direction across the sample surface. The data sets were filtered to remove non-reliably indexed measurements by accepting only measurements with a confidence index (CI) >0.1 . Contoured pole figures and inverse pole figures were processed using a Gaussian convolution with a half width of 15° and a harmonic series expansion of $L=26$ and displayed as contour plots in multiples of uniform distribution (m.u.d). The reference frame for the sample and pole figures is shown in Fig. 6.1. The texture index J (Bunge 1985) was used to evaluate the strength of the CPO.

6.3 Results

6.3.1 Starting material

The starting material is characterised by polygonal grains with a grain size of $150\text{-}300\ \mu\text{m}$ (Fig. 6.2a). The grain boundaries are straight to gently curved. Grain triple junctions intersect at an angle of roughly of 120° . The grains show no internal deformation substructure. Overall, the starting material shows a statically recrystallised equilibrium foam structure. Secondary electron (SE) images (Fig. 6.2b) clearly show that porosity is present in form of pockets along grain boundaries forming a three dimensional network for fluid transport. The water content of the starting material, estimated by FTIR, was 35 ppm.

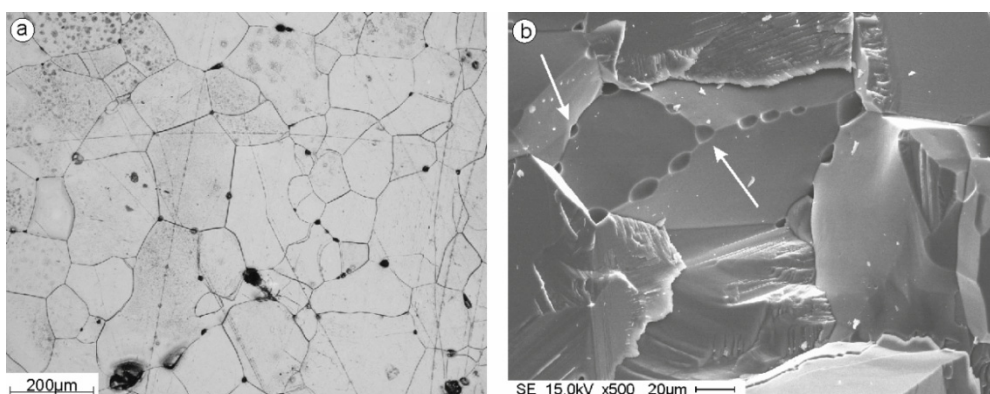


Fig. 6.2. a) Reflected light micrograph of the starting material showing the characteristic foam structure. b) SE image of a fractured block of the starting material showing linear arranged pores (white arrows) along grain boundaries.

6.3.2 Mechanical behaviour

The strength of the deforming rocksalt was inversely related to the temperature: highest at 100°C, lowest at 300°C. The data presented are not corrected for the strength of the copper jacket.

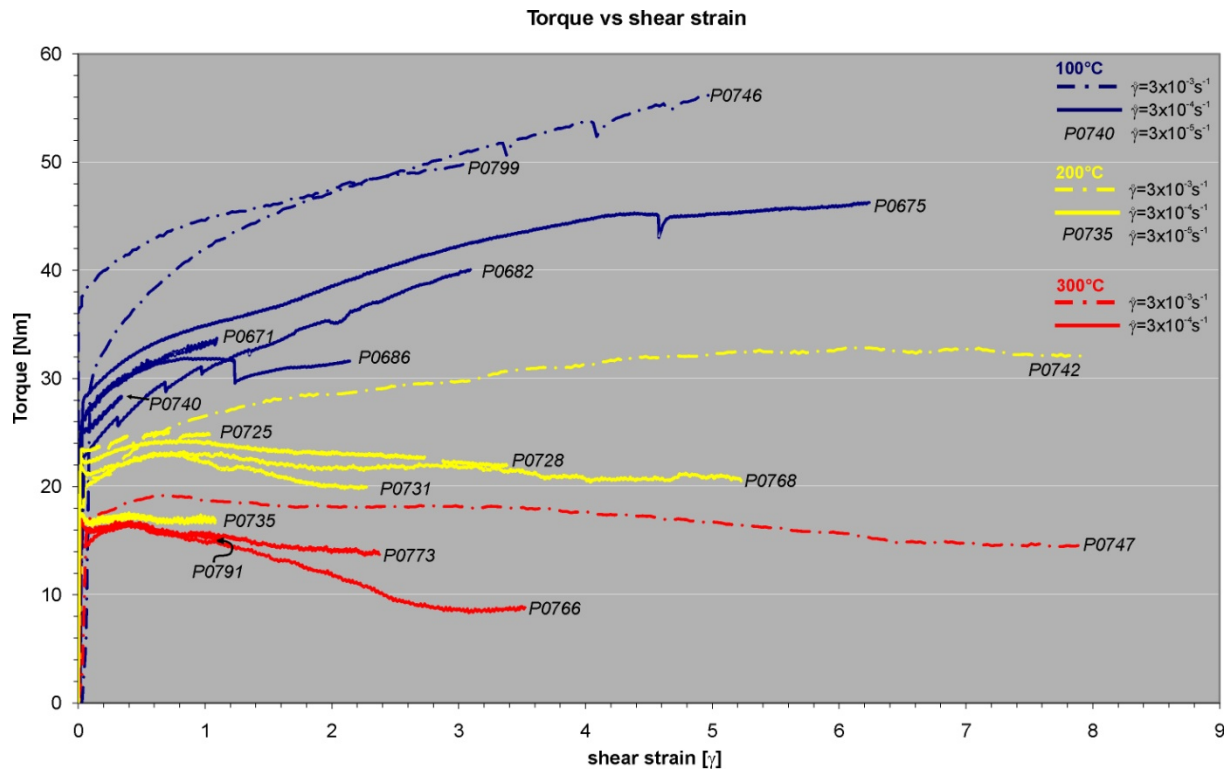


Fig. 6.3. Torque vs shear strain curves showing the mechanical behaviour of salt and copper jacket. Blue curves show experiments at 100°C, yellow curves for 200°C and red curves for 300°C. Data are not corrected for jacket strength.

Typical torque – shear strain curves for samples deformed in torsion are shown in Fig. 6.3. The corresponding experimental details of the performed tests are given in Table 6.1. At 100°C constant work hardening up to a shear strain of $\gamma \sim 5$ was observed. At a shear strain higher than $\gamma \sim 5$ the hardening rate is reduced. The torque is higher for the faster shear strain rates and for higher shear strain. At 200°C the material is weaker than at 100°C. After the apparent yield point for applied shear strain rates of 10^{-4} and 10^{-5} s^{-1} the material is work hardening to a shear strain of $\gamma \sim 0.5$ followed by weakening. By applying a faster shear strain rate of 10^{-3} s^{-1} the material shows a constant work hardening up to a shear strain of $\gamma \sim 4$ followed by steady state flow to the final shear strain of $\gamma \sim 8$. At 300°C the material shows a similar behaviour as at 200°C but with lower strength. The material starts to harden, reaches a peak strength and strain softening takes place after a shear strain of $\gamma \sim 0.5$ at strain rates of 10^{-3} s^{-1} and in the sample deformed at 10^{-4} s^{-1} at a shear strain of $\gamma \sim 1$.

Sample	length	diameter	Water content	T	Strain rate	Shear strain	Yield torque	Torque at finite strain	comments
	[mm]	[mm]	[%]	[°C]	[s ⁻¹]	[γ]	[Nm]	[Nm]	
P0740	9.6	14.8	47.9	100	3x10 ⁻⁵	0.3	25.0	28.3	
P0671	10.0	14.7	37.5	100	3x10 ⁻⁴	1.1	25.0	33.7	
P0686	9.9	14.7	30.2	100	3x10 ⁻⁴	2.1	25.9	31.6	stick slip
P0682	10.0	14.7	37.0	100	3x10 ⁻⁴	3.1	21.9	40.0	
P0675	10.1	14.8	95.5	100	3x10 ⁻⁴	6.3	27.8	46.2	stick slip
P0797	5.0	14.7	---	100	3x10 ⁻³	0.4	31.7	36.5	
P0799	5.1	14.8	15.3	100	3x10 ⁻³	3.1	37.5	59.8	
P0746	5.0	14.8	55.2	100	3x10 ⁻³	5.0	23.3	50.6	stick slip
P0735	9.8	14.8	36.7	200	3x10 ⁻⁵	1.1	17.7	16.9	
P0725	9.9	14.7	70.8	200	3x10 ⁻⁴	1.0	23.5	24.9	
P0731	10.0	14.8	29.6	200	3x10 ⁻⁴	2.3	20.3	20.0	
P0728	10.1	14.8	48.6	200	3x10 ⁻⁴	3.4	22.6	22.0	stick slip
P0768	9.1	14.8	20.1	200	3x10 ⁻⁴	5.2	22.0	20.	
P0742	5.0	14.8	64.0	200	3x10 ⁻³	7.9	21.3	32.1	
P0791	8.7	14.8	20.3	300	3x10 ⁻⁴	1.1	17.0	15.3	
P0773	9.5	14.8	12.9	300	3x10 ⁻⁴	2.4	16.9	13.8	
P0766	8.8	14.8	9.7	300	3x10 ⁻⁴	3.5	14.7	8.9	
P0747	5.1	14.8	32.1	300	3x10 ⁻³	7.9	17.7	14.7	

Table 6.1. Experimental conditions and results of torsion experiments on synthetic polycrystalline rocksalt. All experiments were performed at constant temperature, confining pressure of 250MPa and at a constant twist rate. Shear strain rates correspond to those at the rim of the sample. Water content of samples measured after deformation by means of FTIR, show that samples were "wet" (water contents >9ppm).

6.3.3 Microstructures

The microstructures developed in the deformed samples depend strongly upon temperature and the amount of shear strain.

100°C

Optical micrographs of samples deformed at 100°C are shown in Fig. 6.4. At 100°C and shear strains of $\gamma \leq 3$ the microstructure is characterised by sheared and elongated grains (Fig. 6.4a-d and 6.4f) in agreement with the finite strain ellipse. These grains contain blocky subgrains, thin etched lines and domain structures (cf. chapter 5). Grain boundaries are straight in grains containing no subgrains (P0740) and become serrated in grains containing subgrains. At $\gamma \sim 3$, the average grain size is similar to the grain size of the starting material (130-220 μm). At shear strains $\gamma \geq 3$ the grain size decreases to values of 25 μm . The highest shear strain sample (P0675, $\gamma \sim 6$, Fig. 6.5e) consists of two characteristic features:

- i) a matrix of small new formed grains (average 25 μm). The size of the smallest grains ($\sim 4\mu\text{m}$) is similar to the size of the subgrains ($\sim 4\mu\text{m}$) formed at low shear strain. The previous grain elongation and grain boundaries form a visible foliation close to the shear plane.
- ii) new grains, slightly larger in size (50-80 μm), show sometimes a rhombic but always idiomorphic shape and appear in bands subparallel to the shear plane. These idiomorphic and deformation substructure free grains seemed to be formed along initial grain boundaries.

Sample P0746 (Fig. 6.4g) deformed to a shear strain of $\gamma \sim 5$ is characterised by larger polygonal grains (size between 80-200 μm) with straight grain boundaries and grains that meet at triple junctions of $\sim 120^\circ$, similar to the microstructure of the starting material. Within these polygonal grains, trails or patches are left comprising grains that are much smaller ($< 40\mu\text{m}$) than the surrounding polygonal grains. Here, the grain shapes are not in agreement with the finite strain ellipse.

200°C

The microstructure for samples deformed at 200°C series is shown in Fig. 6.5. The sample (P0735) deformed slowly to a shear strain of $\gamma \sim 1$ (Fig. 6.5a) is characterised by large ($\sim 500\mu\text{m}$) substructure free grains with straight or bulged grain boundaries. Besides these grains, the sample shows grains containing subgrains and some irregularly shaped grains with a weak deformation substructure. The microstructure of samples with a finite shear strain of $\gamma \sim 1$ to $\gamma \sim 3$ (Fig. 6.5b-d) are dominated by grains containing networks of polygonal subgrains. The grain boundaries show a cusped/lobate structure. The cusps and lobes trace thereby the shape of the subgrains flanking the grain boundary. Smaller grains occur in these samples and exhibit bulged grain boundaries and subgrains. However, grains containing hardly any deformation substructure are also observed. In the samples deformed to shear strains $\gamma \geq 5$ (Fig. 6.5e-f), the grain size decreased to $\sim 48\mu\text{m}$ (P0768) and to $36\mu\text{m}$ (P0742). The new formed grains show a uniform grain size that is most pronounced in the high shear strain sample ($\gamma \sim 8$, Fig. 6.5f).

300°C

The optical micrographs of samples deformed at 300°C are shown in Fig. 6.6. The sample deformed to a finite shear strain of $\gamma \sim 1$ is characterised by large grains (Fig. 6.6a). Some of these grains exceed a size of 1mm without any internal substructure. Only a few spots are occupied by deformed grains containing polygonal subgrains. Samples deformed to shear strains from $\gamma \sim 2$ to $\gamma \sim 8$ (Fig. 6.6b-d) show a microstructure that consists of irregularly shaped grains containing polygonal subgrains and by grains without deformation substructure. However, the maximum grain size of these samples is smaller than at $\gamma \sim 1$.

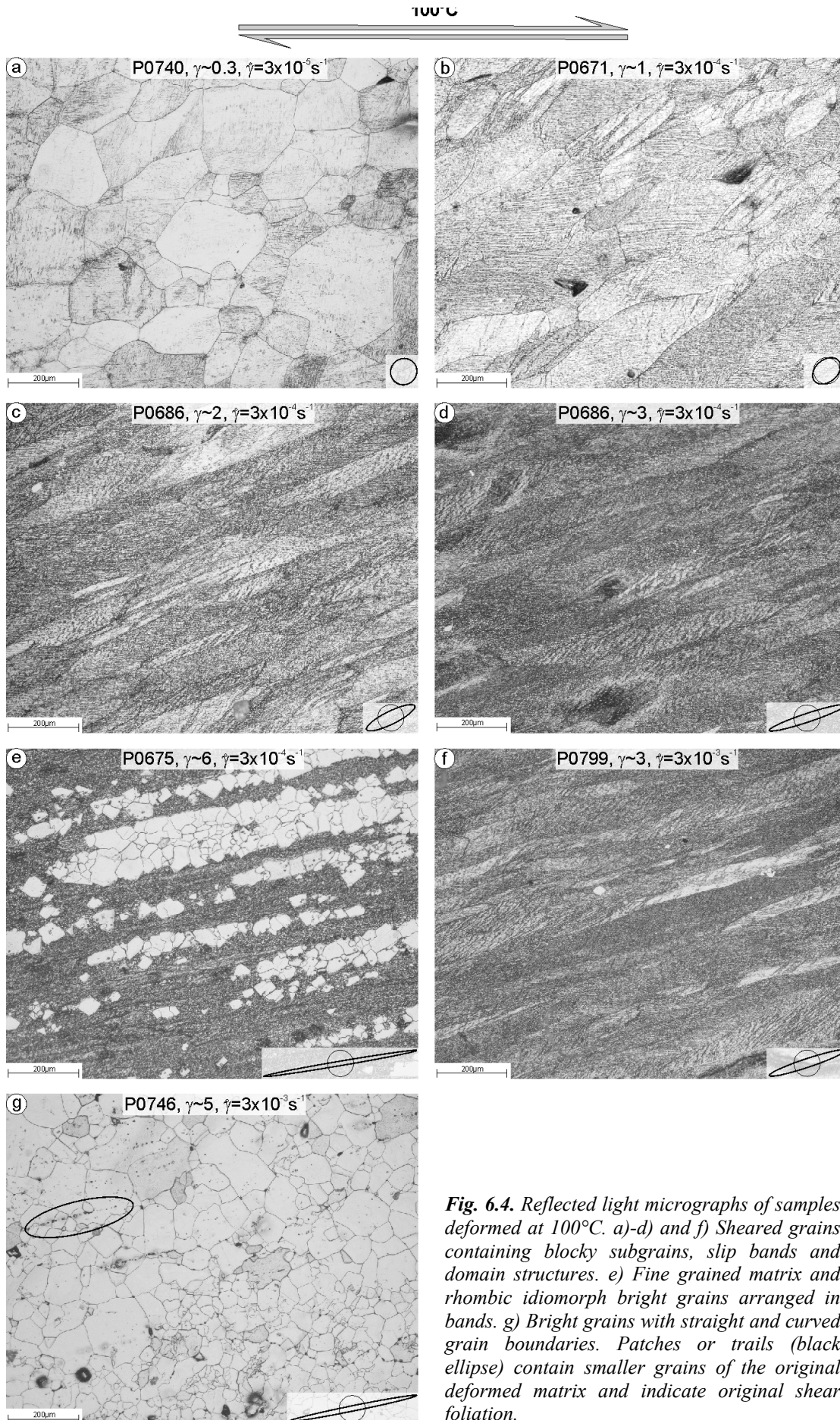


Fig. 6.4. Reflected light micrographs of samples deformed at 100°C. a)-d) and f) Sheared grains containing blocky subgrains, slip bands and domain structures. e) Fine grained matrix and rhombic idiomorph bright grains arranged in bands. g) Bright grains with straight and curved grain boundaries. Patches or trails (black ellipse) contain smaller grains of the original deformed matrix and indicate original shear foliation.

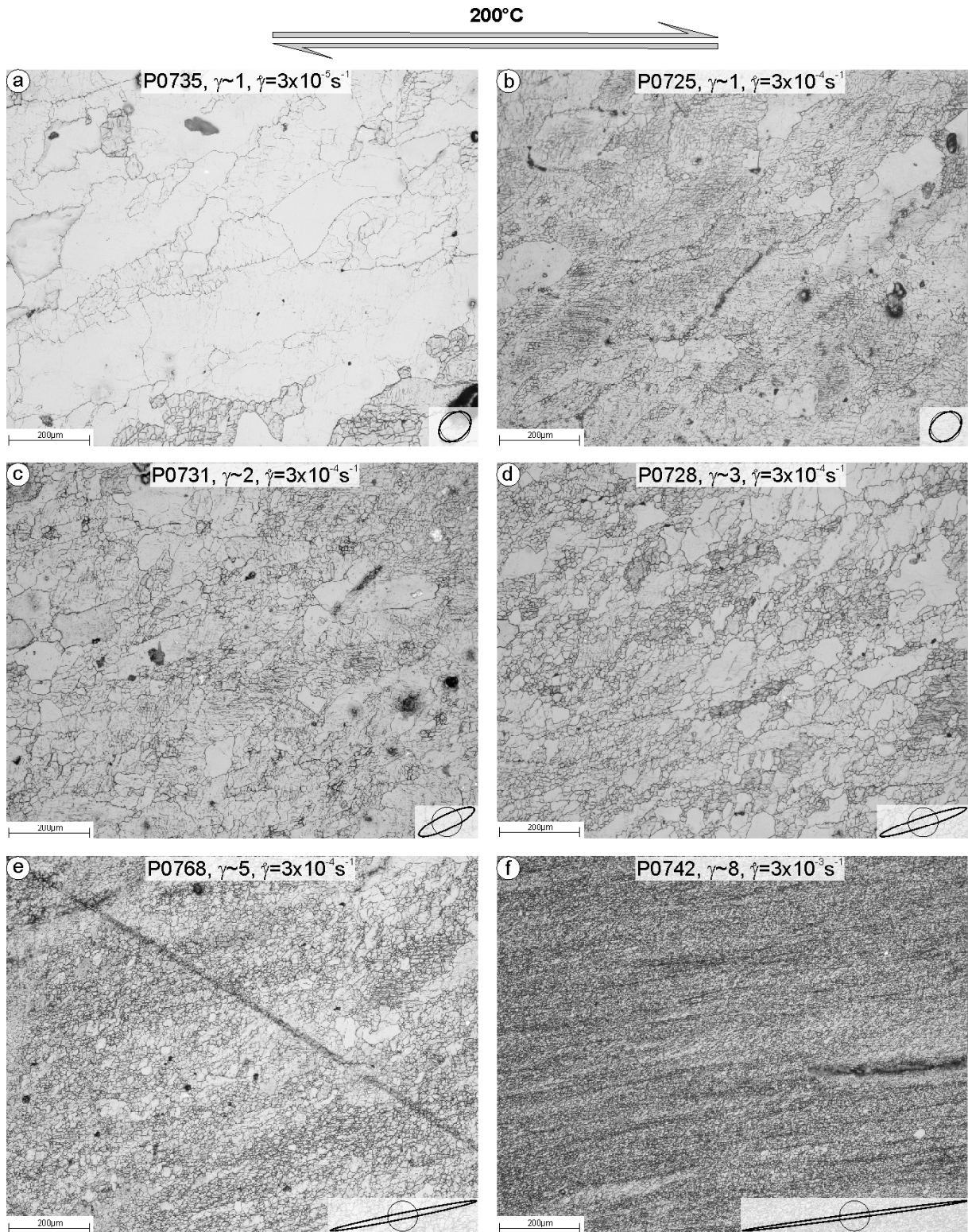


Fig. 6.5. Reflected light micrographs of samples deformed at 200°C. *a)* Large bright grains indicating grain growth. *b-c)* Sheared grains with cusped and lobate grain boundaries containing polygonal subgrains. *d)* Irregular shaped grains with bulged grain boundaries and subgrains. *e)* New formed grains containing subgrains, irregular shaped and smaller in grain size. *f)* Fine grained mylonitic microstructure.

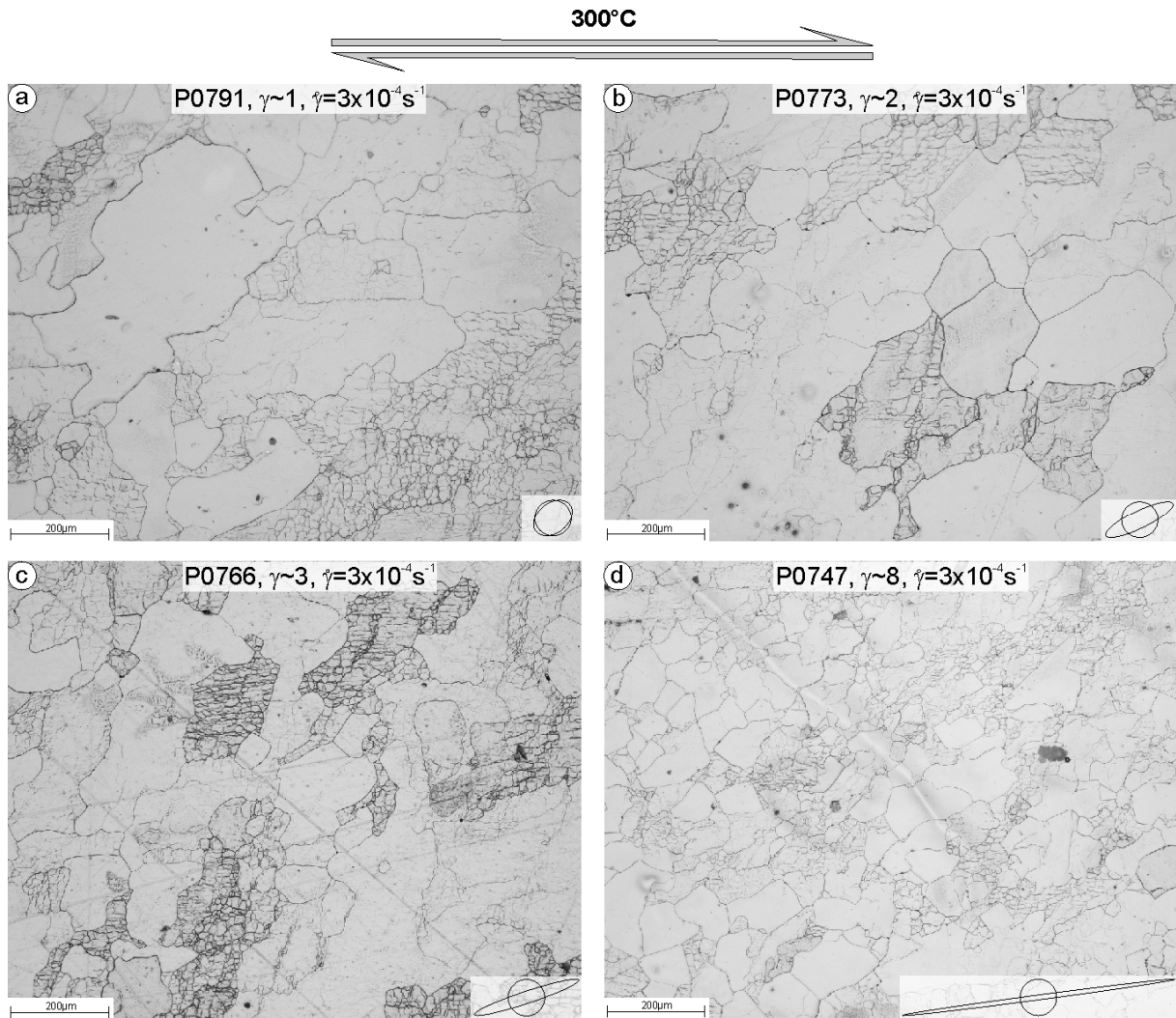


Fig. 6.6. Reflected light micrographs of samples deformed at 300°C. a-d) Grain growth (bright grains) dominates microstructure, also new formed grains with subgrains are present.

6.3.4 CPOs

The pole figures for the starting material (Fig 6.7) show a near randomly distributed CPO with a J index of 1.02.

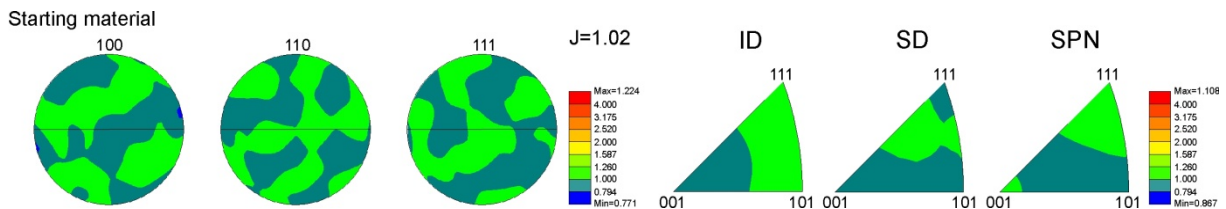


Fig. 6.7. Pole figures and inverse pole figures for the starting material indicating a near randomly distributed CPO.

Pole figures showing the poles to the {100}, {110} and {111} planes and inverse pole figures for intermediate direction (ID), shear direction (SD) and shear plane normal (SPN) for all analysed samples with the corresponding temperature, shear strain and shear strain rate are shown in Fig. 6.8-6.10. Details of the scanned area, the indexed points, the number of grains, the strength of the CPO (J-index) and the CPO type are presented in Table 6.2.

Sample	T	Strain rate	Shear stain	Size OIM map	Average CI	Data points	J index	CPO type
	(°C)	(s ⁻¹)	(γ)	(mm)		(CI>0.1)		
Starting				6x7	0.49	377 249	1.02	random
P0740	100	3x10 ⁻⁵	0.34	4x9	0.61	328 440	1.08	SD
P0671	100	3x10 ⁻⁴	1.09	6x8	0.55	424 744	1.30	SD
P0686	100	3x10 ⁻⁴	2.15	7x7	0.43	244 469	1.43	SD
P0682	100	3x10 ⁻⁴	3.09	7x7	0.29	129 075	1.44	SD
P0675	100	3x10 ⁻⁴	6.24	6x8	0.35	132 477	1.24	Rx & GG
P0799	100	3x10 ⁻³	3.43	4x5	0.24	48 393	1.55	SD & Rx
P0746	100	3x10 ⁻³	5.3	7x5	0.55	290 646	1.09	? GG?
P0735	200	3x10 ⁻⁵	1.08	6x10	0.52	544 391	1.54	GG
P0725	200	3x10 ⁻⁴	1.03	6x9	0.50	432 825	1.28	SD
P0731	200	3x10 ⁻⁴	2.27	7x8	0.42	445 720	1.39	GG & SD
P0728	200	3x10 ⁻⁴	3.38	6x9	0.49	439 482	1.45	Rx
P0768	200	3x10 ⁻⁴	5.23	3x7	0.46	161 858	1.75	Rx
P0742	200	3x10 ⁻³	7.90	6x5	0.26	112 250	2.31	Rx
P0791	300	3x10 ⁻⁴	1.11	5x8	0.66	383 027	1.94	GG
P0773	300	3x10 ⁻⁴	2.38	3x9	0.64	258 168	1.58	C
P0766	300	3x10 ⁻⁴	3.52	5x7	0.64	329 713	1.41	C
P0747	300	3x10 ⁻³	7.92	6x4	0.51	208 814	1.60	C

Table 6.2. Details from orientation analysis of the investigated samples. Orientation imaging maps (OIM maps) are derived from EBSD scans at the outer margin of the sample. Number of grains were calculated by the OIM 5 software, edge grains were excluded from analysis. J-index was also calculated by the OIM 5 software. CPO type abbreviations are, SD = shear deformation CPO, Rx = recrystallisation CPO, GG = grain growth CPO and C = composite CPO.

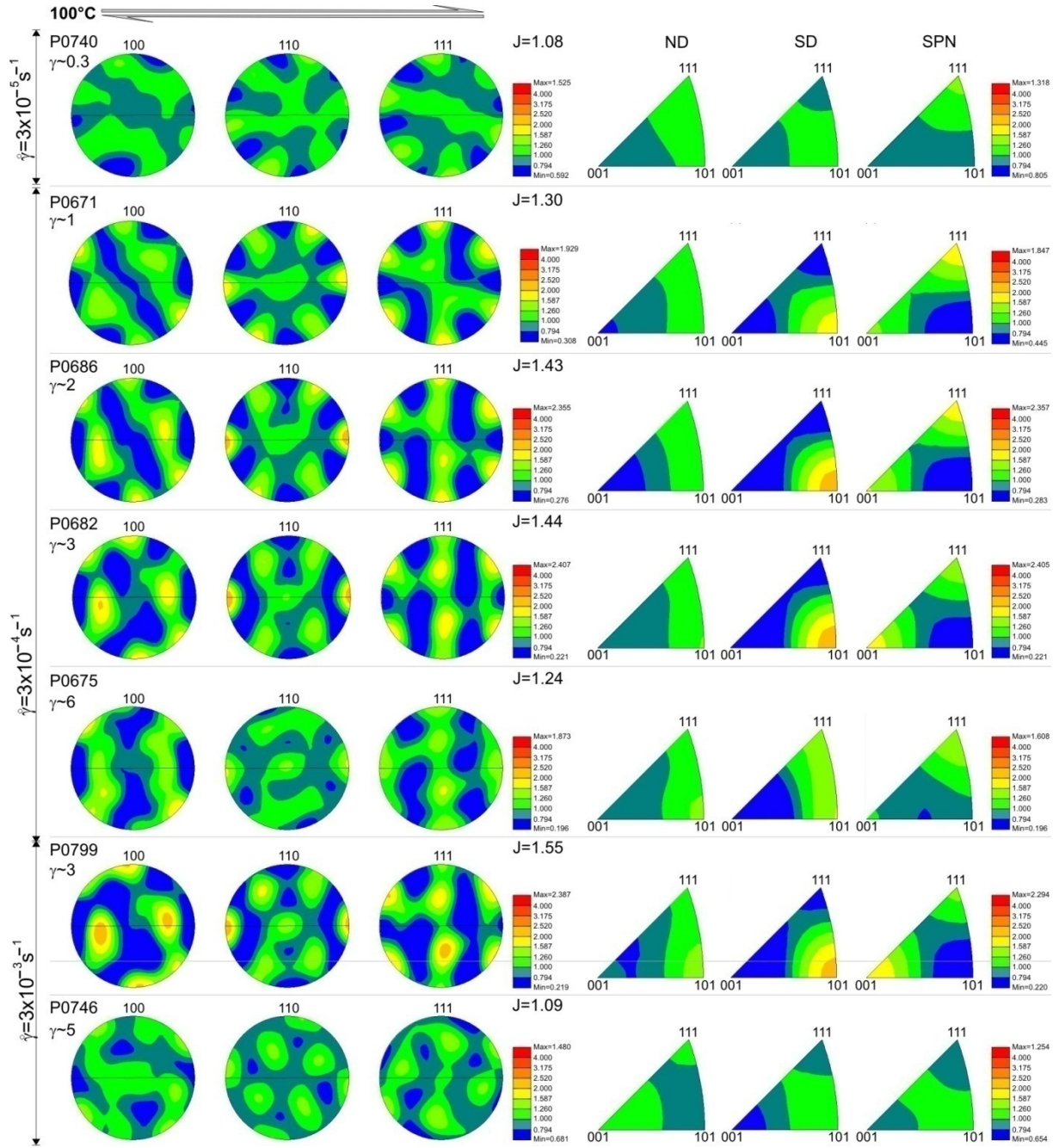


Fig. 6.8. CPO of samples deformed at 100°C and strain rates at $3 \times 10^{-5} s^{-1}$ to $3 \times 10^{-3} s^{-1}$. Contoured pole and inverse figures are displayed.

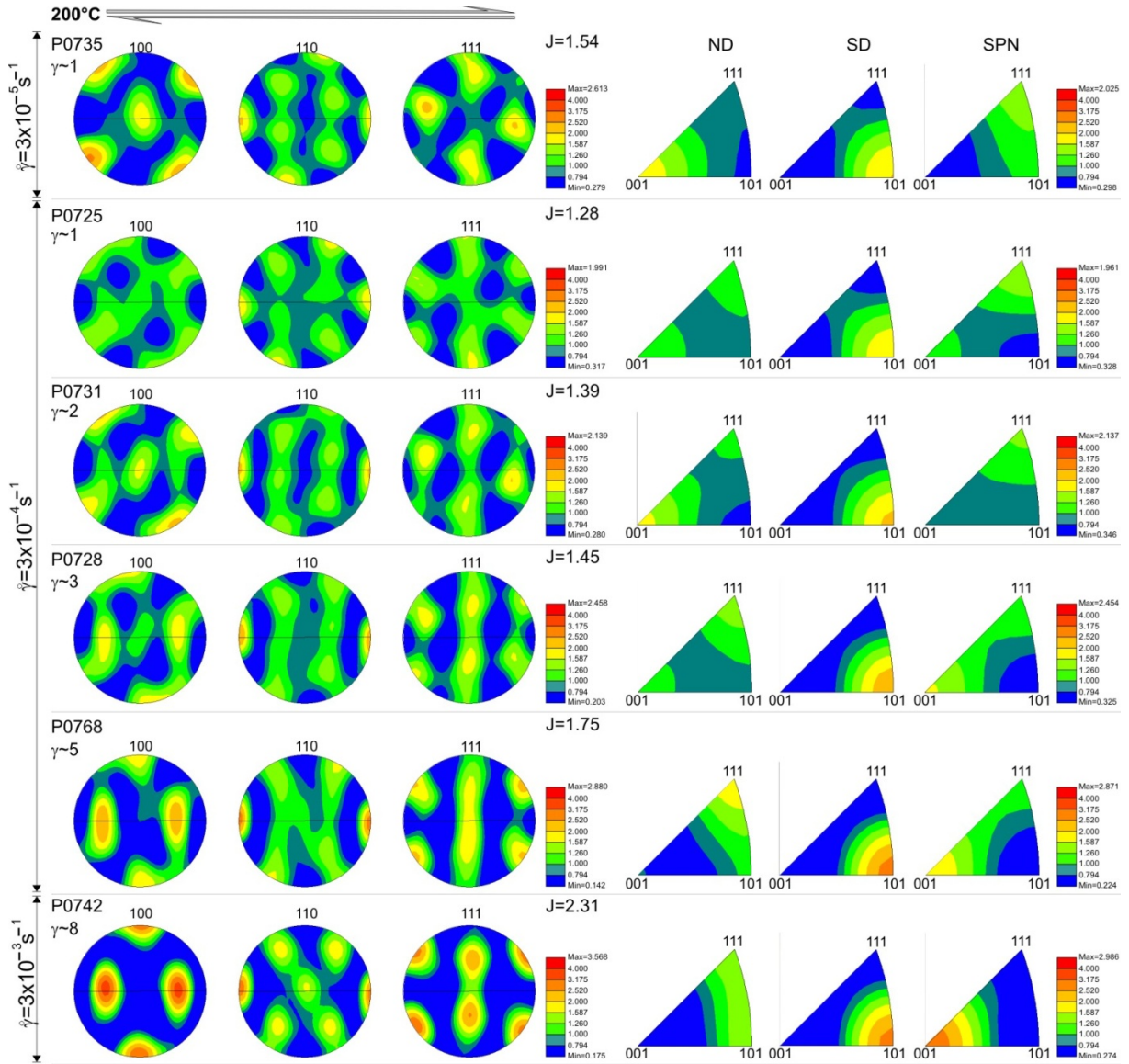


Fig. 6.9. CPOs of samples deformed at 200°C and to strain rates at $3 \times 10^{-5} \text{ s}^{-1}$ to $3 \times 10^{-3} \text{ s}^{-1}$. Contoured pole and inverse figures are displayed.

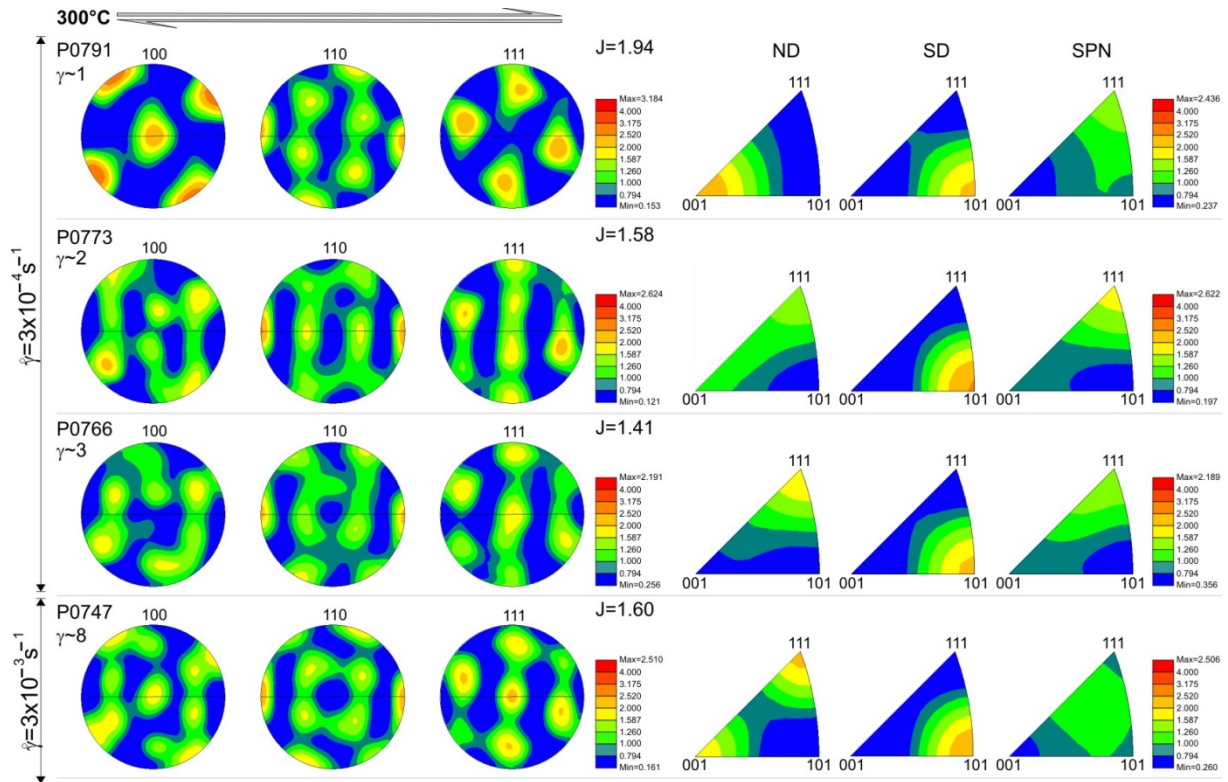


Fig. 6.10. CPOs of samples deformed at 300°C and to strain rates at $3 \times 10^{-5} \text{ s}^{-1}$ to $3 \times 10^{-3} \text{ s}^{-1}$. Contoured pole and inverse figures are displayed.

Three main CPO types were recognised, and will be described in the following section:

Fig. 6.11 shows an example (P0671) for the CPO that developed at 100°C (cf. Fig. 6.8) up to a shear strain of $\gamma \sim 3$ in samples P0671, P0686 and P0682 and at 200°C at a shear strain of $\gamma \sim 1$ in sample P0725. The CPO is characterised by two $\{100\}$ maxima. One maximum is oblique to the shear direction and to the shear plane, aligned opposite to the sense of shear, whereas the second maximum is normal to the shear plane. The $\{110\}$ maxima show different strengths around the pole figure periphery with the strongest maximum parallel to the shear direction. Poles to $\{111\}$ are aligned around the pole figure periphery with three equally strong maxima. The symmetry of the CPO is monoclinic.

The inverse pole figures show preferentially a $[101]$ direction of grains near the shear direction. The shear plane coincides preferentially with either (111) or (100) planes. This type of CPO consists of two components, a pronounced $\{111\}\langle 110 \rangle$ component and a weaker $\{001\}\langle 110 \rangle$ component.

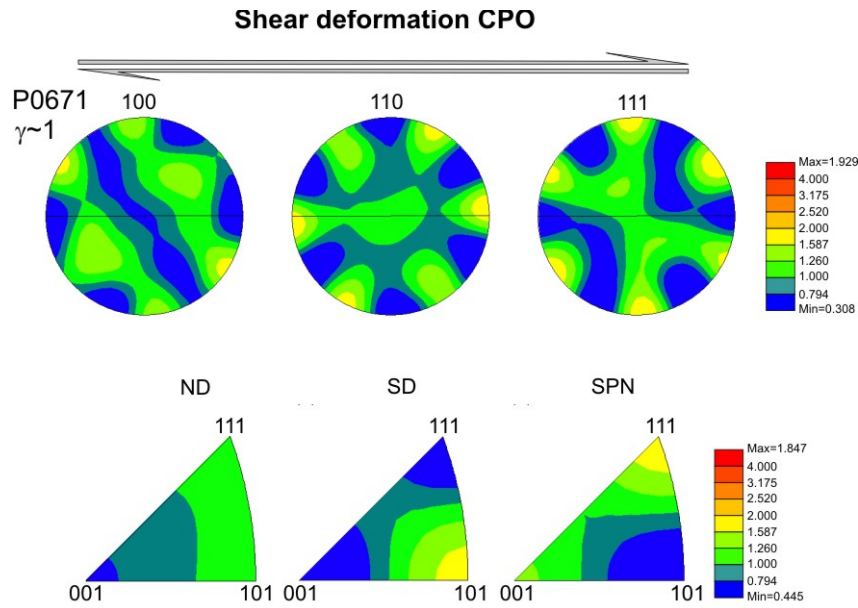


Fig. 6.11. Shear deformation CPO. Characteristic CPO developed at low shear strains, as an example the CPO for P0671 ($\gamma \sim 1$) at 100°C is shown.

At shear strains of $\gamma \geq 3$ at 100 and at 200°C the CPO (cf. Fig. 6.9) is characterised by a strong $\{100\}$ maximum normal to the shear plane and a strong $\langle 110 \rangle$ maximum parallel to the shear direction. Poles to $\{111\}$ show several maxima with different strengths around the pole figure periphery and further inside. This CPO is strongest and best developed in the high shear strain sample (P0742, $\gamma \sim 8$) at 200°C (Fig. 6.12). The CPO shows an orthorhombic symmetry.

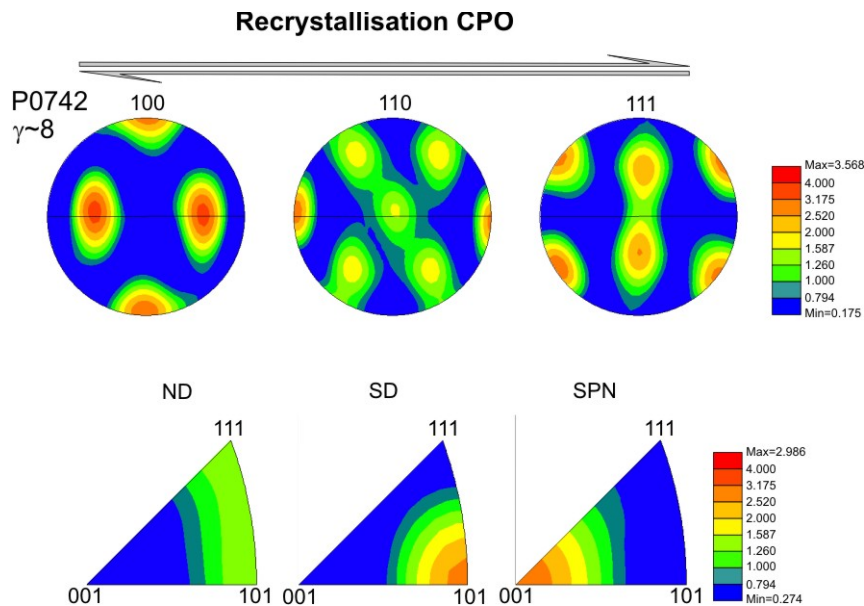


Fig. 6.12. Recrystallisation CPO. Characteristic CPO developed at high shear strains, as an example the CPO for P0742 $\gamma \sim 8$, at 200°C is shown.

Inverse pole figures show that grains are preferentially aligned with $[101]$ parallel to the shear direction and with $[001]$ normal to the shear plane. This results in a single $\{001\}\langle 110\rangle$ texture component.

In three samples (P0735, P0731 and P0791, Fig. 6.9 and Fig. 6.10) a third type of CPO developed. This CPO (example is shown in Fig. 6.13) is characterised by two $\{100\}$ maxima at about 45° between the shear direction and the shear plane normal. As the maxima are rotated with the sense of shear from the symmetric 45° position, the CPO shows a monoclinic symmetry. The inverse pole figures show that grains with a $[101]$ axis are preferentially aligned in the shear direction as well as normal to the shear plane (besides of $[111]$ occupation) and a $[001]$ axis parallel to the intermediate direction of the sample. This CPO type is characterised by a slightly rotated $\{110\}\langle 110\rangle$ texture component.

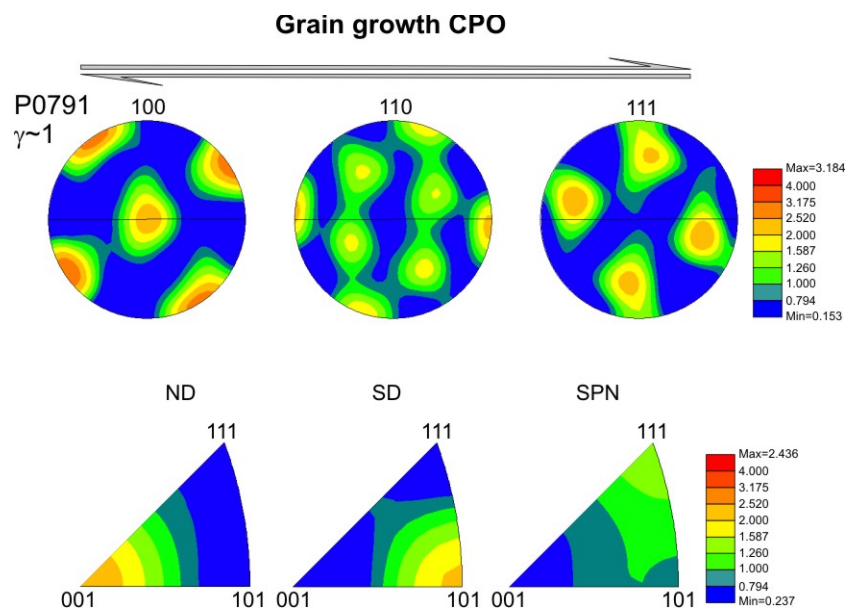


Fig. 6.13. Grain growth CPO. Characteristic CPO developed in samples showing large new grains, as an example the CPO for P0791, at 300°C is shown.

A fourth type of CPO (an example is shown in Fig. 6.14) contains components of the three already described CPO types and is called here composite CPO. The CPO shows a monoclinic symmetry and is characterised by two $\{100\}$ maxima at 45° between shear direction and shear plane and a second weaker $\{100\}$ maximum perpendicular to the shear plane. The pole figure for $\{110\}$ shows several maxima aligned around the pole figure periphery with one pronounced maximum aligned parallel to the shear direction. The maxima for $\{111\}$ are aligned further inside of the pole figure. The inverse pole figures show that grains are preferentially aligned with $[111]$ and $[001]$ in the intermediate direction and grains with $[101]$ parallel to the shear direction. Composite CPOs occur in sample P0746 deformed at 100°C and in samples deformed to a shear strain of $\gamma \sim 2$ to $\gamma \sim 8$ at 300°C .

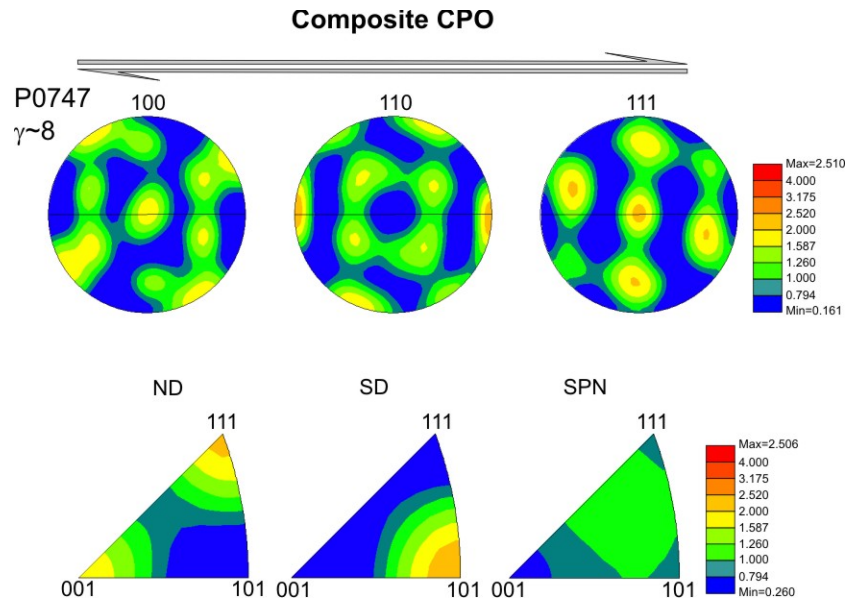


Fig. 6.14. Composite CPO. Characteristic CPO developed preferable in samples deformed at 300°C, as an example the CPO for P0747, at 300°C is shown.

6.4 Discussion

The results show that the microstructure and the CPO experienced an evolution with increasing shear strain and with increasing temperature. The evolution from a shear deformation mode into a recrystallisation regime is presumably controlled by the kinetics of recrystallisation processes. The presence of subgrains, slip bands and the occurrence of crystallographic preferred orientations indicate that deformation of rocksalt at the investigated temperatures and shear strain range occurred by dislocation processes.

6.4.1 Deformation and recrystallisation mechanisms

Deformation

The low shear strain microstructure is characterised by the formation of subgrains and slip bands with sometimes a wavy character. Blocky subgrains formed at 100°C are a result of pencil glide as discussed in chapter 5. The formation of polygonal subgrains at 200 and 300°C suggests that recovery processes, i.e. the climb of edge dislocations were active at elevated temperature. The linear etch lines can be viewed as slip bands (cf. chapter 5) caused by the glide of dislocations in a crystallographic glide plane. The wavy character of the thin etched lines in rocksalt has been interpreted as cross-slip of screw dislocations on $\{100\}$ and $\{111\}$ planes, bridging parallel $\{110\}$ slip planes (Skrotzki and Liu 1982, Senseny et al. 1992, Carter et al. 1993).

Dynamic recrystallisation

The formation of new grains during deformation is called dynamic recrystallisation (Hobbs 1968, Hobbs et al. 1982, Urai et al. 1986a). The result of dynamic recrystallisation is the alteration of the deformation microstructure. The formation of new irregularly shaped grains with subgrains and/or slip bands is an evidence that recrystallisation in the samples occurred synkinematically, i.e. during deformation. Usually, two dynamic recrystallisation mechanisms can be distinguished (Drury and Urai 1990): subgrain rotation recrystallisation and grain boundary migration recrystallisation. Subgrain rotation recrystallisation involves the progressive misorientation of low angle subgrain boundaries into high-angle boundaries. The formation of new grains with grain sizes similar to the subgrain size at 100°C and at 200°C at shear strains $\gamma \geq 3$ suggests that subgrain rotation recrystallisation occurred. Grain boundary migration recrystallisation causes the grain boundary to move from a grain with no internal strain energy into neighbouring grains with higher internal strain energy (e.g. Poirier 1985, Humphreys and Hatherly 2004). Irregularly shaped grains with bulged or lobate grain boundaries, especially at 200 and 300°C indicate that grain boundary migration occurred. Grain boundary migration recrystallisation is a major component in samples deformed at these temperatures and is rather absent at 100°C. This can be explained by the increase of the grain boundary mobility with temperature (Drury and Urai 1990, Humphreys and Hatherly 2004, Piazzolo et al. 2006). Dynamic recrystallisation by grain boundary migration leads to an increase in the mean grain size with respect to starting material, due to removal of grains containing a dense substructure by grains with little substructure as shown by Ter Heege et al. (2005).

Static recrystallisation

Static recrystallisation, also called secondary recrystallisation, takes place after deformation (Humphreys and Hatherly 2004). Idiomorphic and sometimes rhombic shaped grains (as in sample P0675) that show no deformation structure and exhibit straight grain boundaries, suggests that these grains formed after deformation. The large ($>500\mu\text{m}$) grains at 200 and 300°C indicate rapid grain growth. This grain growth can have several reasons. The cause for the grain growth at 200 and 300°C may be the heating time period prior to deformation. This pre-heating may have caused a grain growth of the starting material to a larger grain size prior to deformation, which may have an effect on the deformation microstructure later. The large grains size that occurred in sample P0735 deformed at 200°C and sample P0791 deformed at 300°C may thus be caused by the pre-heating history of the sample. Another point to consider is the latent heat during the quenching period. The cooling period for samples deformed at 300°C is longer as for samples deformed at lower temperature. This can additionally lead to grain growth after deformation and can be an explanation for the grain growth microstructure at 300°C. Grain growth that occurred in the two samples deformed at 100°C might be caused by the release of the high internal stored strain energy, shortly after deformation stopped.

6.4.2 CPO

The occurrence of a CPO is related to the activity and the alignment of grains with certain slip system(s) with respect to the imposed deformation mode. NaCl deforms by slip on {110}, {100} and {110} planes in $\langle 110 \rangle$ direction (Carter and Heard 1970). The easiest slip system activated is the slip system with the lowest critical resolved shear stress (crss). For rocksalt at

low temperature the easiest slip system is $\{110\}\langle 1\bar{1}0\rangle$, while $\{100\}\langle 011\rangle$ and $\{111\}\langle 1\bar{1}0\rangle$ have a higher crss and are subordinate at low temperature (100°C). With increasing temperature $\{110\}\langle 1\bar{1}0\rangle$ and $\{100\}\langle 011\rangle$ become more equally active (e.g. Wenk et al. 1997).

The obtained CPOs in this study indicate that grains do not align preferentially with the easiest slip system in a so called "easy-glide" orientation, which would mean that one $[110]$ axis is parallel to the shear direction, and another one normal to the shear plane. Instead, at low shear strains two texture components developed that suggest grains are oriented that either the $\{111\}\langle 1\bar{1}0\rangle$ or the $\{100\}\langle 011\rangle$ slip systems are active and suitable aligned. However, the model of "easy-glide" preferred orientations may not be applicable here, were the easiest slip system has only two independent variants and the subordinate harder $\{100\}\langle 011\rangle$ and $\{111\}\langle 1\bar{1}0\rangle$ with three and five independent variants respective, have to be activated simultaneously as pointed out by Skrotzki et al. (1995) and by Wenk et al. (1997).

The observed monoclinic symmetry is considered to represent the simple shear geometry (Wenk and Christie 1991). This CPO type is characteristic for samples that show a microstructure which consists of sheared elongated grains containing subgrains which in turn display the shear deformation. The CPO developed in these samples is therefore called a shear deformation CPO. The CPO developed at high shear strains and occurred due to recrystallisation mechanisms, and is called recrystallisation CPO. The CPO with a slightly rotated $\{110\}\langle 110\rangle$ component developed in samples (P0735 and P0791) which were characterised by grain growth, and is therefore called a grain growth CPO.

The CPO developed especially in samples at 300°C differs from the previous discussed CPOs. The microstructure of the corresponding samples consists of deformed grains including subgrains, dynamically recrystallised grains and statically recrystallised grains. Because the CPO represents components of deformation ($\{111\}\langle 110\rangle$), recrystallisation ($\{001\}\langle 110\rangle$) and grain growth ($\{110\}\langle 110\rangle$) and is called a composite CPO.

Texture development on halite has been examined by a number of authors (Kern and Braun 1973, Skrotzki and Welch 1983, Franssen and Spiers 1990, Franssen 1994, Skrotzki et al. 1995, Trimby et al. 2000, Ter Heege et al. 2005, Pennock et al. 2006). Only Franssen and Spiers (1990) carried out experiments in simple shear at 250-350°C that are comparable with the deformation mode in this study. All other experiments were carried out in compression, extension or pure shear. For this reason we would like to focus on the comparison with the simple shear experiments by Franssen and Spiers (1990). In their set of experiments the shear direction and the shear plane normal were exchanged which was later corrected by Franssen (1996). The corrected inverse pole figures for experiments carried out between 300 and 550°C to shear strains of $\gamma \sim 1$ indicate as well that a $\{100\}\langle 110\rangle$ and $\{111\}\langle 110\rangle$ component developed. This is in agreement with the shear deformation CPO developed in this study at low shear strains and at temperatures of 100 and 200°C. However, in our experiments at 300°C, instead of a shear deformation CPO as observed by Franssen (1990, 1996) a grain growth CPO developed. The development of this grain growth CPO in the samples deformed in this study may have several reason. First, the experiments by Franssen (1996) were carried out on dry rocksalt, whereas our salt samples contained a significant amount of water. The grain boundary mobility in dry salt is suppressed by the fact that no water is present. Second, the grain growth CPO in this study is mainly a static grain growth feature that occurred during quenching after deformation had stopped.

6.4.3 Effect of strain

An increase in strain clearly has an effect on the microstructure and hence on the CPO development. With increasing shear strain the CPO symmetry changes from monoclinic into orthorhombic. This transition can be seen in the pole figures of samples deformed to a shear strain of $\gamma \sim 3$ at 100 and 200°C (cf. Fig. 6.8 and Fig. 6.9), where the $\{111\}\langle 110 \rangle$ texture component representing shear deformation reduces, while the $\{001\}\langle 110 \rangle$ texture component representing recrystallisation strengthens. The change in the CPO can be well related to the microstructure, where a change from a deformation microstructure to a dynamic recrystallisation microstructure at 100 and 200°C occurred.

6.5 Conclusions

We have performed torsion experiments on wet synthetic rocksalt samples in the temperature range 100-300°C and at strain rates of 10^{-5} - 10^{-3} s⁻¹ to different shear strains. Our results show that microstructure and CPO go through an evolution with increasing shear strain, shear strain rate and temperature.

- The microstructure at 100 and 200°C changed from a deformation microstructure at low strain characterised by sheared grains including networks of polygonal subgrains into a dynamic recrystallisation microstructure at large strains. The transition takes place at a shear strain of $\gamma > 3$. Dynamic recrystallisation is dominant at 300°C from low shear strains to high shear strains.
- The CPO records the evolution from a monoclinic shear deformation texture with a strong $\{111\}\langle 110 \rangle$ and a weaker $\{001\}\langle 110 \rangle$ components to a recrystallisation texture indicated by a orthorhombic symmetry with a single $\{001\}\langle 110 \rangle$ component. A third type of CPO develops during grain growth and shows a slightly rotated $\{110\}\langle 110 \rangle$ component.
- Dynamic recrystallisation in form of subgrain rotation recrystallisation occurs predominately at lower temperature (100 and 200°C) and shear strains $\gamma \geq 3$ whereas grain boundary migration is pervasive at elevated temperatures (300°C).
- Temperature has clearly an effect on the microstructure during deformation, but it also changes the microstructure significantly after the experiment, especially at 300°C.

6.6 References

- Bons, P.D. & den Brok, B. 2000. Crystallographic preferred orientation development by dissolution-precipitation creep. *Journal of Structural Geology* 22(11-12), 1713-1722.
- Bunge, H.J. 1985. Representation of preferred orientations. In: *Preferred orientations in deformed metals and rocks: An introduction to modern texture analysis* (edited by Wenk, H. R.). Academic Press, Orlando, 73-108.
- Carter, N.L. & Hansen, F.D. 1983. Creep of Rocksalt. *Tectonophysics* 92(4), 275-333.

- Carter, N.L. & Heard, H.C. 1970. Temperature and Rate Dependent Deformation of Halite. *American Journal of Science* 269(3), 193-&.
- Carter, N.L., Horseman, S.T., Russell, J.E. & Handin, J. 1993. Rheology of Rock-Salt. *Journal of Structural Geology* 15(9-10), 1257-1271.
- Casey, M., Kunze, K. & Olgaard, D.L. 1998. Texture and microstructure for Solnhofen limestone deformed to high strains in torsion. *Journal of Structural Geology* 20, 255-268.
- Delle Piane, C., Burlini, L, Kunze, K., Brack, P. & Burg, J.-P. 2008. Rheology of dolomite: large strain torsion experiments and natural examples. *Journal of Structural Geology* 30, 767-776.
- Dingley, D.J. 1984. On-line determination of crystal orientation and texture determination in an SEM. *Proceedings of the Royal Society of London* 19, 74-75.
- Drury, M.R. & Urai, J.L. 1990. Deformation-Related Recrystallization Processes. *Tectonophysics* 172(3-4), 235-253.
- Franssen, R.C.M.W. 1993. Rheology of synthetic rocksalt. PhD thesis, Universiteit Utrecht.
- Franssen, R.C.M.W. 1994. The Rheology of Synthetic Rock-Salt in Uniaxial Compression. *Tectonophysics* 233(1-2), 1-40.
- Franssen, R.C.M.W. 1996. Mechanical anisotropy of synthetic polycrystalline rocksalt. In: *Fourth Conference on the Mechanical Behaviour of Salt*. TTP Trans Tech Publications, Clausthal-Zellerfeld, Germany, The Pennsylvania State University, June 17 and 18, 1996, 63-75.
- Franssen, R.C.M.W. & Spiers, C.J. 1990. Deformation of polycrystalline salt in compression and in shear at 250-350°C. In: *Deformation Mechanisms, Rheology and Tectonics* (edited by Knipe, R. J. R., E.H.) 45. Geological Society Special Publication, 201-213.
- Goldsby, D.L. & Kohlstedt, D. 2001. Superplastic deformation of ice: experimental observations. *Journal of Geophysical Research* 106, 11017-11030.
- Guillopé, M. & Poirier, J.P. 1979. Dynamic Recrystallization During Creep of Single-Crystalline Halite - Experimental-Study. *Journal of Geophysical Research* 84(NB10), 5557-5567.
- Heard, H.C. 1972. Steady-state flow in polycrystalline halite at pressure of 2 Kilobars. In: *Flow and Fracture of Rocks* (edited by H.C. Heard, I. Y. B., N.L. Carter and C.B. Raleigh) 16. Geophysical Monograph, 99-115.
- Hobbs, B.E. 1968. Recrystallization of Single Crystals of Quartz. *Tectonophysics* 6(5), 353-401.
- Hobbs, B.E., Means, W.D. & Williams, P.F. 1982. Relationships between foliation and strain: an experimental investigation. *Journal of Structural Geology* 4(4), 411-428.
- Humphreys, F.J. & Hatherly, M. 2004. Recrystallization and related annealing phenomena. Elsevier, 628.
- Kern, H. & Braun, G. 1973. Deformation and Preferred Orientation in Rock Salt at 20-200 Degrees C. *Contributions to Mineralogy and Petrology* 40(2), 169-182.

- Lebensohn, R.A., Dawson, P.R., Kern, H.M. & Wenk, H.R. 2003. Heterogeneous deformation and texture development in halite polycrystals: comparison of different modeling approaches and experimental data. *Tectonophysics* 370(1-4), 287-311.
- Paterson, M.S. & Olgaard, D.L. 2000. Rock deformation tests to large shear strains in torsion. *Journal of Structural Geology* 22(9), 1341-1358.
- Pennock, G.M., Drury, M.R., Peach, C.J. & Spiers, C.J. 2006. The influence of water on deformation microstructures and textures in synthetic NaCl measured using EBSD. *Journal of Structural Geology* 28(4), 588-601.
- Piazolo, S., Bestmann, M., Prior, D.J. & Spiers, C.J. 2006. Temperature dependent grain boundary migration in deformed-then-annealed material: Observations from experimentally deformed synthetic rocksalt. *Tectonophysics* 427(1-4), 55-71.
- Pieri, M., Burlini, L., Kunze, K., Stretton, I. & Olgaard, D.L. 2001. Rheological and microstructural evolution of Carrara marble with high shear strain: results from high temperature torsion experiments. *Journal of Structural Geology* 23(9), 1393-1413.
- Poirier, J.P. 1985. *Creep of crystals*. Cambridge University Press.
- Prior, D.J., Boyle, A.P., Brenker, F., Cheadle, M.C., Day, A., Lopez, G., Peruzzo, L., Potts, G.J., Reddy, S., Spiess, R., Timms, N.E., Trimby, P., Wheeler, J. & Zetterstrom, L. 1999. The application of electron backscatter diffraction and orientation contrast imaging in the SEM to textural problems in rocks. *American Mineralogist* 84(11-12), 1741-1759.
- Rutter, E.H., Casey, M. & Burlini, L. 1994. Preferred crystallographic orientation development during the plastic and superplastic flow of calcite rocks. *Journal of Structural Geology* 10, 1431-1446.
- Schmid, S.M., Panozzo, R. & Bauer, R. 1987. Simple shear experiments on calcite rocks: rheology and microfabrics. *Journal of Structural Geology* 9, 747-778.
- Senseny, P.E., Hansen, F.D., Russell, J.E., Carter, N.L. & Handin, J.W. 1992. Mechanical-Behavior of Rock Salt - Phenomenology and Micromechanisms. *International Journal of Rock Mechanics and Mining Sciences & Geomechanics Abstracts* 29(4), 363-378.
- Skrotzki, W. & Liu, Z.G. 1982. Analysis of the Cross Slip Process in Alkali-Halides. *Physica Status Solidi a-Applied Research* 73(2), K225-K229.
- Skrotzki, W. & Welch, P. 1983. Development of texture and microstructure in extruded ionic polycrystalline aggregates. *Tectonophysics* 99(1), 47-61.
- Skrotzki, W., Helming, K., Brokmeier, H.-G., Dornbusch, H.-J. & Welch, P. 1995. Textures in pure shear deformed rock salt. *Textures and Microstructures* 24, 133-141.
- Skrotzki, W., Dornbusch, H.-J., Helming, K., Dornbusch, H.-J. & Welch, P. 1996. Development of microstructure and texture in pure shear deformed salt. In: *4th Conference on the Mechanical Behaviour of Salt* (edited by Aubertin, M. & Hardy, H. R.), Montreal, Canada, 203-211.
- Spiers, C.J., Urai, J.L., Lister, G.S., Boland, J.N. & Zwart, H.J. 1986. The influence of brine (inherent or added) on rheology and deformation mechanisms in salt rock. In: *The Mechanical*

Behaviour of Salt: Proceedings of the Second Conference (edited by Hardy, H. R. & Langer, M.). Trans Tech Publications, 89-102.

Ter Heege, J.H., De Bresser, J.H.P. & Spiers, C.J. 2005. Dynamic recrystallization of wet synthetic polycrystalline halite: dependence of grain size distribution on flow stress, temperature and strain. *Tectonophysics* 396(1-2), 35-57.

Trimby, P.W., Drury, M.R. & Spiers, C.J. 2000. Recognising the crystallographic signature of recrystallisation processes in deformed rocks: a study of experimentally deformed rocksalt. *Journal of Structural Geology* 22(11-12), 1609-1620.

Urai, J.L., Means, W.D. & Lister, G.S. 1986. Dynamic recrystallization of minerals. *Geophysical Monograph, American Geophysical Union* 36, 161-199.

Urai, J.L., Spiers, C.J., Peach, C.J., Franssen, R.C.M.W. & Liezenberg, J.L. 1987. Deformation mechanisms operating in naturally deformed halite rocks as deduced from microstructural investigations. *Geologie en Mijnbouw* 66, 165-176.

Venables, J.A. & Harland, C.J. 1973. Electron back-scattering patterns - A new technique for obtaining crystallographic information in the scanning electron microscope. *Philosophical Magazine* 27(5), 1193-1200.

von Mises, R. 1928. Mechanics of the ductile form changes of crystals. *Zeitschrift Fur Angewandte Mathematik Und Mechanik* 8, 161-185.

Wenk, H. R. 1985. *Preferred orientation in deformed metals and rocks: An introduction to modern texture analysis*. Academic Press, Orlando.

Wenk, H.R. & Christie, J.M. 1991. Comments on the Interpretation of Deformation Textures in Rocks. *Journal of Structural Geology* 13(10), 1091-1110.

Wenk, H.R., Canova, G., Brechet, Y. & Flandin, L. 1997. A deformation-based model for recrystallization of anisotropic materials. *Acta Materialia* 45(8), 3283-3296.

Chapter 7

Summary and further research

This chapter summarises the results of this study and gives a brief outlook on further research topics.

7.1 Summary

This study has focused on the deformation behaviour, the microstructural processes and on the formation of CPO in synthetic rocksalt deformed at temperatures of 100, 200 and 300°C, deformed in torsion up to high shear strains ($\gamma \sim 8$), applying shear strain rates of $3 \times 10^{-5} \text{s}^{-1}$, $3 \times 10^{-4} \text{s}^{-1}$ and $3 \times 10^{-3} \text{s}^{-1}$ at a constant confining pressure of 250MPa. The most important findings are summarised in the following section:

- Deformation of synthetic rocksalt under the applied conditions takes place by dislocation processes. At 100°C deformation occurs by the glide of dislocations, as inferred from the presence of slip bands and blocky subgrains. Cross-slip also occurs at this temperature as observed by the occurrence of wavy slip bands. The microstructure at 100°C represents a typical strain hardening microstructure. At 200 and 300°C deformation occurs by dislocation creep mechanisms, in particular with dislocation climb producing polygonal shaped subgrains. The microstructure at these temperatures represents a typical recovery microstructure.
- The characteristic microstructural feature of the samples deformed at 100°C is the development of a domain structure, wavy or straight slip bands and blocky subgrains. The domain structure and the blocky subgrains developed as a result of the high crystal plastic anisotropy of halite at this temperature. The microstructure at 200 and 300°C consists of dynamic recrystallised grains, whereas the 300°C samples are influenced by static recrystallisation to some extent.
- Recrystallisation in the samples occurred under dynamic and under static conditions. Two dynamic recrystallisation mechanisms could be observed in the deformed samples. Subgrain rotation recrystallisation is preferentially present at 100 and 200°C and grain boundary migration recrystallisation is equally active with rotation recrystallisation at 200°C but dominates the microstructure at 300°C. Subgrain rotation recrystallisation leads with increasing shear strain to a major grain size reduction resulting in a mylonitic matrix of the deformed samples. Grain boundary migration recrystallisation however, causes grain coarsening.
- Static recrystallisation, leading to the growth of new strain free grains occurred preferentially at 200 and 300°C and to some extent at 100°C. Grain growth at 200 and 300°C occurred due to increased temperature and accelerated grain boundary kinetics, whereas grain growth at 100°C occurred due to the release of high internal strain energy

stored in the highly deformed samples. Static recrystallisation erases of the deformation microstructure.

- The CPOs that developed are consistent with the observed microstructure. Three main CPO types could be distinguished. These are:
 - i) a deformation CPO at low shear strain with a monoclinic symmetry and characterised by two texture components (a strong $\{111\}\langle 110 \rangle$ and a weak $\{001\}\langle 110 \rangle$ component)
 - ii) a recrystallisation CPO ($\{001\}\langle 110 \rangle$ component) at high shear strain with orthorhombic symmetry and characterised by one strong texture component and
 - iii) a grain growth CPO with a rotated $\{110\}\langle 110 \rangle$ texture component.
- The development of microstructure and CPO at 100 and 200°C is strongly influenced by the finite shear strain. Microstructure and CPO changed from a shear deformation mode at low shear strains ($\gamma \leq 3$) into a recrystallisation mode at shear strains $\gamma \geq 3$. The change in the microstructure is observed in the reduction of the grain size and in the formation of new high angle boundaries. The change in the CPO is observed in the change in the texture component from a $\{111\}\langle 110 \rangle$ component at low shear strains to a $\{001\}\langle 110 \rangle$ component at high shear strain.
- The development of the microstructure and the CPO is also influenced by temperature. An increase in temperature leads to an increase in the subgrain- and in the grain size. At 300°C the microstructure experienced a continuous reworking by several dynamic recrystallisation cycles and thus at this temperature no evolution with shear strain is observed. This also appears in the CPOs formed at 300°C which show a composition of deformation and recrystallisation.

7.2 Further research

➤ Further experimental work

The true stress-strain behaviour of rocksalt in the low temperature range (100-300°C) in this study could not be determined in a satisfying way. This is due to the problem of the non negligible strength of the jacket material (cf. chapter 4). Therefore, it is of great importance to repeat the presented set of experiments by using a jacket material that has a negligible strength at temperatures of 100-300°C. Possible jacket materials include FEP, lead-tin alloys, silver-tin alloys and indium (up to 150°C). This would allow the rate-controlling mechanisms active in synthetic rocksalt to be determined in the torsion mode. This newly obtained data on the rheological behaviour of rocksalt could then be linked to the observed microstructure. This would allow the mechanical weakening and the dynamic recrystallisation to be correlated. Furthermore, the obtained mechanical and rheological data could be extrapolated to natural conditions, which is a need in experimental rock deformation. Additionally, new experiments should be carried out by applying strain rates of at least a magnitude slower than the strain rates applied in this study. This would allow the deformation behaviour of rocksalt to be simulated closer to natural conditions. Rocksalt in nature usually deforms under temperature conditions below the temperature range used in this study. Therefore, it would be essential to carry out new experiments at temperatures below 100°C to investigate the behaviour of rocksalt in terms of mechanics, microstructure and CPO. Also, experiments

using natural rocksalt samples would be of great interest. Natural rocksalt can contain amounts of gas and second phase particles which may have an influence on the mechanical behaviour as well as on the development of the microstructure and the microstructural processes acting during deformation. Furthermore, natural rocksalt occurs in layered evaporitic sequences that consist of several mineral phases, displaying a contrast in strength. Therefore, experiments using two or even three phase salt mineral assemblages would be an interesting subject to study.

➤ **Additional studies on the microstructure of the deformed samples**

One of the most interesting finding in this study was the occurrence of the domain structures at 100°C. More work is needed to explain the formation of these structures in a satisfying way. The relationship between the two domains with respect to the rotation axis around which the two domains rotated is an interesting subject to study. The EBSD technique, as shown in chapter 5, is for this purpose an excellent tool to carry more research on this subject. It was also shown in chapter 5 that EBSD is helpful in understanding the recrystallisation mechanisms acting in the deformed samples. Also, here a lot more work can be done to investigate the relationship between recrystallised grains and host grains and to answer the following questions: To what extend are the new recrystallised grains host controlled? What are the misorientation axis between the single subgrains, new recrystallised grains and the host grain? A lack in this study was clearly the analysis of the subgrain size and its relation to the applied stress. It would be good to correlate these data with the data obtained by Guillopé and Poirier (1979) and by Franssen (1994). Also, the dynamic recrystallised grain size was not determined and thus could not be correlated with the applied stress. In chapter 5 and 6 it was shown that especially at 300°C the microstructure was immensely influenced by grain boundary migration, either during dynamic recrystallisation or under static conditions. Measurements on the grain boundary mobility would help to understand how fast grain boundary migration can occur. Here, in-situ heating experiments would shed some light on that problem. Up to date, these kinds of experiments were carried out on dry rocksalt by Piazzolo et al. (2006) and Bestmann et al. (2005). Therefore, it would be interesting to know how fast grain boundary migration occurs in wet deformed samples and to what extend the heating influences the deformed microstructure and the pre-existing CPO. The developed of blocky subgrains and slip bands at 100°C are an interesting topic for further studies by investigating these structures with the TEM in detail to study these features at a higher magnification scale. This would allow to relate these structures with the low temperature deformation structures found in metals, like aluminium.

➤ **Texture simulation**

Numerical texture simulation can be a good tool to gain more knowledge which slip systems are responsible for the formation of a texture produced in experiments and in nature. Therefore texture simulations are important and can shed some light on the development and evolution of CPOs during experiments.

7.3 References

Bestmann, M., Piazzolo, S., Spiers, C.J. & Prior, D.J. 2005. Microstructural evolution during initial stages of static recovery and recrystallization: new insights from in-situ heating experiments combined with electron backscatter diffraction analysis. *Journal of Structural Geology* 27(3), 447-457.

Franssen, R.C.M.W. 1994. The Rheology of Synthetic Rock-Salt in Uniaxial Compression. *Tectonophysics* 233(1-2), 1-40.

Guillopé, M. & Poirier, J.P. 1979. Dynamic Recrystallization During Creep of Single-Crystalline Halite - Experimental-Study. *Journal of Geophysical Research* 84(NB10), 5557-5567.

Piazzolo, S., Bestmann, M., Prior, D.J. & Spiers, C.J. 2006. Temperature dependent grain boundary migration in deformed-then-annealed material: Observations from experimentally deformed synthetic rocksalt. *Tectonophysics* 427(1-4), 55-71.

Curriculum Vitae

Marina Armann

Personal Details

Date of Birth: 14.02.1979
Place of Birth: Sonneberg/Germany
Nationality: German

Education

2008 – 2003 PhD student at the Geological Institute ETH Zurich
2003 – 1998 Studies of Geology at University of Erlangen (Germany)
Major: Structural Geology and Regional Geology
Minor: Mineralogy and Palaeontology
Diploma Thesis: Deformation history and metamorphism in the SE Cantabrian Zone (Northern Spain)
1998 – 1997 First year Studies of Geology at University of Freiburg (Germany)
1997 – 1993 Gymnasium Sonneberg, Abitur

Work Experience

2003 – 2008 Assistant at the Geological Institute
2000 – 2002 Student assistant at the Geological Institute Erlangen
8/1999 and 8/1998 Work placement at Umweltgeologie Sonneberg (Germany)

Appendices

Appendix A

List of conducted experiments

Sample [Run #]	Material	diameter [mm]	length [mm]	Temperature [°C]	shear strain rate	shear strain	comment
P0655	rocksalt	14.8	10.0	100	5x10 ⁻⁴	4.2	stepping
P0671	rocksalt	14.7	10.0	100	3x10 ⁻⁴	1.1	
P0675	rocksalt	14.8	10.1	100	3x10 ⁻⁴	6.2	
P0682	rocksalt	14.7	10.0	100	3x10 ⁻⁴	3.1	
P0686	rocksalt	14.7	9.9	100	3x10 ⁻⁴	2.2	
P0725	rocksalt	14.7	9.9	200	3x10 ⁻⁴	1.0	
P0727	rocksalt	14.7	10.0	200	6x10 ⁻⁵	4.4	stepping
P0728	rocksalt	14.8	10.1	200	3x10 ⁻⁴	3.2	
P0731	rocksalt	14.8	10.0	200	3x10 ⁻⁴	2.3	
P0735	rocksalt	14.8	9.8	200	3x10 ⁻⁵	1.1	
P0740	rocksalt	14.8	9.6	100	3x10 ⁻⁵	0.3	
P0742	rocksalt	14.8	5.0	200	3x10 ⁻³	7.9	
P0746	rocksalt	14.8	5.0	100	3x10 ⁻³	5.2	
P0747	rocksalt	14.8	5.1	300	3x10 ⁻³	7.9	
P0748	rocksalt	14.7	9.9	300	1x10 ⁻⁴	3.8	stepping
P0766	rocksalt	14.8	8.8	300	3x10 ⁻⁴	3.5	
P0768	rocksalt	14.8	9.1	200	3x10 ⁻⁴	5.2	
P0773	rocksalt	14.8	9.5	300	3x10 ⁻⁴	2.4	
P0791	rocksalt	14.8	8.7	300	3x10 ⁻⁴	1.1	
P0799	rocksalt	14.8	5.1	100	3x10 ⁻³	3.4	
P0822	PTFE	15.2	1.3	100	3x10 ⁻³	8.1	
P0823	PTFE	15.1	1.2	200	3x10 ⁻⁴	7.1	
P0824	PTFE	15.1	1.2	200	3x10 ⁻³	8.8	
P0825	PTFE	15.1	1.2	300	3x10 ⁻⁴	4.1	
P0829	PTFE	15.0	2.1	100	3x10 ⁻⁴	5.2	
P0839	PTFE	15.1	2.5	300	3x10 ⁻³	3.3	
P0918	rocksalt	15.0	9.3	100	3x10 ⁻⁴	2.7	stepping
P0926	rocksalt	15.0	10.1	200	3x10 ⁻⁴	3.6	Stepping

Appendix B

HKL files for NaCl (halite)

MaterialName Sodium Chloride
Formula NaCl
Symmetry 43
Lattice Constants 5.630 5.630 5.630 90.000 90.000 90.000
Number Families 4
hkl Families 0 0 2
hkl Families 0 2 2
hkl Families 2 2 2
hkl Families 0 2 4

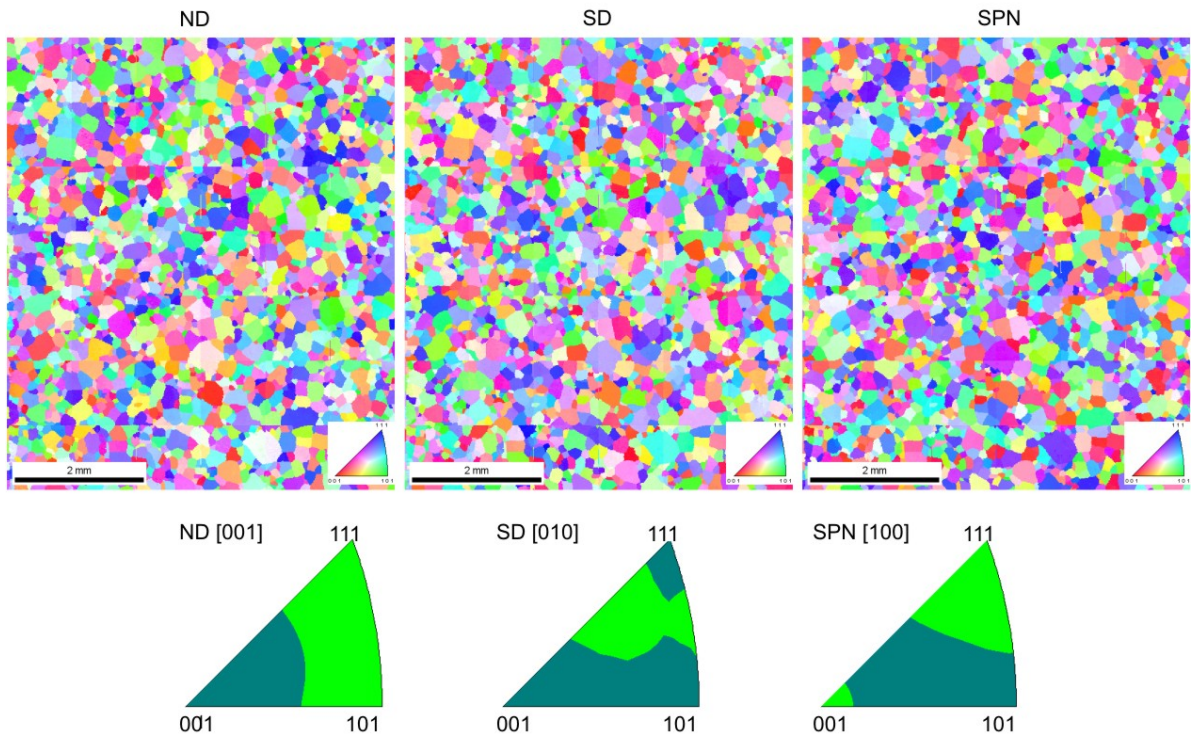
Appendix C

List of EBSD bulk scans

Sample	step size [μm]	size OIM map [μm]
starting material	10	6000x7000
P0671	10	6000x8000
P0675	10	6000x8000
P0682	10	7000x7000
P0686	10	7000x7000
P0725	10	6000x9000
P0728	10	6000x9000
P0731	10	7000x8000
P0735	10	6000x10000
P0740	10	4000x9000
P0742	10	6000x5000
P0746	10	7000x5000
P0747	10	6000x4000
P0766	10	5000x7000
P0768	10	3000x7000
P0773	10	3000x9000
P0791	10	4000x7000
P0799	10	4000x5000

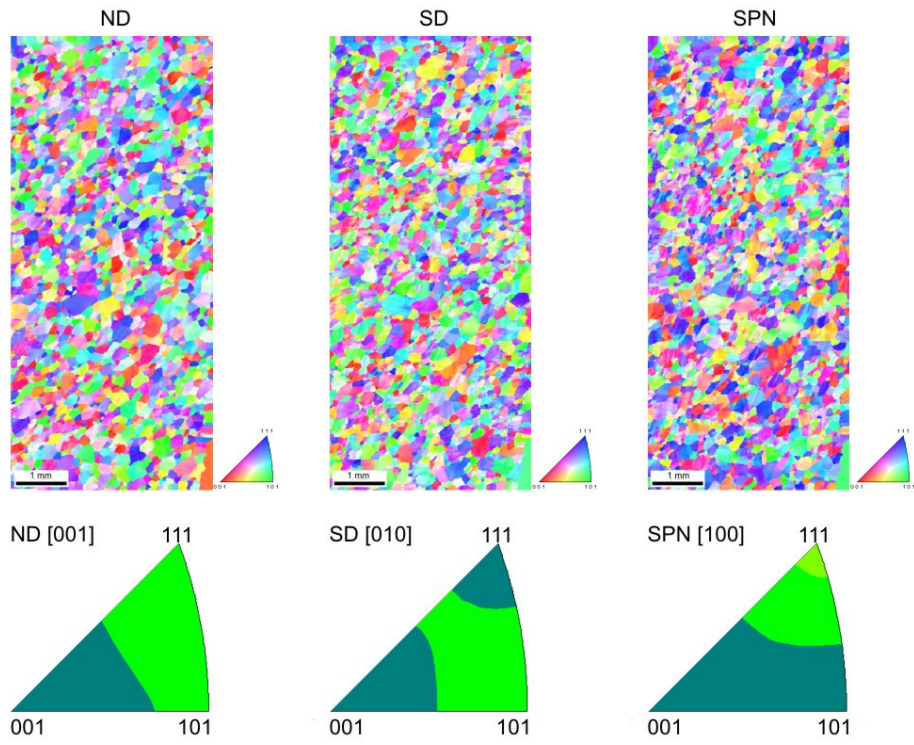
Following pages EBSD bulk maps

Starting material

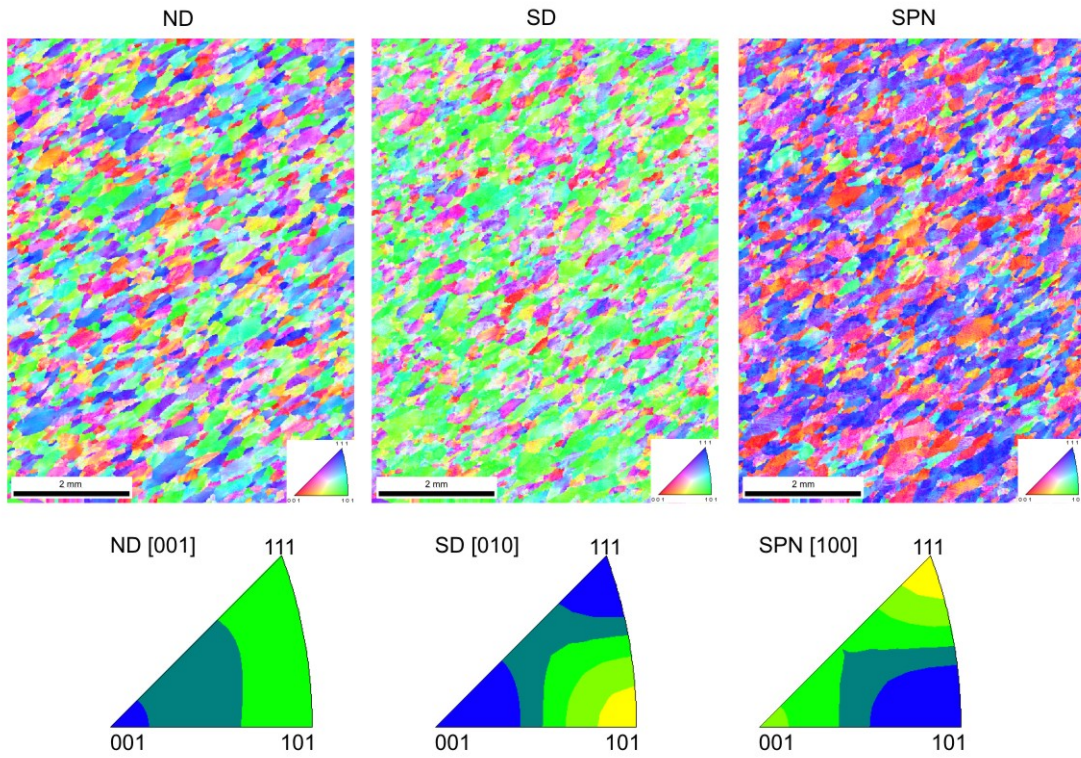


100°C

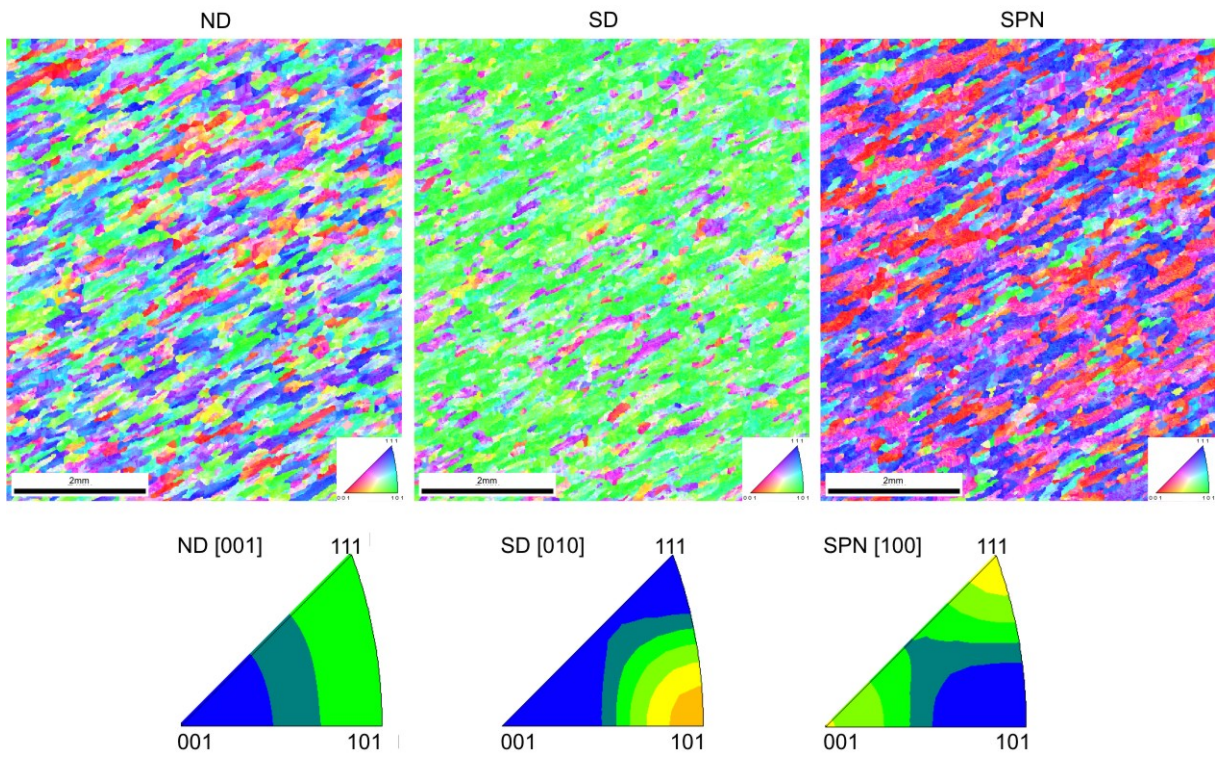
P0740, $\gamma \sim 0.3$, $\dot{\gamma} = 3 \times 10^{-5} \text{ s}^{-1}$



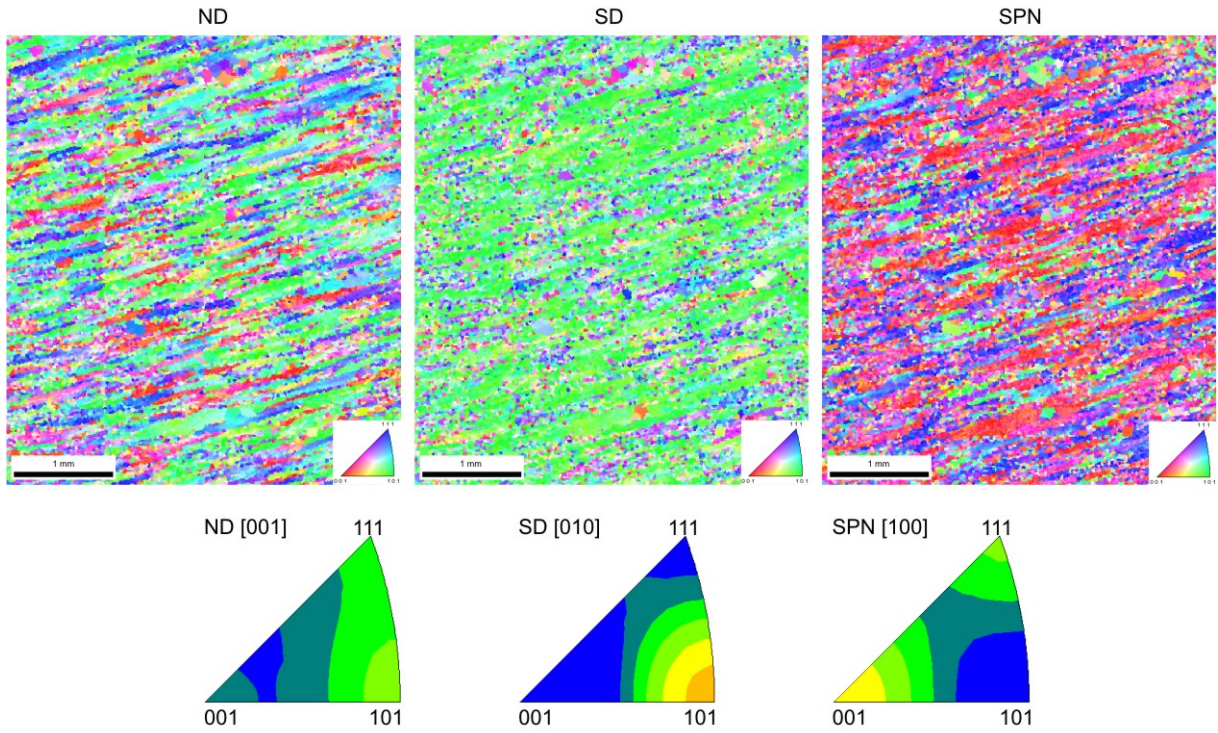
P0671, $\gamma \sim 1$, $\dot{\gamma} = 3 \times 10^{-3} \text{ s}^{-1}$



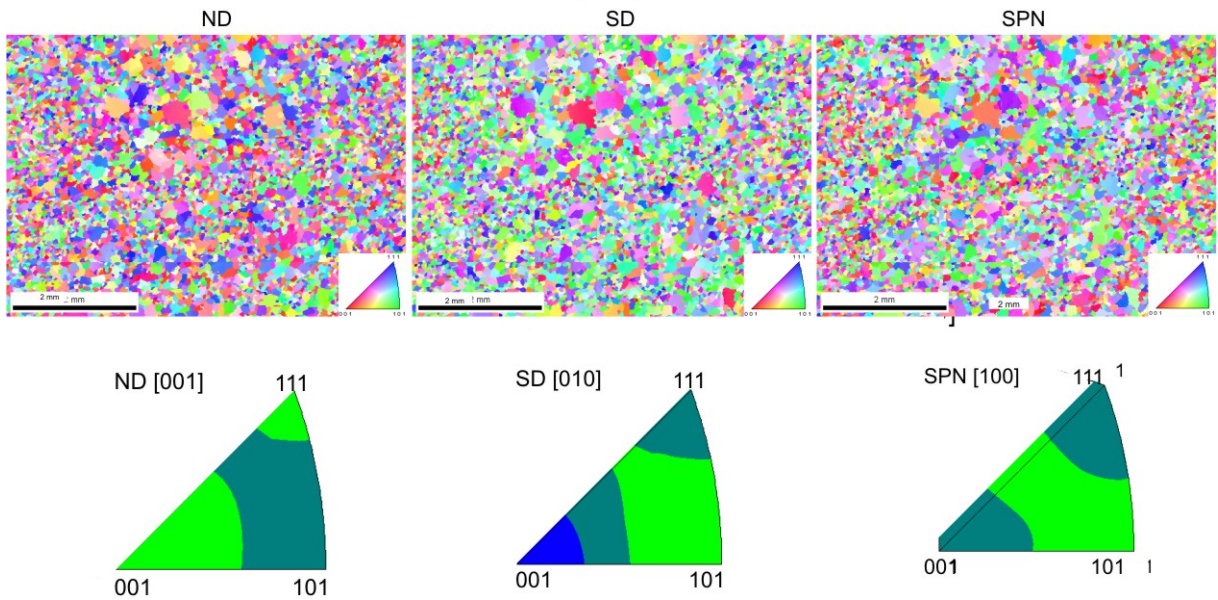
P0686, $\gamma \sim 2$, $\dot{\gamma} = 3 \times 10^{-4} \text{ s}^{-1}$



P0799, $\gamma \sim 3$, $\dot{\gamma} = 3 \times 10^{-3} \text{ s}^{-1}$

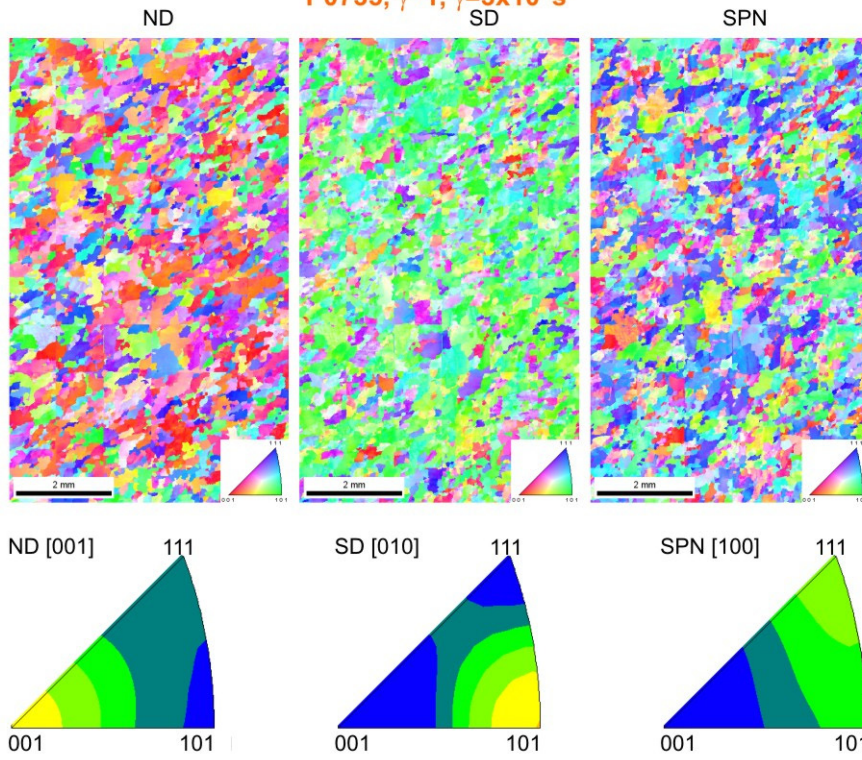


P0746, $\gamma \sim 5$, $\dot{\gamma} = 3 \times 10^{-3} \text{ s}^{-1}$

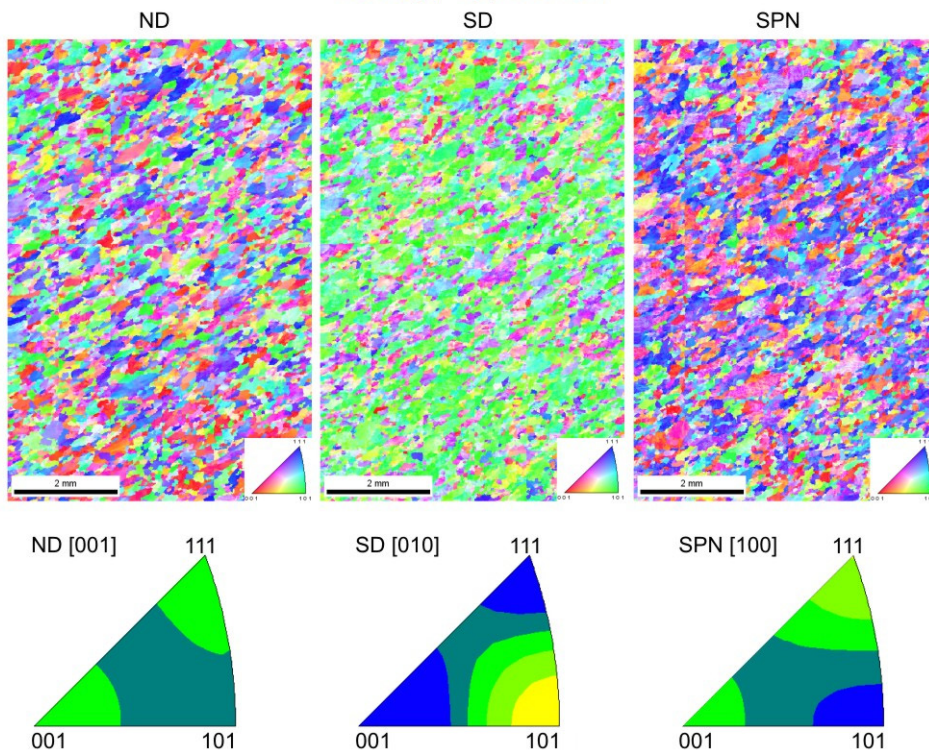


200°C

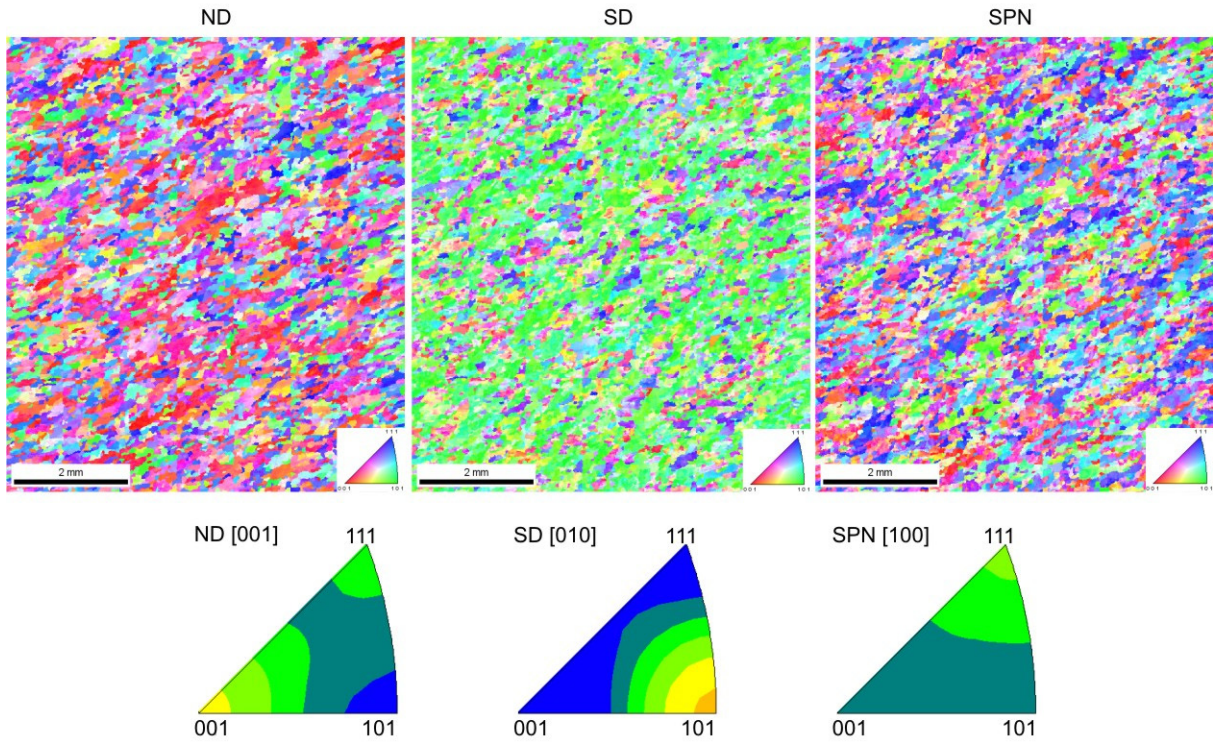
P0735, $\gamma \sim 1$, $\dot{\gamma} = 3 \times 10^{-5} \text{ s}^{-1}$



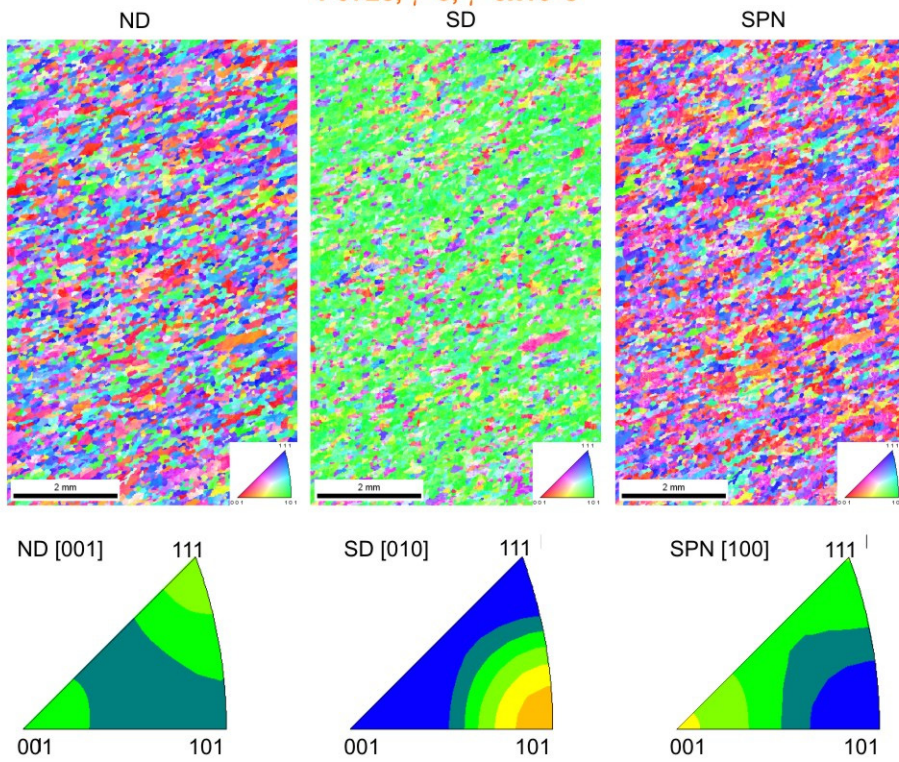
P0725, $\gamma \sim 1$, $\dot{\gamma} = 3 \times 10^{-4} \text{ s}^{-1}$



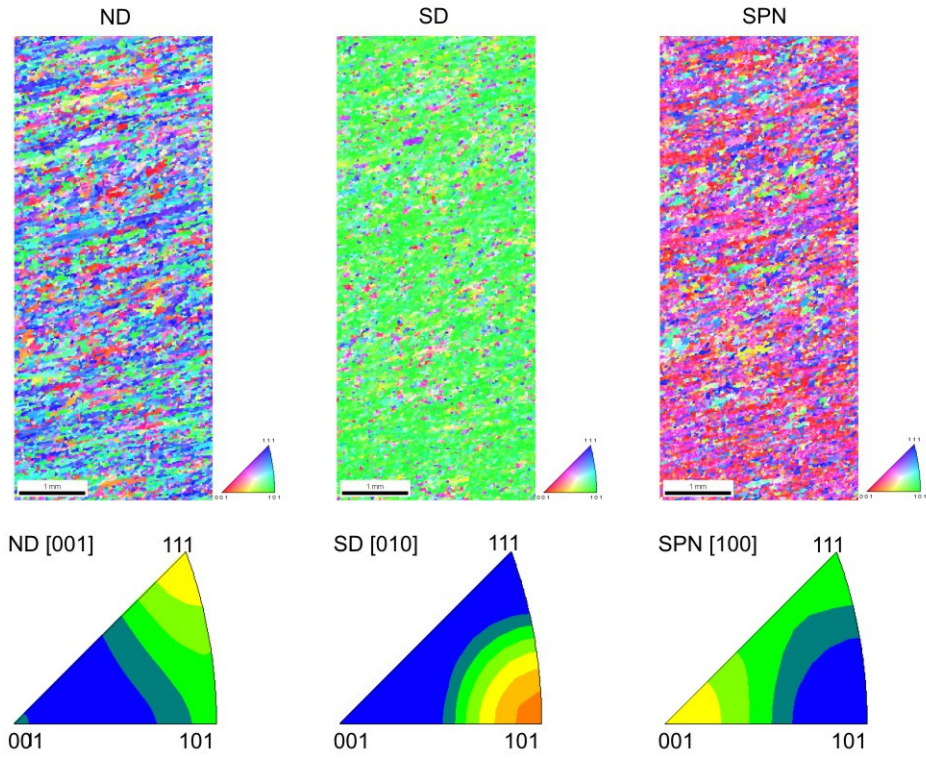
P0731, $\gamma \sim 2$, $\dot{\gamma} = 3 \times 10^{-4} \text{ s}^{-1}$



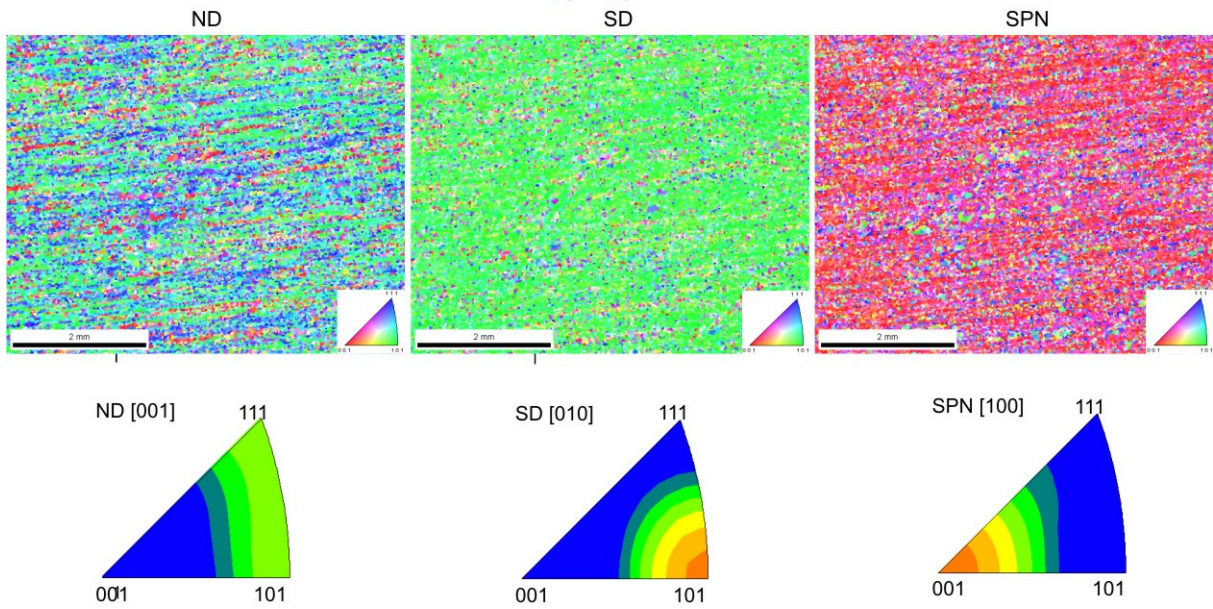
P0728, $\gamma \sim 3$, $\dot{\gamma} = 3 \times 10^{-4} \text{ s}^{-1}$



P0768, $\gamma \sim 5$, $\dot{\gamma} = 3 \times 10^{-4} \text{ s}^{-1}$

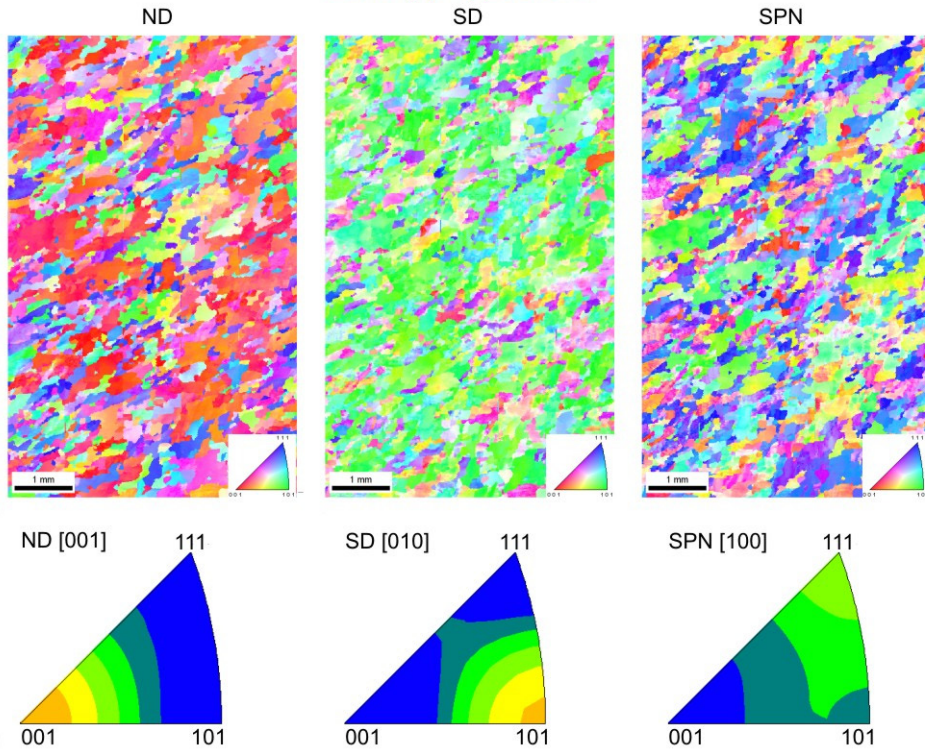


P0742, $\gamma \sim 8$, $\dot{\gamma} = 3 \times 10^{-3} \text{ s}^{-1}$

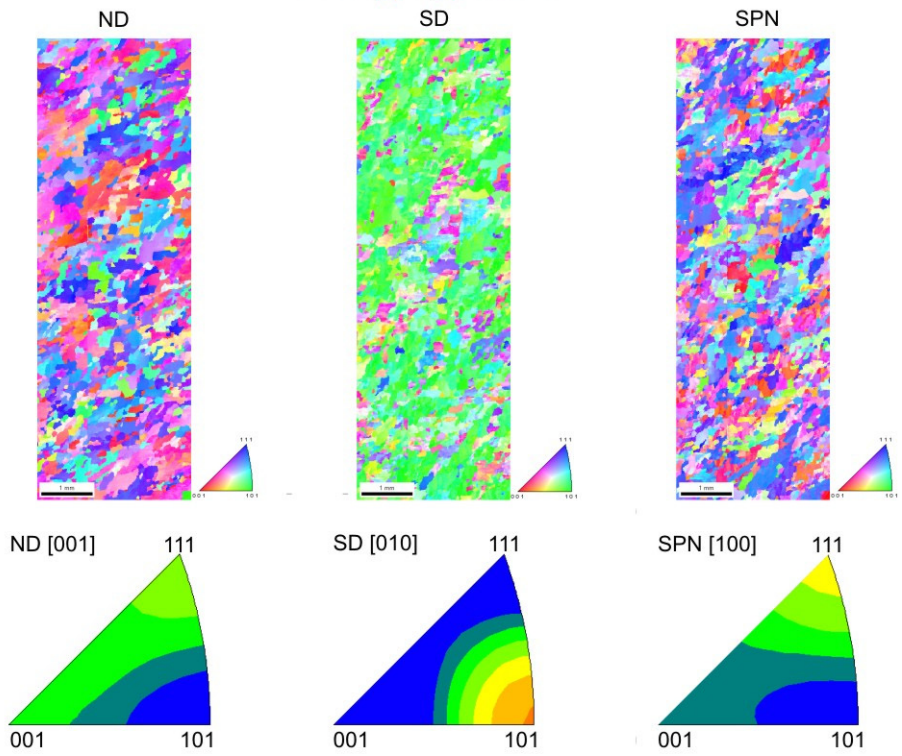


300°C

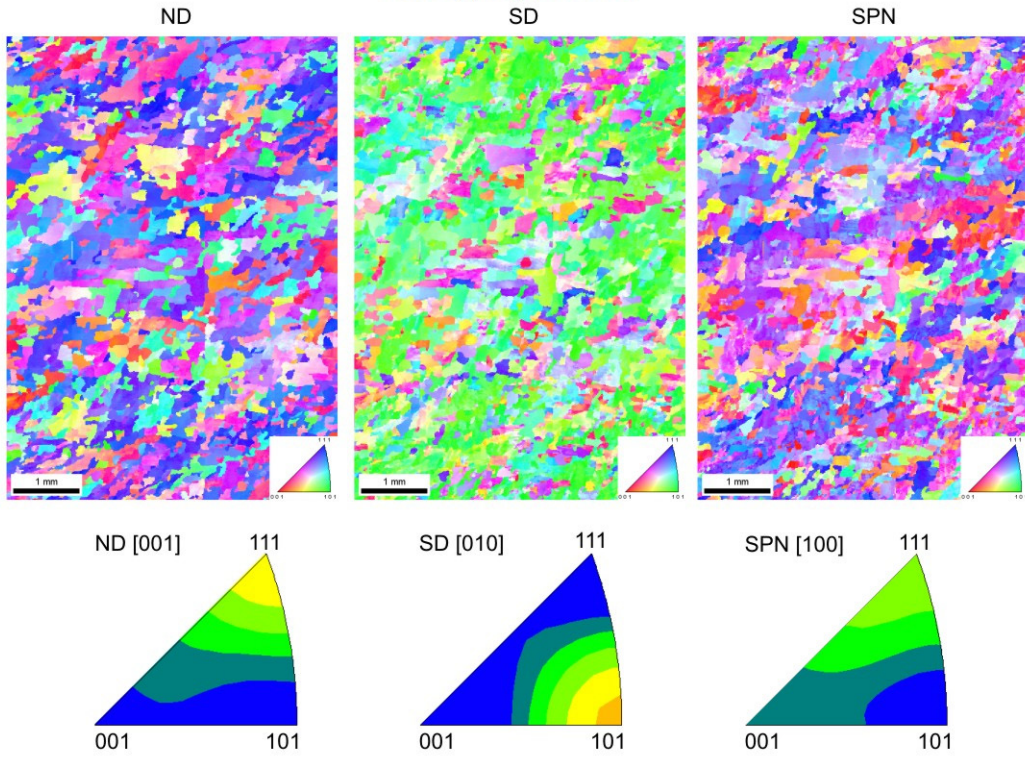
P0791, $\gamma \sim 1$, $\dot{\gamma} = 3 \times 10^{-4} \text{ s}^{-1}$



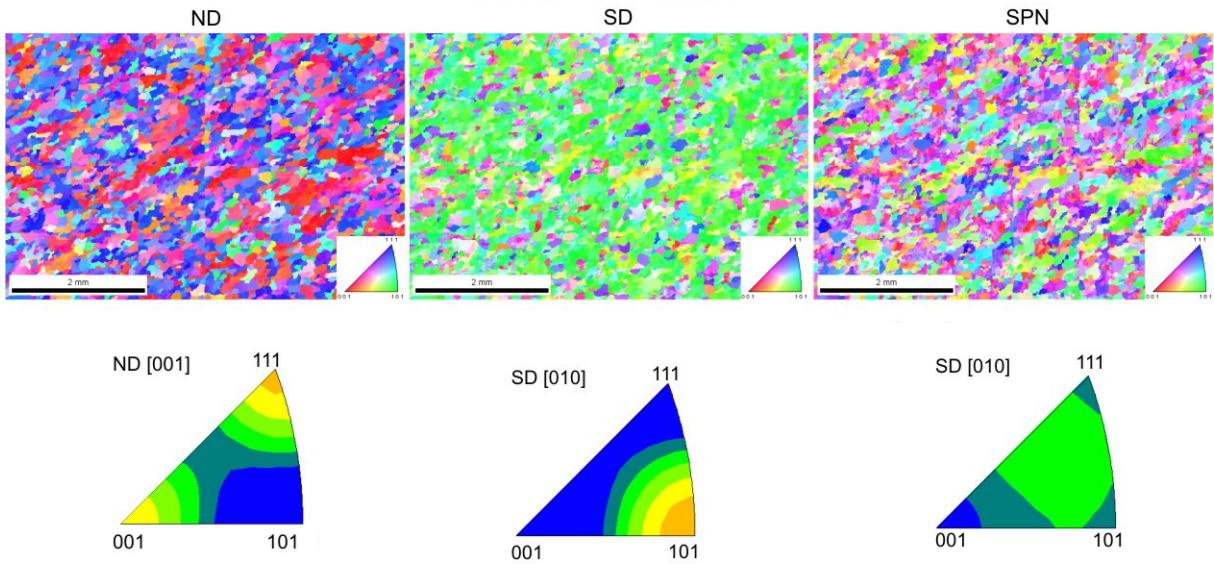
P0773, $\gamma \sim 2$, $\dot{\gamma} = 3 \times 10^{-4} \text{ s}^{-1}$



P0766, $\gamma \sim 3$, $\dot{\gamma} = 3 \times 10^{-4} \text{s}^{-1}$



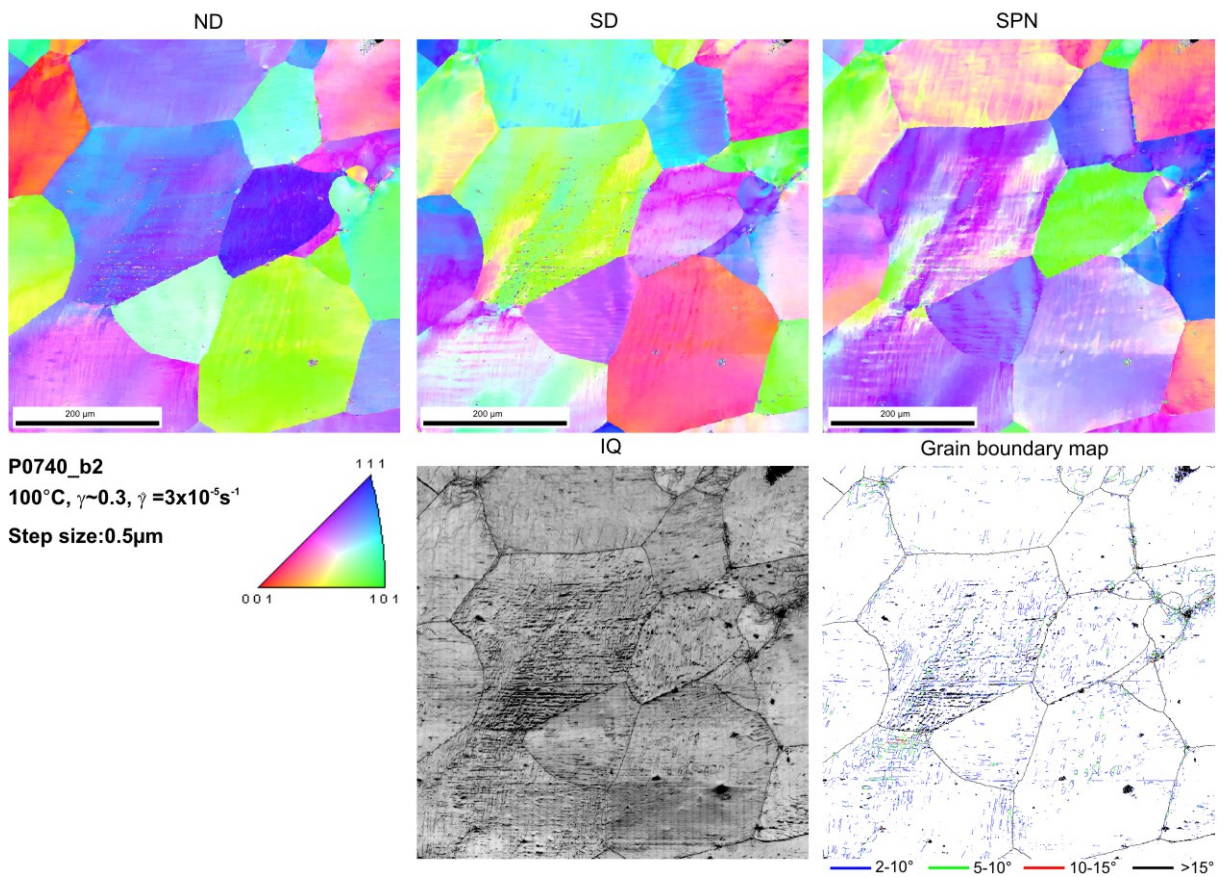
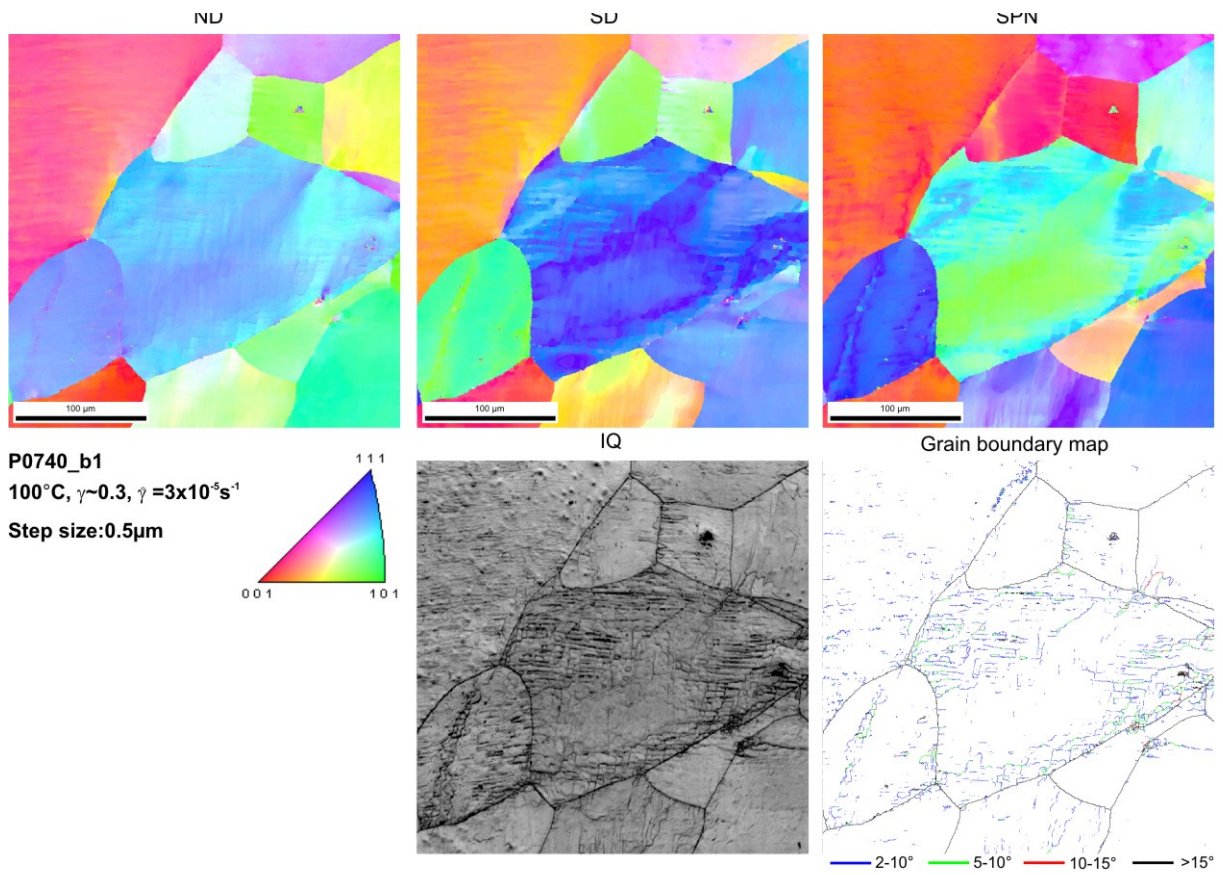
P0747, $\gamma \sim 8$, $\dot{\gamma} = 3 \times 10^{-3} \text{s}^{-1}$

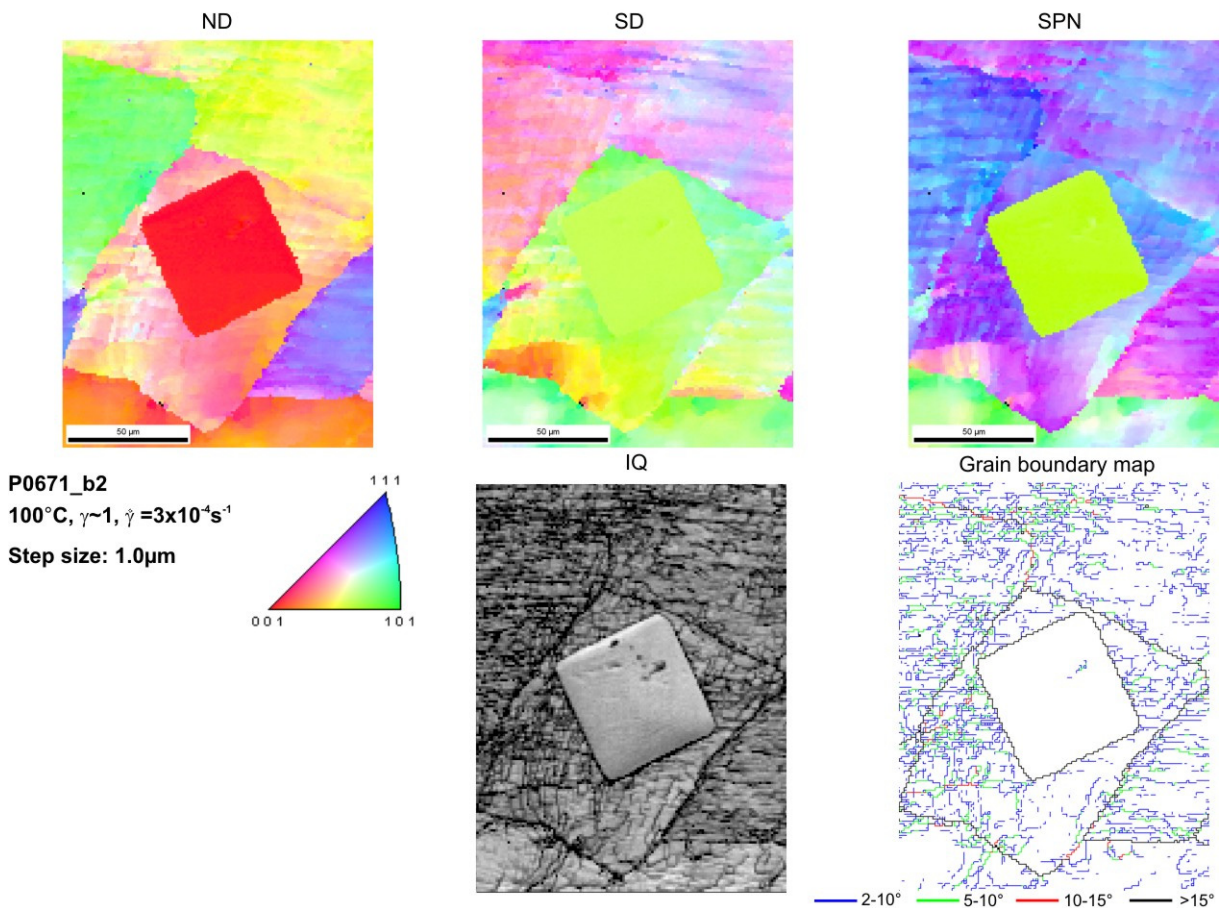
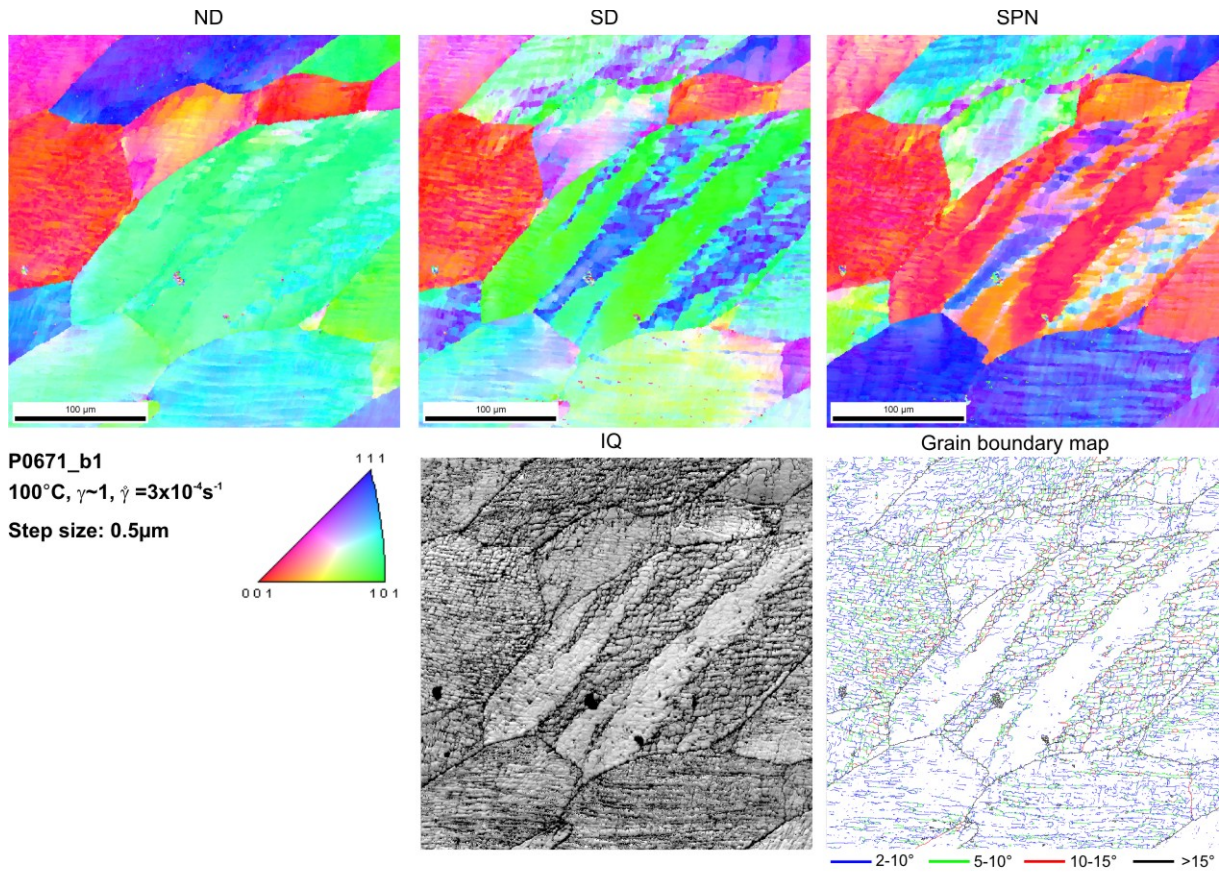


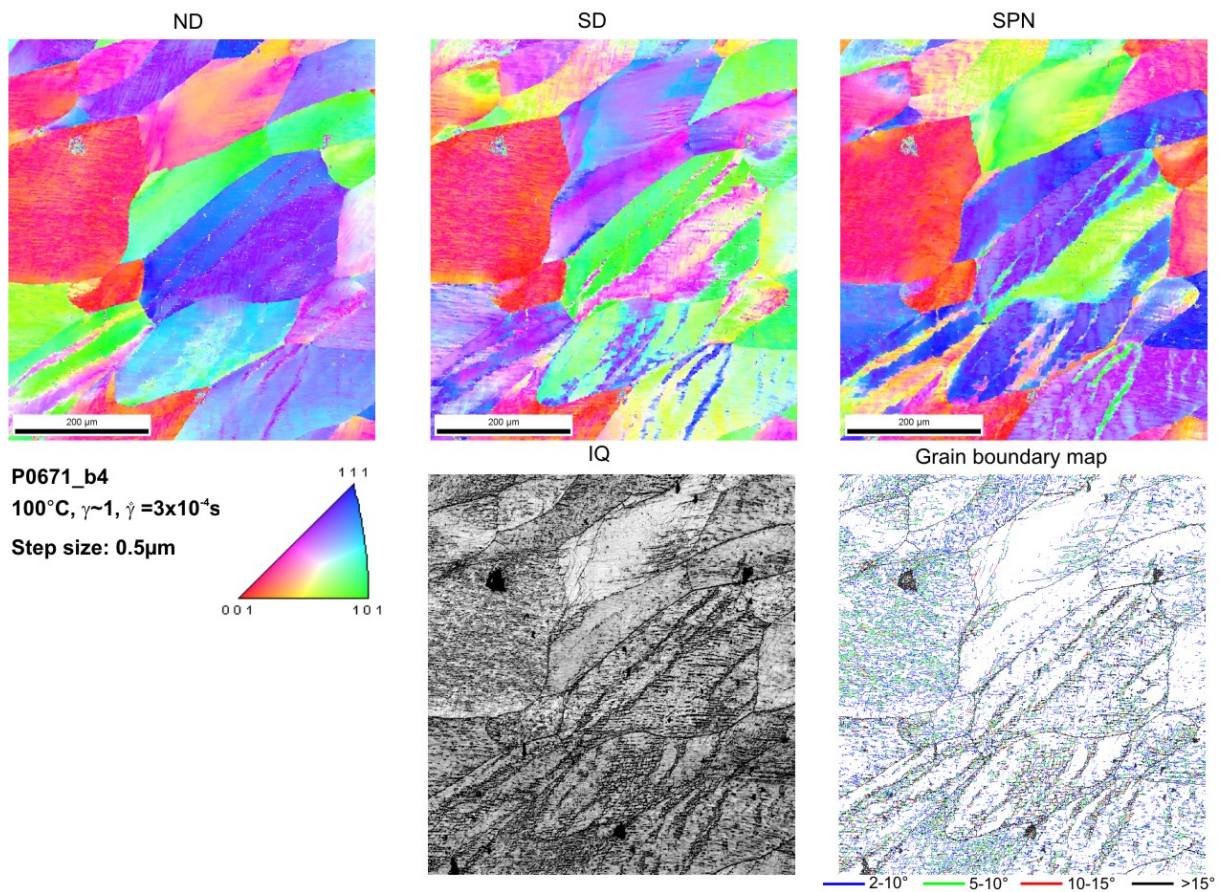
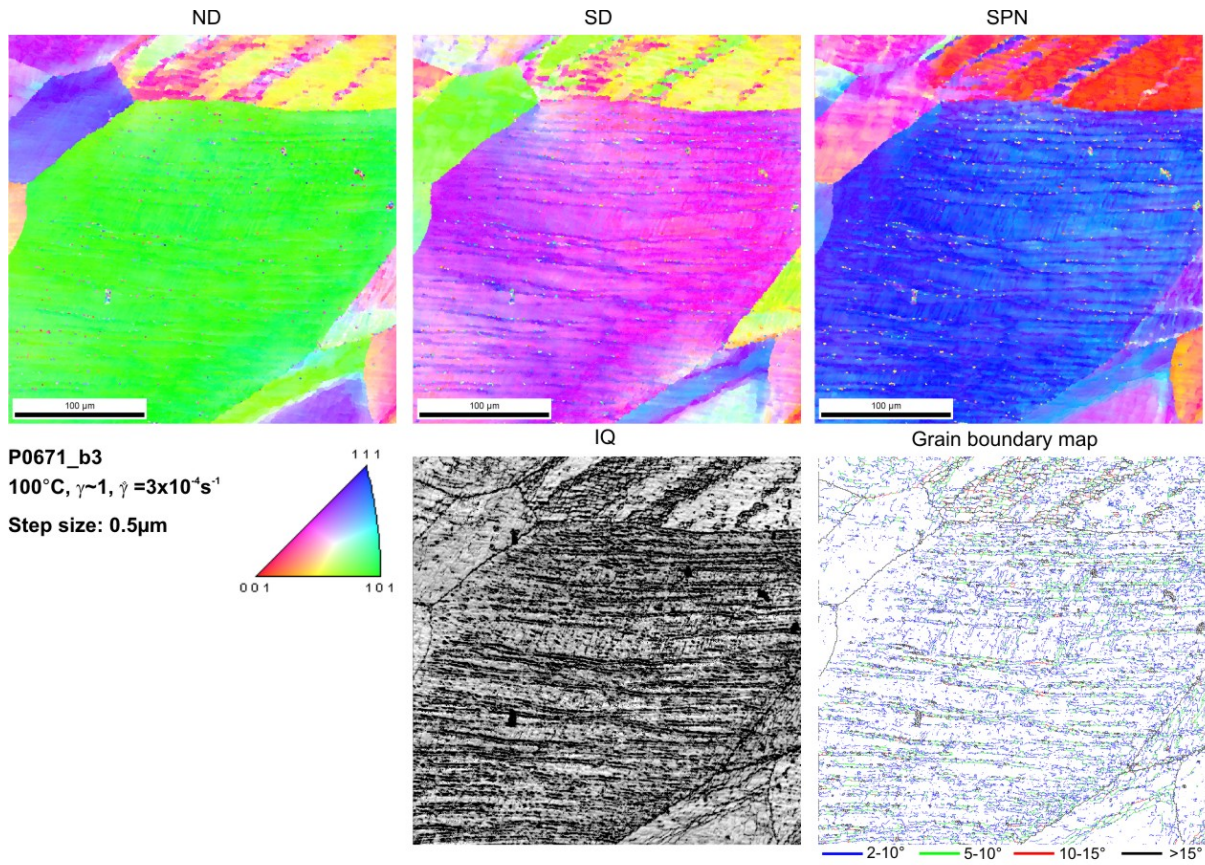
List of EBSD detail scans

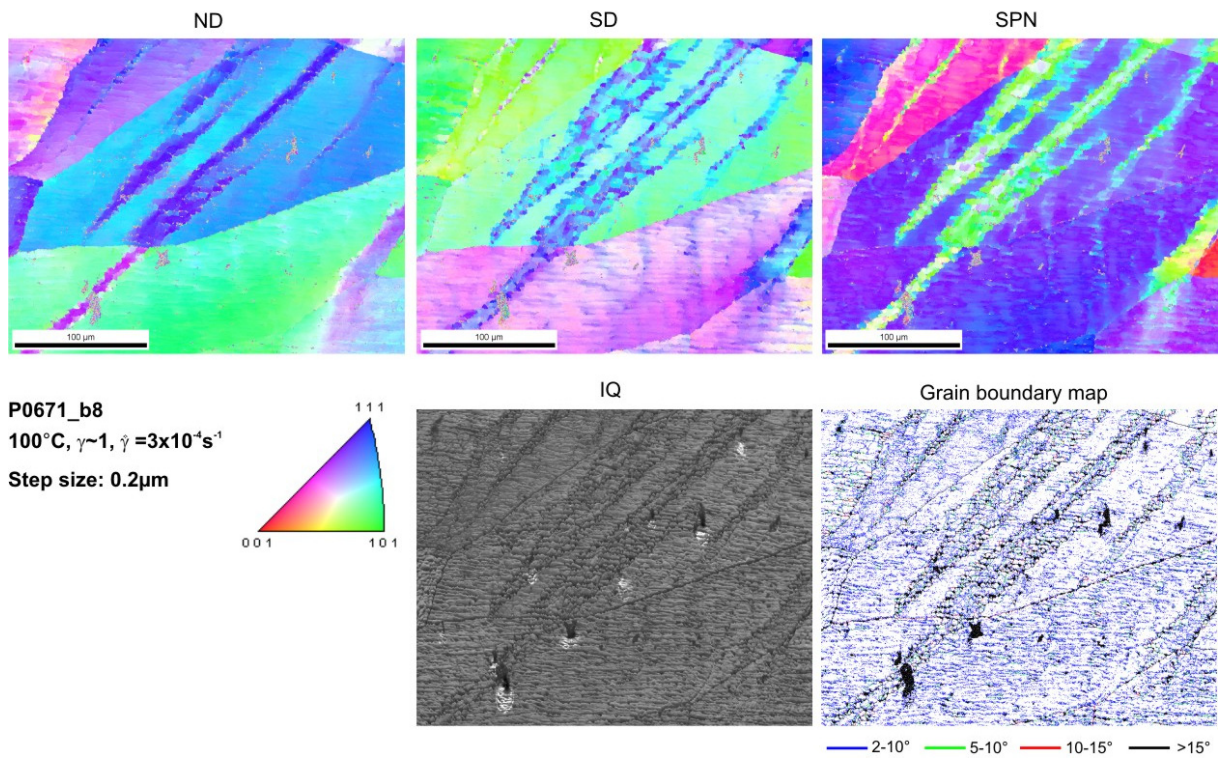
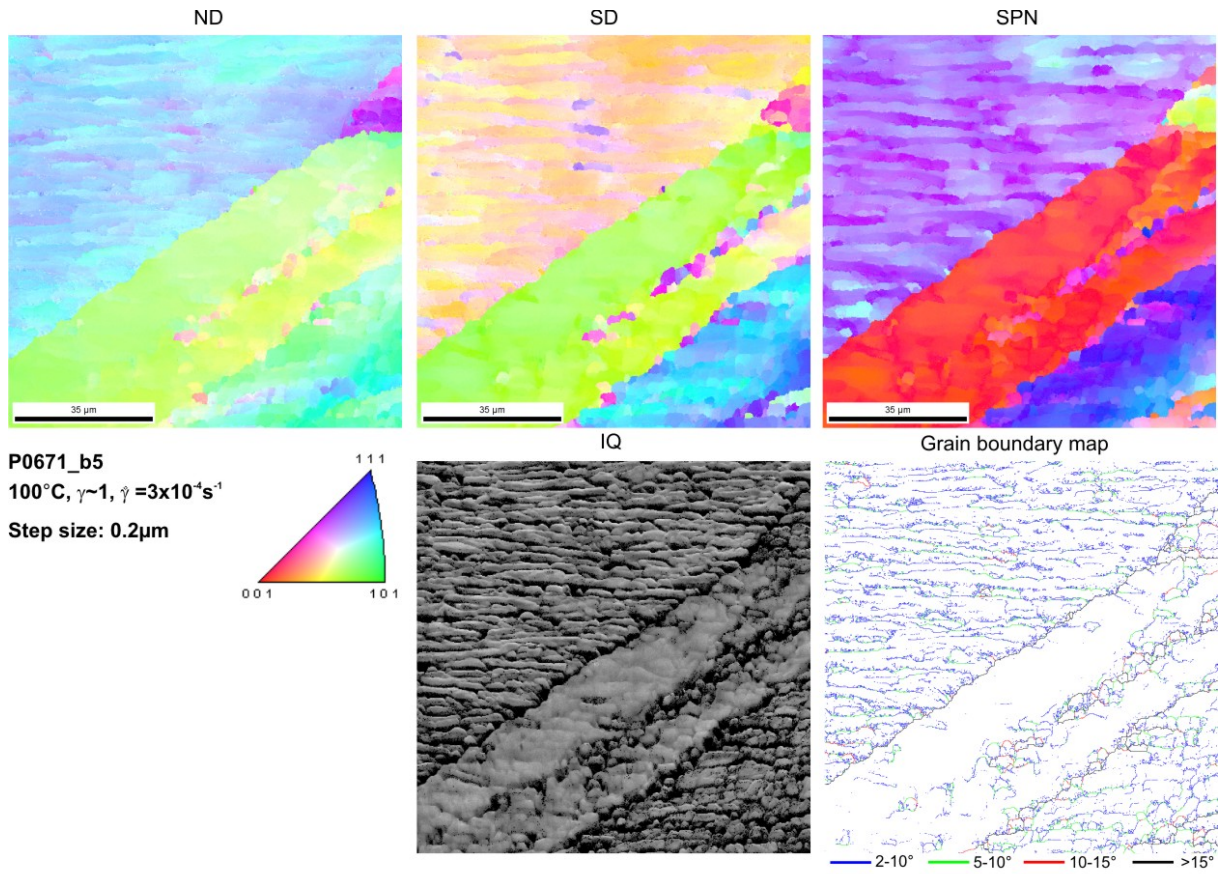
Sample	detail scan	step size	size OIM map	SEM
P0740	P0740_b1	0.5	300x300	CamScan
	P0740_b2	0.5	550x550	CamScan
P0671	P0671_b1	0.5	300x300	CamScan
	P0671_b2	1	130x170	CamScan
	P0671_b3	0.5	300x300	CamScan
	P0671_b4	0.5	550x600	CamScan
	P0671_b5	0.2	100x100	Quanta
	P0671_b8	0.2	300x240	Quanta
	P0671b_b1	0.5	300x300	CamScan
	P0671b_b2	0.5	300x300	CamScan
P0686	P0686_b1	1.0	500x500	CamScan
	P0686_b2	0.5	550x310	CamScan
P0682	P0682_b1	0.5	300x300	CamScan
	P0682_b2	0.5	550x400	CamScan
P0675	P0675_b1	0.5	300x300	CamScan
P0799	P0799_b1	0.5	300x300	CamScan
P0746	P0746_b1	0.5	300x300	CamScan
P0735	P0735_b1	0.5	300x300	CamScan
P0725	P0725_b1	0.5	300x300	CamScan
	P0725_b2	0.5	550x750	CamScan
P0731	P0731_b1	0.5	300x300	CamScan
	P0731_b2	0.5	550x510	CamScan
P0728	P0728_b1	0.5	300x300	CamScan
	P0728_b2	0.5	550x550	CamScan
P0768	P0768_b1	0.5	300x300	CamScan
	P0768_b2	0.5	550x700	CamScan
P0742	P0742_b1	0.5	550x630	CamScan
	P0742_b2	0.5	300x300	CamScan
P0791	P0791_b1	0.5	300x300	CamScan
P0773	P0773_b1	0.5	300x300	CamScan
	P0773_b2	0.5	550x650	CamScan
P0766	P0766_b1	0.5	300x300	CamScan
	P0766_b2	0.5	550x700	CamScan
P0747	P0747_b1	0.5	300x300	CamScan
	P0747_b2	0.5	550x560	CamScan

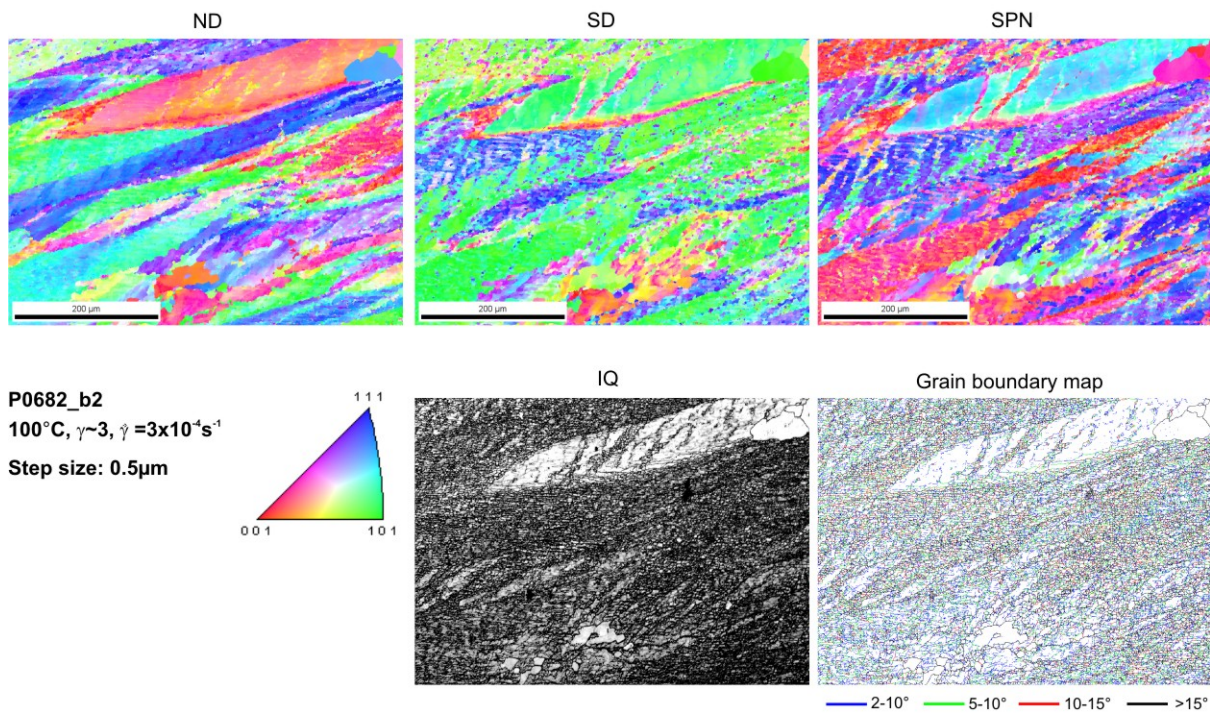
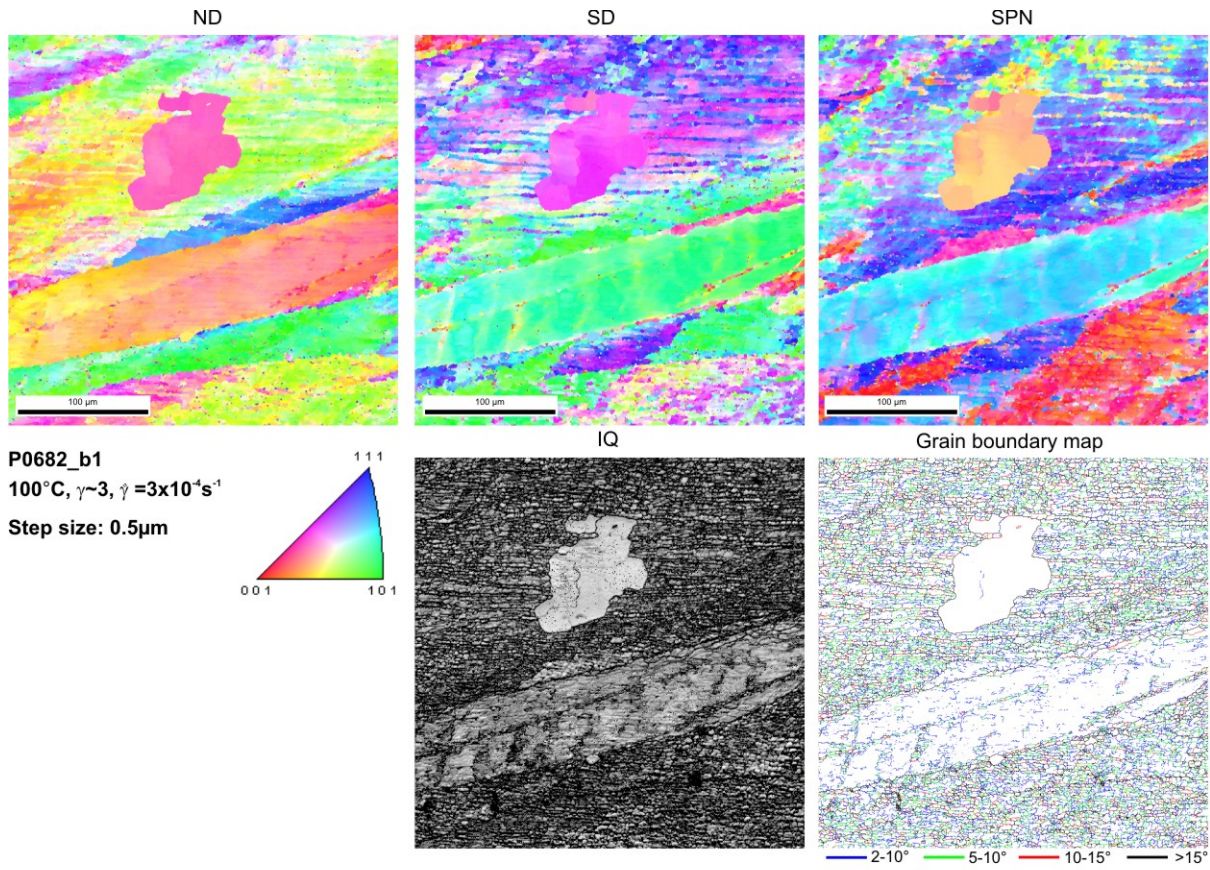
Following pages EBSD detail maps

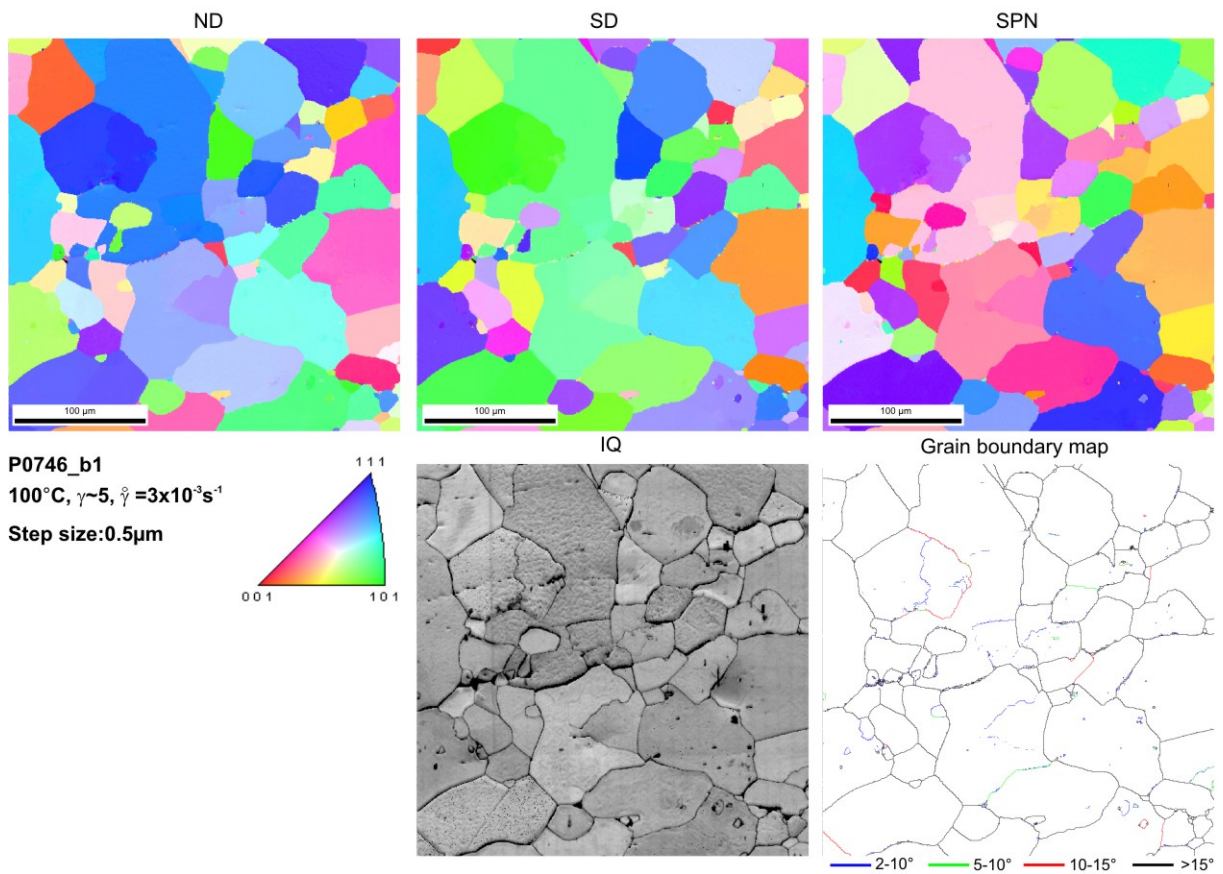
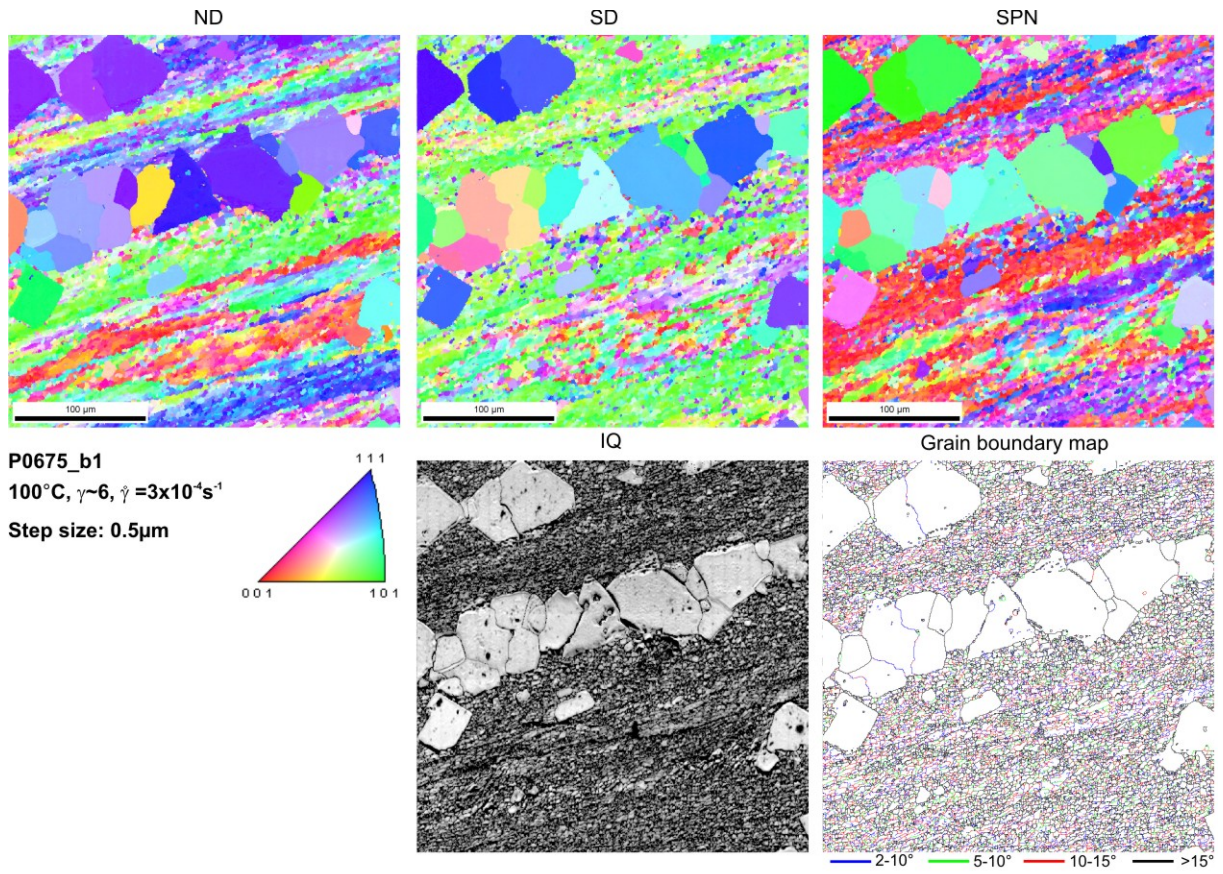


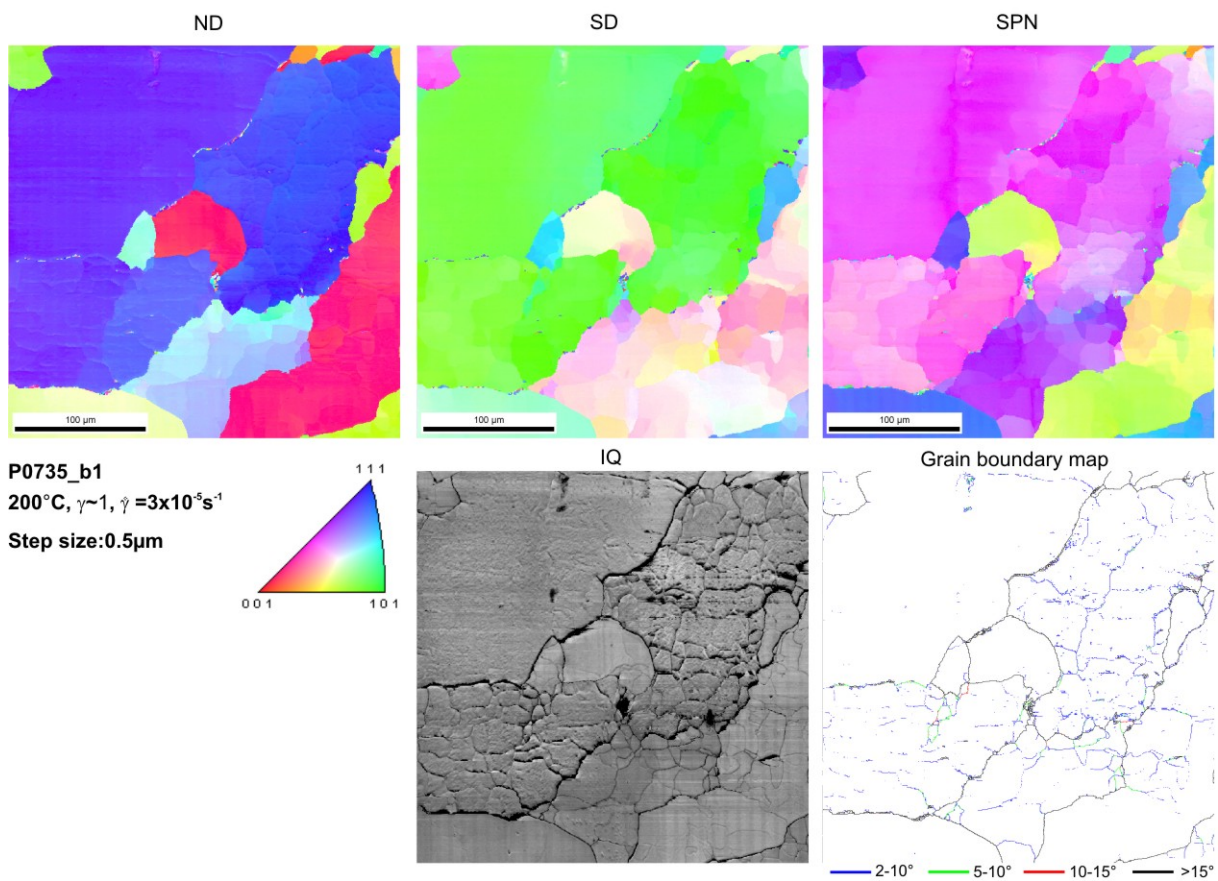
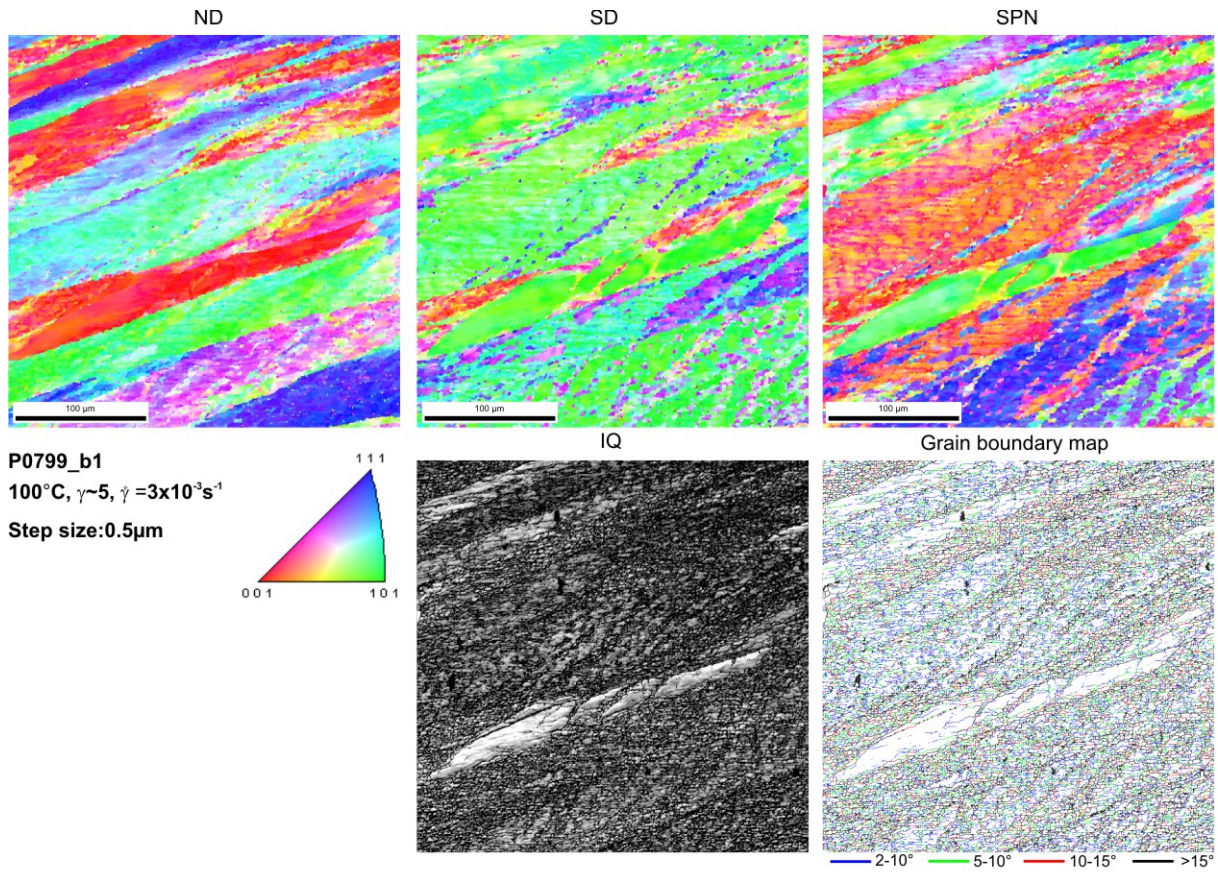


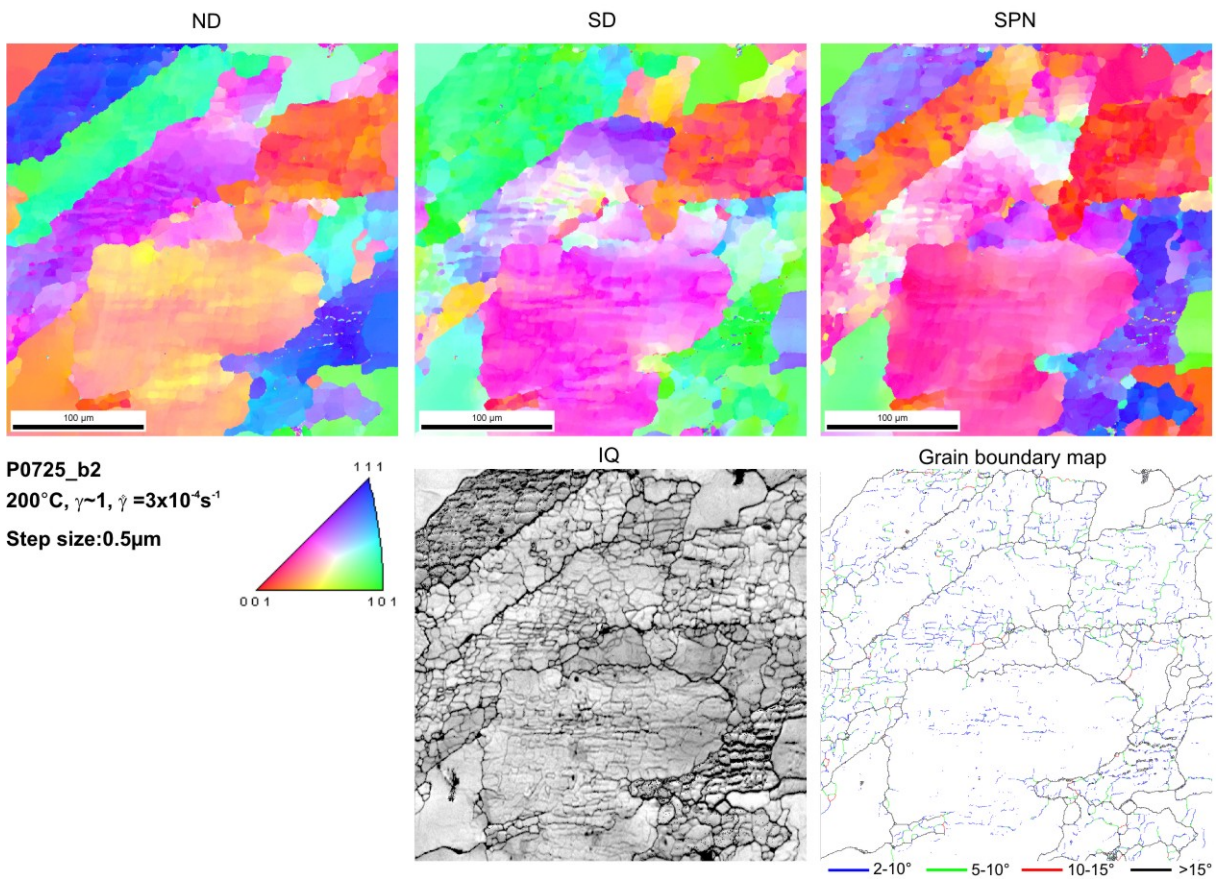
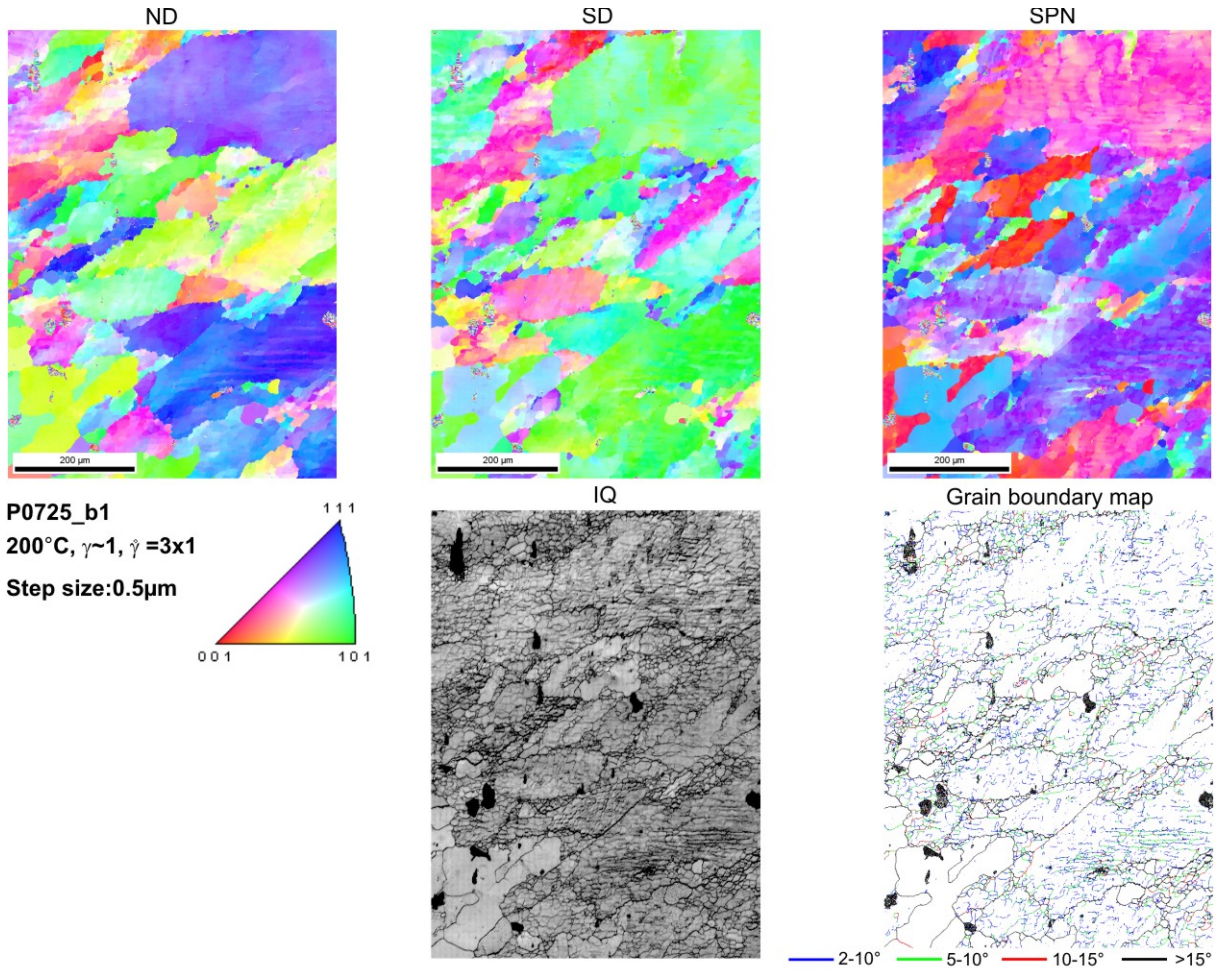


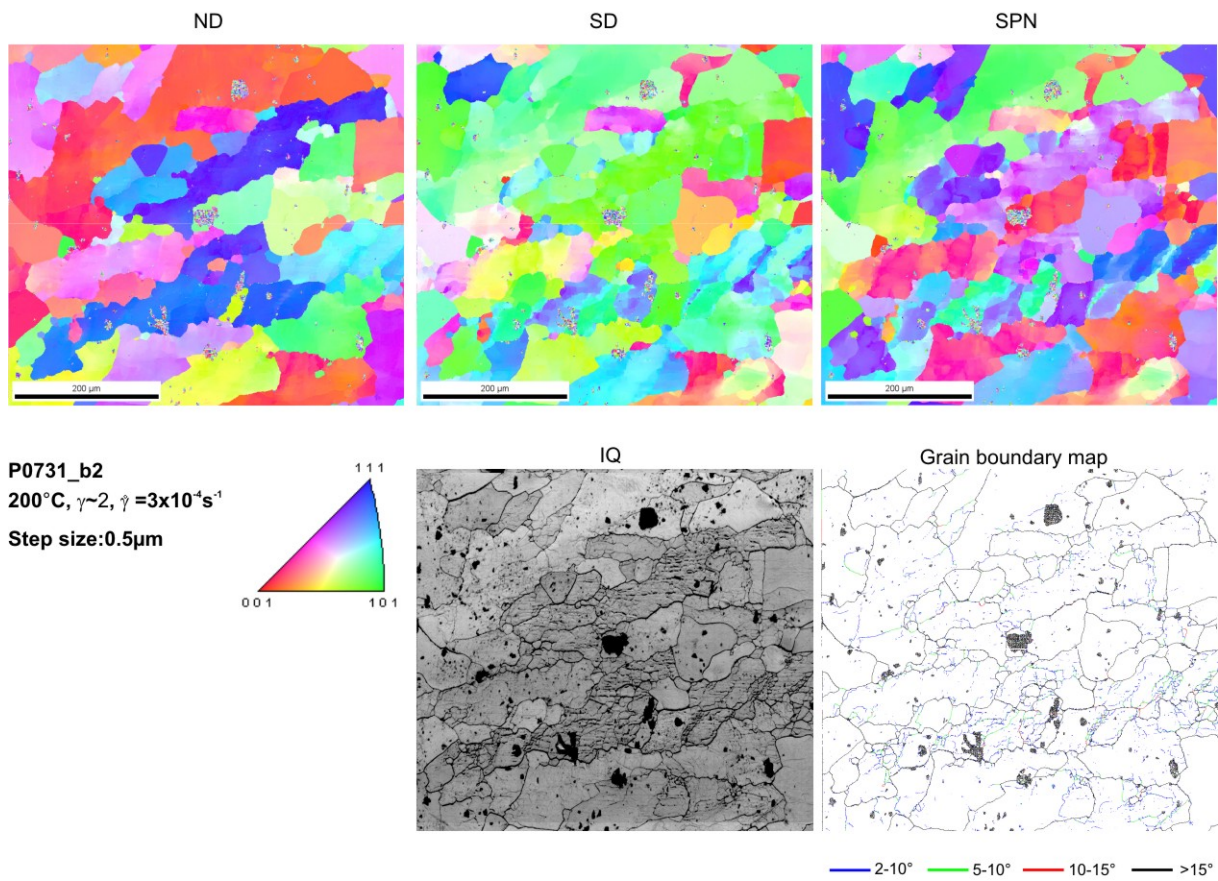
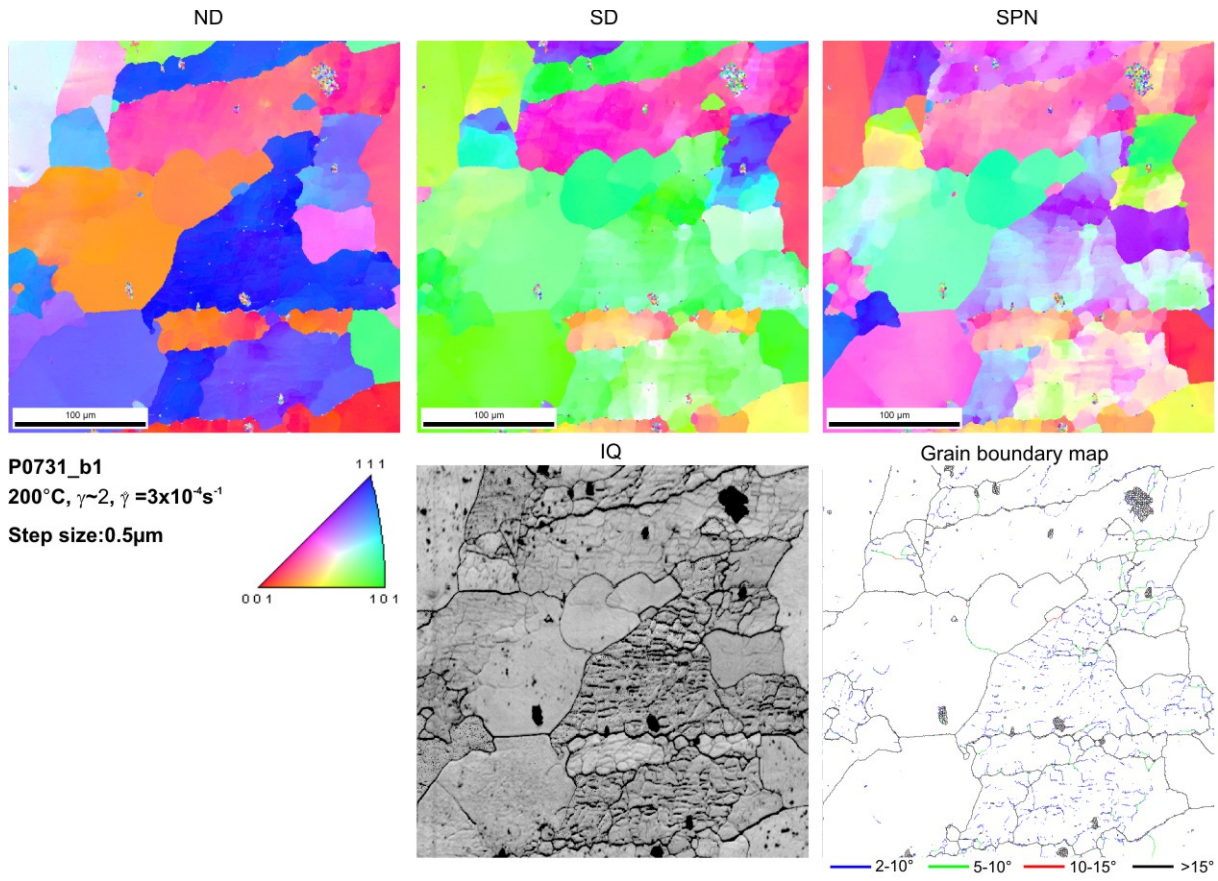


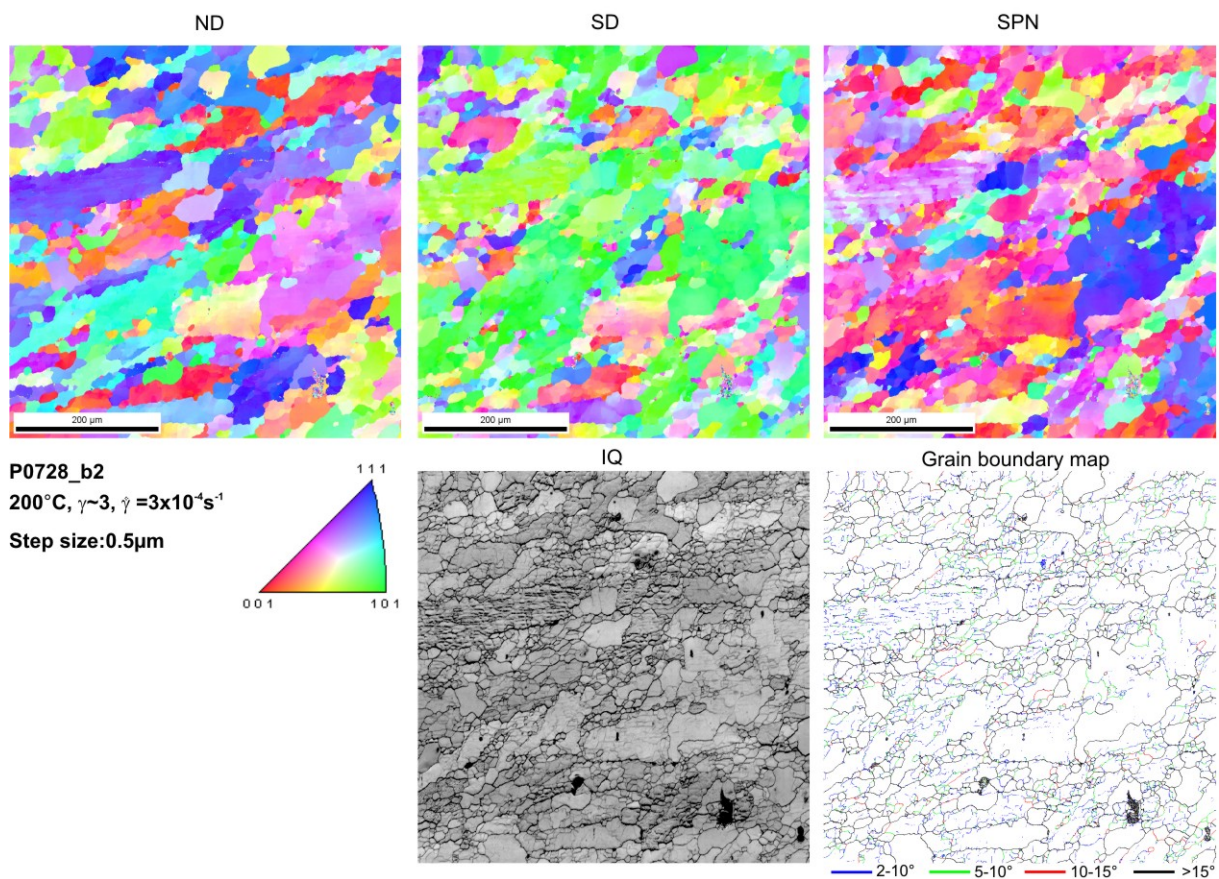
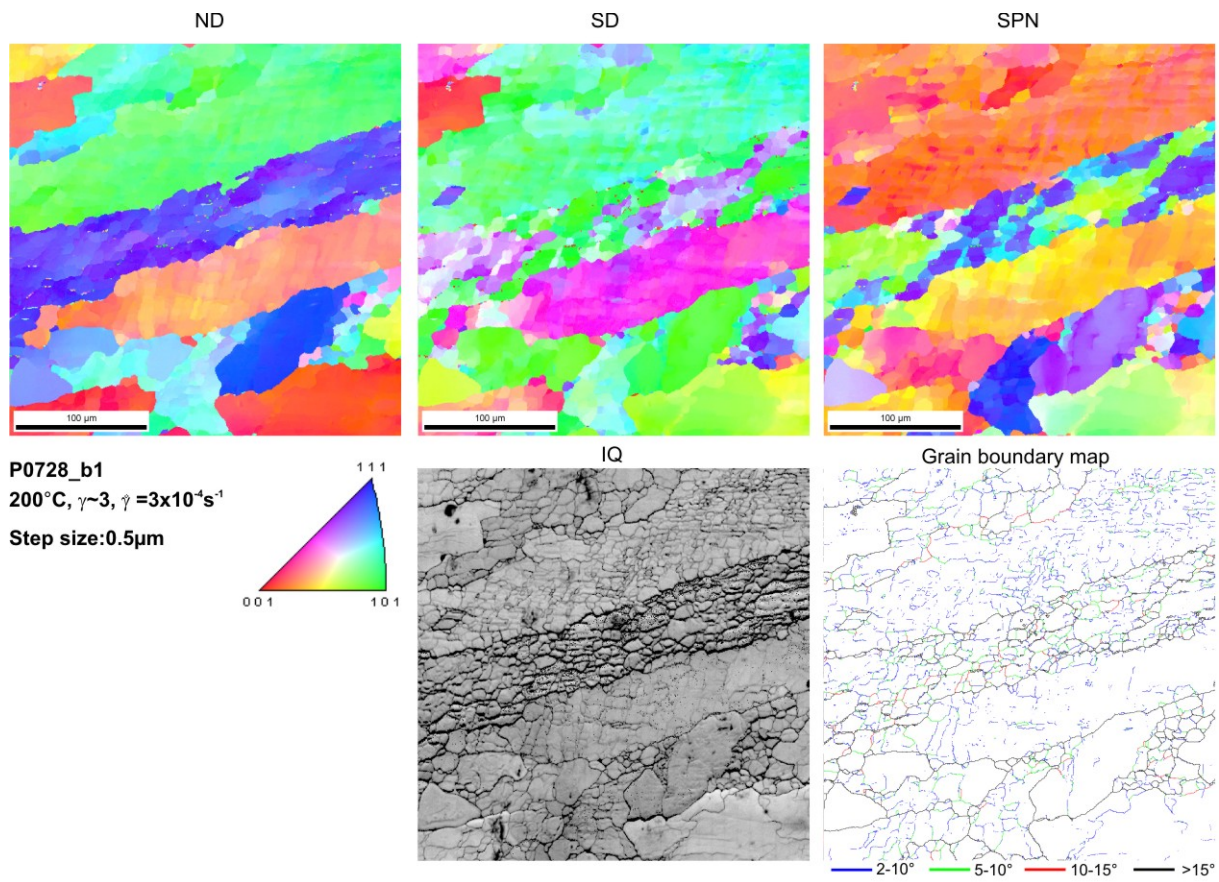


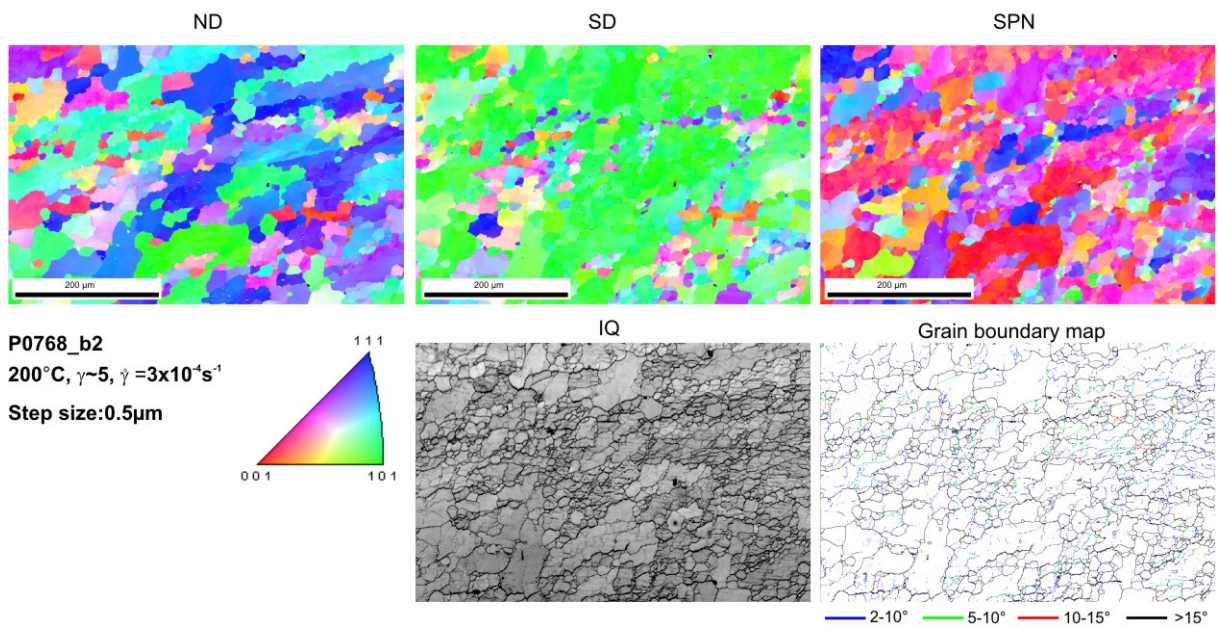
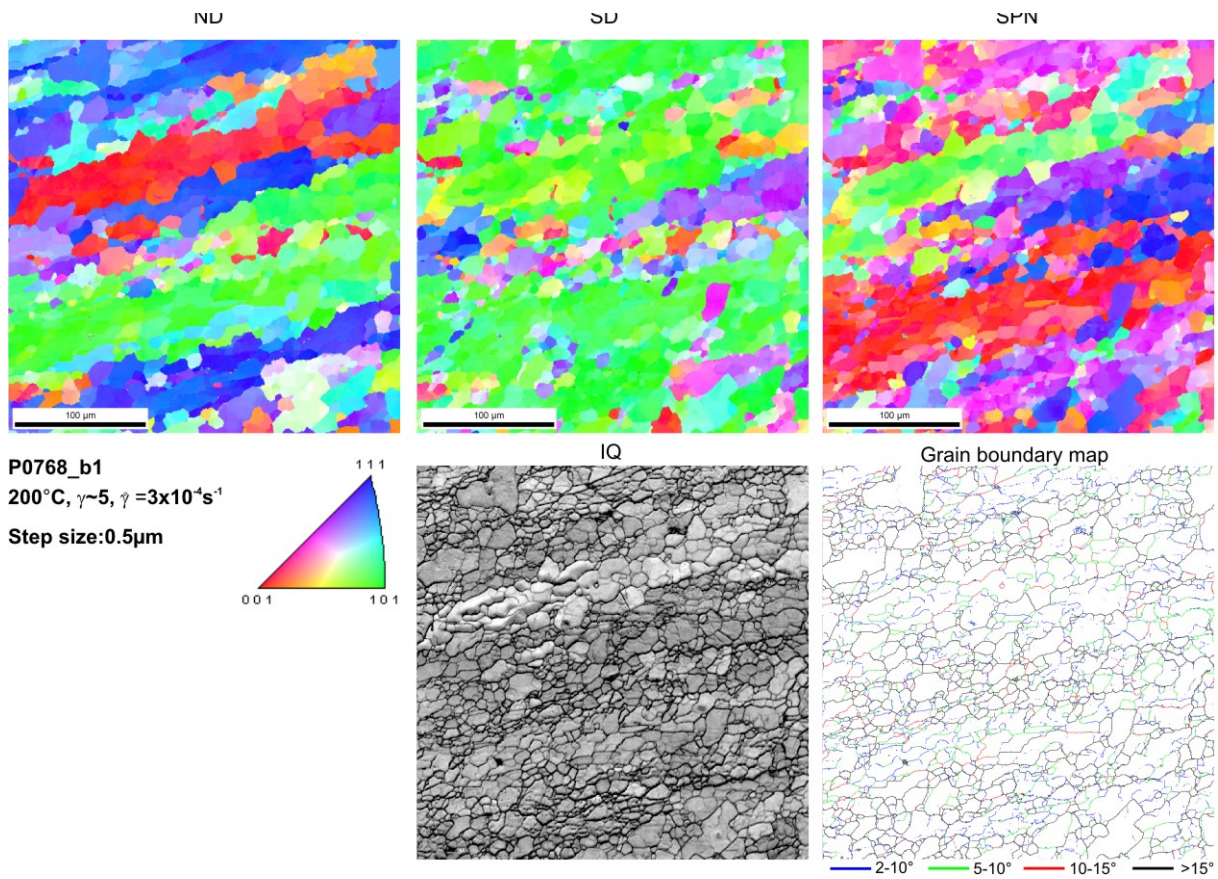


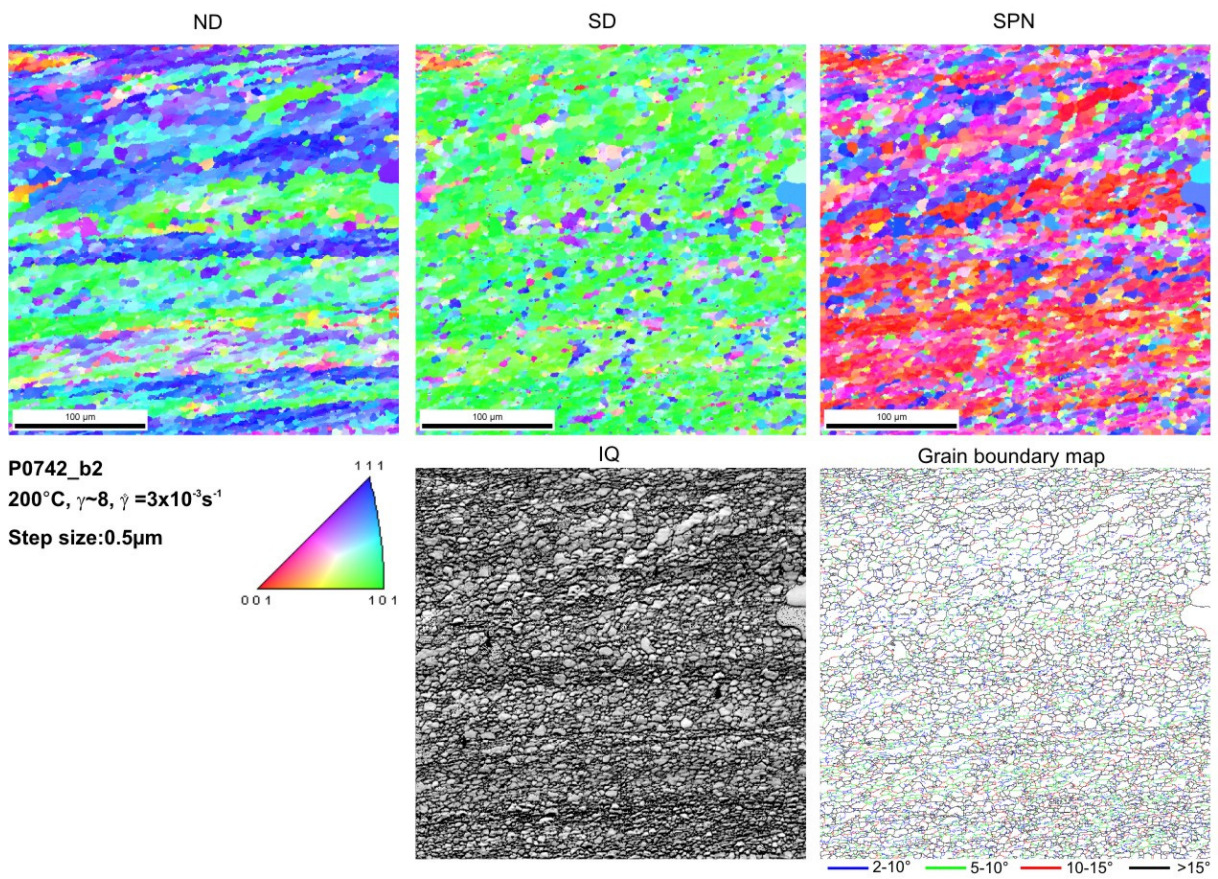
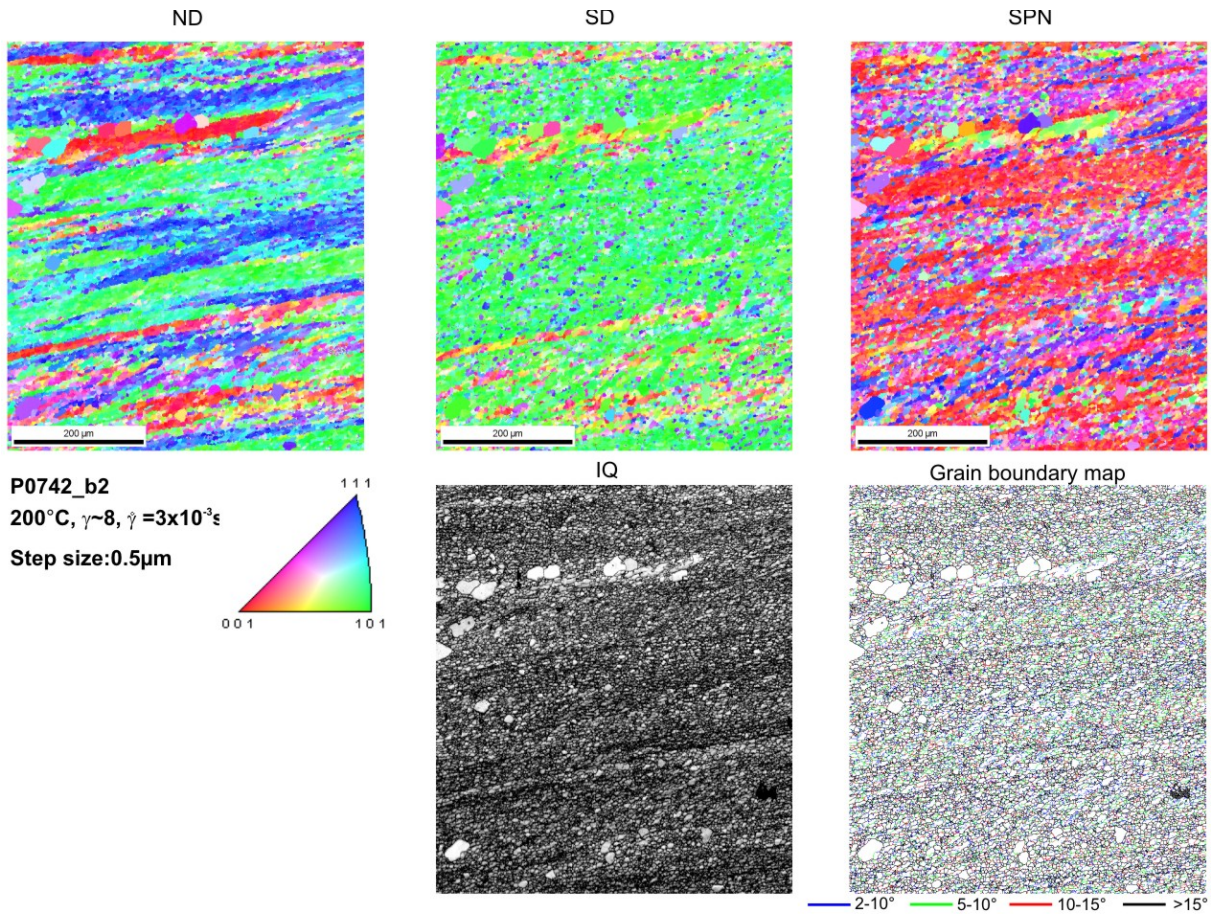


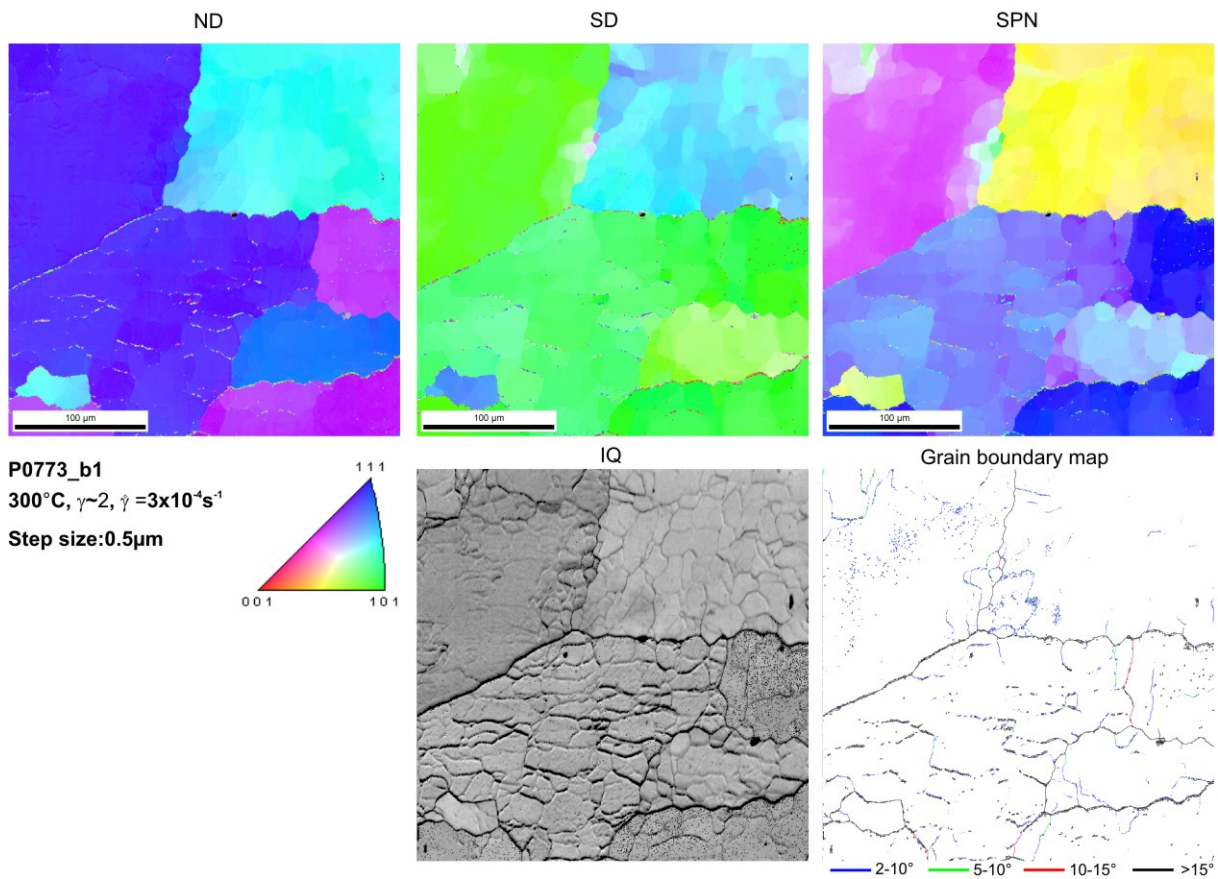
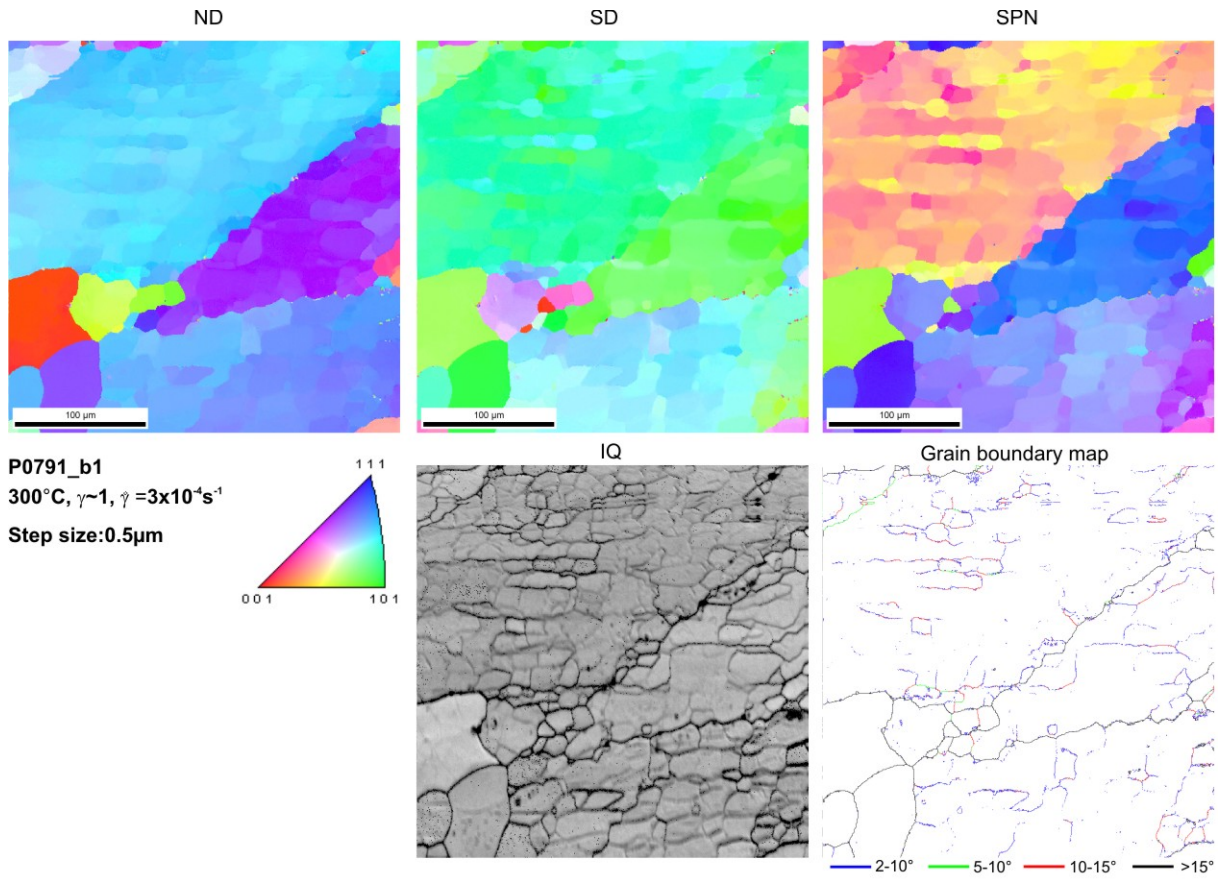


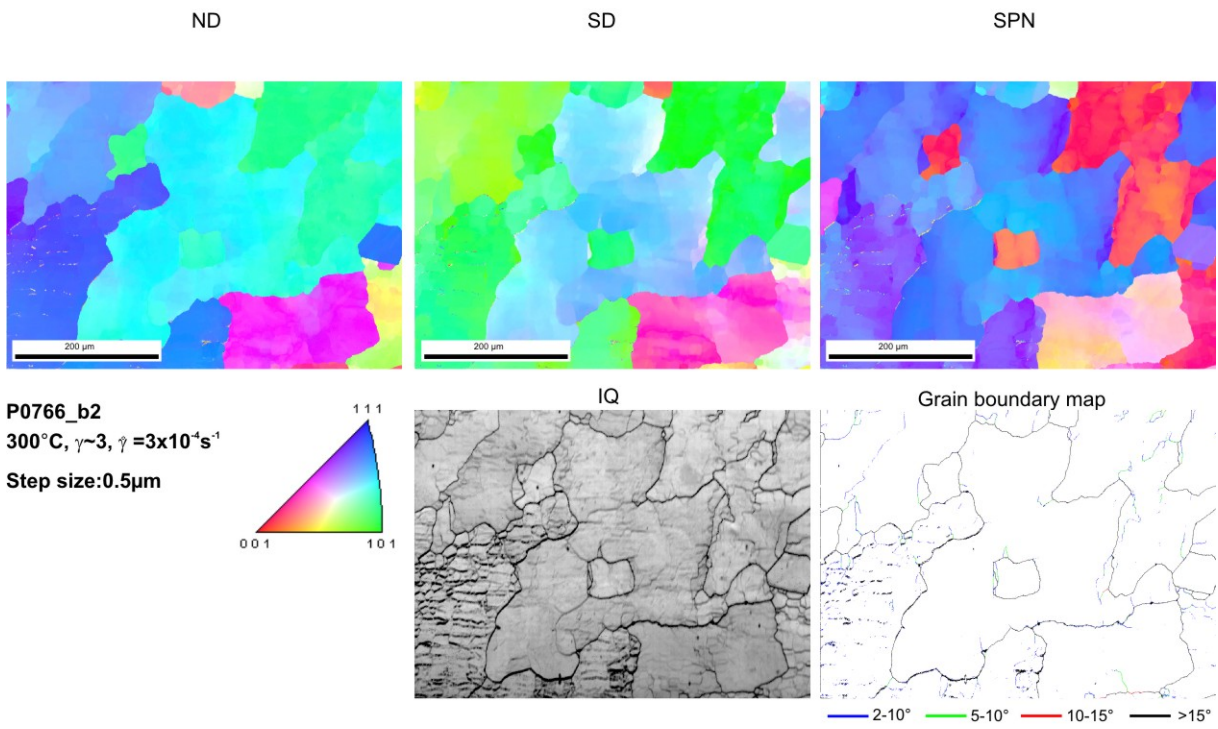
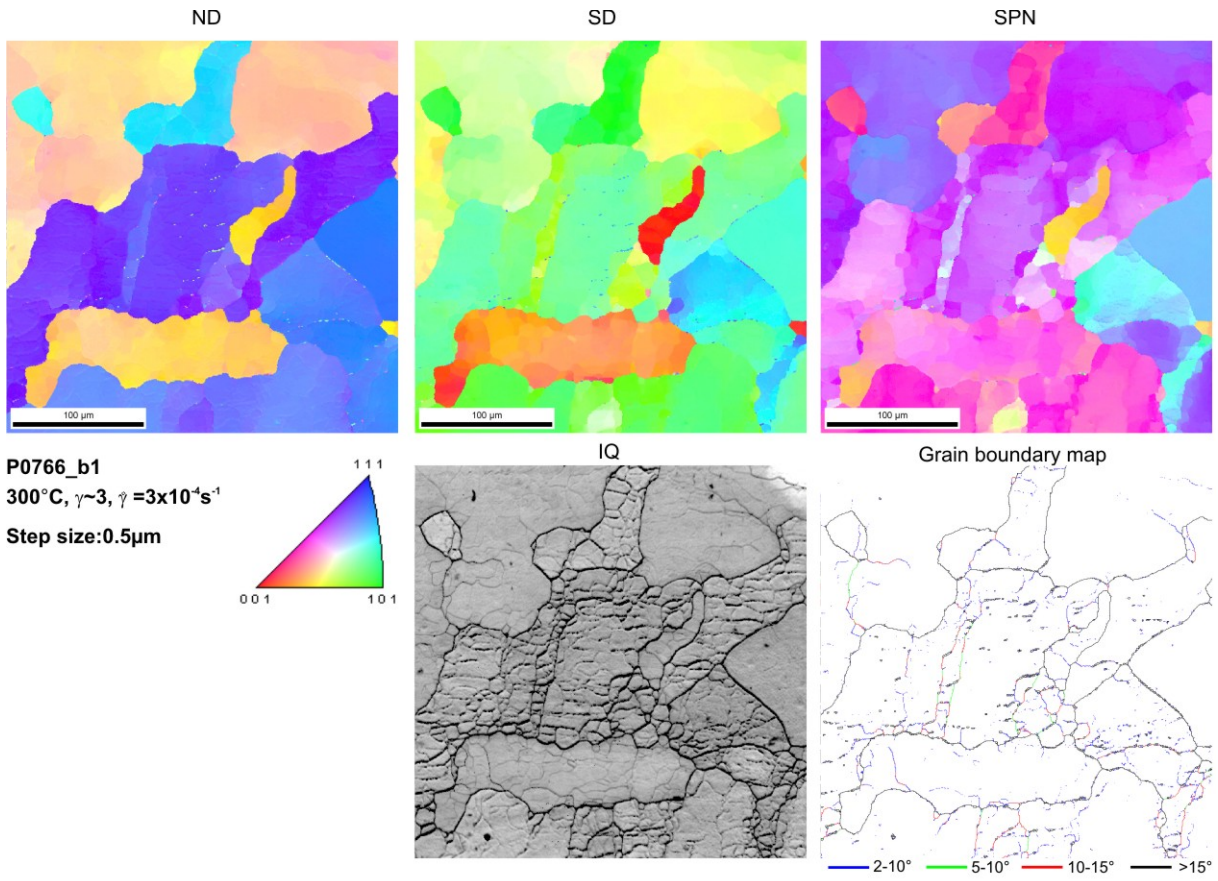


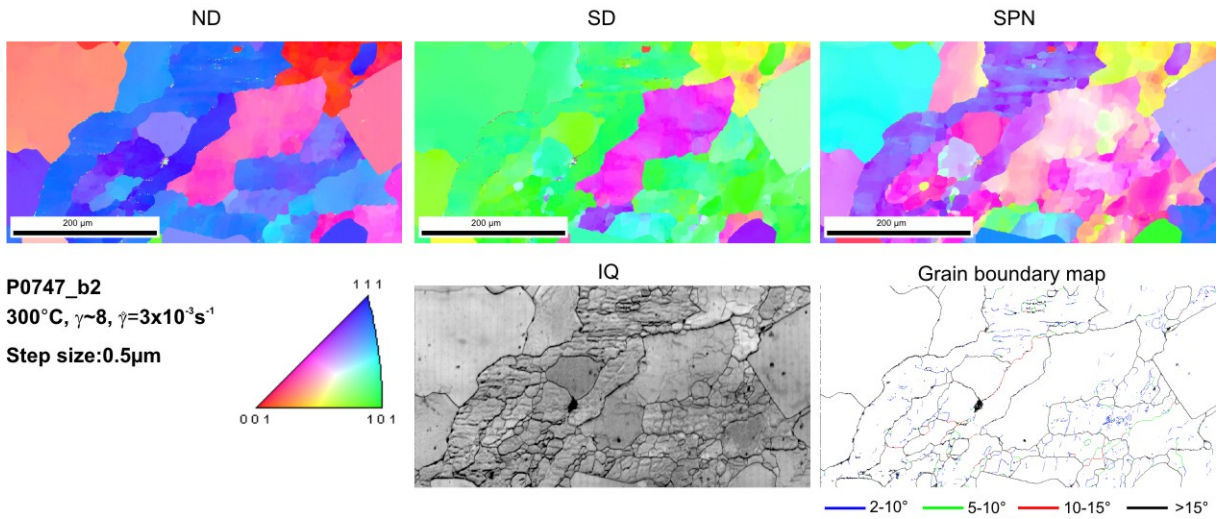
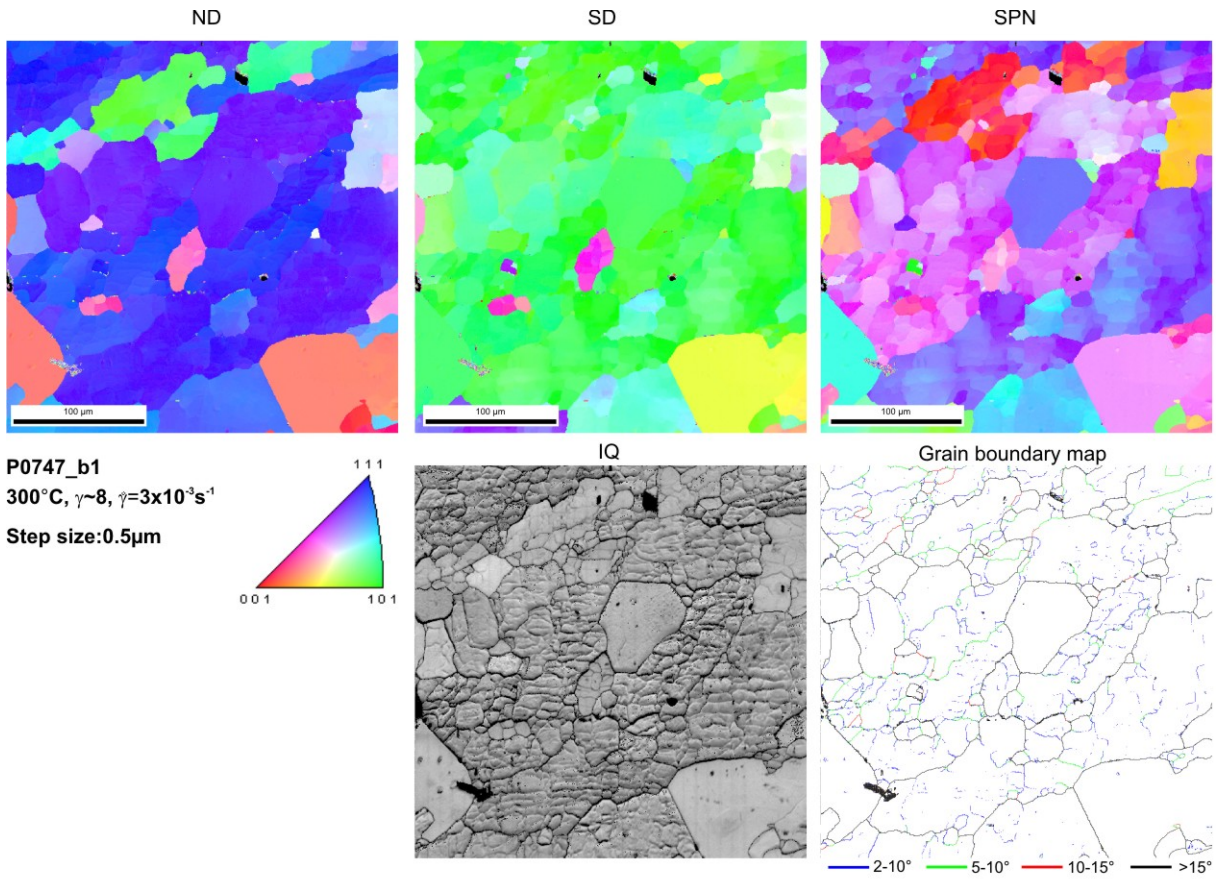












Appendix E

Uniaxial compression of sodium chlorate single crystals – application to pressure solution

Pressure solution is an important rock deformation mechanism, but a reliable pressure solution *creep law* does not exist. The major difficulty is that we do not understand the microstructure of grain boundaries in rocks that deform by pressure solution. It appears that the initially flat surface of a solid under stress is unstable and turns into a rough structure when material transport can take place, e.g. by solution transport through an aqueous fluid film. Pressure solution creep flow laws based on flat "thin fluid film" grain boundaries (Rutter 1976) are entirely different from those based on rough, "island-channel" grain boundaries (Spiers et al. 1990).

The study of the evolution of a solid-fluid interface under stress is essential for the understanding of deformation by dissolution-precipitation creep ("pressure solution"). According to the theory of (Srolovitz et al. 1985) a nominally flat surface of a soluble material turns into a rough surface when the solid is mechanically stressed and when material transport (e.g. by diffusion) is possible. This roughness consists of regular patterns of μ -scale grooves oriented perpendicular to the maximum compressive stress. The wavelength of the groove-pattern depends on surface energy and stress. Srolovitz' theory was investigated experimentally by den Brok & Morel (2001) using potassium alum ($\text{KAl}(\text{SO}_4)_2 \cdot 12\text{H}_2\text{O}$) as a rock analogue material.

The focus of this study lies on an experimental investigation using sodium chlorate (NaClO_3) as a rock analogue material. NaClO_3 is cubic brittle and very soluble salt, similar to K-alum. It is colourless and optical isotrop. The crystals are commonly rectangular and bounded by the prismatic (100) faces.

The experiments were carried out in a newly designed "see-through" deformation rig. The apparatus consists of two cells, the outer cell with the plastic frame and the inner cell where the crystal is localised. The inner cell consists of two 50x50x2 mm glass slides, a rubber ring and a pedestal for the crystal, two plastic stoppers and the piston. The saturated aqueous solution was filled by a syringe, which is placed in between the plastic frame and the two glass slides. The stress was applied on the crystal by a spring which is localised in a tube that is connected with the piston. The deformation apparatus rests horizontally on the microscope table. The NaClO_3 crystals were uniaxially stressed "in-situ" in a small see-through vessel filled with saturated NaClO_3 solution. For each experiment crystals were polished. After polishing, the crystal was measured and put in the apparatus and the rubber ring was filled with the saturated sodium chlorate solution. We leave the crystal unstressed for 1 to 2 hours so that it is in equilibrium with the fluid. After that time the crystal was loaded horizontally with stresses ranging from experiment to experiment from ~8 MPa under atmospheric fluid pressure. The experiment duration ranged between one to three days. The horizontal orientation was chosen so as to minimise possible effects due to gravity. (Koehn et al. 2004) proposed that gravity-induced convection in the saturated solution would possibly be responsible for migration of the grooves.

Our results (Fig.1) support previous observations made on K-alum. On sodium-chlorate surfaces, and in a horizontal position, a dynamically stable surface roughness is developed, with grooves moving around and changing shape and orientation. As soon as stress is removed, grooves stop moving and slowly disappear.

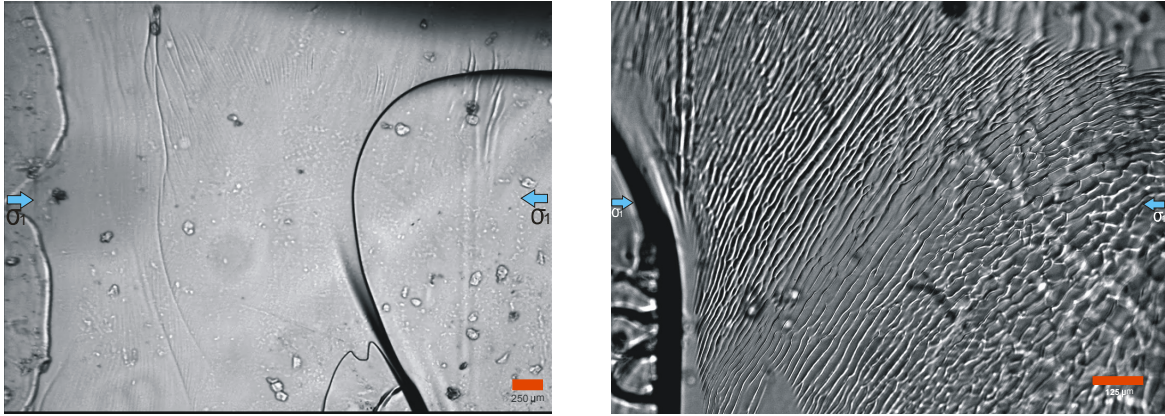


Fig 1: Deformation of a NaClO_3 crystal (Experiment NaClO_3_1). The crystal was stressed horizontally at 8 MPa. It shows grooves which develop in the upper part of the crystal. The grooves are perpendicular to the main stress orientation.

Our experiments essentially corroborate earlier results obtained on potassium alum. Grooves form according to Srolovitz' theory and they are mobile, i.e. slowly change position and orientation during the experiments. Our experiments further show: (i) gravity plays no significant role during the groove formation; (ii) the distance between the grooves increases with time. The grooves run mostly perpendicular to the principal stress direction and parallel to each other but show some braided geometries where grooves divert and re-join. The formation of these grooves can be explained with the Assaro-Tiller-Grinfeld instability caused by stress concentrations at the tips of microscopic imperfections in the crystal. This drives dissolution and thereby the formation of the grooves perpendicular to the principal stress (Asaro & Tiller 1972, Grinfeld 1986). With time the roughness of the grooves increase forming a strong coarsening pattern. Further studies clearly need to be carried out to understand the development of this surface roughness.

References

- Asaro, R. J. & Tiller, W. A. 1972. Interface morphology development during stress corrosion cracking: Part I, via surface diffusion. *Metallurgical and Material Transactions* **3**, 1789-1796.
- den Brok, S. W. J. & Morel, J. 2001. The effect of elastic strain on the microstructure of free surfaces of stressed minerals in contact with an aqueous solution. *Geophysical Research Letters* **28**(4), 603-606.
- Grinfeld, M. A. 1986. Instability of the separation boundary between a non-hydrostatically stressed solid and a melt. *Soviet Physics Doklady* **31**, 831.
- Koehn, D. 2004. Transient dissolution patterns on stressed crystal surfaces. *Geochemica et Cosmochimica Acta* **68**(16), 3317-3325.
- Rutter, E. H. 1976. Kinetics of Rock Deformation by Pressure Solution. *Philosophical Transactions of the Royal Society of London Series a-Mathematical Physical and Engineering Sciences* **283**(1312), 203-219.
- Spiers, C. J., Schutjens, P. M. T. M., Brzesowsky, R. H., Peach, C. J., Liezenberg, J. L. & Zwart, H. J. 1990. Experimental determination of constitutive parameters governing creep of rocksalt by pressure solution. In: *Deformation Mechanisms, Rheology and Tectonics* (edited by Knipe, R. J. R., E.H.) **54**. Geological Society Special Publication, 215-227.

Srolovitz, D. J., Grest, G. S. & Anderson, M. P. 1985. Computer-Simulation of Grain-Growth
.5. Abnormal Grain-Growth. *Acta Metallurgica* **33**(12), 2233-2247.